

Achieving electroweak precision at future electron-positron colliders

Dissertation
zur Erlangung des Doktorgrades
an der Fakultät für Mathematik, Informatik
und Naturwissenschaften
Fachbereich Physik
der Universität Hamburg

vorgelegt von
Jakob Beyer

Hamburg

2022

Gutachterin/Gutachter der Dissertation:	Dr. Jenny List Prof. Dr. Elisabetta Gallo
Zusammensetzung der Prüfungskommission:	Dr. Jenny List Prof. Dr. Elisabetta Gallo Prof. Dr. Bernd Andreas Kniehl Prof. Dr. Gudrid Moortgat-Pick Dr. Jürgen Reuter
Vorsitzende/r der Prüfungskommission:	Prof. Dr. Bernd Andreas Kniehl
Datum der Disputation:	01.12.2022
Vorsitzender Fach-Promotionsausschuss PHYSIK:	Prof. Dr. Wolfgang J. Parak
Leiter des Fachbereichs PHYSIK:	Prof. Dr. Günter H. W. Sigl
Dekan der Fakultät MIN:	Prof. Dr.-Ing. Norbert Ritter

Abstract

The particle physics community is currently discussing the next large-scale electron-positron collider experiment, with a major interest in the Higgs production threshold around 250 GeV. Multiple proposals have emerged for such a machine, differing in machine and detector designs, as well as energy stages and luminosities. Striving for a machine with the best possible precisions requires both an optimization of each proposal as well a careful examination of the differences between them.

The optimization of the individual proposals needs dedicated studies based on detailed simulation of the experiment. Such studies can point out the most critical aspects in the precision, such as e.g. specific steps in the event reconstruction.

For understanding the differences between the proposals, a generic approach can be insightful. By neglecting some details and focusing on specific differences, the trade-offs of a choice of one specific collider become clearer. This is especially relevant for the 250 GeV energy stage, which is common to most proposals and central to the physics program.

This work contains two studies, corresponding to the two tasks above.

The first is a full-simulation study of vector boson scattering (VBS) in the hadronic final state at the 1 TeV stage of the International Linear Collider. This study focuses on the different reconstruction aspects in hadronic final states, which have the highest cross-sections of all W/Z decay modes.

A second, more extensive study performs electroweak fits using a generic 250 GeV e^+e^- collider with varying beam polarisation and luminosity scenarios. The trade-off between luminosity and availability of beam polarisation is one of the key differences between the proposed colliders. This study investigates how these choices impact the precision on physical and systematic parameters - including the polarisations themselves - and the correlations between physical parameters and systematic effects. It further directly includes a detector systematic to see whether beam polarisation leads to a smaller impact of chirality-independent systematic effects.

The body of this thesis gives an overview of the current theory and future collider landscapes, and describes both studies in full detail, including the datasets, methods, and findings.

The VBS study finds that the clustering of hadronic final states, the removal of background particles in forward jets, and semi-leptonic decays within jets all significantly degrade the resolution. High level reconstruction remains a limiting factor of electroweak precision, and future studies can look into improving the above named reconstruction aspects to improve the precision in hadronic events.

The study of electroweak fits finds that beam polarisation gives access to chiral observables, which allows assumption-free measurement of fermion pair production parameters, and adds significant sensitivity to the measurement of triple gauge couplings. In this context, higher luminosities can only make up for a lack of beam polarisation when introducing a strong set of assumptions. The measurement of beam polarisation

in parallel to electroweak parameters with only one polarised beam leads to strong correlations of polarisations with physical parameters, which disappear when both beams are polarised. Finally, the explicitly included detector systematic does not affect any chiral observables, and the fit can extract the exact shape of the systematic effect with high precision. These results show that a careful examination of the impact of beam polarisation is necessary in order to understand the qualitative and quantitative impacts on the achievable precision. Especially the impact on systematic uncertainties will require further studies. For the discussion among different collider proposals, beam polarisation will play a key role and will shape the future of electroweak precision measurements.

Zusammenfassung

In der Teilchenphysik wird derzeit über das nächste große Elektron-Positron-Collider-Experiment diskutiert. Dabei steht die Higgs-Produktionsschwelle bei 250 GeV im Mittelpunkt. Es gibt mehrere Vorschläge für eine solche Anlage. Diese Vorschläge unterscheiden sich in Design der Maschine und des Detektors, sowie in den Energiestufen und Luminositäten. Das Streben nach einer Maschine mit der bestmöglichen Genauigkeit erfordert sowohl eine Optimierung der einzelnen Vorschläge als auch eine sorgfältige Untersuchung der Unterschiede zwischen ihnen.

Die Optimierung der einzelnen Maschinen erfordert spezielle Studien auf der Grundlage detaillierter Simulationen der Experimente. Solche Studien können die kritischsten Aspekte bei der Genauigkeit aufzeigen, wie z.B. bestimmte Schritte bei der Rekonstruktion von Kollisionsereignissen.

Um die Unterschiede zwischen den Vorschlägen zu verstehen, ist ein allgemeiner Ansatz aufschlussreich. Wenn man einige Details vernachlässigt und sich auf spezifische Unterschiede konzentriert, werden die Kompromisse bei der Wahl eines bestimmten Kolliders deutlicher. Dies ist besonders für die 250 GeV-Energiestufe relevant, die den meisten Vorschlägen gemein ist und im Mittelpunkt des Physikprogramms steht.

Diese Doktorarbeit umfasst zwei Studien, die den beiden oben genannten Aufgaben entsprechen.

Die erste ist eine Studie mit vollständiger Detektorsimulation für Vektorbosonenstreuung (VBS) im hadronischen Endzustand bei 1 TeV des International Linear Collider. Diese Studie konzentriert sich auf die verschiedenen Rekonstruktionsaspekte in hadronischen Endzuständen, die die höchsten Wirkungsquerschnitte aller W/Z -Zerfallsarten aufweisen.

In einer zweiten, umfassenderen Studie werden elektroschwache Fits an einem generischen 250 GeV e^+e^- Collider mit unterschiedlichen Strahlpolarisationen und Luminositätsszenarien durchgeführt. Der Kompromiss zwischen Luminosität und Verfügbarkeit der Strahlpolarisation ist einer der Hauptunterschiede zwischen den vorgeschlagenen Collidern. In dieser Studie wird untersucht, wie sich diese Entscheidungen auf die Präzision der physikalischen und systematischen Parameter - einschließlich der Polarisationen selbst - und die Korrelationen zwischen physikalischen Parametern und systematischen Effekten auswirken. Darüber hinaus wird eine Detektorsystematik direkt einbezogen, um festzustellen, ob die Strahlpolarisation zu einer geringeren Auswirkung von chiralitätsunabhängigen systematischen Effekten führt.

Der Hauptteil dieser Arbeit gibt einen Überblick über die aktuelle Theorie und eine Einführung in zukünftige Collider, und beschreibt beide Studien in allen Einzelheiten, einschließlich der Datensätze, Methoden und Ergebnisse.

Die VBS-Studie zeigt, dass das Clustern von hadronischen Endzuständen, das Entfernen von Hintergrundteilchen in Vorwärtsjets und semi-leptonische Zerfälle in Jets die Auflösung erheblich verschlechtern. Die High-Level Rekonstruktion bleibt ein begrenzender Faktor der elektroschwachen Präzision, und zukünftige Studien können sich mit

der Verbesserung der oben genannten Rekonstruktionsaspekte befassen, um die Präzision bei hadronischen Ereignissen zu verbessern.

Die Untersuchung der elektroschwachen Fits zeigt, dass die Strahlpolarisation Zugang zu chiralen Observablen bietet, was eine annahmefreie Messung von Parametern der Fermionenpaarproduktion ermöglicht und die Messung von Dreifach-Eichkopplungen deutlich empfindlicher macht. In diesem Zusammenhang können höhere Luminositäten das Fehlen der Strahlpolarisation nur dann ausgleichen, wenn eine Reihe strenger Annahmen getroffen wird. Die Messung der Strahlpolarisation parallel zu elektroschwachen Parametern mit nur einem polarisierten Strahl führt zu starken Korrelationen der Polarisierungen mit physikalischen Parametern, die verschwinden, wenn beide Strahlen polarisiert sind. Die explizit berücksichtigte Detektorsystematik wirkt sich nicht auf chirale Messgrößen aus, und die Fits können die genaue Form des systematischen Effekts mit hoher Genauigkeit bestimmen. Diese Ergebnisse zeigen, dass eine sorgfältige Untersuchung des Einflusses der Strahlpolarisation notwendig ist, um die qualitativen und quantitativen Auswirkungen auf die erreichbare Genauigkeit zu verstehen. Insbesondere die Auswirkungen auf die systematischen Unsicherheiten müssen weiter untersucht werden. In der Diskussion zwischen verschiedenen Collider-Vorschlägen wird die Strahlpolarisation eine Schlüsselrolle spielen und die Zukunft der elektroschwachen Präzisionsmessungen bestimmen.

Contents

List of Figures	xiii
List of Tables	xvii
Abbreviations	xx
1 Introduction	1
2 Theory	3
2.1 The current Standard Model of particle physics	3
2.2 The Standard Model as an effective field theory	19
3 Future e^+e^- collider proposals	25
3.1 Overview and common aspects	25
3.2 The International Linear Collider	34
3.3 The International Large Detector	42
4 Previous studies and open questions	49
4.1 The Impact of beam polarisation at e^+e^- colliders	49
4.2 Gauge boson self-coupling in e^+e^- collisions	51
4.3 Purpose of this work	54
5 Datasets	55
5.1 The ILC/ILD Monte-Carlo production	55
5.2 Datasets at 1 TeV	57

CONTENTS

5.3	Datasets at 250 GeV	59
6	Separating hadronic decays of boson pairs	63
6.1	Reconstructing the hadronic di-boson decay	64
6.2	Quantification of di-boson separation	65
6.3	Identifying reconstruction challenges	66
6.4	Comparing detector models	74
6.5	Conclusion	74
7	Impact of beam polarisation on electroweak fits	77
7.1	Assembling electroweak fits	77
7.2	Choosing collider scenarios	80
7.3	Choosing processes, parameters and effects	83
7.4	Including the muon acceptance	98
7.5	Fits in this study	110
7.6	Two-fermion fits: Chiral disentangling with beam polarisation	111
7.7	Four-fermion fits: Polarisation measurement in the presence of physical parameters	126
7.8	Combining two- and four-fermion fits	144
7.9	Conclusions	155
8	Conclusion	161
	References	163
	Appendix	a-1
A	Datasets	a-2
B	Separating hadronic decays of boson pairs	a-3
C	Impact of beam polarisation on electroweak fits	a-19

Contents (detailed)

List of Figures	xiii
List of Tables	xvii
Abbreviations	xx
1 Introduction	1
2 Theory	3
2.1 The current Standard Model of particle physics	3
2.1.1 Introducing and breaking the symmetries of electroweak interactions .	5
2.1.2 The strong interaction of Quantum Chromo-Dynamics	10
2.1.3 Calculating fermion pair production	13
2.1.4 What the SM (probably) cannot explain	19
2.2 The Standard Model as an effective field theory	19
2.2.1 The SM as low-energy effective theory	20
2.2.2 Experimental insight using the EFT approach	21
2.2.3 Anomalous Triple Gauge Couplings	23
3 Future e^+e^- collider proposals	25
3.1 Overview and common aspects	25
3.1.1 Physics at future e^+e^- colliders	25
3.1.2 Advanced e^+e^- proposals	27
3.1.3 Beam polarisation	29
3.1.4 Beam-induced backgrounds	33
3.2 The International Linear Collider	34
3.2.1 Luminosity measurement	37
3.2.2 Polarisation implementation	38

Contents (detailed)

3.2.3	Polarisation measurement	40
3.3	The International Large Detector	42
3.3.1	Detector design	42
3.3.2	Recent optimization efforts	45
3.3.3	Relevant performance aspects	46
4	Previous studies and open questions	49
4.1	The Impact of beam polarisation at e^+e^- colliders	49
4.2	Gauge boson self-coupling in e^+e^- collisions	51
4.2.1	Triple Gauge Couplings	51
4.2.2	Quartic Gauge Couplings and Vector Boson Scattering	53
4.3	Purpose of this work	54
5	Datasets	55
5.1	The ILC/ILD Monte-Carlo production	55
5.1.1	Event generation for the ILC	55
5.1.2	The ILD detector simulation and event reconstruction chain	56
5.1.3	Truth-level information in the production chain	57
5.2	Datasets at 1 TeV	57
5.3	Datasets at 250 GeV	59
6	Separating hadronic decays of boson pairs	63
6.1	Reconstructing the hadronic di-boson decay	64
6.2	Quantification of di-boson separation	65
6.3	Identifying reconstruction challenges	66
6.3.1	Understanding the kinematics	66
6.3.2	Deciphering steps of the reconstruction	69
6.3.3	Identifying the most relevant effects	70
6.3.4	Guiding improvements in the event reconstruction	73
6.4	Comparing detector models	74
6.5	Conclusion	74
7	Impact of beam polarisation on electroweak fits	77
7.1	Assembling electroweak fits	77

7.1.1	Explanation of the fit on a single polarised dataset	78
7.1.2	Fits using multiple polarised datasets	79
7.1.3	External constraints	80
7.1.4	Nature of the framework	80
7.2	Choosing collider scenarios	80
7.2.1	Scenarios inspired by proposed colliders	81
7.2.2	Impact of luminosity sharing on event numbers	83
7.3	Choosing processes, parameters and effects	83
7.3.1	Processes and their differential distributions	84
7.3.2	Parameterising fermion pair production	86
7.3.3	WW parametrisation	93
7.3.4	TGC sensitivity of W pair production	95
7.3.5	Including systematic effects	98
7.4	Including the muon acceptance	98
7.4.1	A simple muon acceptance model	99
7.4.2	Impact of the muon acceptance on generator-level distributions	100
7.4.3	Implementation challenges in muon pair production	103
7.4.4	Fit-Parametrisation of the muon acceptance	105
7.4.5	Validating the parametrisation	105
7.4.6	Validating the physics-systematics factorisation	107
7.4.7	Simple demonstration of a fitted systematic effect	109
7.5	Fits in this study	110
7.6	Two-fermion fits: Chiral disentangling with beam polarisation	111
7.6.1	Access to chiral information with beam polarisation	116
7.6.2	Translating unpolarised measurements to chiral parameters	117
7.6.3	Polarisation and theory knowledge in the forward-backward asymmetry interpretation	118
7.6.4	Comparison to dedicated Z -pole runs	120
7.6.5	Small impact of muon acceptance	126
7.7	Four-fermion fits: Polarisation measurement in the presence of physical parameters	126
7.7.1	Polarisation measurement gains from additional datasets	131
7.7.2	Polarisation measurement with one polarised beam	133
7.7.3	Roles of asymmetry and normalisation information in W pair production	136
7.7.4	Impact of polarised beams on the TGC measurement	138
7.7.5	Negligible role of muon acceptance in W pair production	144
7.8	Combining two- and four-fermion fits	144
7.8.1	Direct improvements for systematic effects	150
7.8.2	Indirect improvements for physical effects	152

Contents (detailed)

7.8.3	Final precisions and limitations of this study	153
7.9	Conclusions	155
7.9.1	Recommendations for future studies	157
8	Conclusion	161
	References	163
	Appendix	a-1
A	Datasets	a-2
A.1	Uncertainties on fractional cross-sections	a-2
B	Separating hadronic decays of boson pairs	a-3
B.1	Mass distributions	a-3
B.2	Complete set of fits to mass distributions	a-6
B.3	Idealization steps in the small ILD model	a-15
B.4	ROC curves for the idealization steps	a-17
C	Impact of beam polarisation on electroweak fits	a-19
C.1	Detailed derivation of the $2f$ parametrisation	a-19
C.2	Implementation of the WW chiral cross-section parameters	a-24
C.3	Details on TGC rescanning with WHIZARD	a-25
C.4	TGC impact on differential distributions	a-28
C.5	Muon acceptance cut impact	a-31
C.6	Additional muon acceptance validity check plots	a-34
C.7	Fit results in numbers	a-38
C.8	Polarisation measurement with one polarised beam (Details)	a-59
C.9	Unpolarised polarisation measurement in W pair production	a-70

List of Figures

2.1	Schematic overview of the SM symmetries.	4
2.2	TGC and QGC vertices in the SM.	9
2.3	Schematic overview of jet formation in $e^+e^- \rightarrow q\bar{q}$ [23].	11
2.4	$e^+e^- \rightarrow q\bar{q}$ candidate event at ALEPH [30].	12
2.5	General $e^+e^- \rightarrow f\bar{f}$ Feynman diagram.	13
2.6	Feynman diagram and kinematics overview for $e^+e^- \rightarrow Z \rightarrow f\bar{f}$	14
2.7	Feynman diagrams explaining the return-to-Z process.	18
2.8	Energy-dependent impact of TGCs on the total unpolarised $e^+e^- \rightarrow W^+W^-$ cross-section [57].	21
3.1	Dominant processes in e^+e^- collision, depending on \sqrt{s} [69].	26
3.2	Higgsstahlung Feynman diagram.	26
3.3	Running plans for the four main e^+e^- collider proposals.	28
3.4	Schematic of the SLC polarised e^- source [96].	31
3.5	Time-dependent polarisation build-up at HERA [97].	31
3.6	Impact of e^- and e^+ polarisations on \mathcal{D}_{eff} value and uncertainty [94].	32
3.7	Schematic overview of beam-induced background production [116].	34
3.8	Schematic of 250 GeV stage of the ILC [119].	35
3.9	Schematic of the ILC beams [120].	35
3.10	Running scenario of the ILC [73].	36
3.11	Schematic of the push-pull setup for detectors at the ILC [82].	36
3.12	Schematic of QED Bhabha scattering.	37
3.13	Overview of very-forward detectors at the ILC [125].	37
3.14	Schematic of the polarised e^+ source and spin flipper section at the ILC [80, 128].	39
3.15	Schematic of alternative unpolarised e^- -drive e^+ source at the ILC [133].	40
3.16	Schematic overview of polarimetry at the ILC [60].	40
3.17	Schematics of the polarimeters at the ILC [140].	41
3.18	Schematic and cross-section of the ILD [82, 123].	42
3.19	Comparison of traditional and particle flow calorimetry [149], and example reconstructed event in ILD [150].	43
3.20	Composition of the jet energy resolution at ILD [150] and overview of confusion processes [151].	44

List of Figures

3.21	Cross-section comparisons of large and small ILD models [123].	45
3.22	ILD jet energy resolution in barrel and forward regions [123].	47
5.1	$\nu_e\nu_e qqqq$ signal and irreducible background Feynman diagrams.	58
5.2	$e^+e^- \rightarrow W^+W^-$ production channels.	60
5.3	Overview of kinematic split of $e^+e^- \rightarrow \mu^+\mu^-$ dataset into different categories.	60
6.1	1D and 2D reconstructed WW and ZZ mass distributions.	64
6.2	Example of fit of sum of two Gaussians to reconstructed WW and ZZ mass distributions.	66
6.3	Example ROC curve for fully reconstructed WW/ZZ mass distribution.	67
6.4	Kinematic distribution of jets and bosons in WW/ZZ signal events at generator and reconstructed level.	68
6.5	WW/ZZ mass distributions for generator-level and fully idealized high-level reconstruction.	70
6.6	Step-by-step idealizations of the high-level event reconstruction process on WW/ZZ mass distributions in large ILD model.	71
6.7	Step-by-step idealizations of the high-level event reconstruction process on WW/ZZ Gaussian separation and AUC.	72
6.8	Comparison of WW/ZZ mass distributions for large and small ILD model for full reconstruction and idealized high-level reconstruction.	75
7.1	1D differential distributions of μ production angle in μ pair production.	85
7.2	2D and 1D projections of 3D differential distributions of W pair production.	86
7.3	Fit of tree-level $\mu^+\mu^-$ production shape to differential distributions without and with corrected ISR.	87
7.4	Fits to $\mu^+\mu^-$ differential distributions without and with correction term.	88
7.5	Impact of TGCs on σ_0 and A_{LR} in semi-leptonic W pair production.	95
7.6	χ^2 checks of TGC-sensitivity from the overall shape and normalisation, and from individual angles in $e^+e^- \rightarrow \mu^+\nu qq$	96
7.7	Impact of TGCs on $\cos\theta_{W^-}$ distribution of the $e_L^-e_R^+ \rightarrow \mu^-\bar{\nu}qq$	97
7.8	μ acceptance in SiD [82], and simplified box model.	99
7.9	Angular distribution of μ 's in the detector frame for semi-leptonic W pair production.	100
7.10	Angular distributions of μ 's in the detector frame for μ pair production.	101
7.11	Impact of 7° μ acceptance cut on selection of differential distributions of μ pair production and semileptonic W pair production.	102
7.12	Impact of changes in center parameter of μ acceptance on bin content in μ pair production.	104

7.13	Selection of χ^2 tests of mismodeling due to polynomial parametrisation for μ pair production and semileptonic W pair production.	106
7.14	Changes of linear coefficient of μ acceptance polynomial with non-SM TGC values and vice-versa.	107
7.15	Test of bias in TGC and μ acceptance parametrisation due to factorised approach.	108
7.16	Parameter uncertainties in μ pair production fits.	112
7.17	Parameter correlations in μ pair production fits.	114
7.18	Relative $\{A_e, A_\mu\}$ limits from $\mu^+\mu^-$ fits in both energy ranges.	117
7.19	Dependence of absolute A_μ uncertainty from unpolarised A_{FB} measurements on \mathcal{D} , A_e , and ϵ_μ uncertainties.	119
7.20	Comparison of relative $\{A_e, A_\mu\}$ limits of return-to- Z events in $\mu^+\mu^-$ fits with Z -pole runs of future colliders.	120
7.21	Parameter uncertainties in semileptonic W pair production fits.	127
7.22	Parameter correlations in semileptonic W pair production fits.	129
7.23	A_{LR} uncertainties from $\mu\nu qq$ fits with fixed TGCs and free A_{LR}	136
7.24	Comparison of the TGC uncertainties from $\mu\nu qq$ fit with two polarised beams with extrapolation from higher-energy ILC full simulation-studies.	139
7.25	Comparison of the TGC uncertainties from the fits with free or fixed A_{LR} parameter.	141
7.26	2D-confidence ellipses of the TGC parameters in the $\mu\nu qq$ fits.	141
7.27	Parameter uncertainties in combined fits.	145
7.28	Parameter correlations in combined fits.	148
7.29	Uncertainty ratios of combined fit over individual final state fits.	151
B.1	2D mass distributions of WW/ZZ events at different idealization levels.	a-4
B.2	1D mass distributions of WW/ZZ events at different idealization levels.	a-5
B.3	Fits of sum of two Gaussians to WW and ZZ mass distributions: IDR-L, $m_{VV} > 500$ GeV.	a-7
B.4	Fits of sum of two Gaussians to WW and ZZ mass distributions: IDR-S, $m_{VV} > 500$ GeV.	a-9
B.5	Fits of sum of two Gaussians to WW and ZZ mass distributions: IDR-L, $m_{VV} < 500$ GeV.	a-11
B.6	Fits of sum of two Gaussians to WW and ZZ mass distributions: IDR-S, $m_{VV} < 500$ GeV.	a-13
B.7	Step-by-step idealizations of the high-level event reconstruction process on WW/ZZ mass distributions in small ILD model.	a-16
B.8	ROC curves from WW/ZZ mass distributions for different idealization levels.	a-18
C.1	$\cos \theta_{W^-}$ and $\cos \theta_l^*$ distributions of $\mu^- \nu qq$ final state.	a-29
C.2	ϕ_l^* distributions of $\mu^- \nu qq$ and $\mu^+ \nu qq$ final states.	a-30

List of Figures

C.3	Impact of a 7° muon acceptance cut on the return-to-Z event distributions of μ pair production.	a-32
C.4	Impact of a 7° muon acceptance cut on the high- $\sqrt{s^*}$ event distributions of μ pair production.	a-32
C.5	Impact of a 7° muon acceptance cut on the $e_L^- e_R^+ \rightarrow \mu^- \nu qq$ and $e_R^- e_L^+ \rightarrow \mu^- \nu qq$ distributions.	a-33
C.6	χ^2 tests on $e^+ e^- \rightarrow \mu^+ \mu^- (m_{\mu\mu} \approx m_Z)$ to validate polynomial approach to μ acceptance.	a-35
C.7	χ^2 tests on $e^+ e^- \rightarrow \mu^+ \mu^- (m_{\mu\mu} \approx 250 \text{ GeV})$ to validate polynomial approach to μ acceptance.	a-36
C.8	χ^2 tests on $e^+ e^- \rightarrow \mu\nu qq$ to validate polynomial approach to μ acceptance.	a-37
C.9	Numbered parameter correlations in μ pair production fits.	a-43
C.10	Numbered parameter correlations in W pair production fits.	a-51
C.11	Numbered parameter correlations in combined fits.	a-57

List of Tables

2.1	Fermions and their charges in the SM.	4
3.1	Running plans for the four main e^+e^- collider proposals.	27
3.2	Overview of chiral e^+e^- combinations and corresponding cross-section weights.	29
5.1	Cross-sections of signal processes in VBS study at 1 TeV.	58
5.2	Chiral cross-sections of signal processes in electroweak fit study at 250 GeV.	59
6.1	Overview of the different idealization steps and the corresponding reconstruction steps.	69
7.1	Collider scenarios in electroweak fit study.	81
7.2	Overview of processes and applicable effects in electroweak fit study.	84
7.3	Binning of differential distributions in the electroweak fit study.	84
7.4	$\mu^+\mu^-$ parameter values of categories in 250 GeV MC dataset.	90
7.5	Tests of fitting only μ acceptance on unpolarised distributions ($L = 2 \text{ ab}^{-1}$) for different final states.	109
7.6	Overview of the different fit setups and which final states and parameter sets they use.	110
7.7	Estimated numbers of $e^+e^- \rightarrow \mu^+\mu^-$ events with $Q^2 \approx m_Z$ in fits from this study, from SLD and from LEP1.	120
7.8	TGCs uncertainties from fit in different collider scenarios compared to LEP results.	139
7.9	Absolute uncertainties of the combined fits at 2 ab^{-1}	154
C.1	Rescanned TGC points.	a-25
C.2	Absolute uncertainties of fits of the $\mu^+\mu^-$ final state with the default parameter set (table 7.6).	a-39
C.3	Absolute uncertainties of fits of the $\mu^+\mu^-$ final state with fixed luminosity and otherwise default parameters.	a-40
C.4	Absolute uncertainties of fits of the $\mu^+\mu^-$ final state with fixed polarisations and otherwise default parameters.	a-41

List of Tables

C.5	Absolute uncertainties of fits of the $\mu^+\mu^-$ final state with fixed μ acceptance and otherwise default parameters.	a-42
C.6	Absolute uncertainties of fits of the $\mu\nu qq$ final state with the default parameter set (table 7.6).	a-45
C.7	Absolute uncertainties of fits of the $\mu\nu qq$ final state with fixed luminosity and otherwise default parameters.	a-46
C.8	Absolute uncertainties of fits of the $\mu\nu qq$ final state with fixed polarisations and otherwise default parameters.	a-47
C.9	Absolute uncertainties of fits of the $\mu\nu qq$ final state with fixed μ acceptance and otherwise default parameters.	a-48
C.10	Absolute uncertainties of fits of the $\mu\nu qq$ final state with fixed total cross sections and otherwise default parameters.	a-49
C.11	Absolute uncertainties of fits of the $\mu\nu qq$ final state with free left-right asymmetry and otherwise default parameters.	a-50
C.12	Absolute uncertainties of the combined fits with the default parameter set (table 7.6).	a-53
C.13	Absolute uncertainties of the combined fits with fixed luminosity and otherwise default parameters.	a-54
C.14	Absolute uncertainties of the combined fits with fixed polarisations and otherwise default parameters.	a-55
C.15	Absolute uncertainties of the combined fits with fixed μ acceptance and otherwise default parameters.	a-56

Abbreviations

aQGC	anomalous Quartic Gauge Coupling
AUC	area under the curve
BSM	Beyond the Standard Model
DM	Dark Matter
EFT	Effective Field Theory
EWSB	Electroweak symmetry breaking
HL-LHC	High Luminosity LHC
IDR	ILD Interim Design Report
IDR-L	Large IDR-era ILD model
IDR-S	Small IDR-era ILD model
ILC	International Linear Collider
ILD	International Large Detector
IP	interaction point
ISR	Initial-State Radiation
JER	Jet Energy Resolution
LCC	Linear Collider Collaboration
LCGG	Generator group of the Linear Collider Collaboration
LEP	Large Electron-Positron Collider
PF	Particle Flow (event reconstruction / calorimetry)
QCD	Quantum chromodynamics
QED	Quantum electrodynamics
ROC	receiver operating characteristic

List of Tables

SiD Silicon Detector

SLC Stanford Linear Collider

SM Standard Model (of particle physics)

SMEFT Standard Model effective field theory

TGC Triple Gauge Coupling

TPC Time-Projection Chamber

VBS Vector Boson Scattering

VEV Vacuum Expectation Value

WIMP Weakly-Interacting Massive Particles

1. Introduction

The field of high-energy particle physics finds itself in an extraordinary situation. It has managed to come up with a Standard Model (SM) which explains the vast majority of experimental observations. And at the same time, the SM has inherent flaws - e.g. lacking a clear motivation for its structure and parameters, and failing to explain cosmological observations.

The particle physics community is currently undergoing an extensive discussion on how to address these issues with the next large-scale experiment [1]. A consensus is that the way forward is through high-precision tests with a high-energy electron-positron collider. Multiple proposals for such a machine are under consideration, differing in both machine and detector technologies, as well as in the details of the physics program. Knowledge about how these choices impact the final precisions is an important input for the discussion.

One of the targets of the proposed e^+e^- machines is the electroweak sector of the SM, which contains the weak and electromagnetic forces, and is tightly connected to the only recently experimentally observed Higgs sector. Electron-positron colliders provide a well-known initial state of elementary particles and a low-background detector environment, which together allow for electroweak measurements of high precisions. The LEP and SLC experiments in the 1990s are powerful examples of this capability [2, 3]: to this day, the results of these two e^+e^- colliders are some of the highest-precision measurements in the electroweak sector.

LEP and SLC also illustrate some of the trade-offs that come with the choice of a specific e^+e^- collider design. LEP was a circular collider, which enabled measurements with high luminosities at and above the Z-pole. SLC on the other hand was a linear collider, with a design that only allowed a moderate luminosity on the Z-pole, and that instead provided the opportunity of a spin-polarised e^- beam. This polarisation gave SLC direct access to the chiral structure of the SM, which is a fundamental part of the electroweak sector. With around 25 times less luminosity, SLC was able to measure the electroweak mixing angle $\sin^2 \theta_w$ with approximately the same precision as LEP. The advantages of beam polarisation are now again one of the active points of discussion for a future e^+e^- collider.

This thesis means to contribute to the ongoing discussions by addressing the challenges which electroweak measurements face. It starts (chapter 2) with a summary of the current status of the SM, and how a generic effective theory approach can help in the search for new physics. Following this is an overview of the proposed future e^+e^- colliders (chapter 3), with a special focus on the International Linear Collider (ILC) and

1. Introduction

one of its detector. Preceding the new work in this thesis, there is an additional short review (chapter 4) of previous studies that addressed similar questions as those of this thesis, and a summary of the datasets which are the basis of the studies here (chapter 5).

The work performed for this thesis has two parts. In the first part (chapter 6), a study of vector boson scattering at a 1 TeV ILC serves to investigate the challenges that come with the reconstruction of hadronic final states. The second, more extensive part (chapter 7) uses an electroweak fit to two- and four-fermion final states to investigate how the choice of luminosity and polarisation influence the electroweak precision at a 250 GeV e^+e^- collider.

2. Theory

Particle physics tries to uncover the fundamental laws that govern the universe. These laws take the shape of theoretical mathematical models, which provide predictions for experiments to test. The general philosophy and hope is that the most fundamental underlying theory is the results of very few, well-motivated assumptions, which then give rise to all the known behaviour of the fundamental particles and forces of our universe.

This chapter reviews the model that currently best describes the experimental particles physics results - the Standard Model (section 2.1) -, and shows how the view of that theory as a low-energy effective theory can guide the search for yet unknown physics (section 2.2).

2.1. The current Standard Model of particle physics

Through the last century, the particle physics community has converged on a theory that manages to describe the existence and behaviour of all known particles and forces (with the notable exception of gravity). This theory is called the Standard Model (SM) of particle physics.

The SM is a quantum field theory, basing itself on the principles of quantum mechanics and describing “matter particles” and “force particles” through fields. Underlying this theory is the stationary-action principle with an action

$$S = \int dx \mathcal{L} \tag{2.1}$$

which is the integral of the lagrangian density \mathcal{L} over the space-time coordinates x . The lagrangian \mathcal{L} , containing terms describing the fields and their interactions, fully describes the theory. By applying the stationary-action principle

$$\frac{\partial S}{\partial \phi_i} = 0, \tag{2.2}$$

the lagrangian supplies equations for the dynamics of the fields.

The all-determining question is how the terms of the SM lagrangian look. To answer this question, the SM postulates additional principles that give rise to the different fields and interactions. These principles are

- **Lorentz-invariance**, which respects the principles of general relativity,

2. Theory

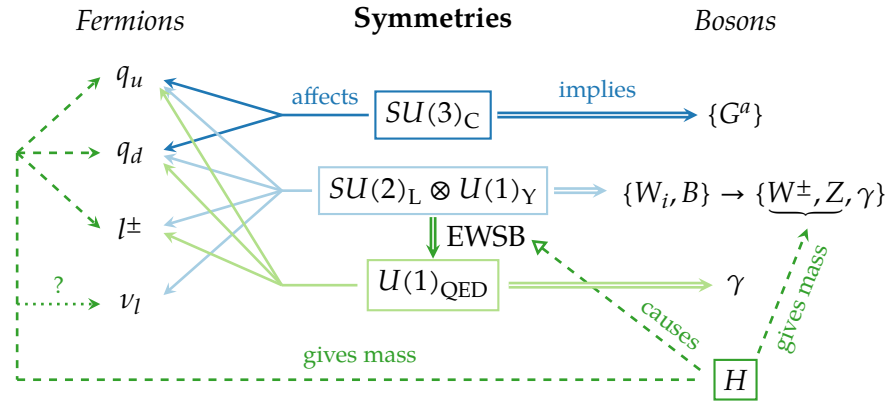


Figure 2.1.: The Standard Model of particle physics revolves around gauge symmetries which have different effects on the different fermions (“matter particles”) and require the existing of gauge bosons (“force particles”). In addition, the Higgs mechanism introduces a Higgs boson and leads to electroweak symmetry breaking (EWSB), giving rise to fermion and boson masses.

Table 2.1.: The SM contains four types of fermion: up-type quarks (q_u), down-type quarks (q_d), charged leptons (l^-) and neutrinos (ν_l). Each fermion type has three generations of fermions, given here with their respective masses or experimental mass limits [4], and all generations of each type have the same quantum numbers ($I_W^{(3)}$ of $SU(2)_L$, Y of $U(1)_Y$, Q of $U(1)_{QED}$ and C of $SU(3)_C$). The quantum numbers of $SU(2)_L \otimes U(1)_Y$ differ between fermions of left-handed (L) and right-handed (R) chirality.

	Generation			Gauge symmetry charges			
	1.	2.	3.	$I_W^{(3)}: L / R$	$Y: L / R$	Q	C
q_u :	u 2.2 MeV	c 1.27 GeV	t 173 GeV	$+\frac{1}{2} / 0$	$-\frac{1}{3} / +\frac{4}{3}$	$+\frac{2}{3}$	✓
q_d :	d 4.7 MeV	s 93 MeV	b 4.18 GeV	$-\frac{1}{2} / 0$	$+\frac{1}{3} / +\frac{2}{3}$	$-\frac{1}{3}$	✓
l^- :	e^- 511 keV	μ^- 106 MeV	τ^- 1.78 GeV	$-\frac{1}{2} / -$	$-1 / -2$	-1	o
ν_l :	ν_e < 1.1 eV	ν_μ < 0.19 MeV	ν_τ < 18.2 MeV	$+\frac{1}{2} / -$	$-1 / 0$	0	o

- **Invariance under the $U(1)_Y \otimes SU(2)_L \otimes SU(3)_C$ gauge groups** [5–8], which determine the interactions of the fields, and
- **The breaking of $U(1)_Y \otimes SU(2)_L$ to $U(1)_{QED}$ through electroweak symmetry breaking**, which gives mass to the particles. [9–13]

Applying these principles leads to the SM lagrangian (given here in a summarized form) [4]

$$\begin{aligned} \mathcal{L}_{SM} = & - \underbrace{\frac{1}{4} F_{\mu\nu}^\alpha F^{\alpha,\mu\nu}}_{\text{Boson kin. terms}} + \underbrace{i\bar{\Psi}^k \not{D}\Psi^k}_{\text{Fermion kin. terms}} \\ & \underbrace{+ (i\bar{\Psi}_L^k y_{kn} \phi \Psi_R^n + \text{h.c.})}_{\text{Fermion-Higgs couplings}} + \underbrace{|D_\mu \phi|^2}_{\text{Higgs kin. term}} - \underbrace{V(\phi)}_{\text{Higgs potential}} \end{aligned} \quad (2.3)$$

& gauge couplings & fermion-boson couplings
& fermion-boson couplings

containing the spin-1/2 fermion fields Ψ (“matter fields”), the spin-1 gauge bosons (“force particles”) in the field strength tensors F and in the covariant derivative $\not{D} = \gamma_\mu D^\mu$, and the spin-0 Higgs boson ϕ .

There are four types of fermions in the SM with differing quantum numbers, and each type contains three generations differing in mass (table 2.1). Each symmetry and the corresponding force is only relevant to a fermion if that fermion has a non-zero charge of that symmetry (fig. 2.1).

The following explains and explores how the different sectors of the SM lagrangian which are of relevance to this work.

2.1.1. Introducing and breaking the symmetries of electroweak interactions

The construction of the SM starts out with the lagrangian¹ for a set of simple massless Dirac spinors Ψ_k [14].

$$\mathcal{L} = i\bar{\Psi}_k \gamma^\mu \partial_\mu \Psi_k \equiv i\bar{\Psi}_k \not{\partial} \Psi_k \quad (2.4)$$

Forces find their way into the lagrangian through the requirement of local gauge symmetries. These local gauge symmetries mathematically mean that a coordinate-dependent change of the complex phase of the fields cannot make a difference for the behaviour of the field. The simplest possible local gauge symmetry is $U(1)$, where the lagrangian is invariant under a scalar change of the phase

$$\Psi_k \rightarrow \Psi'_k = e^{i\hat{Q}\varphi(x)} \Psi_k, \quad (2.5)$$

where \hat{Q} is the $U(1)$ -charge operator ($\hat{Q}\Psi_k = Q_k \Psi_k$) and $\varphi(x)$ is the coordinate-dependent scalar phase shift.

¹The langragians here include an implicit summation over the index k of these spinors.

2. Theory

For charge-zero fields with $\hat{Q}\Psi_k = 0$, the corresponding parts of the lagrangian are automatically invariant under that gauge symmetry. For the remaining fields, the shift (eq. (2.5)) introduce also a shift in the lagrangian.

$$\mathcal{L} \rightarrow \mathcal{L}' = \mathcal{L} + \bar{\Psi}_k i \hat{Q}(\partial\varphi) \Psi_k \quad (2.6)$$

This means that the simple massless Dirac lagrangian is not invariant under $U(1)$.

To recover the invariance, the theory needs to introduce a new spin-1 vector-field A_μ into the lagrangian that interacts with the spinors

$$\mathcal{L}_{U(1)} = i\bar{\Psi}_k \not{\partial} \Psi_k + \bar{\Psi}_k i g_{U(1)} \hat{Q} A \Psi_k = i\bar{\Psi}_k \not{D} \Psi_k \quad (2.7)$$

with a corresponding coupling $g_{U(1)}$ and the covariant derivative

$$D_\mu = \partial_\mu + i g_{U(1)} \hat{Q} A_\mu. \quad (2.8)$$

The transformation of A under $U(1)$ then can take exactly the necessary form

$$A_\mu \rightarrow A'_\mu = A_\mu - \frac{1}{g_{U(1)}} \partial_\mu \varphi \quad (2.9)$$

that leaves the new lagrangian (eq. (2.7)) invariant under $U(1)$.

In order for the new field A_μ to be physically meaningful, it needs an additional term in the lagrangian that describes the kinematics of the field. Relativity dictates the shape of that term for the vector field

$$\mathcal{L}_{U(1),\text{Kin}} = -\frac{1}{4} F^{\mu\nu} F_{\mu\nu}, \quad (2.10)$$

where the field strength tensor

$$F^{\mu\nu} = \partial^\mu A^\nu - \partial^\nu A^\mu + i g_{U(1)} [A^\mu, A^\nu] = \partial^\mu A^\nu - \partial^\nu A^\mu \quad (2.11)$$

generally contains the field commutator $[A^\mu, A^\nu]$ which ensures gauge invariance, and which vanishes for $U(1)$. This field strength tensor $F^{\mu\nu}$ is identical to the field strength tensor of electromagnetism, so that the full $U(1)$ lagrangian described here

$$\mathcal{L}_{U(1)} = -\frac{1}{4} F^{\mu\nu} F_{\mu\nu} + i\bar{\Psi}_k \not{D} \Psi_k \quad (2.12)$$

represents quantum electrodynamics (QED) for massless fermions.

The electroweak lagrangian

The simple $U(1)$ gauge symmetry requirement leads to the introduction of the electromagnetic force. For the weak force, responsible e.g. for the decay of neutrons, that same

gauge group does not manage to capture the experimentally established behaviour. Specifically, the $U(1)$ lagrangian does not violate parity invariance.

Parity invariance means that the theory is the same when flipping the sign of all space-time coordinates ($x \rightarrow -x$). Weak decays violate parity invariance, which shows up in different interactions with the different chiral states of the fermions. For highly-relativistic particles ($E \gg m$), those chiral states correspond to the spin direction either with (right-handed / R) or against (left-handed / L) the flight direction. Experiments show that only left-handed fermions and right-handed anti-fermions take part in charged current interactions [15, 16].

The simplest gauge group that includes parity violation is $SU(2)$, in which fields with a non-zero $SU(2)$ -charge ($I_W^{(3)}$) are doublets. To fit the structure of the weak decays, the participating left-handed fermions must form pairs of either a charged lepton and a neutrino or an up-type quark and a down-type quark

$$\begin{pmatrix} \nu_e \\ e \end{pmatrix}_L, \dots, \begin{pmatrix} u \\ d \end{pmatrix}_L, \dots \quad (2.13)$$

and the right-handed fermions are singlets

$$e_R, \dots, u_R, \dots, d_R, \dots \quad (2.14)$$

with an $SU(2)$ -charge of zero.

Only the left-handed fields change under this $SU(2)_L$ gauge symmetry

$$\Psi_L \rightarrow \Psi'_L = e^{i \sum_{j=1}^3 \frac{\sigma_j}{2} \alpha_j(x)} \Psi_L, \quad (2.15)$$

where σ_j are the Pauli matrices, and α_j are the phase shifts. Right-handed fields stay invariant.

$$\Psi_R \rightarrow \Psi'_R = \Psi_R \quad (2.16)$$

Like for the $U(1)$ case (eq. (2.6)), the lagrangian is not invariant under this transformation. To regain invariance, the lagrangian requires the introduction of three new fields W^1 , W^2 , and W^3 , which transform under $SU(2)_L$ to exactly cancel out the terms arising from transformation of the fermions.

In the SM, this $SU(2)_L$ gauge symmetry, together with a $U(1)_Y$ gauge symmetry with a charge Y and a field B , form the electroweak lagrangian

$$\mathcal{L}_{U(1)_Y \otimes SU(2)_L} = i \bar{\Psi}_k \not{D} \Psi_k - \frac{1}{4} B^{\mu\nu} B_{\mu\nu} - \frac{1}{4} W_i^{\mu\nu} W_{\mu\nu}^i \quad (2.17)$$

where $B^{\mu\nu}$ and $W_i^{\mu\nu}$ are the field strength tensors of the B and W fields and D_μ is the

2. Theory

new covariant derivative

$$D_\mu = \partial_\mu + ig' \hat{Y} B_\mu + ig \frac{\sigma_i}{2} W_\mu^i. \quad (2.18)$$

with the couplings g' and g of the $SU(2)_L$ and $U(1)_Y$, respectively.

The fields observed in charged and neutral current interactions are linear combinations of the W and B fields

$$W_\mu^\pm = \frac{1}{\sqrt{2}} (W_\mu^1 \mp iW_\mu^2) \quad (2.19)$$

$$\begin{pmatrix} Z_\mu \\ A_\mu \end{pmatrix} = \begin{pmatrix} \cos \theta_w & -\sin \theta_w \\ \sin \theta_w & \cos \theta_w \end{pmatrix} \begin{pmatrix} W_\mu^3 \\ B_\mu \end{pmatrix} \quad (2.20)$$

where W^\pm and Z are the charged and neutral bosons of the weak interaction, A the photon of QED, and θ_w is the electroweak mixing angle (“Weinberg angle”) with the relation

$$\tan \theta_w = \frac{g'}{g}. \quad (2.21)$$

Electroweak symmetry breaking

In the discussion so far, all fermions and bosons are massless. To describe reality, the SM needs to introduce mass terms into the lagrangian both for the fermions and for the W^\pm and Z bosons. Here, the theory runs into a problem, because Dirac mass terms like $m\bar{\Psi}\Psi$ are not invariant under $SU(2)_L$. The SM solves this by introducing a mechanism called electroweak symmetry breaking (EWSB) [9–13].

This mechanism first introduces a new scalar $SU(2)_L$ -doublet ϕ - the “Higgs field” - into the lagrangian together with an $SU(2)_L$ -invariant potential

$$L_\phi = (D^\mu \phi)^\dagger D_\mu \phi - \mu^2 \phi^\dagger \phi - \lambda (\phi^\dagger \phi)^2 \quad (2.22)$$

where μ^2 and λ are free parameters of the potential.

If μ^2 is negative, then the potential has a minimum at a non-zero value ϕ_0

$$|\phi_0| = \frac{\vartheta}{\sqrt{2}} = \sqrt{-\frac{\mu^2}{2\lambda}} \quad (2.23)$$

where ϑ is the vacuum expectation value (VEV). This means that at low energies the Higgs field assumes a fixed non-zero minimum, which locally breaks the $SU(2)_L$ gauge symmetry.

The masses of the gauge bosons and the fermions then arise through coupling terms to the Higgs field ϕ in the lagrangian. At low energies, the Higgs field in those coupling terms assumes the VEV, and the coupling terms transform into mass terms. This mecha-

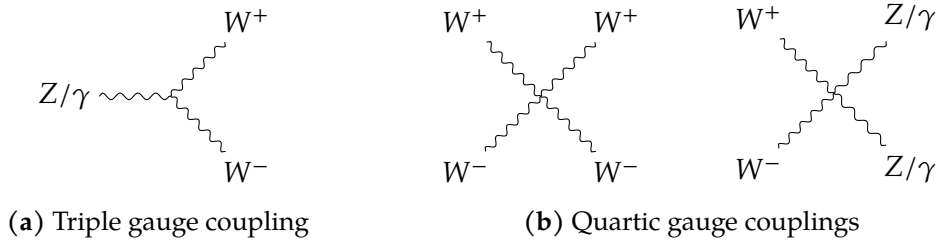


Figure 2.2.: The gauge structure of the $SU(2)_L \otimes U(1)_Y$ group predicts the existence of (a) triple and (b) quartic gauge boson self-couplings.

nism spontaneously breaks the symmetry at low energies, leaving only invariance under $U(1)_{\text{QED}}$, and leaves the overall theory invariant under $U(1)_Y \otimes SU(2)_L$.

The mechanism also predicts a Higgs boson H , representing the perturbative deviations from the VEV, which is massive and interacts with all massive fermions and bosons. In 2012, the ATLAS and CMS experiments at the LHC discovered a candidate for such a Higgs boson with a mass of around 125 GeV [17, 18], and subsequent analyses so far show that all observed couplings behave like the SM predicts [19, 20].

Gauge boson self-interactions

The field strength tensor of $U(1)$ (eq. (2.11)) contained a vanishing commutator term $[A^\mu, A^\nu]$. For the fields W_μ^i of $SU(2)_L$, those commutators do not vanish and lead to an additional term in the field strength tensor.

$$W_i^{\mu\nu} = \partial^\mu W_i^\nu - \partial^\nu W_i^\mu - g\epsilon_{ijk} W_j^\mu W_k^\nu \quad (2.24)$$

This $W_j^\mu W_k^\nu$ term in the field strengths predicts the existence of gauge boson self interactions (fig. 2.2) involving either three boson (triple gauge couplings) or four bosons (quartic gauge couplings). The existence of these couplings is a prediction of the fundamental gauge structure of the SM. For this reason, experimental explorations of the nature of the SM often target these gauge boson self-interactions.

In addition, the quartic gauge boson interaction has a crucial interplay with the Higgs. The massive modes of the weak boson introduce a divergence into that interaction, which leads to an interaction probability that increases linearly with the center-of-mass energy. At an energy around 1.2 TeV, this would violate unitarity. The interference with interactions like $W^+W^- \rightarrow H \rightarrow W^+W^-$ cancels that divergence if the Higgs has a mass below 1 TeV. Any changes in the behaviour of the Higgs compared to the SM can lead to strong changes in this sensitive cancellation. This puts additional emphasis on the experimental exploration of quartic gauge couplings.

2. Theory

2.1.2. The strong interaction of Quantum Chromo-Dynamics

The third interaction in the SM is the strong force, gaining its name from the strong attraction of the protons and neutrons in nuclei. In the SM, this interaction corresponds to the $SU(3)_C$ gauge symmetry of quantum chromo-dynamics (QCD) [8, 21, 22].

The corresponding charge C of $SU(3)_C$ is called the color charge, and only the quarks have a non-zero color charge. Like the doublets for $SU(2)$, each quark forms a triplet under $SU(3)_C$, where the three triplet-components correspond to the three color-states. The transformation of the quark fields under $SU(3)_C$

$$\Psi \rightarrow \Psi' = e^{\sum_{a=1}^8 i \frac{\lambda_a}{2} \theta_a(x)} \Psi \quad (2.25)$$

introduces eight coordinate-dependent phase shifts θ_a . These shifts again lead to new terms in the lagrangian, and require the introduction of eight new gauge fields G_a - the gluons - to restore the gauge invariance.

Analogous to the other gauge symmetries, the $SU(3)_C$ lagrangian

$$L_{SU(3)_C} = i \bar{\Psi}_k \not{\partial} \Psi_k - g_S G_a^\mu \sum_q \bar{\Psi}_q \gamma_\mu \frac{\lambda_a}{2} \Psi_q - \frac{1}{4} G_a^{\mu\nu} G_{\mu\nu}^a \quad (2.26)$$

contains a gluon-fermion interaction term with the strong coupling g_S , and the field strength tensor

$$G_a^{\mu\nu} = \partial^\mu G_a^\nu - \partial^\nu G_a^\mu - g_S f_{abc} G_b^\mu G_c^\nu. \quad (2.27)$$

Similar to the $SU(2)$ case, the $SU(3)_C$ field strength tensor contains a gluon self-coupling term.

Hadronic jet formation

The QCD interactions have some unique properties that do not appear in the electroweak interactions, and that pose unique challenges to the detection of final states that include quarks or gluons (“hadronic final states”).

One is what is called “color confinement”, which means that only states of total color-charge zero (“color neutrals”) can appear as free particles in nature [24]. As a consequence, experiments can only detect combinations of quarks known as hadrons, and can never directly detect individual quarks or gluons.

Another unique property of QCD is the shape of potential between a bound quark anti-quark pair [25]

$$V_{q\bar{q}} = -\frac{4}{3} \cdot \frac{\alpha_S}{r} + k \cdot r \quad (2.28)$$

where r is the distance between the pair and $\alpha_S = g_S^2/4\pi$ is the strong coupling constant.

At small distances, or equivalently at collision energies, the potential becomes negligible and the quarks are quasi-free. This effect is called asymptotic freedom [26, 27].

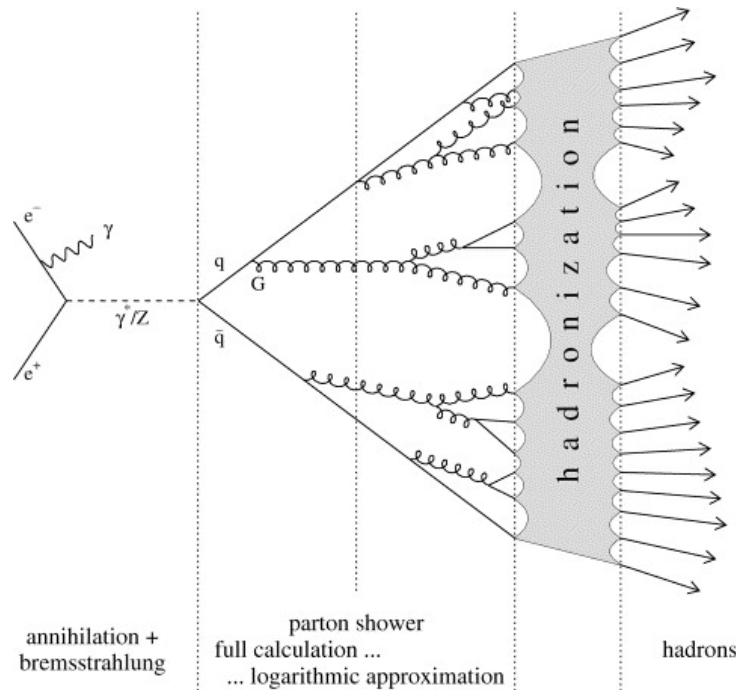


Figure 2.3.: Quarks in the final state form jets through the radiation of gluons and quark-antiquark pair production, followed by the hadronization where all quarks and antiquarks combine to color-neutral hadrons. The graph shows this process on the example of $q\bar{q}$ production from an e^+e^- collision. Copied from [23].

At large distances, the potential increases linearly. This means that at some distance the potential energy surpasses the combined mass of an additional quark-antiquark pair. At that distance, the original pair will radiate a gluon that creates a new pair. For a high-energy quark-antiquark pair, this process keeps repeating itself and leads to a parton shower of gluons, quarks and anti-quarks. In addition, color confinement means that these partons must form color-neutral hadrons in a process called hadronisation. This means that the individual quarks and gluons in the final state of a collision are not directly visible in experiments, and instead produce a shower of hadrons (fig. 2.3). Experiments can only reconstruct such showers of hadrons, which are referred to as “jets” [28, 29].

Jet clustering for experiments

Since experiments can only reconstruct jets, and not directly the quarks and gluons of the final state, they require a procedure to assign the particles in the detector to jets. For this, the experiments use jet clustering algorithms.

The underlying idea of jet clustering algorithms is that the particles originating from the same origin are in some way “close to each other” in the detector (fig. 2.4). A simple

2. Theory

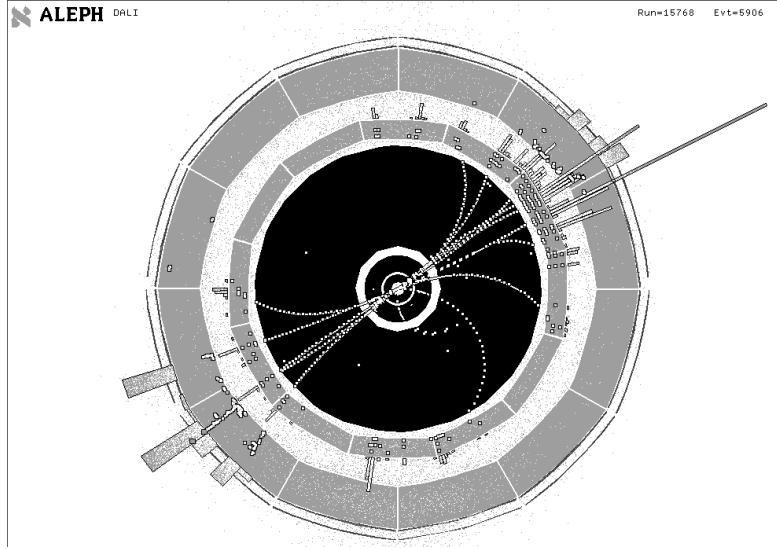


Figure 2.4.: Hadronic final states form jets of particles in the detector, seen here in an $e^+e^- \rightarrow q\bar{q}$ candidate event at ALEPH. Copied from [30].

way to define this close-ness is the angle between particles. Modern algorithms often use distance measures that combine angular and momentum information [31–33].

Once a distance measure is set, the jet clustering algorithms perform an iterative clustering. In each step, the algorithm finds the two objects with the smallest distance and replaces them by a merged object with the summed four-momentum. This combining continues until it reaches a given stopping criterium. Such a criterium can either be a minimum number of objects (jets) or a maximal distance above which objects are no longer combined.

Two such iterative jet clustering algorithms play a role in this work; the exclusive k_T algorithm [34], and the Durham or $ee-k_T$ algorithm [35].

In the exclusive k_T algorithm, the distance parameter

$$d_{ij} = \min(p_{T,i}^2, p_{T,j}^2) \cdot \frac{\Delta R_{ij}^2}{R^2} \quad (2.29)$$

uses the transverse momenta p_T and the angular distances $\Delta R = \sqrt{(y_i - y_j)^2 + (\varphi_i - \varphi_j)^2}$ between particle i and j , with the pseudorapidity y and the azimuthal angle φ , and the jet-radius parameter R . Additionally, this algorithm defines a distance to the beam

$$d_{iB} = p_{T,i}^2. \quad (2.30)$$

of particle i . If at any iteration step that d_{iB} of a particle i is the smallest distance, then the algorithm discards that particle. The underlying assumption is that beam-induced backgrounds mainly produce particles with low p_T .

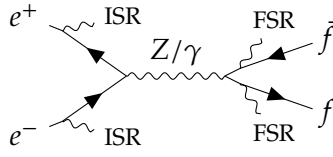


Figure 2.5.: General Feynman diagram for SM fermion pair production in e^+e^- collision, including initial state radiation (ISR) and final state radiation (FSR).

In Durham jet clustering, the distance parameter

$$d_{ij} = 2 \min(E_i^2, E_j^2) \cdot (1 - \cos \theta_{ij}) \quad (2.31)$$

uses the energies E of the two particles and the angle θ_{ij} between their directions at the interaction point. The original version of this algorithm used the normalised distance parameter $y_{ij} = d_{ij}/\sqrt{s}$.

Both of the algorithms contain free parameters. In both cases, this includes the definition of a stopping criterium. In the exclusive k_T algorithm this additionally includes a radius parameter R . For a given analysis, the expected signal final state and the dominant backgrounds determine the choice of these parameters.

2.1.3. Calculating fermion pair production

The previous sections introduced the different terms and aspects of the SM lagrangian through the introduction of gauge symmetries. With this mathematical theory at hand, the task becomes to predict what will happen in the experiments. For example, the theory can predict the expected number of events with a given initial and final state. This event number

$$N = L \cdot \sigma \quad (2.32)$$

divides into the luminosity L and the interaction cross-section σ . The properties of the colliding beams (e.g. particle density) determine the luminosity, and the interaction cross-section encodes the probability of a given scattering process of two beam particles.

The following paragraphs give an overview of the calculation of the cross-section and how experiments use the results, using the specific example fermion pair production in e^+e^- collision (fig. 2.5) which is of special interest to this study.

For a $2 \rightarrow 2$ scattering process with negligible incoming and outgoing particle masses ($E \gg m$), the differential cross-section in the center-of-mass frame has the general form [36]

$$\frac{d\sigma}{d\Omega^*} = \frac{1}{64\pi^2 s} |\mathcal{M}|^2, \quad (2.33)$$

where Ω^* is the angular phase-space element for the final state particles, \mathcal{M} is the matrix

2. Theory

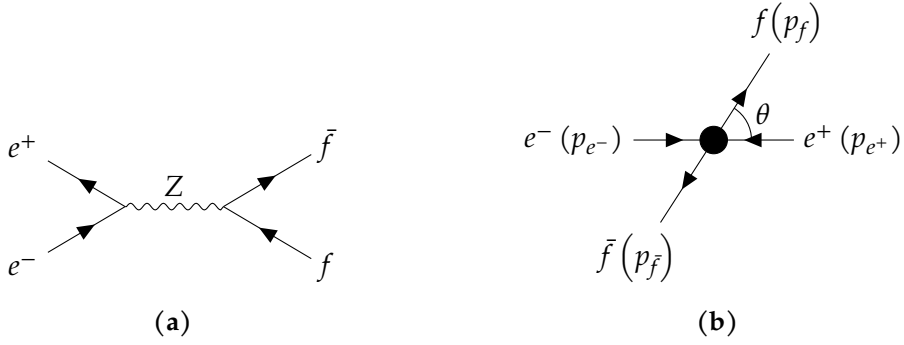


Figure 2.6.: For simplicity, the calculation here focuses only on s-channel Z exchange (a). Given a collision energy, the scattering angle θ fully determines the kinematics of that process in the center-of-mass frame (b).

element of the scattering process, and

$$s = (p_{i1} + p_{i2})^2 = (E_{i1} + E_{i2})^2 - (\vec{p}_{i1} + \vec{p}_{i2})^2 \quad (2.34)$$

is the squared center-of-mass energy calculated from the four-momenta of the two incoming particles.

The matrix element \mathcal{M} encodes all the potential intermediate processes for the given scattering. It is here where the model of the fundamental particle interactions enters. The calculation of such matrix elements uses the Feynman rules for each possible intermediate state [37].

Calculation on the Z-pole

The calculation of the matrix element \mathcal{M} for a given process needs to sum up all possible intermediate states. For fermion pair production (excluding the e^+e^- final state) in leading order perturbation theory, two intermediate s-channel processes are possible: γ -exchange or Z -exchange. In collisions with $\sqrt{s} \approx m_Z$, the γ -contribution becomes negligible and only relevant process is Z -exchange (fig. 2.6a).

The couplings of the Z to fermions differ for the different chiralities of incoming and outgoing particles. In the SM, the only non-zero $Z \rightarrow f\bar{f}$ vertices are those where the fermion and the anti-fermion have opposite chiralities. This leaves four possible processes

$$\begin{aligned} e_L^- e_R^+ &\rightarrow f_L \bar{f}_R \quad (\text{short: } Ll), \\ e_L^- e_R^+ &\rightarrow f_R \bar{f}_L \quad (\text{short: } Lr), \\ e_R^- e_L^+ &\rightarrow f_L \bar{f}_R \quad (\text{short: } Rl), \\ e_R^- e_L^+ &\rightarrow f_R \bar{f}_L \quad (\text{short: } Rr). \end{aligned} \quad (2.35)$$

The shortened notation uses capital letters to mark the initial electron chirality and lower case letters to mark the final state fermion chirality. Since the initial or final states have different quantum numbers, these four processes do not interfere with each other and have separate matrix elements.

Using the Feynman rules for this process [36], the shape of the matrix element e.g. for $e_L^- e_R^+ \rightarrow f_L \bar{f}_R$

$$M_{LI} = \left[\underbrace{\bar{v}(p_{e^+})}_{\text{incoming } e^+} \underbrace{(-ic_L^e g_Z \gamma^\mu P_L)}_{eeZ \text{ vertex}} \underbrace{u(p_{e^-})}_{\text{incoming } e^-} \right] \underbrace{\frac{-ig_{\mu\nu}}{(s - m_Z^2 + im_Z \Gamma_Z)}}_{Z \text{ propagator}} \left[\underbrace{\bar{u}(p_f)}_{\text{outgoing } f} \underbrace{(-ic_L^f g_Z \gamma^\nu P_L)}_{ffZ \text{ vertex}} \underbrace{v(p_{\bar{f}})}_{\text{outgoing } \bar{f}} \right] \quad (2.36)$$

reflects the different parts of the Feynman diagram (fig. 2.6a). Therein, u and v are the particle and antiparticle spinors, respectively, P_L is the projector for the left-handed chirality, m_Z and Γ_Z are the mass and decay width of the Z , $c_{L/R}^f$ are the fermion couplings to the Z

$$c_L^f = I_W^{(3)} - Q_f \sin^2 \theta_w, \quad c_R^f = -Q_f \sin^2 \theta_w, \quad (2.37)$$

and g_Z is the coupling constant of the Z

$$g_Z = \frac{\sqrt{4\pi\alpha}}{\sin \theta_w \cos \theta_w}. \quad (2.38)$$

The calculation of the square of this matrix element (details in [36]) ends up with a simple form

$$\begin{aligned} |M_{LI}|^2 &= g_Z^4 (c_L^e)^2 (c_L^f)^2 \left| \frac{1}{(s - m_Z^2 + im_Z \Gamma_Z)} \right|^2 \left| [\bar{v}(p_{e^+}) \gamma^\mu P_L u(p_{e^-})] g_{\mu\nu} [\bar{u}(p_f) \gamma^\nu P_L v(p_{\bar{f}})] \right|^2 \\ &= g_Z^4 (c_L^e)^2 (c_L^f)^2 |\chi(s)|^2 (1 + \cos \theta)^2 \end{aligned} \quad (2.39)$$

that only includes the couplings, the only free final state coordinate θ corresponding to the direction of the final-state fermion wrt. the electron direction (fig. 2.6b), and the center-of-mass energy in the term

$$\chi(s) = \frac{s}{s - m_Z^2 + im_Z \Gamma_Z}. \quad (2.40)$$

2. Theory

Finally, the squared matrix element directly yields the differential cross-section (eq. (2.33))

$$\frac{d\sigma_{Ll}^f}{d\cos\theta} = \frac{N_C^f g_Z^4}{32\pi s} |\chi(s)|^2 (c_L^e)^2 (c_L^f)^2 (1 + \cos\theta)^2 \quad (2.41)$$

$$\frac{d\sigma_{Lr}^f}{d\cos\theta} = \frac{N_C^f g_Z^4}{32\pi s} |\chi(s)|^2 (c_L^e)^2 (c_R^f)^2 (1 - \cos\theta)^2 \quad (2.42)$$

$$\frac{d\sigma_{Rl}^f}{d\cos\theta} = \frac{N_C^f g_Z^4}{32\pi s} |\chi(s)|^2 (c_R^e)^2 (c_L^f)^2 (1 - \cos\theta)^2 \quad (2.43)$$

$$\frac{d\sigma_{Rr}^f}{d\cos\theta} = \frac{N_C^f g_Z^4}{32\pi s} |\chi(s)|^2 (c_R^e)^2 (c_R^f)^2 (1 + \cos\theta)^2 \quad (2.44)$$

where the azimuthal angle is already integrated out, and the calculation of the other chirality combinations follows the same steps as for Ll . This now also includes the number of colored states N_C^f , which is one for leptons and three for quarks. All chirality combinations show a $(1 \pm \cos\theta)^2$ shape.

Asymmetry observables on the Z-pole

The differential cross-sections contain the fermion couplings $c_{L/R}^f$, which themselves contain the electroweak mixing angle in the form $\sin^2\theta_w$ (eq. (2.37)). This angle is experimentally interesting due to its sensitivity to higher-order corrections [2].

One way to access this parameter is through the fermion chiral asymmetry [2]

$$A_f = \frac{(c_L^f)^2 - (c_R^f)^2}{(c_L^f)^2 + (c_R^f)^2} = \frac{2(1 - 4|Q_f|\sin^2\theta_w)}{1 + (1 - 4|Q_f|\sin^2\theta_w)^2}. \quad (2.45)$$

This method also minimizes the impact of common systematic uncertainties, which cancel out in the ratio. For charged leptons with $|Q_f| = 1$, the asymmetry takes the simple form

$$A_{l\pm} \stackrel{\sin^2\theta_w \approx 1/4}{\approx} 8 \left(\frac{1}{4} - \sin^2\theta_w \right). \quad (2.46)$$

Colliders running on the Z-pole (where eq. (2.41) is valid) can access the chiral asymmetries directly through the asymmetry observables

$$A_{LR} = \frac{\sigma_{LR} - \sigma_{RL}}{\sigma_{LR} + \sigma_{RL}} = A_e, \quad (2.47)$$

$$A_{LR,FB}^f = \frac{(\sigma_{LR,F}^f - \sigma_{RL,F}^f) - (\sigma_{LR,B}^f - \sigma_{RL,B}^f)}{\sigma_{LR,F}^f + \sigma_{RL,F}^f + \sigma_{LR,B}^f + \sigma_{RL,B}^f} = \frac{3}{4} A_f, \quad (2.48)$$

where A_{LR} is the final-state independent left-right asymmetry and $A_{LR,FB}^f$ is the final-

state dependent left-right forward-backward asymmetry, and

$$\sigma_{LR/RL,F}^f = \int_0^1 \frac{d\sigma_{LR/RL}^f}{d\cos\theta} d\cos\theta, \quad \sigma_{LR/RL,B}^f = \int_{-1}^0 \frac{d\sigma_{LR/RL}^f}{d\cos\theta} d\cos\theta \quad (2.49)$$

are the integrated chiral cross-sections in the forward and backward parts of the detector. This notation uses ‘‘LR’’ to refer to the $e_L^- e_R^+$ initial state and ‘‘RL’’ to refer to the $e_R^- e_L^+$ initial state.

These formulas for the asymmetry observables assume independent cross-section measurements of the two initial-states. In reality, the experiments require polarised beams (section 3.1.3) to measure both of the initial-states, and the degree of polarisation enters into the experimental formulas for these asymmetry observables [38].

If a collider does not have access to polarised beams, it can still measure the unpolarised forward-backward asymmetry

$$A_{FB}^f = \frac{\sigma_F^f - \sigma_B^f}{\sigma_F^f + \sigma_B^f} = \frac{3}{4} A_e A_f \quad (2.50)$$

where

$$\sigma_{F/B}^f = \sigma_{LR,F/B}^f + \sigma_{RL,F/B}^f. \quad (2.51)$$

This unpolarised asymmetry only grants access to the combined asymmetry product $A_e A_f$.

Including photon-exchange

The formulas above focus on the case of $\sqrt{s} \approx m_Z$, where the pure s-channel Z contribution dominates. At different center-of-mass energies, the contribution from γ exchange and the interference between Z and γ contribution are in general not negligible.

Without derivation here, the general formula for that case is [39]

$$\begin{aligned} \frac{s}{\pi\alpha^2 N_C^f} \frac{d\sigma_{LR/RL}^f}{d\cos\theta} &= \underbrace{Q_f^2 (1 + \cos^2\theta)}_{\gamma \text{ exchange}} \\ &\quad - \underbrace{2Q_f [(v_e \pm a_e) v_f (1 + \cos^2\theta) + 2(v_e \mp a_e) a_f \cos\theta] \operatorname{Re}\chi(s)}_{Z/\gamma\text{-interference}} \\ &\quad + \underbrace{[(v_e \pm a_e)^2 (v_f^2 + a_f^2) (1 + \cos^2\theta) \pm 4(v_e \pm a_e)^2 v_f a_f \cos\theta] |\chi(s)|^2}_{Z \text{ exchange}} \end{aligned} \quad (2.52)$$

2. Theory

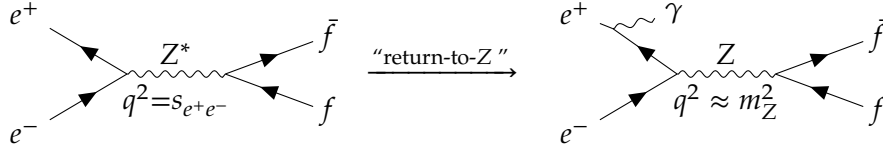


Figure 2.7.: In the return-to-Z process at center-of-mass energies \sqrt{s} above the Z mass, an incoming particle radiates an ISR photon that returns the Z to its on-shell mass. A realistic treatment of this process goes beyond the tree-level discussion here.

where

$$\begin{aligned} v_f &= c_L^f + c_R^f = I_W^{(3)} - 2Q_f \sin^2 \theta_w, \\ a_f &= c_L^f - c_R^f = I_W^{(3)} \end{aligned} \quad (2.53)$$

are the vector (v_f) and axial-vector (a_f) couplings of fermion f .

This formula shows that the value of χ determines the strength of each contribution. While the γ contribution is always of order 1, the interference term is proportional to $\text{Re } \chi$ and the Z contribution proportional to $|\chi|^2$. Taking for example the values at the Z-pole and for 250 GeV collisions

$$\begin{aligned} \text{Re } \chi(m_Z^2) &= 0, \quad |\chi(m_Z^2)|^2 \approx 1336 \\ \text{Re } \chi((250 \text{ GeV})^2) &\approx 1.15, \quad |\chi((250 \text{ GeV})^2)|^2 \approx 1.33 \end{aligned} \quad (2.54)$$

shows that the Z contribution is by far dominant on the Z-pole, and that at high energies all contribution have the same order-of-magnitude.

Radiative return to the Z-pole

Beyond the tree-level diagram for Z-exchange, one of the incoming particles can radiate an initial-state radiation (ISR) photon. This process requires an additional $ee\gamma$ vertex, and therefore sees a suppression by a factor $\alpha = e^2/(4\pi)$. At the same time, this additional radiation can reduce the effective energy of the e^+e^- back to the Z mass resonance (fig. 2.7), significantly increasing the cross-section (eq. (2.54)). That process is called a radiative return to the Z.

An estimate of the cross-section for this process at a 250 GeV e^+e^- machine yields that the return-to-Z cross-section is in the order of tens of picobarn $[40]^2$. Future colliders with luminosities in the several ab^{-1} range can expect tens of millions of such return-to-Z resonance events. This can provide a way to measure Z resonance parameters without directly running on the Z-pole, as a later part of this study will show (section 7.6).

²The estimate uses eq. 4 in the reference together with known Z resonance parameters.

2.1.4. What the SM (probably) cannot explain

The Standard Model describes the data from particle physics experiments to a remarkable precision over many orders of magnitude, and has correctly predicted particles and their properties before their experimental observation [41]. At the same time, a growing set of experimental observations eludes the expectations of the SM. Some of the perhaps most notable shortcomings of the SM include the absence of explanations for the gravitational force, for the matter-antimatter asymmetry [42], and for dark matter.

Dark matter (DM) is an elusive matter that only very weakly if at all interacts within the three forces of the SM, and has so far only shown itself through its gravitational impact [43, 44]. The evidence for this matter permeates all through the fields of astronomy and cosmology, ranging from the velocity distributions in galaxies [45], to gravitational lensing observations [46–48] and cluster formation in the early universe [49] (to name just a few). These observations also set requirements on the nature of dark matter [43]: it must have been non-relativistic (“cold”) in the structure formation stage of the universe, and it can only have very weak interactions with itself and with ordinary matter. One candidate for such matter are weakly-interacting massive particles (WIMPs), which can potentially also solve other open questions in particle physics [50].

WIMPs are a generic group of potential new particles with masses in the GeV to TeV range [51]. This means these candidates are in the reach of the current or next generation of colliders. Given the weak interactions and potentially large mass, there is no guarantee that any collider will be able to directly observe the resonance that corresponds to new DM particles. Colliders therefore need to search both for resonances and for potentially small deviations in cross-sections that hint at new particles beyond the energy reach of the collider.

2.2. The Standard Model as an effective field theory

Current and future particle physics experiments try to find clues that help explain the well-known shortcoming of the SM. The search for such beyond the SM (BSM) physics requires a description of what the new physics could look like in the experiments.

Unfortunately, the evidence for BSM physics like dark matter so far does not point towards a very specific type of new physics. A description of potential BSM effects at current and future experiments therefore needs to be generic, with the hope that the experiments gradually or suddenly limit the space of potential BSM candidates. Effective field theory (EFT) offers such a generic BSM parametrisation for physics that is outside the direct energy reach of current experiments (section 2.2.1). The measurement of the EFT couplings allows an exploration of the nature of these potential BSM effects in the data (section 2.2.2). This will be of special importance for one part of this study (chapter 7), which uses the EFT approach to describe anomalous triple gauge couplings (section 2.2.3).

2. Theory

2.2.1. The SM as low-energy effective theory

The underlying idea of effective theories is very general; not everything matters at every scale. At a given (energy, size, ...) scale, there will be effects that are far off in either direction. An effective theory can treat such effects either with a simplified approximation or by ignoring them completely, as appropriate. To this day there is no universal theory of everything, so that every theory in use today is in some way an effective theory.

The description so far defines effective theories in a “top-down” way, assuming knowledge and existing of a more detailed theory. Reality also often works in the reverse ‘bottom-up’ way; we know that our theory works very well at one scale, and that it breaks at some other scale. In that case, the effective theory mindset offers a path to supplement the current theory in a generic way that can point us in the direction of the underlying detailed theory. That path builds on two assumptions. First, that the scale difference of the previously ignored effects to the current theory suppresses the impact of those new effects. Second, that the new effects do not break the current theory at the scale where we already know that the current theory works. These two assumptions provide the instructions for a generic way to describe new effects: add potential new effects to the theory that respect all rules of the theory at the current scale, and suppress those effects by the new scale. Experiments can then look for these suppressed new effects at the current scale. The results will restrict the options for a new, more detailed theory by specifying what needs to happen in the limit of going to the current scale.

This also applies to the SM, which in its current form ignores dark matter and gravity. And the SM describes the current collider results well. One reason for this can be that the current colliders do not reach the necessary collision energy to see high-mass BSM effects. This is the assumption behind the Standard Model effective field theory (SMEFT) approach [52].

SMEFT assumes that the high energy scale Λ of the new physics suppresses the new effects, and that all symmetry assumptions of the SM are valid at the current scale. The effective theory expresses itself through an effective lagrangian \mathcal{L}_{eff} . This lagrangian consists of the SM lagrangian \mathcal{L}_{SM} and operators $O_i^{(d)}$ of higher orders d [53, 54].

$$\begin{aligned}\mathcal{L}_{\text{eff}} &= \mathcal{L}_{\text{SM}} + \sum_{d>4,i} \frac{c_i^{(d)}}{\Lambda^{d-4}} O_i^{(d)} \\ &= \mathcal{L}_{\text{SM}} + \frac{1}{\Lambda^2} \sum_i c_i^{(6)} O_i^{(6)} + \frac{1}{\Lambda^4} \sum_i c_i^{(8)} O_i^{(8)} + \dots\end{aligned}\tag{2.55}$$

The new energy scale Λ normalises the new operator terms to the mass-dimension of \mathcal{L}_{SM} and suppresses their effect, and the Wilson coefficients $c_i^{(d)}$ describe the coupling strength of each operator. All operators respect Lorentz invariance and the $SU(3)_C \otimes SU(2)_L \otimes U(1)_Y$ gauge invariance, and baryon and lepton number conservation prohibits operators of odd dimension [55]. With increasing dimension d , the operators contain vertices with more and more fields or momentum terms.

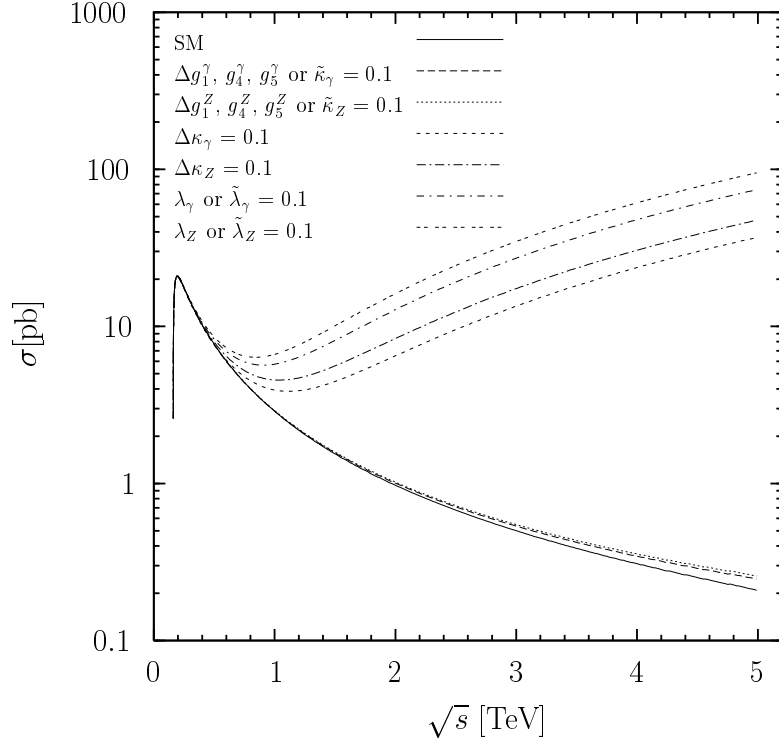


Figure 2.8.: The effect of EFT operators increases with energy, as seen here for variations of the individual triple gauge couplings (see section 2.2.3) on the total unpolarised cross-section of $e^+e^- \rightarrow W^+W^-$. Copied from [57].

Since Λ is large compared to the energy scale of the current measurements, it is possible to treat \mathcal{L}_{eff} as a perturbative expansion, and to break the sum of new operators at some power of $1/\Lambda$. This is necessary for the experiments, since the number of free couplings is infinite in the full series. Stopping the expansion at lowest order - at $1/\Lambda^2$ and operator dimension 6 -, the SMEFT lagrangian contains 59 additional operators [56].

2.2.2. Experimental insight using the EFT approach

Experiments look for the impact that the new EFT operators leave on the measured differential or inclusive cross-sections. The factor $c_i^{(d)}/\Lambda^{d-4}$, composed of the Wilson coefficient $c_i^{(d)}$ and the new energy scale Λ , determines the magnitude of the contribution of the i -th (relevant) EFT operator. A measurement is therefore only sensitive to the combined factor

$$F_i = \frac{c_i^{(d)}}{\Lambda^{d-4}}. \quad (2.56)$$

These combined factors F_i have a mass dimension of GeV^{4-d} . For convenience, the measurements often multiply those factors by a relevant physics scale (e.g. the W mass)

2. Theory

to measure a dimensionless coupling. This is the case for example for the triple gauge couplings described below (section 2.2.3).

The center-of-mass energy of a collider crucially determines the sensitivity to the EFT operators. In general, the impact of the EFT operators increases with energy (fig. 2.8), and more so if the operator contains momentum-terms. For that reason, the precision on the factors F_i generally increases with the center-of-mass energy of the collider, assuming a constant luminosity.

Another important aspect of an EFT measurement is the subset of operators that the measurement uses. One criterion is the restriction to only those operators that play a role in the production of the investigated processes. In addition, the measurement must define an order in the inverse of the new physics scale Λ at which it stops the EFT expansion [58]. The lowest possible order (for electroweak processes) is beyond the pure SM is $1/\Lambda^2$, corresponding to dimension-six operators.

By default, experiments resort to breaking the EFT expansion at dimension-six, since it provides the simplest setup to look for any deviations from the SM. There are two reasons why EFT measurements would go beyond dimension-six. The first reason is that dimension-six operators are relatively generic with each operator affecting a large set of processes. This can be an issue if one is interested in parametrising potential deviations in a specific process, and measurements in other processes already strongly restrict all the relevant operators. One example for this is the parametrisation of quartic gauge couplings, where only the dimension-8 expansion includes operators specific to that coupling [59].

A second reason to employ higher dimensional operators is if the EFT measurement itself indicates that they are relevant. For a measurement with the dimension-six operators, the EFT operators modify the SM cross-section by an interference term proportional to $1/\Lambda^2$ and a pure dim.-6 EFT term proportional to $1/\Lambda^4$.

$$\frac{\sigma_{\text{meas}}}{\sigma_{\text{SM}}} = 1 + \sum_i F_i \alpha_i + \sum_{i,j} F_i F_j \beta_{ij} = 1 + \sum_i \frac{c_i^{(6)}}{\Lambda^2} \alpha_i + \sum_{i,j} \frac{c_i^{(6)} c_j^{(6)}}{\Lambda^4} \beta_{ij} \quad (2.57)$$

Here, there α and β generically describe the impact of the operators in the cross-section. To test the relevance of higher-order operators, the measurement can perform an extraction of the F_i with and without the $1/\Lambda^4$ term. The interference-terms of the dimension-8 operators have the same $1/\Lambda^4$ -prefactor. If the inclusion of the $1/\Lambda^4$ term makes a significant difference in the measured values of the F_i at dimension-six, then stopping of the EFT-expansion before dimension-8 operators is not valid.

Previous studies have shown that stopping at dimension-6 does not significantly change the results on simulated SM events [60]. This study therefore uses only a small subset dimension-six operators relevant to triple gauge couplings (section 2.2.3), and does not need to worry about the appearance of effects of higher-order operators.

2.2.3. Anomalous Triple Gauge Couplings

Gauge boson self-interactions are a special target since they encode the fundamental gauge structure of the interactions (section 2.1.1). Part of this study focuses on one such process: the triple gauge boson interactions with the corresponding triple gauge couplings (TGC).

The Standard Model at tree-level only contains so-called charged triple-gauge boson interactions with the vertices WWZ and $WW\gamma$, often generalized as WWV ($V = Z/\gamma$). In a first very general step, the phenomenological effective lagrangian for these vertices includes all operators up to dimension-six which conform with the Lorentz structure of the bosons [61, 62].

$$\begin{aligned}
 \frac{i}{g_{WWV}} \mathcal{L}_{\text{eff}}^{WWV} = & g_1^V V^\mu (W_{\mu\nu}^- W^{+\nu} - W_{\mu\nu}^+ W^{-\nu}) + \kappa_V W_\mu^+ W_\nu^- V^{\mu\nu} \\
 & + \frac{\lambda_V}{m_W^2} V^{\mu\nu} W_\nu^{+\rho} W_{\rho\mu}^- + i g_5^V \varepsilon_{\mu\nu\rho\sigma} [(\partial^\rho W^{-\mu}) W^{+\nu} - W^{-\mu} (\partial^\rho W^{+\nu})] V^\sigma \\
 & + i g_4^V W_\mu^- W_\nu^+ (\partial^\mu V^\nu + \partial^\nu V^\mu) - \frac{\tilde{\kappa}_V}{2} W_\mu^- W_\nu^+ \varepsilon^{\mu\nu\rho\sigma} V_{\rho\sigma} \\
 & - \frac{\tilde{\lambda}_V}{2m_W^2} W_{\rho\mu}^- W^{+\mu} \varepsilon^{\nu\rho\alpha\beta} V_{\alpha\beta}
 \end{aligned} \tag{2.58}$$

This general Lagrangian contains two overall couplings of the two vertices

$$g_{WW\gamma} = e, \quad g_{WWZ} = e \cot \theta_w, \tag{2.59}$$

and 14 additional complex couplings ($g_1^V, g_4^V, g_5^V, \kappa_V, \tilde{\kappa}_V, \lambda_V, \tilde{\lambda}_V; V = Z/\gamma$), corresponding to 28 free real-numbered variables. In the pure SM the four couplings $g_1^Z, g_1^\gamma, \kappa_Z$ and κ_γ are one, all others are zero.

The LEP parametrisation

The LEP experiments were the first ones to achieve a precision good enough to measure the triple gauge boson interaction [3, 58]. Since the precision was not good enough to measure all possible 28 parameters, the experiments introduced a ‘‘LEP parametrisation’’ that employs additional assumptions and constraints to reduce the number of parameters [54, 58, 61, 63]. The study here uses that same parametrisation, with the assumptions described in the following.

First is the restriction to C- and P-conserving parameters. This step brings the largest reduction in the number of parameters, leaving only 6 free parameters: $g_1^\gamma, g_1^Z, \kappa_\gamma, \kappa_Z, \lambda_\gamma$, and λ_Z . At LEP, the motivation for this harsh restriction was a lack of sensitivity and statistics [58]. Introducing electromagnetic gauge invariance further fixes $g_1^\gamma = 1$. The last assumption is the invariance under $SU(2)_L \otimes U(1)_Y$, which requires two additional

2. Theory

conditions.

$$\Delta\kappa_Z = -\Delta\kappa_\gamma \tan^2 \theta_w + \Delta g_1^Z, \quad \lambda_\gamma = \lambda_Z \quad (2.60)$$

This imposition of the gauge invariances also means that the remaining operators are SMEFT operators.

Only three free couplings remain in the LEP parametrisation of the TGCs: $g_1^Z, \kappa_\gamma, \lambda_\gamma$. Their SM values are $g_1^Z = \kappa_\gamma = 1$ and $\lambda_\gamma = 0$, and the study here uses the deviations from these values: $\Delta g_1^Z, \Delta\kappa_\gamma$, and $\Delta\lambda_\gamma$.

BSM physics can introduce non-zero values in these three deviation parameters. For example, MSSM models predict deviations in the 10^{-4} to 10^{-2} range [64, 65], and new vector-like leptons typically introduce deviations from a below a few 10^{-4} to maximally a few 10^{-3} [66]. A precision at the 10^{-4} will be necessary to ultimately confirm or exclude such models.

The future of TGCs

Limited sensitivity and statistics required the reduction of the parameter set at LEP. Future e^+e^- likely will have sufficient precision to perform a global fit of all dimension-six SMEFT operators [57, 67]. A full SMEFT operator set minimizes the set of assumptions, and takes potential correlations between different effects into account (e.g. TGCs and Zff couplings). While the study here still uses the LEP parametrisation - both for technical reasons and simplicity -, future studies can and will use the available tools to move towards a full set of SMEFT operators.

3. Future e^+e^- collider proposals

The field of particle physics is currently focusing on high precision measurements. Open questions like the nature of electroweak symmetry breaking and dark matter require searches for very rare processes. In high-energy physics, a future collider can shed light on these questions if it reaches the required precisions.

An e^+e^- collider will be the ideal environment for these kinds of precision studies, as previously demonstrated by LEP and SLD [2, 3]. The use of e^\pm beams has the advantage of colliding elementary particles with no known substructure, leading to collisions with a well-defined energy and few backgrounds in the central detector. In addition, the detector occupancy is low compared to for example pp colliders, which allows for detector optimisation that targets high-precision event reconstruction.

This chapter first presents a general overview of the physics motivation and common aspects of different e^+e^- collider proposals (section 3.1). It then zooms in on a particular example; the International Linear Collider (section 3.2) and its ILD detector (section 3.3). This collider both bares direct relevance for the work presented here and serves as a concrete example of what such a machine looks like.

3.1. Overview and common aspects

Recent discussions on the future of high-energy particle physics include several proposals for future e^+e^- colliders [68]. These proposals contain a lot of commonalities, and subtle differences, both on the side of the physics goals as well on the technologies. This section explains the physical motivation for these proposals and the corresponding run plans, and gives an overview of some important commonalities and differences between possible future machines.

3.1.1. Physics at future e^+e^- colliders

The physics program of the proposed e^+e^- colliders provides insight into which collision energies are essential for such a future collider.

The primary target of the currently proposed machines is a thorough measurement of the Higgs sector, in order to understand electroweak symmetry breaking and to look for unexpected effects in this unique part of the SM. A great effort is already underway at the LHC to explore this sector [70], and the current results indicate agreement with the SM Higgs with around or above 10% precision in the most precise channels. Future high luminosity-LHC (HL-LHC) measurements will provide precision of a few percent

3. Future e^+e^- collider proposals

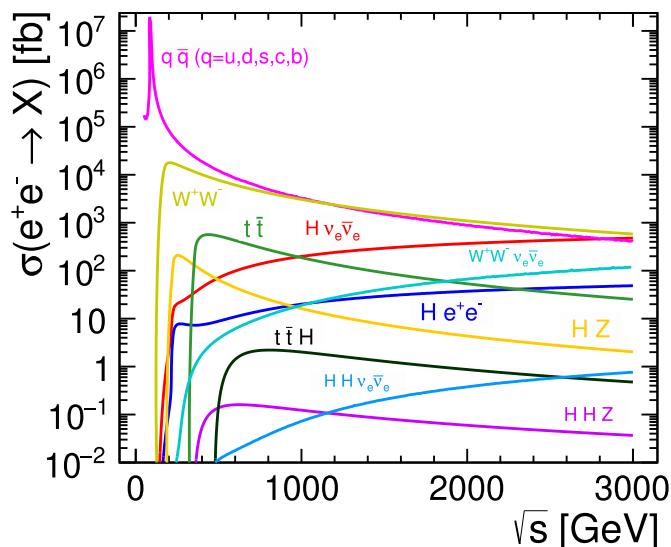


Figure 3.1.: The production cross-sections of different final states in e^+e^- collisions varies with collision energy, so that the different stages of e^+e^- colliders can focus on different processes. Copied from [69].

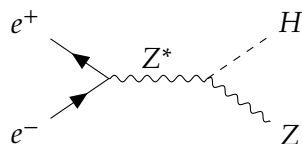


Figure 3.2.: The Higgsstrahlung process is the lowest energy Higgs production process accessible at e^+e^- colliders.

or worse, depending on the final state [71]. A large set of BSM models causes deviations at the percent level or below, escaping even the HL-LHC sensitivity [72]. For this reason, future e^+e^- colliders aim at precision at or below the percent level in the Higgs couplings [73, 74]. In addition to the Higgs, the top quark plays a special role as the heaviest known elementary particle. Like for the Higgs, only hadron colliders have so far measured the top directly, and e^+e^- colliders will provide complementary precise measurement of its properties [75]. More generally, e^+e^- colliders can explore the predominantly electroweak interactions for any new physics, and perform focused searches for any kind of unexpected signature [76].

The energy-dependent cross-sections of those target processes (fig. 3.1) set the necessary collision energy range of the colliders. Any measurement of the Higgs sector in e^+e^- collisions requires a minimum energy of around 240 – 250 GeV, where the Higgsstrahlung process (fig. 3.2) peaks as the first significant Higgs production process. Higher collision energies up to the multi-TeV range grant access to additional Higgs production channels, and to measurements of the Higgs self-coupling. Measurements

Table 3.1.: Running plans for future e^+e^- colliders consider energies from the Z-pole to multi-TeV stages [77], including optional (*) ILC stages. Only the linear collider proposals use longitudinal beam polarisation.

	\sqrt{s}	L [ab^{-1}]	$ \mathcal{D}_{e^-} / \mathcal{D}_{e^+} $
ILC	(*) m_Z	0.1	80% / 30%
	(*) $2m_W$	0.5	80% / 30%
	250 GeV	2.0	80% / 30%
	350 GeV	0.2	80% / 30%
	500 GeV	4.0	80% / 30%
	(*) 1 TeV	8.0	80% / 20%
CLIC	380 GeV	1.0	80% / 0
	1.5 TeV	2.5	80% / 0
	3 TeV	5.0	80% / 0
FCC-ee	m_Z	150	0 / 0
	$2m_W$	10	0 / 0
	240 GeV	5	0 / 0
	365 GeV	1.5	0 / 0
CEPC	m_Z	16	0 / 0
	$2m_W$	2.6	0 / 0
	240 GeV	5.6	0 / 0

of the top quark show a similar situation, requiring at least 350 GeV for $t\bar{t}$ production, and with additional channels available at higher energies.

Electroweak processes like Z/γ and WW production have the highest cross-sections at all planned energies. At low energies down to the Z pole, the high cross-sections allow exceptionally high statistics studies of the W and Z bosons. Meanwhile, higher energy collisions will have a higher sensitivity to high-mass BSM effects. Any energy stage of a future e^+e^- collider can therefore contribute to the program of EW precision measurements. It is an active field of discussion whether the best gain will come from high-statistics low-energy stages or lower-statistics high-energy stages.

3.1.2. Advanced e^+e^- proposals

In the last decades, the high-energy physics community has proposed multiple concepts for high-energy e^+e^- colliders. Now, the discussions focus on four of these proposals, differing in shape and running parameters like energy range and luminosity. These colliders are two linear colliders (ILC [78–83] and CLIC [84–86]) and two circular colliders (FCC-ee [87, 88] and CEPC [89, 90]). All of these proposals include energy stages at or close to the Higgsstrahlung peak around 250 GeV, demonstrating the focus of these machines on precise Higgs measurements. For this reason, these machines are often referred to as “Higgs factories”. Besides those stages, the proposed energy stages run

3. Future e^+e^- collider proposals

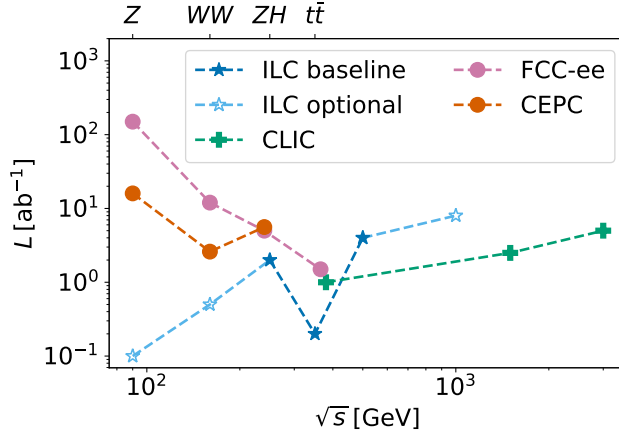


Figure 3.3.: Integrated luminosities of the current running plans for future e^+e^- colliders [77], including optional ILC stages. Circular colliders (FCC-ee, CEPC) focus on lower energy stages, while linear colliders (ILC, CLIC) can access TeV-range energies.

from the Z-pole around 91 GeV to multi-TeV energies, depending on the collider design (fig. 3.3).

The circular colliders focus on the lower energy stages from the Z-pole up to the $t\bar{t}$ threshold. A circular design has the principal advantage that it can collide each bunch many times after accelerating it once to the collision energy. This allows a high collision frequency for a low per-collision power input. For high-energy e^\pm beams, the beam loses significant energy due to synchrotron radiation in the bending magnets, which weakens this advantage. This energy loss increases quartically with the gamma factor or energy of the beam, and decreases only linearly with the collider radius [91].

$$\Delta E_{\text{synchrotron}} \sim \frac{\gamma^4}{R} = \frac{1}{R} \left(\frac{E}{m_e} \right)^4 \quad (3.1)$$

If a collider with a fixed power increases the collision energy, then the beam intensity decreases rapidly - and with that the luminosity. To remedy this, the collider can increase the input power or radius like E^4 . Since this exponentially increases the cost, current circular collider proposals do not go beyond the $t\bar{t}$ threshold.

Linear colliders provide an alternative that does not suffer from that radiation loss [92], at the trade-off of only using each bunch once in collision. The length and gradient of the linear accelerator determine the maximal beam energy. This means that the cost of such linear colliders increases linearly with collision energy, compared to the exponential increase for circular colliders. For collisions around 200 GeV the cost of both machines is roughly the same [93], and above that the linear collider becomes more economic. This is why linear colliders generally can focus on higher energy stages up to 3 TeV. Runs below the ZH peak are in principle also possible with linear colliders with

Table 3.2.: The four possible chirality combinations of e^+e^- collisions, corresponding (for $m_e \approx 0$) to the spin-direction in the colliding beams. The beam polarisations \mathcal{P}_{e^\pm} in a dataset determine how much each combination contributes to the measured cross-section (see eq. (3.3)). Adapted from [94].

e^-	Spin: \Rightarrow Flight: \longrightarrow	e^+	weighted contribution to polarised cross-section
R	$\Rightarrow\Rightarrow\Rightarrow$ $\Leftarrow\Leftarrow\Leftarrow$	R	$\frac{1+\mathcal{P}_{e^-}}{2} \cdot \frac{1+\mathcal{P}_{e^+}}{2} \cdot \sigma_{RR}$
L	$\Leftarrow\Leftarrow\Leftarrow$ $\Leftarrow\Leftarrow\Leftarrow$	L	$\frac{1-\mathcal{P}_{e^-}}{2} \cdot \frac{1-\mathcal{P}_{e^+}}{2} \cdot \sigma_{LL}$
L	$\Leftarrow\Leftarrow\Leftarrow$ $\Leftarrow\Leftarrow\Leftarrow$	R	$\frac{1-\mathcal{P}_{e^-}}{2} \cdot \frac{1+\mathcal{P}_{e^+}}{2} \cdot \sigma_{LR}$
R	$\Rightarrow\Rightarrow\Rightarrow$ $\Leftarrow\Leftarrow\Leftarrow$	L	$\frac{1+\mathcal{P}_{e^-}}{2} \cdot \frac{1-\mathcal{P}_{e^+}}{2} \cdot \sigma_{RL}$

a lower luminosity than circular colliders.

In addition to the energy range, the collider proposals differ in the availability of longitudinal beam polarisation. While the circular proposals do not use longitudinally polarised beams, the linear proposals polarise one or both of the beams.

3.1.3. Beam polarisation

One of the key differences between the collider proposals is the availability of beam polarisation. This beam property grants direct access to the chirality-dependence of particle interactions, and is key to the work presented here. The following paragraphs will introduce the concept and its basic advantages.

Beam polarisation is an ensemble property of the beam. It describes to which extent the spins of beam particles align along a certain direction. When the alignment is along the particle flight direction it is called longitudinal polarisation, perpendicular to the flight direction it is called transversal. The explanations here limit themselves to longitudinal polarisation.

The alignment of a particle spin along its flight direction corresponds to the particles helicity. For particles with momenta much higher than their rest mass - e.g. electrons at high energy colliders - the helicity corresponds to the chirality of the particle (table 3.2). Right-handed chirality ("R") corresponds to the spin pointing in the flight direction, and left-handed chirality ("L") to spin pointing against flight direction. The value of the polarisation describes the asymmetry between the number of right- and left-handed particles in the particle bunch.

$$\mathcal{P}_{e^\pm} = \frac{N_R^\pm - N_L^\pm}{N_R^\pm + N_L^\pm} \quad (3.2)$$

Its sign determines whether right-handed ($\mathcal{P} > 0$) or left-handed ($\mathcal{P} < 0$) particles predominate, and the absolute value is a measure of that dominance.

3. Future e^+e^- collider proposals

The polarisation is an important input to any e^+e^- collider measurement because electroweak interactions depend on the chirality (section 2.1.1). Any measured cross-section is a combination of the different chiral cross-sections, i.e. the cross-sections for each of the four possible chiral combinations (LR,RL,LL,RR; table 3.2). For beams with fixed polarisations, the fraction of each chirality in the beams determines the contribution of that chirality.

$$\frac{N_R^\pm}{N_L^\pm + N_R^\pm} = \frac{1 + \mathcal{D}_{e^\pm}}{2}, \quad \frac{N_L^\pm}{N_L^\pm + N_R^\pm} = \frac{1 - \mathcal{D}_{e^\pm}}{2} \quad (3.3)$$

The measured polarised cross-section (differential or integrated) is a weighted combination of the chiral cross-sections [95].

$$\begin{aligned} \sigma_{\text{pol}}(\mathcal{D}_{e^-}, \mathcal{D}_{e^+}) = & \frac{1 + \mathcal{D}_{e^-}}{2} \cdot \frac{1 + \mathcal{D}_{e^+}}{2} \cdot \sigma_{RR} + \frac{1 - \mathcal{D}_{e^-}}{2} \cdot \frac{1 - \mathcal{D}_{e^+}}{2} \cdot \sigma_{LL} + \\ & \frac{1 - \mathcal{D}_{e^-}}{2} \cdot \frac{1 + \mathcal{D}_{e^+}}{2} \cdot \sigma_{LR} + \frac{1 + \mathcal{D}_{e^-}}{2} \cdot \frac{1 - \mathcal{D}_{e^+}}{2} \cdot \sigma_{RL} \end{aligned} \quad (3.4)$$

A precise knowledge of the polarisation is therefore a necessity for any cross-section measurement. Colliders use dedicated polarimeter setups for such measurements (e.g. section 3.2.3).

When a collider has access to a polarised beam, it can generally also “flip” the spins in the beam to change the sign of the polarisation. This is possible either directly at the source or in dedicated magnet setups [80]. The result is that a polarised collider can divide its total luminosity amongst multiple datasets with different beam polarisation combinations. Each of these polarised datasets has a different dominant chirality combination.

If the switch between the different polarisation signs of a beam is possible on a short enough timescale (e.g. train-to-train), then a majority of systematic effects will correlate amongst the datasets. This is referred to as “fast spin flip” or “fast helicity reversal”. The SLC already implemented such a method for a polarised electron beam [96]. While the availability for fast spin flipping does not affect the physics in the collisions, it plays an important role in reducing systematic effects in polarised measurements [60], as described later in this section.

Methods to polarise a beam

In order to make use of polarisation at the interaction point (IP), colliders need to polarise the beam at some point before the collision.

Linear colliders opt to produce polarised beams directly with a polarised source, and then use a set of spin-turning magnets to deliver that polarisation to the IP. The SLC, the only previous linear collider, used this technique for the e^- beam [98]. At the basis of the polarised source is a circularly polarised photon beam, for example a laser. When hitting a target, the polarisation of the photons transmits itself to a longitudinal polari-

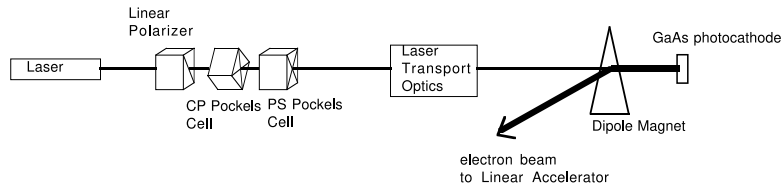


Figure 3.4.: SLC produced polarised e^- bunches by circularly polarising a laser which then hit a GaAs target. Copied from [96].

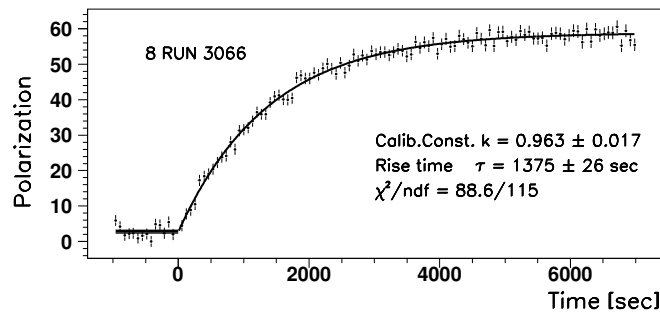


Figure 3.5.: HERA polarimeter data shows the $1 - \exp(-t/\tau)$ transverse polarisation build-up in a circular storage rings. Copied from [97].

sation of the emitted particles [99]. The SLC used a polarised laser hitting a GaAs target (fig. 3.4), and achieved up to almost 80% polarisation [100]. Future colliders can employ essentially the same scheme for the e^- beam. The creation of a polarised e^+ beam can follow a similar principle of a polarised laser beam, and requires additional effort due to the lack of positrons in nature (see section 3.2.2).

Circular colliders can rely on another effect that naturally arises in storage rings; the Sokolov-Ternov effect [101]. When traversing a magnetic field, the spins in a particle beam slowly align themselves with the preferred direction opposite to the magnetic field. In a storage ring, the bunches align their spins along the dipole magnetic fields over time, leading to a transverse polarisation of the beam. The collision can either use this transverse polarisation directly, or use spin rotator magnets to turn the polarisation into the longitudinal direction at the IP. Many storage rings have used this method, including PETRA with transverse polarisation [102], and HERA with both transverse and longitudinal polarisation [103]. At LEP, it was instead more advantageous to energy-dependent depolarising resonances for a precise energy calibration [104].

The rise-time of the Sokolov-Ternov polarisation build-up can limit the use in the experiments. The polarisation builds up exponentially in time like $1 - \exp(-t/\tau)$ (fig. 3.5) with a characteristic build-up time τ that is a function of the magnetic field and the particle energy. For storage rings, the build-up time behaves roughly like R^3/E^5 , where R is the ring radius and E the beam energy [105]. At the same time, radiation damping limits the energy of a storage ring, and the corresponding energy loss per circulation

3. Future e^+e^- collider proposals

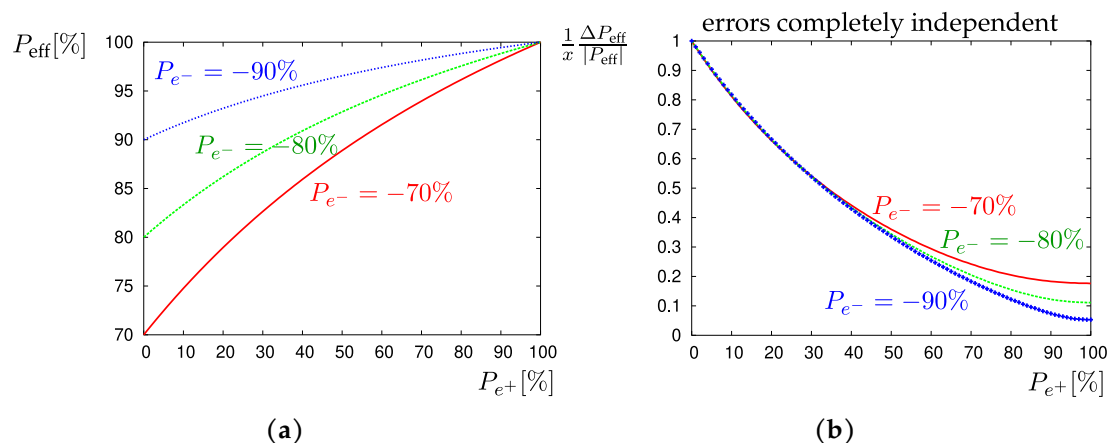


Figure 3.6.: (a) The effective polarisation \mathcal{D}_{eff} gains from both electron and positron beam polarisation. (b) Polarising the positron beam in addition to the electron beam significantly reduces the relative uncertainty on \mathcal{D}_{eff} , which is the primary systematic uncertainty on A_e . Copied from [94].

behaves like E^4/R [91]. Assuming that storage rings will adjust the radius to the energy like $R \sim E^4$, higher energy storage rings will have polarisation rise-times which sharply increase with E^7 .

For future circular colliders like the FCC-ee, the rise-times until a usable polarisation ($> 5\%$) will be multiple hours [106]. At the same time, such machines rely on top-up injection modes to achieve high-luminosities and stable beam qualities, because the beam-beam interaction leads to lifetimes of less than an hour [88]. Colliding bunches therefore cannot build up sufficient polarisation for longitudinally polarised runs, so that the use of transversal polarisation is limited to the high-precision LEP-like energy measurement with dedicated non-colliding bunches [107]. Very small residual longitudinal polarisation could still be present in the colliding bunches. This requires a measurement either with polarimeter or from the collision data, so that the interpretation of electroweak precision observables can properly take that into account [108]. For these reasons, only linear colliders consider longitudinal polarisation runs and all colliders need precise longitudinal polarisation measurements.

Basic advantages of beam polarisation

The discussion on the production of polarised beam at future e^+e^- colliders shows that the availability of beam polarisation is a question of machine design and effort. Current proposals include all possible options; zero, one, or both beams polarised. This makes the potential advantages of beam polarisation an important point in the comparison of these proposals. There are three basic types of advantages from beam polarisation [109–111]; datasets with increased signal purity, direct access to the chiral behaviour of interactions, and a reduced impact of systematic uncertainties. At the core of these benefits

is the chirality-dependence of the SM and potential BSM interactions (section 2.1.1).

A direct consequence of this chirality-dependence is that the different polarised datasets of a polarised collider, differing in the sign of the polarisations, will have different dominant processes. For given analysis there is always at least one dataset with a more favorable signal-to-background ratio than an unpolarised dataset. For example, W boson only couple to left-handed e^- and right-handed e^+ , and the prominence of those specific chiralities will determine the amount of W production [109]. At the same time, the other datasets will act as control regions for the backgrounds of that analysis. This increases the sensitivity of the collider. In practice, datasets with opposite-sign polarisations give the highest sensitivity to s-channel processes that produce a spin-one particle (e.g. Z, γ), while same-sign datasets are unique opportunities to search for BSM physics in relatively background-free environment [110].

The chirality-dependence is itself of interest for collider experiments. Beam polarisation provides access to the chiral behaviour of any visible SM or BSM physics [109–111]. At SLC, electron polarisation gave direct sensitivity to the chiral asymmetry of Z production at the Z pole [112]. This allowed the most sensitive individual measurement of the Weinberg angle [113]. The precision was similar to the combination of the unpolarised LEP measurements which had a factor 25 more events [2]. For a polarised collider, this sensitivity to the chiral asymmetry depends on the effective polarisation

$$\mathcal{P}_{\text{eff}} = \frac{\mathcal{P}_{e^+} - \mathcal{P}_{e^-}}{1 + \mathcal{P}_{e^+}\mathcal{P}_{e^-}}, \quad (3.5)$$

which is also the most important systematic uncertainty. Future colliders can increase \mathcal{P}_{eff} by a larger e^- polarisation and also polarising the e^+ beam (fig. 3.6a), increasing the sensitivity to A_e . Polarised e^+ beams have the additional advantage of reducing the relative uncertainty on \mathcal{P}_{eff} (fig. 3.6b).

As seen already for \mathcal{P}_{eff} , the chirality-dependence of interactions also has a general consequence for systematic uncertainties. Systematic effects are largely independent of the polarisation setting. If the collider provides fast spin flipping, then the systematic effects will fully correlate between the polarised datasets [114]. This in principle allows a decoupling from the physical effects, and even a measurement of the exact shape of the systematic effect [115]. Not much work has been done to test this hypothesis (section 4.1), and part of the work presented here will address this issue (section 7.4).

3.1.4. Beam-induced backgrounds

A common issue for all collider experiments is that backgrounds can occupy the detectors simultaneously to the particles originating from the hard scatterings. The type and severity of such backgrounds depends on the colliding particle types and the machine parameters. In e^+e^- colliders, the most severe of such backgrounds are beam-induced backgrounds and photon-photon collisions [117].

3. Future e^+e^- collider proposals

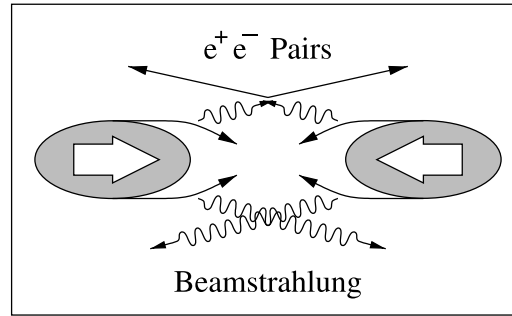


Figure 3.7.: Beam-induced backgrounds in e^+e^- collisions mainly originate from beamstrahlung at the IP, which can lead to fermion pair production from $\gamma\gamma$ collisions. Copied from [116].

Beam-induced backgrounds originate either from beam-beam interactions at the IP or from interactions of the beams with the machine close to the IP. When the two beams get close to each other, they start seeing each others electromagnetic field, which causes the bunches to focus onto each other and radiate beamstrahlung photons (fig. 3.7). The beamstrahlung photons in that strong field can create e^+e^- pairs which then deflect in the field and fly into the detector.

In addition to these beamstrahlung-produced e^+e^- pairs, the beam particles can radiate virtual photons that collide to produce fermion pairs. This is the dominant background at e^+e^- colliders [118]. The results are again low-angle e^+e^- pairs, as well as low-angle quark pairs. While e^+e^- pairs fly at very low angles and are mainly relevant for the very forward calorimeters, low-angle quark pairs can hadronize to jets that occupy a larger angular range of the forward-region. For this reason, low- p_T hadrons are a challenge to jet clustering in low-angle jets (chapter 6).

Additional beam-induced backgrounds originate before the beams arrive at the IP [117]. These include synchrotron radiation from when the beams pass through the focusing magnets, and muons from collisions of the beam halo with the collimators. Reconstruction algorithms can reliably identify such backgrounds by their direction and where they hit the detector. These backgrounds therefore play a minor role compared to originating from $\gamma\gamma$ collisions.

3.2. The International Linear Collider

The International Linear Collider (ILC, fig. 3.8) is currently the most advanced proposal for a high-energy e^+e^- collider [78–83, 119]. It is a linear collider with two polarised beams and possible center-of-mass energies ranging from the Z-pole (91 GeV) up to 1 TeV.

The core part of this machine are its main linear accelerators (“linacs”), composed of superconducting radio-frequency accelerating cavities. These cavities have an accel-

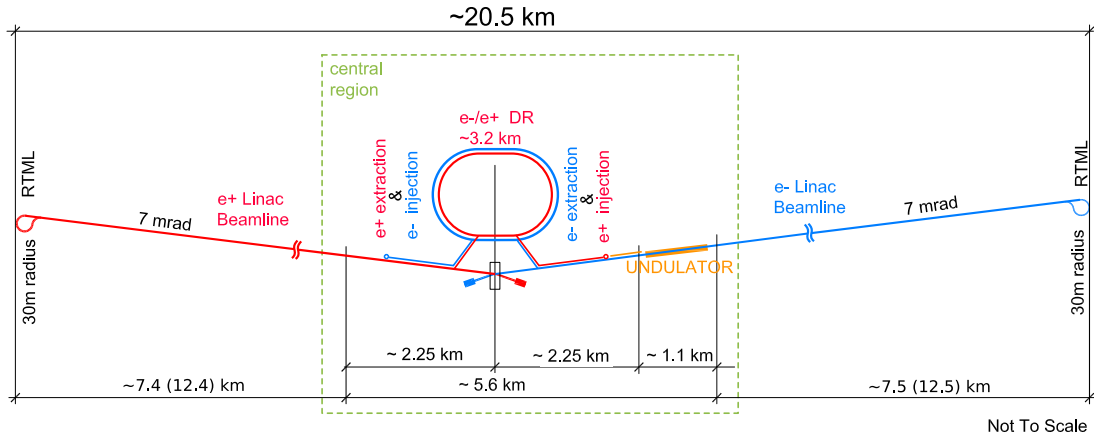


Figure 3.8.: The International Linear Collider - shown here for its 250 GeV and 500 GeV (in brackets) baseline - is a linear e^+e^- collider with two polarised beams. Copied from [119].

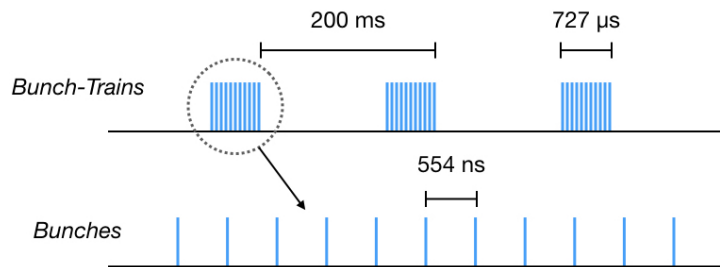


Figure 3.9.: The ILC beams consist of “bunch-trains” with a frequency of 5 Hz (upgradable to 10 Hz), where each train is 727 μ s long and contains 1312 bunches (upgradable to 2625 bunches) [81]. Copied from [120].

erating gradient of around 31.5 – 35 MV/m [121], so that each GeV of beam energy requires around 30 m of acceleration for that beam. More generally the accelerator also determines the structure and timing of the particle bunches and with that the luminosity [81]. The ILC beam consists of bunches which further group into “bunch trains” (fig. 3.9). In the first stage, the repetition rate of each train is 5 Hz, and each train consists of 1312 bunches. A luminosity upgrade can increase the number of bunches per train to 2625. This allows to collect multiple attobarns of luminosity on the timescale of 5 – 10 years, depending on the energy stage.

The running scenario (fig. 3.10) reflects the baseline physics program of the collider [73]. It starts with a run at 250 GeV close to the ZH threshold. After this initial run, an energy upgrade will allow runs at the $t\bar{t}$ threshold at 350 GeV and at 500 GeV where the main Higgs production mode becomes vector boson fusion. The design of the machine also allows runs directly on the Z -pole around 91 GeV and - with an extension of the linacs - at 1 TeV [122]. This large energy range, together with the polarisation of

3. Future e^+e^- collider proposals

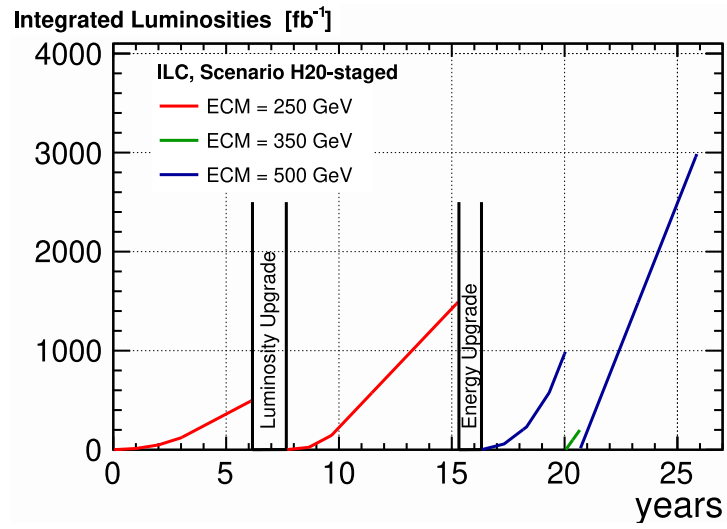


Figure 3.10.: The baseline running scenario of the ILC foresees a first stage at 250 GeV, followed by an extension of the machine that allows runs at 350 GeV and 500 GeV. Copied from [73].

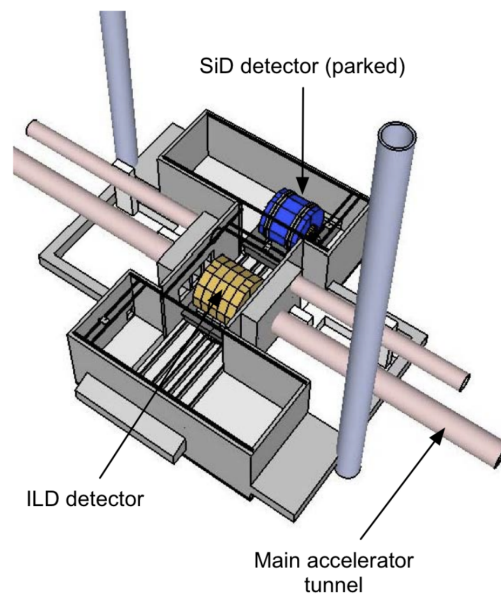


Figure 3.11.: The ILC has one interaction point, at which two detectors can switch places using a push-pull method. Copied from [82].

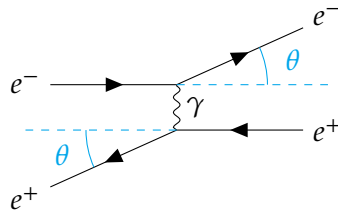


Figure 3.12.: Feynman diagram of t-channel Bhabha scattering. QED-dominated low-angle Bhabha scattering serves as a “standard candle” for the luminosity measurement.

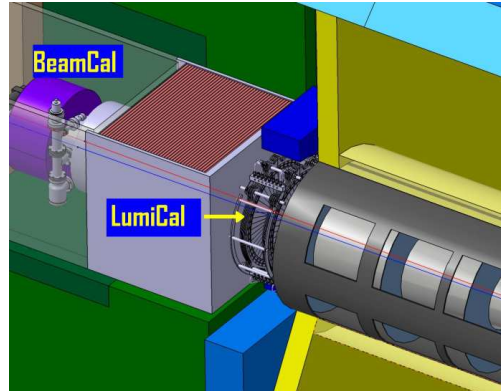


Figure 3.13.: The very-forward region of the detectors at the IP includes an electromagnetic calorimeter for the luminosity measurement via low-angle Bhabha events (“LumiCal”). Copied from [125].

both beams, guarantees a diverse physics program and flexibility for the case that new physics appears anywhere within this range.

Essential for the physics program are also the detectors at the interaction point (IP) that measure the results of the collisions. The ILC has one IP for collisions, and foresees a push-pull method that allows two detectors to share the luminosity 50-50. While one is measuring, the other is “parked” (fig. 3.11). The two proposed detectors concepts are the International Large Detector (ILD) [82, 123] and the Silicon Detector (SiD) [82, 124]. Both of these are high-precision multipurpose detectors with full angular coverage. The complementarity of those two detectors will provide precise and reliable measurements along the whole center-of-mass energy range.

The following presents some detailed aspects which are relevant to this work.

3.2.1. Luminosity measurement

The luminosity is an inevitable input to every cross-section measurement at a collider. The ILC will require a precision of around $\Delta L/L = 1 \cdot 10^{-3}$ for its physics program [82].

For an accurate determination, colliders usually measure the luminosity directly from

3. Future e^+e^- collider proposals

collision data. This requires a process that can serve as a reference, with an already precisely known cross-section. For e^+e^- colliders, the standard choice is low-angle Bhabha scattering $e^+e^- \rightarrow e^+e^-$. At low scattering angles, the pure QED process of t-channel photon exchange dominates this scattering (fig. 3.12) [126]. A precise calculation of this QED process is possible [127], allowing a determination of the luminosity from the measured number of low-angle Bhabha events.

$$L = N_{\text{Bhabha}} / \int \sigma_{\text{Bhabha}} d\Omega_{\text{detector}} \quad (3.6)$$

The detectors at the ILC interaction point foresee a dedicated low-angle electromagnetic calorimeter (“LumiCal”, fig. 3.13) which will measure the low-angle Bhabha events [125]. Each of the two detectors places the LumiCal at a slightly different position, leading to angular coverages of $\theta \in [31 - 77]$ mrad for ILD and $\theta \in [40 - 90]$ mrad for SiD [82].

A dedicated study with the ILD LumiCal at center-of-mass energies of 500 GeV and 1 TeV found that systematic uncertainties dominate the luminosity precision [125]. The effects that cause the largest uncertainties include the deflection of the scattered particles in the electromagnetic fields of the bunches, background events and beam backgrounds, and the LumiCal energy scale. Taking these and more effects into account, the study finds relative uncertainties of $\Delta L/L = 2.6 \cdot 10^{-3}$ at 500 GeV and $1.6 \cdot 10^{-3}$ at 1 TeV. Such precisions do not meet the ILC luminosity precision goals yet, further studies are necessary to further reduce the systematic uncertainties. In the presented work, the introduced precisions serve as a conservative estimate of the ILC luminosity measurement.

3.2.2. Polarisation implementation

The ILC aims to polarise both of its beams, which is of key importance to the ILC physics program [94]. For the physics program it is best to have the highest possible degree of polarisation. To also gain a better control of systematic effects, it is important that the machine can perform a fast flip of the spin directions before the IP. This ensures that the systematic effects correlate between the different polarisation directions of the beam.

The SLC already used a polarised electron source with fast spin flipping capabilities [96, 100], and the ILC source relies on the same principles [80]. A highly polarised laser hits a target cathode in a high-voltage DC gun. The freed electrons from this process have a high degree of polarisation, with a minimum of 80% assumed for the ILC.

In contrast to electrons, positrons do not appear in abundance in nature. The challenge for the positron source is to produce and polarise them at the same time. While no previous collider has used such a source, a concept for such a source first emerged in the '80s [129, 130]. This concept proposes to send an electron beam through a helical undulator to produce circularly polarised high-energy photons. When the polarised photons subsequently hit a target they produce polarised electron-positron pairs. The

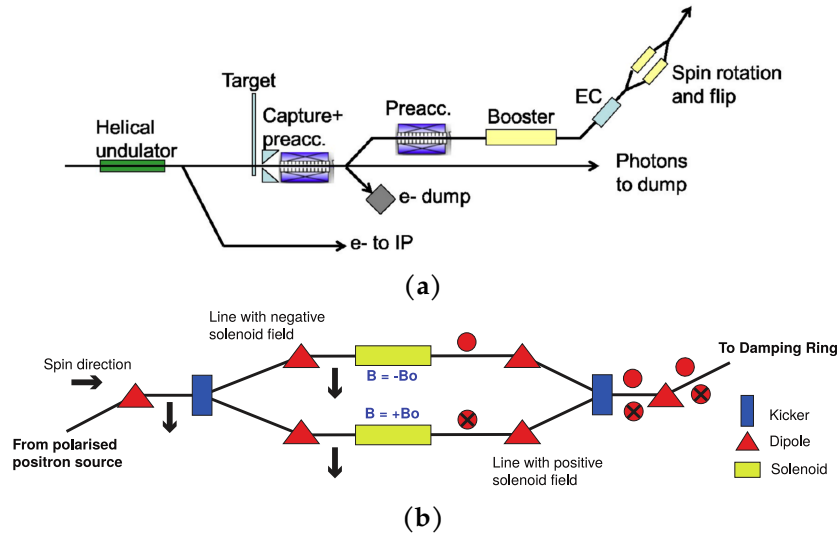


Figure 3.14.: (a) Schematic of the ILC polarised positron source which uses polarised photons from a helical undulator in the electron main linac. (b) Schematic of the spin flipper which sets the direction of the positron polarisation. (a) copied from [128], (b) from [80].

ILC design has adapted this concept (fig. 3.14a) and includes a helical undulator in the main electron linac [131]. This promises a positron polarisation of at least 30%.

One drawback of this technology is that the magnetic field orientation of the undulator fixes the polarisation direction of the positrons. A fast spin flip is not an intrinsic part of this design. The ILC introduces an additional system in the beamline after the positron source that orients the polarisation (fig. 3.14b) [132]. This system consists of two parallel beam lines that each rotate the polarisation in one of the two longitudinal directions, and a fast magnet that sends the bunch into one of the two beam lines. In this way, the ILC can also perform fast spin flipping on the positron beam.

Non-baseline options

The longitudinally polarised beam sources described above are the baseline design for the ILC. In addition to those options, the ILC community has been and is evaluating alternatives to further solidify the case for the ILC. Two such alternative ideas are of particular interest to the work here; an unpolarised “conventional” positron source, and runs with beams that are not longitudinally polarised.

The option of an unpolarised e^- -driven positron source is a back-up solution for the ILC [133, 134]. It consists of an additional linac that accelerates electrons to 3 GeV before colliding it with a target wire to produce electron-positron pairs (fig. 3.15). Compared to the undulator-based source, this e^- -driven source has the advantage that it is a historically well-tested design. Most notably, the SLC employed a very similar concept for

3. Future e^+e^- collider proposals

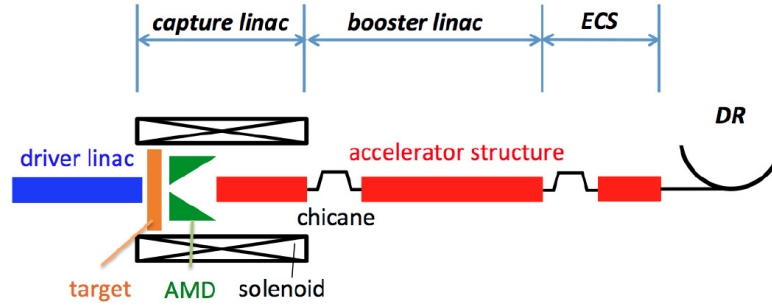


Figure 3.15.: Schematic of the conventional electron-driven source of unpolarised positrons, which is an alternative to the undulator-based polarised source in the ILC baseline design. Copied from [133].

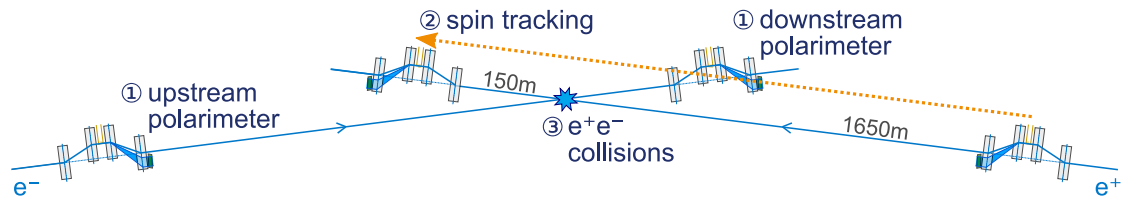


Figure 3.16.: Polarisation measurements at ILC use both up- and downstream polarimeters (1) which require spin-tracking to the IP (2), and direct polarisation measurements from the collision data at the IP (3). Copied from [60].

positron production [135–137]. Part of the work here considers the impact that the absence of positron polarisation will have on the measurement (section 4.1 and chapter 7). For the ILC, the cost of the two positron source designs is comparable [134].

Another non-baseline option is to flip the beam polarisation to a transversal direction before the collisions, or to add depolarised beam settings. These two options serve two different purposes, and require only a different setting of the spin rotators. Transversally polarised beams offer a unique opportunity to directly measure CP-violating effects [111] and EFT-parameters [138], under the condition that both beams are transversally polarised. Unpolarised beams settings do not offer an immediate physical advantage. Their purpose would be an improved control of systematic effects [139]. Transversally polarised settings can offer the same advantages if again they are included in the fast spin flip. In both cases, the additional beam settings will compete with the longitudinal settings for the corresponding fractions of the total luminosity. The work presented here only considers the unpolarised setting directly (chapter 7), which one can consider a conservative estimate for the transversally polarised case.

3.2.3. Polarisation measurement

The exact values of the beam polarisations at the IP determine the composition of chiral interactions. A precise interpretation of these interactions in the collisions requires a

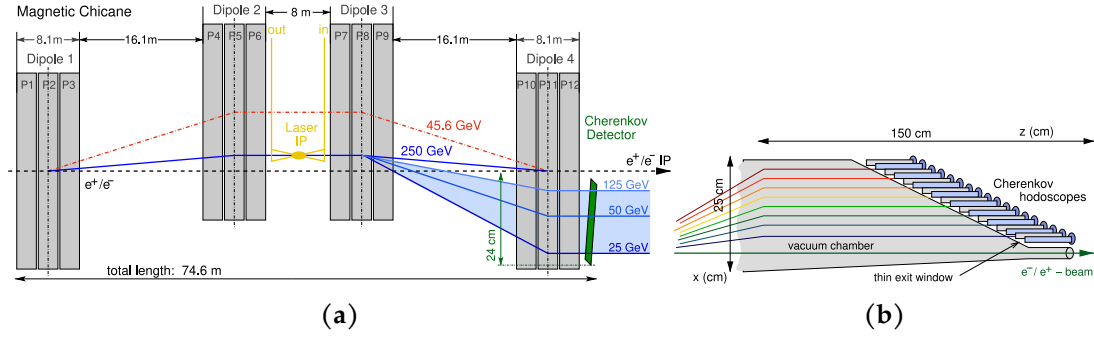


Figure 3.17.: The ILC polarimeters are combination of (a) a magnetic chicane, where the bunches collide with polarised laser beams, and (b) a set of Cherenkov detectors that measures the scattered electron energy spectrum. Copied from [140].

precise knowledge of the polarisation values. The collider must perform measurements of the beam polarisation, short “polarimetry”, to avoid introducing polarisation-related systematic uncertainties. Studies for the ILC show that the necessary level of relative precision is at or below the permille level [141].

The ILC polarimetry is a combination of a direct polarisation measurement from collision data at the IP and polarimeters up- and downstream of the IP (fig. 3.16) [122, 142, 143]. These two methods contribute in different ways to the polarisation measurement.

A direct measurement from the collision data at the IP is possible when at least one beam is polarized [139]. This measurement is sensitive to the luminosity-weighted average polarisation at the IP

$$\langle \mathcal{P} \rangle_L = \frac{\int \mathcal{D}(t)L(t)dt}{\int L(t)dt} \quad (3.7)$$

with the time-dependent polarisation $\mathcal{D}(t)$ and luminosity $L(t)$. It cannot measure the time-dependence of the polarisation. The method requires fast spin flipping so that the different polarised datasets are taken simultaneously, which is part of the ILC baseline. This fast spin flip correlates the other time-dependent systematics from detector and accelerator across the data sets. The correlation allows a polarisation measurement through a comparison of the different polarised datasets. Studies of this method at the ILC show that it can provide the necessary permille or even sub-permille precision on the average polarisation [60, 144, 145] (more details in section 4.1).

The polarimeters (fig. 3.17) provide complementary information to that of the collision data measurement [146]. They measure the individual beam polarisation of each polarised bunch train 1650m before and 150m after the collision (fig. 3.16), and extrapolate that measurement to the polarisation at the IP. This extrapolation is a dominant source of systematic uncertainty [147], and needs to take into account the spin transport between IP and polarimeters as well as the depolarising effects in the collision. While the precision on the single train polarisation is only 0.25% at the ILC [141, 148], the polarimeter measurements provide complementary information to the collision data mea-

3. Future e^+e^- collider proposals

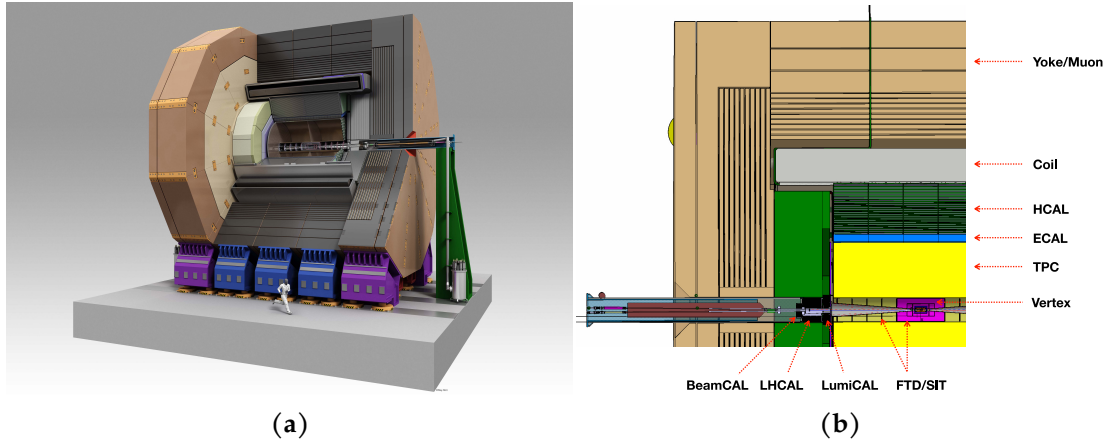


Figure 3.18.: (a) 3D rendering and (b) cross section of the ILD, a general-purpose 4π detector. It uses a TPC tracker and highly granular calorimeters within the magnetic coil to allow optimal Particle Flow reconstruction. (a) copied from [82], (b) from [123].

surement [146]. The advantage of the polarimeters lies in a high-statistics measurement of the polarisation of each bunch train, so that only systematic effects limit the precision [147]. Since those systematic effects largely correlate from train to train, the polarimeters can contribute precise measurements of relative polarisation differences in each beam. This includes the time-dependence of the individual beam polarisations, which complements the luminosity-averaged measurement from collision data. It also includes precise comparisons of the different polarisation settings of a beam, which again requires fast spin flipping to correlate time-dependent systematic effects between those polarisation settings.

With the combination of the collision data measurement and the polarimeters, the ILC can precisely measure each aspect of the beam polarisations. This is the basis for precise measurements of the chiral structure of interactions at the ILC.

3.3. The International Large Detector

The International Large Detector (ILD, fig. 3.18) is one of the two proposed detectors for the ILC interaction region [82]. This section introduces the relevant basics of the ILD concept, including the design, event reconstruction, performance and limitations.

3.3.1. Detector design

The target of the design of the ILD is a precise event reconstruction using particle flow (PF) techniques [123]. PF reconstruction tries to match up all the signals that each particle leaves in all sub-detector components. It then only uses the most precise sub-

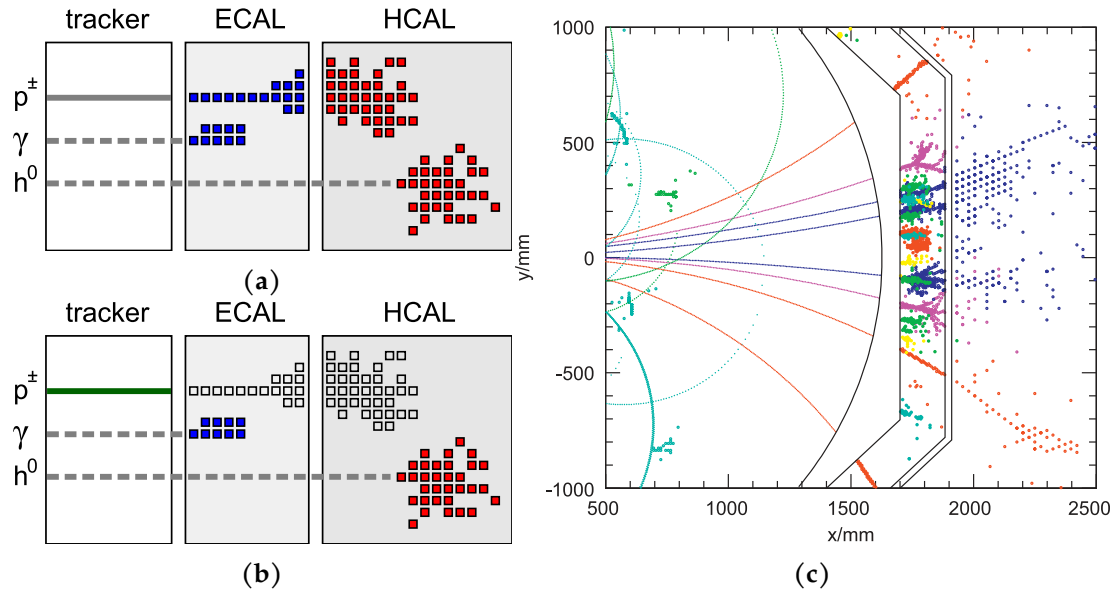


Figure 3.19.: (a) Traditional energy reconstruction ignores tracker information and sums up the energy in the calorimeter systems. (b) Particle Flow calorimetry uses only the most precise sub-detector measurement for each particle. Using PandoraPFA, ILD can disentangle the jet particles even in compact 100 GeV jets (c). (a,b) copied from [149], (c) from [150].

detector measurement for each particle. Based on those precise measurements, it accurately discards the other sub-detector measurements. In practice, it means that the track of charged particles yields a precise momentum measurement. The algorithm marks which hit clusters in the calorimeter originate from those charged particles, and only uses the remaining clusters for the formation of neutral particles. This stands in contrast to the traditional calorimetry in event reconstruction, which ignores tracker information in the energy reconstruction (left in fig. 3.19). As a consequence of this PF technique, the final reconstruction event is a collection of reconstructed particles, where each particle consists of all the assigned sub-detector hits, and only the most accurate sub-detector measurements contribute to the assigned four momentum (fig. 3.19c).

A detector optimization for PF reconstruction implies a focus on the imaging capability of the detector. The reconstruction must be able to precisely separate the contributions of the different particles in each sub-detector and to combine the different components to a reconstructed particle. Such imaging tasks become easier with a higher granularity. The PF-optimization of ILD is most visible in three properties/components of the ILD;

- **A time projection chamber (TPC)** provides up to 220 position points along the particle trajectory, which together with the 3.5 T magnetic field yields precise track recognition, with a minimal impact on the particle due to the low material budget,

3. Future e^+e^- collider proposals

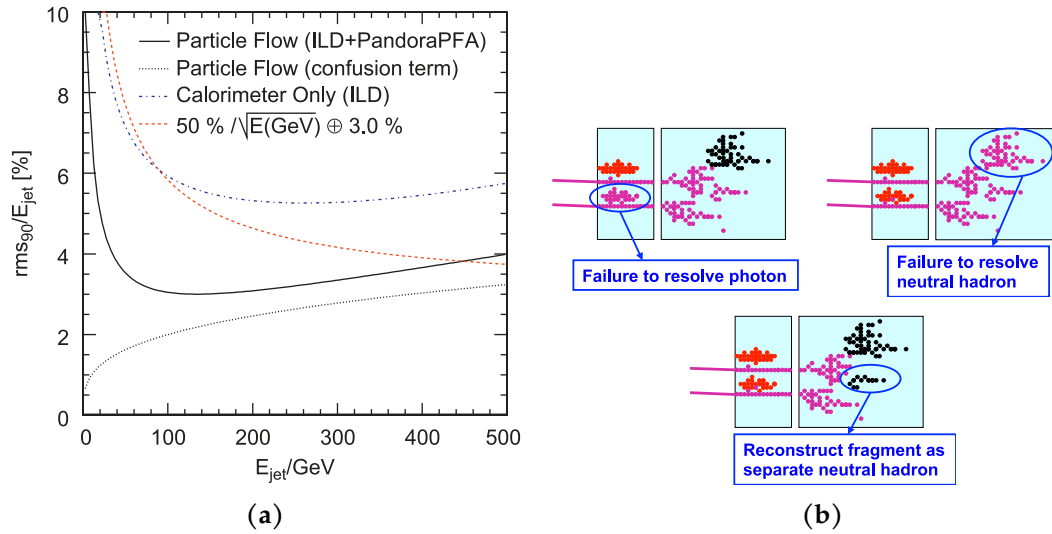


Figure 3.20: (a) The ILD JER shows that the intrinsic calorimeter resolution dominates at low energies, while confusion effects dominate at high energies. (b) Confusion effects can lead to missed or double-counted particles. (a) copied from [150], (b) from [151].

- **Highly granular sampling calorimeters**, with cell sizes down to $5 \times 5 \text{ mm}^2$ for the ECAL and down to $3 \times 3 \text{ cm}^2$ for the HCAL, allow a sharp resolution of the individual calorimeter showers, and
- **The containment of tracker and main calorimeters within the magnetic coil** makes sure that the TPC track and calorimeter clusters are easy to match, and that little energy gets lost before the particle reaches the calorimeter.

Additional detector components ensure a precise momentum measurement (SET), a full angular coverage of the detector (FTD, LumiCal, LHCAL, BeamCAL), precise vertex reconstruction (Vertex detector, SIT), and the detection of muons and calorimeter leakage (muon chambers in return yoke).

Limitations of PF calorimetry in ILD

Even in a highly granular detector using particle flow reconstruction, a number of effects limit the measurement and lead to non-zero resolutions. The most difficult objects for reconstruction are jets due to their diverse particle content and the small angular distance between the particles. Two effects drive the jet energy resolution (JER) of the ILD: the intrinsic calorimeter energy resolution and confusion effects (fig. 3.20). Both of these affect the reconstruction of neutral particles in the calorimeter.

The intrinsic energy resolution of the ILD calorimeters is the result of statistical fluctuations in the shower and in the sampling, noise, and calibration uncertainties. At low

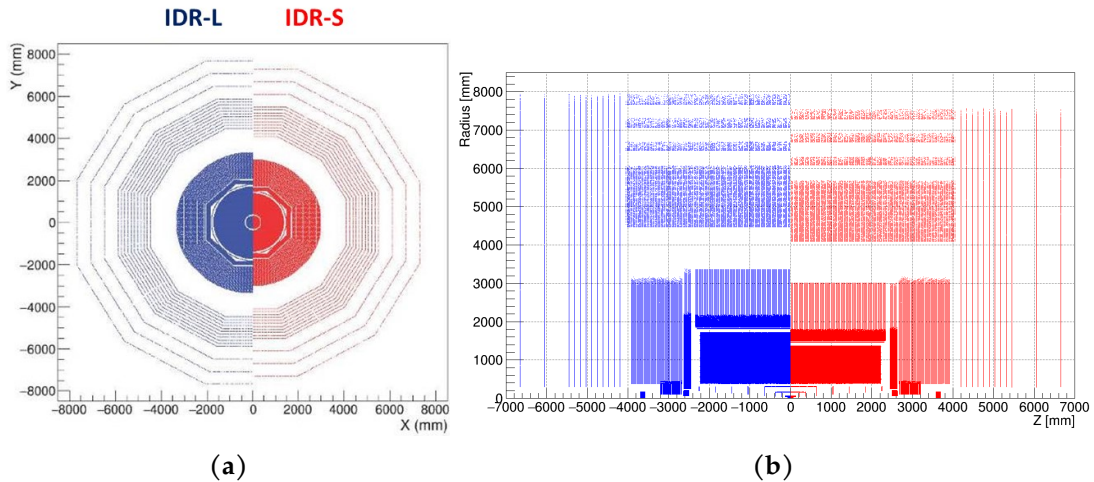


Figure 3.21.: Cross sections comparisons in (a) the xy -plane and (b) the yz -plane of the two ILD models (left halves: large model, right halves: revised small model) show how the small model reduces the TPC radial depth while keeping all other depths constant. Copied from [123].

energies, the $1/\sqrt{E}$ -dependent statistical term becomes large due to the smaller number of particles in the shower. For ILD, this is the dominant limitation for low energy jets with $E_{\text{jet}} \lesssim 100$ GeV. At these lower energies, the jet has a lower boost and the particles arrive well-separated at the detector.

When the jet energy increases above 100 GeV, the jet becomes more boosted and the particles arrive even closer to each other in the calorimeters. This leads to an increase overlap of the showers that each particle produces in the calorimeters. The PF reconstruction tries to disentangle these overlapping clusters. Sometimes, it cannot do this assignment of calorimeter hits to particles perfectly, which leads to confusion effects [150, 151]. Such confusion effects can lead to both an increase or a decrease of the measured neutral particle energy, and even to the false detection of fake neutral particles (fig. 3.20b). The increased particle density of higher energy jets increases this confusion, so that it becomes the limiting factor for the JER of high energy jets.

3.3.2. Recent optimization efforts

The original proposal of the ILD detector (“IDR-L”) used physical performance as the primary target [152]. Since then, the scientific community has put forward a major effort to realize the ILC project. These efforts put new weight on the project cost, and lead to a revision of the cost drivers of the ILD model and the consideration of a revised smaller ILD model (“IDR-S”) [123].

The most costly parts of the original ILD model are the calorimeters, the coil and the yoke. All of these have depths which are necessary for physical performance; the calorimeter depth ensures that the calorimeter captures all showers, and the magnetic

3. Future e^+e^- collider proposals

field dictates the coil and yoke depths. A reduction of all their volumes remains possible; it requires reducing the volume contained by the calorimeters. The revised smaller ILD model achieves this by reducing the radial depth of the TPC (fig. 3.21). This change to the tracking volume will in principle impact the tracking performance, since it reduces the length of the measured tracks before the calorimeters. The small ILD model counters this by increasing the magnetic field, leading to stronger curving tracks and increasing the track length [153]. By reducing the overall volume, and especially the calorimeter volume, the revised small ILD model reduces the detector cost by around 13% (table 9.6 in [123]).

The cost optimization process parameterized the impact of this change on the performance and ultimately chose a revision that will minimally affect that parameterized performance. It was limited to a subset of relevant reconstruction performances and physical results, and used fast detector simulation studies with the SGV tool [154]. A large set of follow-up studies that used full simulations of both models verified that the impact on the high-level analysis performance is minimal [123]. This includes a study which is part of the work presented here (chapter 6).

3.3.3. Relevant performance aspects

The unique particle flow driven design of the ILD detector allows a precise event reconstruction. This includes for example a momentum reconstruction which is an order-of-magnitude more precise than current LHC experiments, as well as precise calorimetry and vertex measurements [123]. Whether these precisions are important is a question of the exact physics analysis, and most importantly the considered final state.

Jet energy resolution

Part of the study presented here focuses on the reconstruction of jets from hadronic decays of W s and Z s. The most relevant reconstruction aspect for such decays is the jet energy resolution (JER) $\Delta E_{\text{jet}}/E_{\text{jet}}$. With the precise particle flow reconstruction of all jet components, ILD can achieve a JER of 3% for jets with $E_{\text{jet}} \gtrsim 100$ GeV (fig. 3.22). This is around a factor 2 better than the current JER of the ATLAS and CMS experiments for similar E_{jet} [155, 156].

As described above (section 3.3.1), the JER in a particle flow detector first improves with energy until confusion effects become dominant and the JER increases again (fig. 3.22) [157, 158]. It also increases when the jet flies more in the forward direction because an increasing percentage of the jet particles cannot traverse the precise tracking detector or are lost in the beam pipe. The two jet observables that determine the JER are therefore angle and energy.

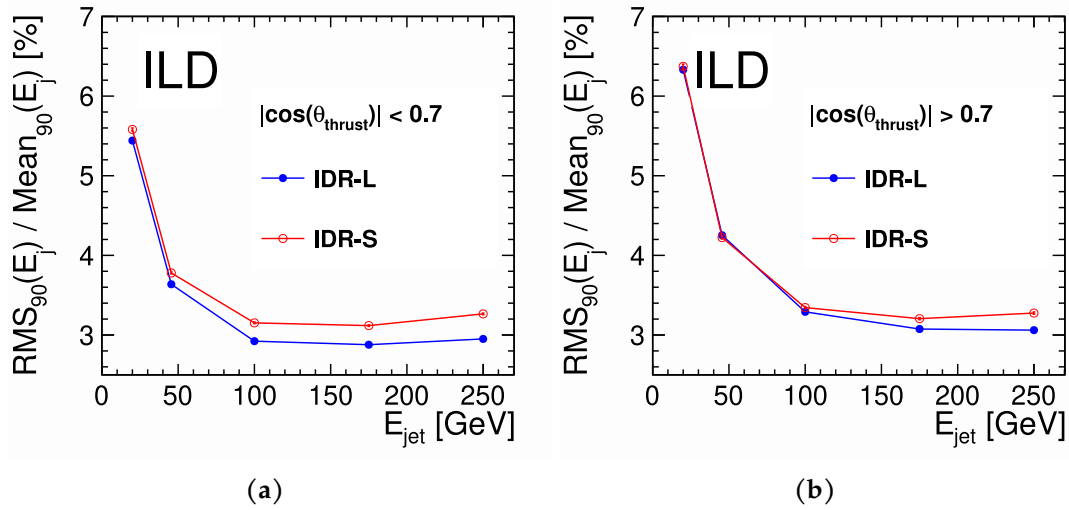


Figure 3.22.: The ILD jet resolution improves with jet energy and is better in (a) the barrel than (b) the forward region. A smaller ILD model will worsen the resolution especially for high-energy jets. Copied from [123].

JER of the cost-optimized ILD model

The JER is a composite of the resolution for charged particles, originating from the tracking resolution, and the resolution for neutral particles, originating from the calorimeter resolution and confusion effects. The cost optimized ILD model reduces the tracking detector radial depth, and correspondingly moves the calorimeters closer into the detector while conserving their depths. A relevant consequence of these changes is an increase in calorimeter cluster overlaps due to the shorter IP-calorimeter distance. Such overlaps can lead to increased confusion in the clustering steps of Particle Flow (section 3.3.1). This affects jets which fly into the central part of the detector, and more so if the jet is more collimated, i.e. has higher energy. The strongest increase in the JER when moving from large to small detector model is around 0.3% in the barrel region (fig. 3.22a). For a given physics analysis, the jet angular and energy distributions will ultimately determine the impact of the choice of detector model.

Track reconstruction

Another detector aspect relevant to this study is the track acceptance. The track acceptance describes, which parts of the detector are able to reconstruct charged particle tracks. For ILD, track reconstruction has a reconstruction efficiency of over 99.8% for particles that have a momentum of at least 1 GeV and that fly at a polar angle below around 18 deg [82]. For particles at lower angles, the efficiency starts to drop and stays above 90% until it reaches around 7 deg. At the lowest angles down to around 7 deg the Forward Tracking Disk (FTD, fig. 3.18b), consisting of five layers on each side of

3. *Future e^+e^- collider proposals*

the IP, can still measure enough hits to reconstruct a track. Below those 7 deg, a track reconstruction is not possible.

4. Previous studies and open questions

This study investigates the limitations of electroweak precision at future e^+e^- colliders, and how to push those limitations to a minimum. In this context, two topics will play a dominant role; the measurement of beam polarisation, and the measurement of electroweak gauge couplings. This chapter provides an overview of previous work on these two topics, presents the open questions on them, and describes the corresponding purpose of this study.

4.1. The Impact of beam polarisation at e^+e^- colliders

Recent discussion of different future e^+e^- collider proposals have re-opened the discussion on the importance of beam polarisation [1]. This also includes a discussion within the ILC design studies on the importance of positron polarisation [131, 133]. The paragraphs below outline the role that previous study contribute to beam polarisation at future e^+e^- colliders.

The SLC powerfully demonstrated how beam polarisation grants direct access to the chiral structure of electroweak interactions [112, 159]. With around a factor 25 fewer events, the SLD experiment achieved the same precision on the electroweak mixing angles as the combination of the LEP experiments [2]. The situation for future colliders will be similar. Both at and beyond the Z-pole, beam polarisation probes the chiral structure to which detectors are otherwise largely insensitive [160, 161]. This can become especially important when the collider discovers unknown particles or interactions with unknown chiral structures [94, 110].

Whether or not a collider runs with polarised beams, the knowledge of the polarisation of the beam is important. An undetected deviation of the polarisation can lead to false discovery claims and distort the measurement of SM parameters. The necessary precision on the polarisations is a question of the exact measurement. For fermion pair production measurements with polarised beams, the relative polarisation precision must be at or below the level of the statistical uncertainty of $1/\sqrt{N_Z}$ [139]. Studies for the ILC confirm this and set the corresponding requirement at the level of a few 10^{-4} [122].

A large range of studies have investigated the achievable precision at previous and future e^+e^- colliders. The basic methods are the same as outlined for the ILC (section 3.2.3); the usage of polarimeters on the individual beams, and measurements of the polarisation from collision data.

4. Previous studies and open questions

The Compton polarimeter at SLD measured the polarisation of every seventh bunch [162], and when averaged by luminosity over the last two years of running achieved a relative precision of around 0.5%. Systematic uncertainties fully determined this precision on the luminosity-weighted average polarisation (eq. (3.7)). Studies for future collider conclude an improvement in the single-train polarisation precision of a factor 2 [141]. This will fall short of the necessary few 10^{-4} precision by almost an order of magnitude, and the role of polarimeters mainly becomes the tracking of the time-dependence.

Polarised colliders can use the polarisation measurement in collision data to make up for this deficit. The original proposal for a method based on fermion pair production polarised cross-sections, named Blondel method, considered the LEP Z-pole run with a fixed polarisation direction [139]. It pointed out that the method requires polarisation of both beams. A later study adapted the method to colliders at higher energies with the ability to reverse the polarisation direction [109]. That study found that the method gets close to the few 10^{-4} precision. It also introduced a new method using the differential cross-section measurements of W pair production, which works also when only a single beam is polarised. With both of those methods combined, the study concludes a negligible systematic uncertainty from polarisation when both beams are polarised.

Since then, studies have tested a combination of polarimeters, Blondel scheme and differential fits for future colliders, and most prominently the ILC. Some notable conclusions amongst these studies include that the differential measurement with WW and single- W events outperforms the Blondel method [60, 144, 145], that positron polarisation is essential for the control of polarimeter biases [60, 111], and that a collider with two polarised beams can easily simultaneously measure beam polarisations and electroweak parameters in collision data [60, 157]. They also show that the necessary few 10^{-4} polarisation precision is possible for all stages of the ILC.

Open questions

As outlined above, previous studies have started to directly test the simultaneous extraction of beam polarisation and electroweak observables from collision data. These studies had limited themselves to testing Triple Gauge Couplings in W pair and single- W production, and the left-right asymmetry in fermion pair production. This is a rather limited set of physical effects on the relevant final states. One direction to expand these studies is to include a larger set of physical observables which can interfere with the polarisation measurement.

Another open question revolves around the impact of beam polarisation on experimental systematic uncertainties. The experience at SLD has shown that systematic uncertainties only minimally affect chiral observables like the left-right asymmetry [112]. Behind this is a rather simple logic; experimental systematics are independent of the chirality of the initial state, which is a clear contrast against chiral observables. A collider with beam polarisation produces multiple datasets with different chirality com-

binations. Chiral observables have notably different impacts on the different datasets. Experimental systematics on the other hand affect datasets in the exact same way if they are taken in the same macroscopic time period. If the collider can perform fast (and random) helicity reversal, the experimental effects will have the same effect on all polarised datasets. This fundamentally decouples chiral observables from systematic uncertainties. Such a decoupling will come into play whenever the main constraint on a physical effect comes from such chiral observables. This can impact the predictions of a large set of electroweak measurements, including the measurement of chirality-dependent EFT operators.

In the context of beam polarisation measurements, previous studies largely focused on a specific collider with a given polarisation setup. This approach can provide reliable predictions for that specific setup. When it comes to the impact of the availability of beam polarisation on the polarisation measurements, it will be more instructive to perform tests on different collider scenarios within one framework. This entails a trade-off in which the exact predictions for any given scenario will be less realistic, with the gain of clearer messages on the impact of beam polarisation. Such an approach also provides a basis for testing the open questions mentioned here.

4.2. Gauge boson self-coupling in e^+e^- collisions

The interaction of SM electroweak gauge bosons with each other is a direct consequence of the SM gauge symmetry structure (section 2.1.1). Turning this around, measurements of the gauge couplings of these interactions are direct tests of the SM gauge symmetry structure and serve as a way to search for deviations from the SM prediction.

Such precise tests of the SM electroweak sector are a main research interest of future e^+e^- colliders.

4.2.1. Triple Gauge Couplings

Triple gauge couplings (TGCs) are the most accessible way to directly test the gauge symmetry structure of the SM (section 2.1.1). Measurements of the production of multiple bosons can probe the three TGCs g_1^Z , κ_γ and λ_γ (section 2.2.3). When these measurements reach precisions of a few 10^{-3} they start probing at the level of radiative corrections [163]. This would mark a precision test of the SM gauge symmetry structure.

The most precise TGC measurements to date come from e^+e^- collisions at LEP and pp collisions at LHC [164]. Almost all of those measurements use single-parameter fits, which test each parameter individually while keeping all others fixed to their SM value. The LEP single-parameter measurements reached precision of $2 - 4 \cdot 10^{-2}$ [3]. One of the LEP experiments, ALEPH, also tested a simultaneous fit and found that it worsened the TGC precision by less than a factor 1.5 [165]. The ATLAS and CMS experiments at LHC have also measured the TGCs in single-parameter fit, reaching precisions of

4. Previous studies and open questions

$6 - 7 \cdot 10^{-3}$ for g_1^Z [166] and λ_γ [167], and $5 \cdot 10^{-2}$ for κ_γ [168]. Predictions for future measurements with the HL-LHC show that these precisions can increase $2 - 5 \cdot 10^{-3}$ for all three parameters [169]. These measurements are starting to reach the level of radiative corrections.

Future e^+e^- colliders will perform TGCs measurements which will out-pass the 10^{-3} level. This precision is possible due to the clean and well-known collision environment and precise final state reconstruction, as LEP demonstrated. The two principle advantages of future e^+e^- colliders are the higher luminosity and energy, as the TGC sensitivity scales with $\sqrt{L \cdot s}$ [163].

Dedicated studies for different future e^+e^- collider proposals have investigated the achievable precision. All of these studies employ a simultaneous extraction of the three TGCs. The unpolarised circular FCC-ee collider can reach precisions of $3 - 6 \cdot 10^{-4}$ with a limited energy range up to the top pair production threshold, assuming negligible systematic uncertainties [87]. For linear colliders, the most extensive studies - including systematic uncertainties - have looked into measurements at the different energy stages of the ILC with two polarised beams. Studies in full ILD detector simulation have considered TGC measurements in semileptonic W pair production with the 500 GeV and 1 TeV energy stages. The 500 GeV study predicted precision of $6 - 7 \cdot 10^{-4}$ [157]. At 1 TeV, the ILC benefits from the high energy and can achieve $1 - 3 \cdot 10^{-4}$ precisions [170]. An extrapolation of those two studies to the 250 GeV stage yields precisions of $7 - 10 \cdot 10^{-4}$ [60]. All of these ILC studies also confirm that a simultaneous measurement of the polarisation and the TGCs does not disturb either ones precision. The CLIC studies use the ILC predictions as a basis to extrapolate to their higher energy stages [85, 171]. Their extrapolations predict precisions of $5 \cdot 10^{-5} - 1 \cdot 10^{-4}$ for the 1 - 3 TeV stages with e^- polarisation.

An earlier set of studies for the TESLA and CLIC colliders took a more explicit look at the role of longitudinal beam polarisation for the TGC precision [57, 138, 172]. Those studies tested measurement scenarios at 500 GeV and 800 GeV. They found that, compared to unpolarised scenarios, an e^- polarisation of 80% improved the precision by a factor 2, and an additional positron polarisation of 60% brought another factor 1.5 - 2.5. In addition, they tested a transverse polarisation scenario, and found that the precision is only slightly worse than when both beams are longitudinally polarised. Those studies were an important input to the polarisation choice of the ILC [94].

Generally, precisions reachable with future e^+e^- colliders probe an order of magnitude past the level of radiative corrections. This will be a direct precision test of SM gauge symmetry structure.

Open questions

The studies of TGCs measurements for the ILC at the 250 GeV are so far relying on extrapolations. This is a remarkable gap insofar as the ILC in recent years has changed its baseline scenario to start with exactly that stage [121]. A recent study addressed this

issue [60]. Unfortunately, follow-up checks in the context of this study here concluded that the TGC treatment of that previous study was inconsistent. This motivates the focus of this study here on the 250 GeV stage of a future e^+e^- collider, including the TGC measurement in W pair production (section 7.7).

On a broader level, the different studies for the current collider proposals have investigated the TGC measurement with the specific energy stages of their collider. This makes it difficult to single out the effect of beam polarisation on the TGC measurement. The studies that did focus on the impact of beam polarisation used high energy stages, which are not part of every proposed collider. Part of this study here will address this point by testing the TGC measurement with different polarisation setups at the common 250 GeV energy stage (section 7.7.4).

A direct comparison of different polarisation scenarios can address also another open question. So far no study has looked into the interplay of TGC and beam polarisation measurements for a collider with only electron polarisation. The answer to this question will naturally arise in the test of different polarisation scenarios.

4.2.2. Quartic Gauge Couplings and Vector Boson Scattering

The process of electroweak vector boson scattering $WW \rightarrow VV$ ($V = W/Z$) is tightly connected to the Higgs sector of the SM and can contain hints to any new physics [173]. Such potential portals to BSM physics are of high interest in the absence of direct observations of BSM particles at high-energy colliders. Within an EFT-framework (section 2.2), BSM physics in the VBS process can appear as anomalous quartic gauge couplings (aQGCs).

The CMS experiment at the LHC delivered the first observation of electroweak production of same-sign W pairs [174], and both ATLAS and CMS have delivered limits on aQGCs in vector boson scattering (VBS) [174, 175]. These results partially use differing parametrisations. For comparability, a rough conversion between these frameworks is possible (section 1.3.1.4 in [176]), so that results here always reference the EFT-parameters¹ α_4 and α_5 . CMS has set the most stringent limits on these parameters to date, with around 10^{-2} precision [177]. Studies for the high luminosity run of the LHC (HL-LHC) predict precisions in the few 10^{-3} range [169].

Linear e^+e^- collider studies have looked into the possibility of measuring aQGCs at the highest energy stages. The main focus of these studies was on $e^+e^- \rightarrow \nu\bar{\nu}VV$ ($V = W/Z$) channel. Studies for center-of-mass energies around 1 TeV predict a precision around 10^{-2} in $\alpha_{4/5}$. [59, 152, 178], comparable to current LHC results. If the e^+e^- collider includes a CLIC-like 3 TeV, the precision can improve to around $2 \cdot 10^{-3}$, slightly better than current HL-LHC predictions.

In light of the current LHC measurements and the HL-LHC predictions, the aQGC measurements at e^+e^- colliders will not lead to significantly improved bounds on anoma-

¹The details of the aQGC EFT Lagrangian do not bare direct relevance to this work and are omitted here. For details e.g. [176].

4. Previous studies and open questions

lous couplings. Instead, e^+e^- colliders can deliver a complementary check of the pp collider results. Part of this complementarity comes from the possibility to measure all final states of the VBS process with precision. Opposite-sign W pair production, for example, suffers from large backgrounds in pp , whereas e^+e^- collider use it as the prime channel for aQGC measurements. This full set of final states also allows e^+e^- colliders to perform global EFT fits with a minimal set of assumptions. In addition, the validity of an EFT approach is less problematic with the comparatively low energy reach of an e^+e^- collider. An e^+e^- aQGC measurement will be an important and unique cross-check of the HL-LHC results.

Open questions

The studies on VBS at high-energy linear e^+e^- are now almost two decades old [178, 179]. They relied on the detector models at that point in time, and used parameterized detector simulations.

Recently the ILD Collaboration has performed a large set of studies looking into updates of its detector design [123]. This requires an updated study that uses the current design in full simulation and checks the impact of potential changes to the detector. A recent study has started looking into this [180], and the study presented here continues that effort (section 6.4).

That same recent study investigated what limits the VBS analysis [180]. It found that high-level reconstruction is a significant challenge for fully hadronic final states. Part of the work presented later further focuses on these limitations (section 6.3), and aims to identify the individual causes of the limitations to inform the direction of future studies.

4.3. Purpose of this work

This study here contains two parts which address different aspects of electroweak precision measurements.

In the first part (chapter 6), as a continuation of a previous study [180], this study addresses the reconstruction challenges at future e^+e^- colliders in the context of a vector boson scattering measurement. This part aims to provide insight into the different experimental effects that can limit precision measurements, and to guide future studies that want to improve the event reconstruction.

The second part (chapter 7) moves away from the experimental environment of the detector, and addresses the impact of beam polarisation on electroweak precision. A simultaneous fit of physical and systematic effects for various polarisation scenarios of 250 GeV e^+e^- forms the basis of that part. The goal is to understand the benefits for each effect separately and on the interplay between them. A consistent treatment of the effects between the scenarios at a common energy allows a precise look at the gains from polarised beams.

5. Datasets

Studying the precision of proposed e^+e^- colliders requires a prediction of what the experiments will see. One way to provide such predictions is through Monte-Carlo events which emulate the conditions at these colliders. Such Monte-Carlo datasets are the basis the analyses in this study.

All the event datasets in this study are part of a large-scale Monte-Carlo production of the Linear Collider Collaboration and the ILD collaboration (section 5.1). The first part of the study uses fully-reconstructed 6-fermion events at 1 TeV (section 5.2), and the second part uses two- and four-fermion generator-level events for a 250 GeV collider (section 5.3).

5.1. The ILC/ILD Monte-Carlo production

This study aims to test the electroweak precision from measurements at future e^+e^- colliders. Many such studies are being and have been performed, all of which require Monte-Carlo datasets for the collisions at such machines. The paragraphs below describe the central large-scale production of such events for the ILC, and how the ILD collaboration uses these collisions to test the ILD in simulation. Work presented in later chapters uses these Monte-Carlo datasets.

5.1.1. Event generation for the ILC

Studies for measurements for any future collider require large datasets of Monte-Carlo collision events for all relevant final states. For the ILC, the generator group (LCGG) of the linear collider collaboration (LCC) performs this large-scale endeavor [181].

The central tool of the LCGG event generation is the WHIZARD event generator [182], at the base of which is the 0Omega matrix element calculator [183]. Except for initial state radiation, the LCGG-production uses the tree-level calculations in WHIZARD. Instructed by steering files, this event generator can calculate the cross-section and generate Monte-Carlo events for a large variety of initial and final states with given chiralities. It also includes features and plugins that handle beam properties and final state evolution. The large-scale LCGG-production stores the Monte-Carlo events in the `stdhep` and the `LCIO` format [184].

The various settings and plugins in WHIZARD allow the steering of the details of the collision and the occurring processes. Events from the LCGG-production contain many such details which will be present in measured collision data. First, calculations with

5. Datasets

GUINEA-PIG [185] together with the Circe2 tool [186, 187] in WHIZARD provide realistic ILC-like beam spectra at the interaction region. Before the hard scattering, the leptons radiate initial state radiation, which WHIZARD parametrises internally. After the interaction, the final state needs to handle τ decays and the evolution of hadronic final states. The Tauola tool handles the τ decays [188, 189]. Parton shower and hadronization use Pythia6.4 [190], with a tuning to LEP-II results [191].

One part of the study here uses the 250 GeV generator level dataset for the comparison of different collider options (chapter 7). This raises the question whether the datasets are valid for colliders other than the ILC. Of the included details in the simulation, only the beam energy spectra and beam sizes are specific to the ILC. This means that strictly speaking the events from the LCGG-production are only fully valid for studies of the ILC. The study here does not further address this point. Future studies can make use of the dedicated datasets of other linear and circular collider groups.

Beam-induced backgrounds

In addition to the hard scattering, the colliding bunches produce backgrounds that overlap with the particles from the hard scatter (section 3.1.4). The LCGG also simulates these backgrounds. One such background are e^+e^- pairs from pair production in the strong fields of the bunches, which the GUINEA-PIG tool can estimate. A second background is low- p_T hadron pair from photon-photon collisions, for which the LCGG employs either Pythia or a custom tool.

Since those backgrounds are independent of the hard scattering, the simulation of the backgrounds can happen apart from the simulation of the hard scattering process. For the same reason, the generator-level datasets (e.g. the 250 GeV dataset in section 5.3) do not include such backgrounds. Instead, the LCGG supplies a separate dataset of these backgrounds, and the detector collaborations can merge these backgrounds with the hard scattering after applying the detector simulation.

5.1.2. The ILD detector simulation and event reconstruction chain

The LCGG-generated collision events, are the base to test measurements with any detector proposed for the ILC. As one such proposal, the ILD collaboration makes use of these generator level events and runs them through a chain of detector simulation of event reconstruction [192]. Such fully simulated and reconstructed events allow realistic predictions for the measurements at the ILC.

The basis of both the simulation and the reconstruction is the iLCSoft software package. It contains a modular framework called Marlin which can chain together the different steps of the production [193]. An implementation of the two ILD models (section 3.3) into the production is possible with the DD4hep generic detector description framework [194, 195]. For the simulation of particle propagation through the detector and the detector response, the production uses the Geant4 toolkit [196]. This includes

the digitization of the hits, which transforms the deposited energy into a realistic signal of the detector component. The final step before the reconstruction is the overlay of the background events.

One of the most important aspects of the proposed detector models is their realism. The ILD models in the production contain realistic detector dimensions, including e.g. inactive materials. Beam test data determines the resolutions of the components [123]. This makes the simulated detector response a reliable prediction for a future detector.

After the detector simulation, the production chain uses the signals from the detector to reconstruct the event. The main steps of the event reconstruction are the track reconstruction, using the ILD tracking software [197], and a particle flow event reconstruction, using the PandoraPFA toolkit [150, 198]. PandoraPFA assembles reconstructed particles with their measured four-momenta and uses the various reconstructed components of the particles to classify them as e^\pm , μ^\pm , π^\pm , neutral hadron, or γ . A last step in the production chain uses the output of the initial reconstruction and performs a high-level analysis. This high-level analysis includes steps like vertex finding with LCFIPlus [199], and additional particle identification techniques. After all reconstruction steps, the production stores simulated and reconstructed events in the LCI0 format [184].

The first part of this study (chapter 6) uses the fully simulated events and relies on the particle flow reconstructed particles.

5.1.3. Truth-level information in the production chain

Since the whole production uses only simulated data, the software can track the causal connections from generator level particles to detector hits to reconstructed objects. This opens up the possibility to analyse the detector response and reconstruction mistakes on the final stored event data. One tool that makes use of this information is TrueJet [200]. It tracks the jet formation and measurement, and links reconstructed objects back to the generator level final state particles. Later in this study, this tool provides the necessary information to test the impact of steps like jet clustering (section 6.3).

5.2. Datasets at 1 TeV

A first part of this study (chapter 6) considers vector boson scattering (VBS) at a 1 TeV ILC. It only considers the high cross-section hadronic final state $\nu_e\nu_eqqqq$ originating from $W^+W^- \rightarrow VV$ ($V = W/Z$). The events of this dataset are part of the ILD MC production (section 5.1), which used WHIZARD1.95, iLCSoft v02-00-02 and ILDConfig v02-00-02, and include simulations for both the large (ILD_l5_o1_v02/IDR-L) and the small (ILD_s5_o1_v02/IDR-S) ILD model (section 3.3.2).

Datasets produced in the ILD MC production consider all possible tree-level Feynman diagrams in the production of a final state. The study of specifically the VBS process requires a definition of the signal within the $e^+e^- \rightarrow \nu_e\nu_eqqqq$ process (fig. 5.1). A set

5. Datasets

Table 5.1.: Cross sections of the signal processes (after signal definition cuts) for the two kinematic regions of the diboson mass m_{VV} , and the available MC statistics in terms of luminosity for a polarisation of $(\mathcal{P}_{e^-}, \mathcal{P}_{e^+}) = (-80\%, +30\%)$. q_u and q_d are up- and down-type quarks respectively (not including t). The uncertainties are composed of the uncertainty from the phase-space integration of the matrix element (ME) and of the uncertainty from the fraction of MC events (MC) (details: section A.1).

kinematic region	signal	σ [fb]	$L_{MC}^{(-80, +30)}$ [ab^{-1}]
$m_{VV} > 500 \text{ GeV}$	$\nu\nu q_u q_d q_d q_u$ (WW)	$1.37 \pm 0.05_{ME} \pm 0.02_{MC}$	6
	$\nu\nu q_u q_d q_d q_u$ (ZZ)	$0.0054 \pm 0.0002_{ME} \pm 0.0012_{MC}$	6
	$\nu\nu q_u q_u q_u q_u$ (ZZ)	$0.142 \pm 0.020_{ME} \pm 0.001_{MC}$	200
	$\nu\nu q_d q_d q_d q_d$ (ZZ)	$0.386 \pm 0.004_{ME} \pm 0.001_{MC}$	130
$m_{VV} < 500 \text{ GeV}$	$\nu\nu q_u q_d q_d q_u$ (WW)	$20.29 \pm 0.03_{ME} \pm 0.11_{MC}$	1.7
	$\nu\nu q_u q_d q_d q_u$ (ZZ)	$4.21 \pm 0.01_{ME} \pm 0.06_{MC}$	1.7
	$\nu\nu q_u q_u q_u q_u$ (ZZ)	$1.085 \pm 0.002_{ME} \pm 0.008_{MC}$	10
	$\nu\nu q_d q_d q_d q_d$ (ZZ)	$3.96 \pm 0.007_{ME} \pm 0.024_{MC}$	3.2

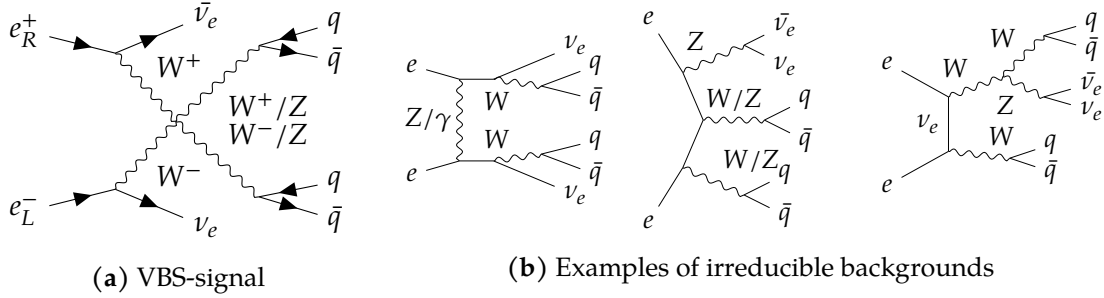


Figure 5.1.: $\nu_e \nu_e q q q q$ production can happen (a) through Vector Boson Scattering and (b) through other irreducible background processes. (The shown backgrounds are a subset of the irreducible backgrounds, see [59])

of cuts on the particle flavors and kinematics at generator level defines the signal in this study, consistent with previous studies [179]. The following describes the steps of this definition. In order to radiate a W from both incoming particles, the incoming e^- must be left-handed and the incoming e^+ must be right-handed. The four quark flavours determine whether an event is a possible WW or ZZ candidate. Mass cuts on the quark pair masses ensure that the event is double-resonant. In order to count as a ZZ candidate, a $(q_1 \bar{q}_2)(q_3 \bar{q}_4)$ double-pair must have invariant masses in the range of $171 \text{ GeV} < m_{inv}^{1,2} + m_{inv}^{3,4} < 195 \text{ GeV}$ and their difference must not exceed $20 \text{ GeV} < |m_{inv}^{1,2} - m_{inv}^{3,4}|$. Almost same criteria apply for the pair to count as WW candidate, only with a different invariant mass range of $(147, 171) \text{ GeV}$. The final candidate is the double-pair with the smallest mass difference. Finally, a cut on the neutrino invariant mass $100 \text{ GeV} > m_{\nu\bar{\nu}}$ removes triple-resonant WWZ production.

The vector boson scattering process is sensitive to low-energy effects of particles with

Table 5.2.: Total chiral cross-sections of the processes in the electroweak fit study at 250 GeV, and the available MC statistics in terms of luminosity for a polarisation of $(\mathcal{P}_{e^-}, \mathcal{P}_{e^+}) = (0, 0)$. The uncertainties are composed of the uncertainty from the phase-space integration of the matrix element (*ME*) and of the uncertainty from the fraction of MC events (*MC*) (details: section A.1).

final state	initial state	σ [fb]	$L_{MC}^{(0,0)}$ [ab^{-1}]
$\mu^- \nu qq$	$e_L^- e_R^+$	$4699.8 \pm 2.5_{ME} \pm 0.9_{MC}$	16
	$e_R^- e_L^+$	$43.50 \pm 0.02_{ME} \pm 0.10_{MC}$	14
$\mu^+ \nu qq$	$e_L^- e_R^+$	$4699.1 \pm 2.5_{ME} \pm 0.9_{MC}$	16
	$e_R^- e_L^+$	$43.43 \pm 0.02_{ME} \pm 0.10_{MC}$	14
$\mu\mu$ ($m_{\mu\mu} > 180$ GeV)	$e_L^- e_R^+$	$4032.9 \pm 2.3_{ME} \pm 0.8_{MC}$	20
	$e_R^- e_L^+$	$3217.1 \pm 1.7_{ME} \pm 0.7_{MC}$	20
$\mu\mu$ ($m_{\mu\mu} \in [81, 101]$ GeV, $p_Z^{\mu\mu} > 0$)	$e_L^- e_R^+$	$2009.2 \pm 1.2_{ME} \pm 0.6_{MC}$	20
	$e_R^- e_L^+$	$1301.6 \pm 0.7_{ME} \pm 0.5_{MC}$	20
$\mu\mu$ ($m_{\mu\mu} \in [81, 101]$ GeV, $p_Z^{\mu\mu} < 0$)	$e_L^- e_R^+$	$2008.7 \pm 1.2_{ME} \pm 0.6_{MC}$	20
	$e_R^- e_L^+$	$1301.9 \pm 0.7_{ME} \pm 0.5_{MC}$	20

masses beyond the collider energy. Sensitivity to such effects lies mainly in events with high momentum exchanges, marked in VBS through a high invariant mass m_{VV} . Low- m_{VV} events on the other hand will be the target of resonance searches. This study splits the $\nu_e \nu_e qqqq$ signal into two kinematic regions; $m_{VV} > 500$ GeV and $m_{VV} < 500$ GeV. The high- m_{VV} region has a much lower cross-section (table 5.1). By request for this study, the LCGG produced a dedicated high-statistics dataset for this high-mass region.

The part of this study that uses the 1 TeV dataset (chapter 6) assumes a luminosity of 1 ab^{-1} for a polarisation of $(\mathcal{P}_{e^-}, \mathcal{P}_{e^+}) = (-80\%, +30\%)$. While this does not reflect a realistic 1 TeV running scenario of the ILC, this choice is consistent with the studies in the ILC Letter of Intent [152]. For both datasets, the available MC statistics exceed this luminosity (table 5.1). In the case of the low- m_{VV} events, the available MC statistics for the *WW* events is only a factor 1.7 higher than the expected number of events for 1 ab^{-1} . For the *WW* events of the dedicated high- m_{VV} dataset, that factor is around six. In both cases, the statistics for the *ZZ* events are less problematic than for the *WW*. This availability of MC statistics which exceed the expected events in a dataset is necessary in order to not suffer from fluctuations in the MC distributions.

5.3. Datasets at 250 GeV

The second part of this study (chapter 7) performs an electroweak fit on generator level distributions for a 250 GeV e^+e^- collider. Events for the datasets of that study are part of the 250 GeV ILC Monte-Carlo production [181], which used WHIZARD2.8.5. The study

5. Datasets

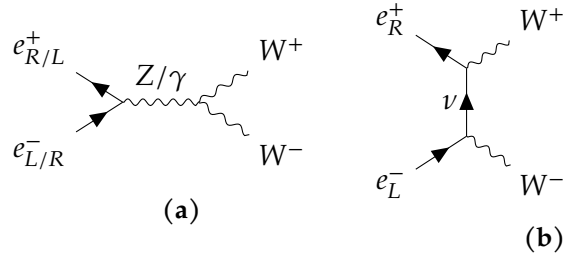


Figure 5.2.: e^+e^- collisions can create W pairs through (a) s-channel and (b) t-channel production.

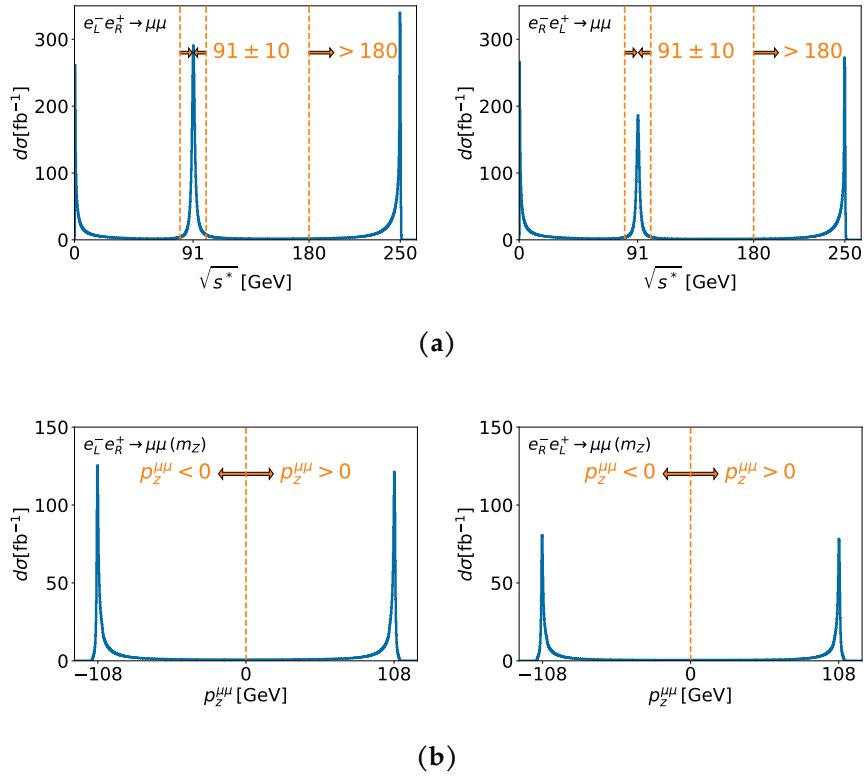


Figure 5.3.: This study splits the $e^-e^+ \rightarrow \mu^-\mu^+$ process (left: $e_L^-e_R^+$, right: $e_R^-e_L^+$) into different categories. First, a $m_{\mu\mu}$ cut creates return-to-Z and high- $\sqrt{s^*}$ categories (a), and then a detector-frame $p_Z^{\mu\mu}$ cut split return-to-Z events into forward- and backward-boosted events (b).

considers two final states: semileptonic W pair production with a μ in the final state ($\mu\nu qq$) and μ pair production ($\mu^+\mu^-$).

The electroweak fit study uses all $\mu\nu qq$ events without any further signal definition cut. Such events at tree level are the result of s- or t-channel W pair production (fig. 5.2), where the s-channel contains a triple gauge boson interaction. The events form two datasets according to the charge of the μ (table 5.2). This μ -charge split avoids a loss of information in the differential distributions.

Fermion pair production at tree level only happens through s-channel production (section 2.1.3). The parameters of that process are energy-dependent, and exactly this energy-dependence is a target in precision electroweak measurements. Ignoring γ -exchange dominated events with low $m_{\mu\mu}$, a 250 GeV collider sees two peaks in the total cross-section of μ pair production (fig. 5.3a). One peak corresponds to events with an effective center-of-mass energy $\sqrt{s^*} = m_{\mu\mu}$ around the center-of-mass energy of the collider. A second peak sits around the Z -pole $m_{\mu\mu} \approx m_Z$, and arises from strong ISR radiation which allows a return of the effective center-of-mass energy to the Z resonance. This study splits μ pair production into two datasets corresponding to these two peaks; a high- $\sqrt{s^*}$ dataset with $m_{\mu\mu} > 180$ GeV and a return-to- Z dataset with $m_{\mu\mu} \in [81, 101]$ GeV. A cross-section comparison shows that for an $e_L^- e_R^+$ initial state high- $\sqrt{s^*}$ events are about as common as return-to- Z events, while for the $e_R^- e_L^+$ initial state the high- $\sqrt{s^*}$ events are about a factor 1.2 more abundant (table 5.2). For technical reasons related to the μ -acceptance (section 7.4.3), the study further splits return-to- Z events by the total z-momentum of the μ pair system into forward- and backward boosted events (fig. 5.3b). The μ pair production parameters in these sub-categories of the return-to- Z dataset are the same since the effective center-of-mass energy is the same. All together, this makes three μ pair production datasets, each with the two allowed initial states $e_L^- e_R^+$ and $e_R^- e_L^+$ (table 5.2).

Both mass ranges, $m_{\mu\mu} \in [81, 101]$ GeV and $m_{\mu\mu} > 180$ GeV, do not use a further binning in $m_{\mu\mu}$. This means that the datasets integrate all physical parameters over the corresponding mass range, weighted by the $m_{\mu\mu}$ -dependent cross-section. Such an integration can be a challenge in the interpretation of the measurement when the integrated parameters are also $m_{\mu\mu}$ -dependent.

The part of this study that uses the 250 GeV dataset (chapter 7) tests various luminosity and polarisation scenarios (section 7.2). Of all the tested scenarios, the one with the highest number of expected events is an unpolarised run with 10 ab^{-1} of luminosity. The available MC statistics for all categories in the 250 GeV exceed this luminosity by at least a factor 1.4 (table 5.2). This again ensures that the study does not suffer from fluctuations in the MC distributions.

6. Separating hadronic decays of boson pairs

High-energy vector boson scattering (VBS) is a sensitive probe to new physics in the electroweak and Higgs sectors [201, 202]. In the SM, the amplitude of the VBS process converges only with the help of the electroweak symmetry breaking mechanism [203, 204]. Changes in that mechanism will therefore strongly perturb the amplitude. Assuming those changes to arise from yet undiscovered new physics at high energies, the disruption will increase with energy towards that new physics.

The low-background environment in the detector at an e^+e^- collider enables the measurement of the fully hadronic decay of the two scattered bosons. Such fully hadronic final states have the highest branching fractions and are as such of high interest for a BSM analysis. The $e^+e^- \rightarrow \nu\nu qqqq$ process is one such fully hadronic process which contains $W^+W^- \rightarrow VV$ vertices, and this is the target final state here.

This study is a continuation of a previous work [180], and has been part of the benchmarking studies for the ILD Interim Design Report (IDR) [123, 205, 206]. The primary goals of this study are to provide results with update-to-date detector model and to understand the limitations of such a VBS measurement (section 4.2.2).

For this, the focus of this study is one of the benchmarks of the analysis of the fully hadronic final state: the kinematic separation of the WW and ZZ final states (section 6.1). Through a quantification of this separation (section 6.2) and with the use of generator level information, it is possible to compare how each step of the event reconstruction and high level analysis impact that separation (section 6.3). In turn, this provides guidance for future studies by identifying the most pressing challenges.

One of the limiting factors of this separation is the resolution of the detector. A change to the detector model, as investigated in the ILD-IDR (section 3.3.2) [123], can also affect this separation. An explicit comparison to a model of reduced size shows that the exact model plays a minor role for this benchmark (section 6.4).

This study generally uses the large ILD model (IDR-L), specifically `l5_o1_v02`, unless specified otherwise. A previous chapter gives a full description of the dataset (sections 5.1 and 5.2), which uses the expected collisions produced at the ILC and detected in the ILD. For consistency with previous studies [152], this study considers the expected events in a single dataset with a polarisation of $(\mathcal{P}_{e^-}, \mathcal{P}_{e^-}) = (-80\%, +30\%)$ and with 1 ab^{-1} of luminosity. That luminosity corresponds to around a third of what a potential 1 TeV run of the ILC foresees for this polarised dataset [207].

6. Separating hadronic decays of boson pairs

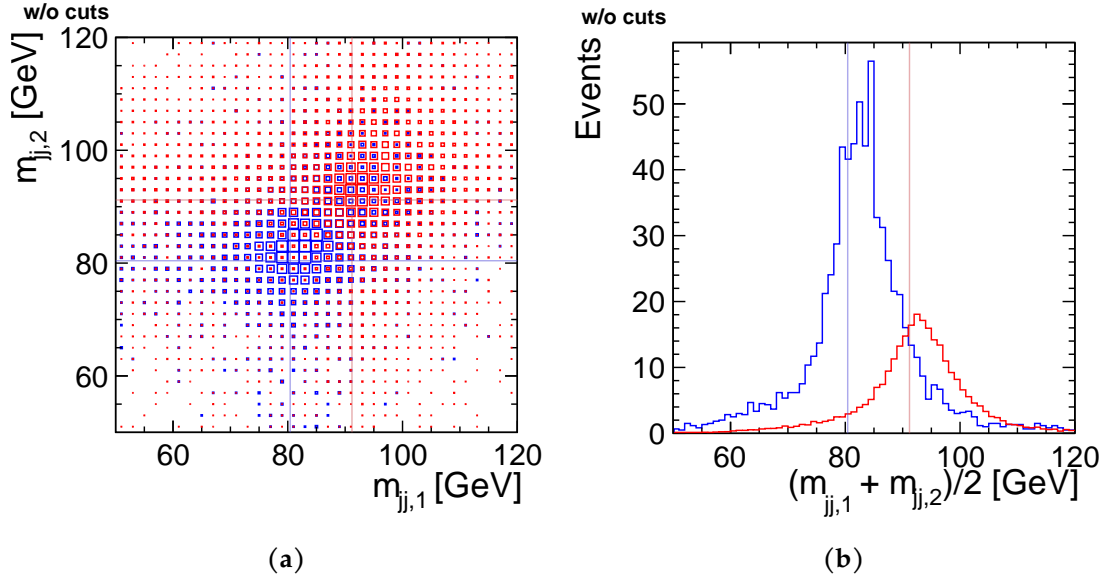


Figure 6.1.: The reconstructed mass distributions of true WW (blue) and ZZ (red) events are the basis of the kinematic separation. While the 2D distribution (a) contains the full mass information, a 1D projection (b) allows a simple cut which is the basis of this study. The examples here use the $m_{VV} > 500$ GeV events. Lines represent the true W and Z mass values in the MC events. (Distributions for other idealization steps in appendix: figs. B.1 and B.2)

6.1. Reconstructing the hadronic di-boson decay

A separation of WW and ZZ events in their hadronic final states requires the reconstruction of the boson kinematics. The high-level reconstruction applies three steps: the cleaning of background particles in the event, the jet clustering, and the subsequent combination to boson candidates. Using the FastJet library [208], an exclusive k_t jet clustering algorithm [34] cleans low- p_T hadronic backgrounds from $\gamma\gamma$ collisions (section 3.1.4) by clustering the reconstructed particles into four jets with a cone parameter of 1.3. An additional $ee - k_t$ jet clustering [208, 209] combines all particles that are included in the previous jets into four new jets. Each combination of the four jets into two pairs of jets is a possible candidate for the di-boson final state. As the two bosons will have approximately the same mass, the pairing that leads to the smallest difference of masses between the two jet pairs $|m_{jj,1} - m_{jj,2}|$ yields the two boson candidates. The sum of the four-momenta of the two jets in the boson candidate gives the boson four-momentum. These boson four-momenta yield the reconstructed boson masses m_{V1} and m_{V2} (fig. 6.1), which are the basis the kinematic separation of WW and ZZ events.

6.2. Quantification of di-boson separation

A simple cut in the $(m_{V1} + m_{V2})/2$ mass projection (fig. 6.1b) allows a kinematic separation of WW and ZZ events. For a given cut value, the kinematic separation labels all events above that value as ZZ , and all below it as WW . This study uses two complementary methods to quantify the separation of the WW and ZZ events.

The first method builds on a fit to the mass projection in the range of 50 GeV to 110 GeV. A simple Gaussian fit is not possible because the mass projections $(m_{V1} + m_{V2})/2$ do not have Gaussian shapes. It turns out that a sum of two Gaussians describes the individual mass projections well - one describing the peak region and another the tail (e.g. fig. 6.2). The modification yields the combined statistical parameters of the peak and tail Gaussians.

$$\mu = f_{peak} * \mu_{peak} + (1.0 - f_{peak}) * \mu_{tail} \quad (6.1)$$

$$\sigma^2 = f_{peak} * \sigma_{peak}^2 + (1.0 - f_{peak}) * \sigma_{tail}^2 + f_{peak} * (1.0 - f_{peak}) * (\mu_{peak} - \mu_{tail})^2 \quad (6.2)$$

Here, f_{peak} is the amplitude fraction of the peak Gaussian, and $\mu_{peak/tail}$ and $\sigma_{peak/tail}$ are the mean and width of the peak and tail Gaussians, respectively. Using the fits to the distributions of the true WW and true ZZ events and the resulting parameters $\mu_{WW/ZZ}$ and $\sigma_{WW/ZZ}$, a quantification of the kinematic separation is possible in form of the Gaussian separation.

$$\text{Separation} = \frac{|\mu_{WW} - \mu_{ZZ}|}{\sqrt{\sigma_{WW}^2 + \sigma_{ZZ}^2}} \quad (6.3)$$

The resulting Gaussian-like separation value gives an intuitive insight into how far the WW and ZZ distributions are separated in terms of standard deviations.

The second method aims at scanning the whole range of possible separation-cut values that a full analysis can use. Receiver operating characteristic (ROC) curves are a tool to visualize the trade-off of such binary classifiers. Here, these curves are the results of scanning the separation-cut values in the one-dimensional mass projection $(m_{V1} + m_{V2})/2$ in the range between 30 GeV and 250 GeV in 4400 steps. Each cut value yields two efficiencies, one for correctly identifying the true WW boson pair in a true WW event, and a corresponding one for true ZZ events. The collection of the points of those two efficiencies forms the ROC-curve (fig. 6.3). The area under the resulting curve summarizes the separation of the two mass event types for the whole scanned mass range. Such an area-under-the-curve (AUC) value reaches a maximum of 1 if the kinematic separation is perfect, and a value of 0.5 if the mass distributions do not allow any separation. A value of one, and a full separation of the boson pairs, only appears here on generator level, where the ROC curve forms a square with unit length.

Both estimators are arbitrary choices for quantifying this specific aspect of the analysis of the $\nu\nu qq\bar{q}\bar{q}$ final state. While the Gaussian separation has a more visual and intuitive

6. Separating hadronic decays of boson pairs

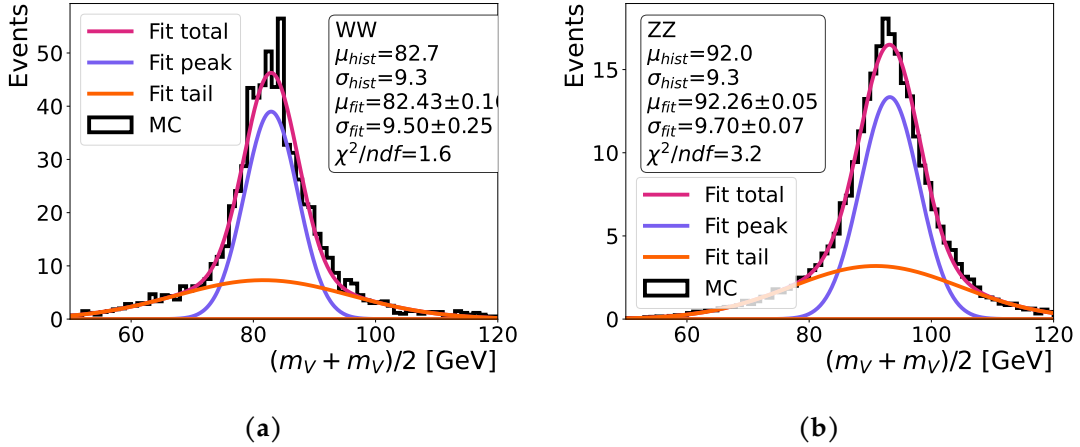


Figure 6.2.: A fit of the sum of two Gaussians yields the statistical moments of the (a) WW and (b) ZZ distributions. The examples here use the fully reconstructed distributions of the $m_{VV} > 500$ GeV events (full set of fits in the appendix: section B.2).

interpretation, the AUC uses the efficiencies that are of direct relevance to the analysis. In addition, the Gaussian separation will indicate changes also when there is no significant overlap of the two distributions. The AUC of the ROC method on the other hand shows sensitivity to changes in the mass distributions only when those changes actually affect the relevant separation efficiency. Together, the two methods allow an assessment of the severity of the change with the Gaussian method and of the relevance for the physical performance with the AUC.

6.3. Identifying reconstruction challenges

The reconstructed boson mass and the quantifiers introduced in the previous section are the basis to investigate which aspects of the reconstruction are most limiting to this analysis. This section focuses on the comparison of the two phase space regions with different physical motivations and different jet kinematics (section 5.3). All results in this section use the large ILD model (IDR-L).

6.3.1. Understanding the kinematics

This study splits the signal events into two kinematic regions: $m_{VV} < 500$ GeV and $m_{VV} > 500$ GeV. The region differ in the distribution of the bosons and jets (fig. 6.4), and this crucially determines which reconstruction effects will be most important. For both kinematic regions, the reconstruction does not significantly change the shape of the one-dimensional distributions.

An EFT analysis will focus on the kinematic region that tests the highest possible energy scales (section 2.2.2). This motivates the first kinematic region of $m_{VV} > 500$ GeV,

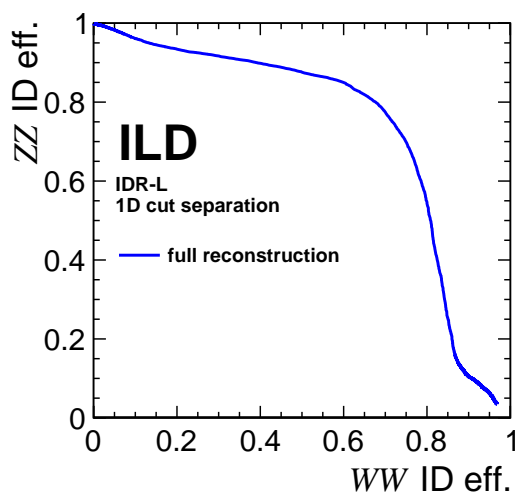


Figure 6.3.: Varying a 1D-cut in the di-boson mass projection yields a ROC-curve, and the area under such curves quantifies the separation of the distributions. The example here use the fully reconstructed mass distribution in the large ILD model for the $m_{VV} > 500$ GeV events (fig. 6.1b). A full set of all ROC-curves produced during this study is in the appendix (fig. B.8).

where m_{VV} is the invariant mass between the two produced electroweak bosons ($V = W, Z$). The bosons in the final state of this kinematic region mainly fly in the forward regions of the detector (fig. 6.4b) with each boson carrying around a third of the center-of-mass energy (fig. 6.4a). In their decay the bosons produce two highly boosted jets. While the boson decay produces back-to-back jets in the boson rest-frame, the strong boost along the boson flight direction leads to a jet angular distribution very similar to that of the boson (fig. 6.4d). The bosons tend to decay with one of the quarks along the bosons flight direction and the other quark against it in the boson rest frame. As a result, the energy is not split evenly between the jets and the jet energy spectrum spreads from very low-energy to energies close to the boson momentum (fig. 6.4c).

The cross-section of the low-mass kinematic region with $m_{VV} < 500$ GeV is more than an order of magnitude larger than that of the high- m_{VV} (table 5.1). Measurements which focus on this region can achieve higher statistical precision and perform searches for new low-mass effects with small couplings. A higher energy contribution to neutrinos or to the initial state radiation (ISR) causes the lower diboson invariant mass. As a result, both of the initial bosons have less energy (fig. 6.4a). The increased energy in the neutrinos or ISR likely affects only one such particle, so that it takes momentum from the di-boson system either in the very-forward or in the very-backward direction. This means that the boson produced in that direction is likely to be more central (fig. 6.4b). For this reason, this kinematic region does not have the same forward-peaking jet distributions as the high- m_{VV} events (fig. 6.4d).

6. Separating hadronic decays of boson pairs

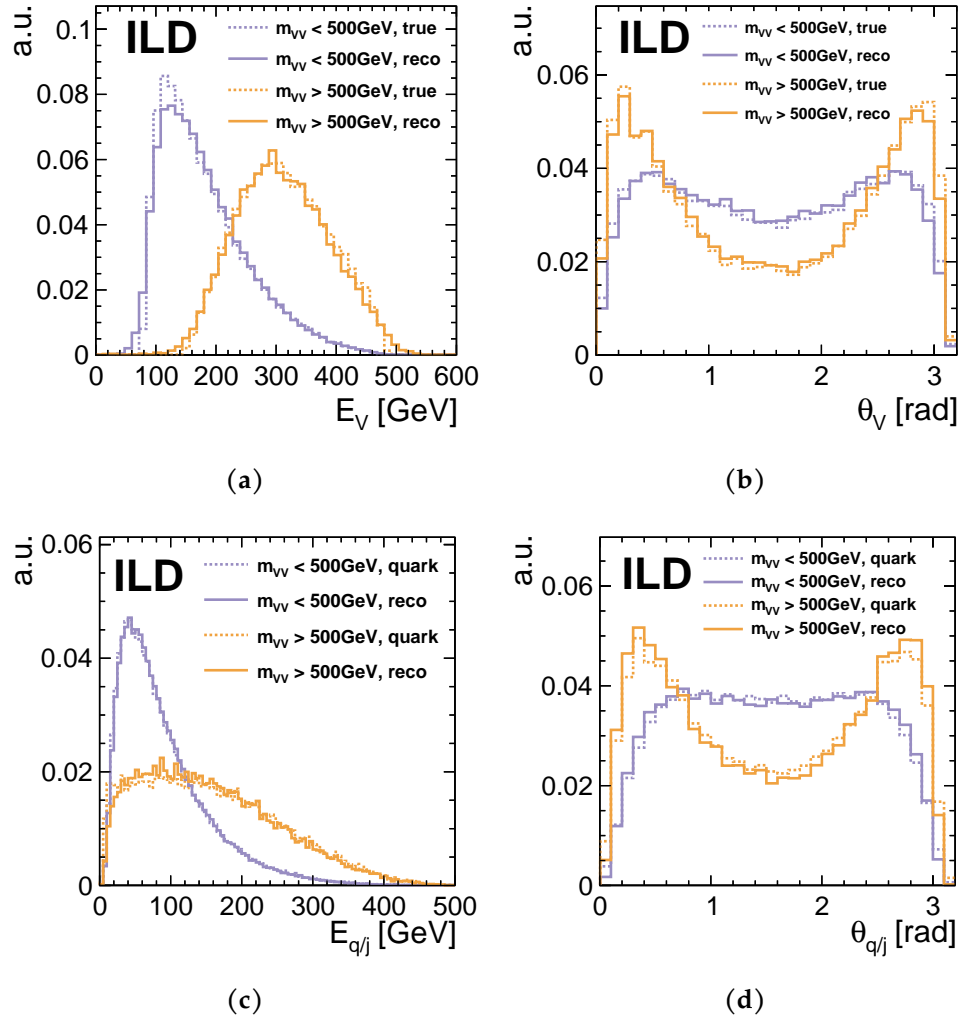


Figure 6.4.: The distribution of the reconstructable objects in the detector determines which effects are most important. Differences between the truth-level distributions and reconstructed distribution turn out small. Each distribution is normalized to unity. Reconstruction-level distributions use the large detector model.

Table 6.1.: Overview of the different idealization steps and the corresponding reconstruction steps. The idealization steps are cumulative from top to bottom.

Idealization step	Explanation	Corresp. reco. step
“Full rec”	Full reconstruction	–
“+ Cheated overlay”	Removing background particles with truth-level information	Exclusive k_T clustering
“+ Cheated jets”	Clustering particles to jets with truth-level information	Inclusive $ee - k_T$ clustering
“+ Cheated bosons”	Clustering jets to bosons with truth-level information	Pair finding by minimal mass difference criterion
“+ no SL-dec”	Ignoring events with truth-level semileptonic B and C decays	– (no ν reconstr. attempted)
“Generator level”	Directly using truth-level final state quarks	Detector resolution and acceptance

6.3.2. Deciphering steps of the reconstruction

The contrasting final state kinematics of the jets in these two m_{VV} regions make it an interesting target to study the reconstruction of hadronic final states. Beside the detector resolution and acceptance, potentially limiting effects in the reconstruction of hadronic boson decays are the removal of background particles, the clustering into individual jets and then into bosons, and the invisible momentum component of the jets. A step-by-step idealization of these effects identifies the most relevant ones. Truth-level information retained in the Monte Carlo dataset allows the idealization of the individual steps. This information includes for example links between reconstructed particles and the true particles that contributed to them (section 5.1.3).

This study tests six steps (overview: table 6.1), each with consecutively more idealized reconstruction. Any idealization from a previous step is also carried out in the next one. The full analysis on reconstructed particles without any idealizations is the baseline.

Starting from there, a first step removes any reconstructed particles that on truth-level do not originate from the hard e^+e^- scattering, so that they do not form parts of the jets. The removed particles mainly originate from $\gamma\gamma$ collisions to low- p_T hadrons (section 3.1.4), and their appearance simultaneous to the hard scattering earns them the name “overlay”.

In the second step, the jet clustering uses the links of reconstructed particles with their truth-level origins together with the TrueJet algorithm [200]. This idealizes the assignment of the reconstructed particles to jets.

The third step employs the same tools to partner the jets into boson candidate pairs

6. Separating hadronic decays of boson pairs

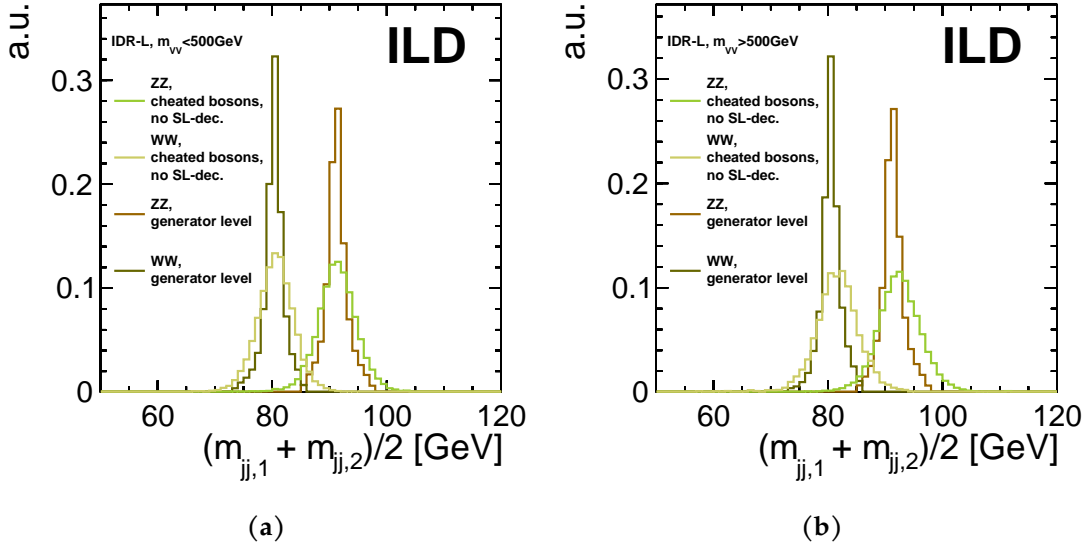


Figure 6.5.: The comparison of the mass distributions for step that idealizes all high-level reconstruction and ignores events with semi-leptonic decays with those of the generator-level boson candidates reveals the impact of the detector resolutions and acceptances. This significantly degrades the resolution of the mass distributions for both (a) low- m_{VV} and (b) high- m_{VV} events, and introduces a slight bias in high- m_{VV} events. Plots here use the large ILD model, and each distribution is normalized to unity.

based on truth-level information.

To test the impact of missing momentum in jets, the fourth step only uses events in with no semi-leptonic C - or B -meson decays on truth-level. Such decays produce neutrinos that the detector cannot directly measure.

The last step again uses all signal events and looks directly at the pure truth-level information of the boson.

6.3.3. Identifying the most relevant effects

Each of these idealization steps yields its own mass distributions (figs. 6.5 and 6.6), and with that values for both of the two separation measures described above (section 6.2): the Gaussian separation (fig. 6.7a) and the area-under-the-curve (AUC) of the WW/ZZ -separation efficiencies (fig. 6.7b). Each idealization step artificially improves the separation. The improvements are not always identical for the two quantifiers; the Gaussian separation is sensitive to changes in the mean and width of each distribution, and the AUC is sensitive only to changes that affect the WW/ZZ separation efficiency.

The two kinematic regions see differences in the influence of each reconstruction step. For the interpretation of these differences it is useful to read the idealization steps in

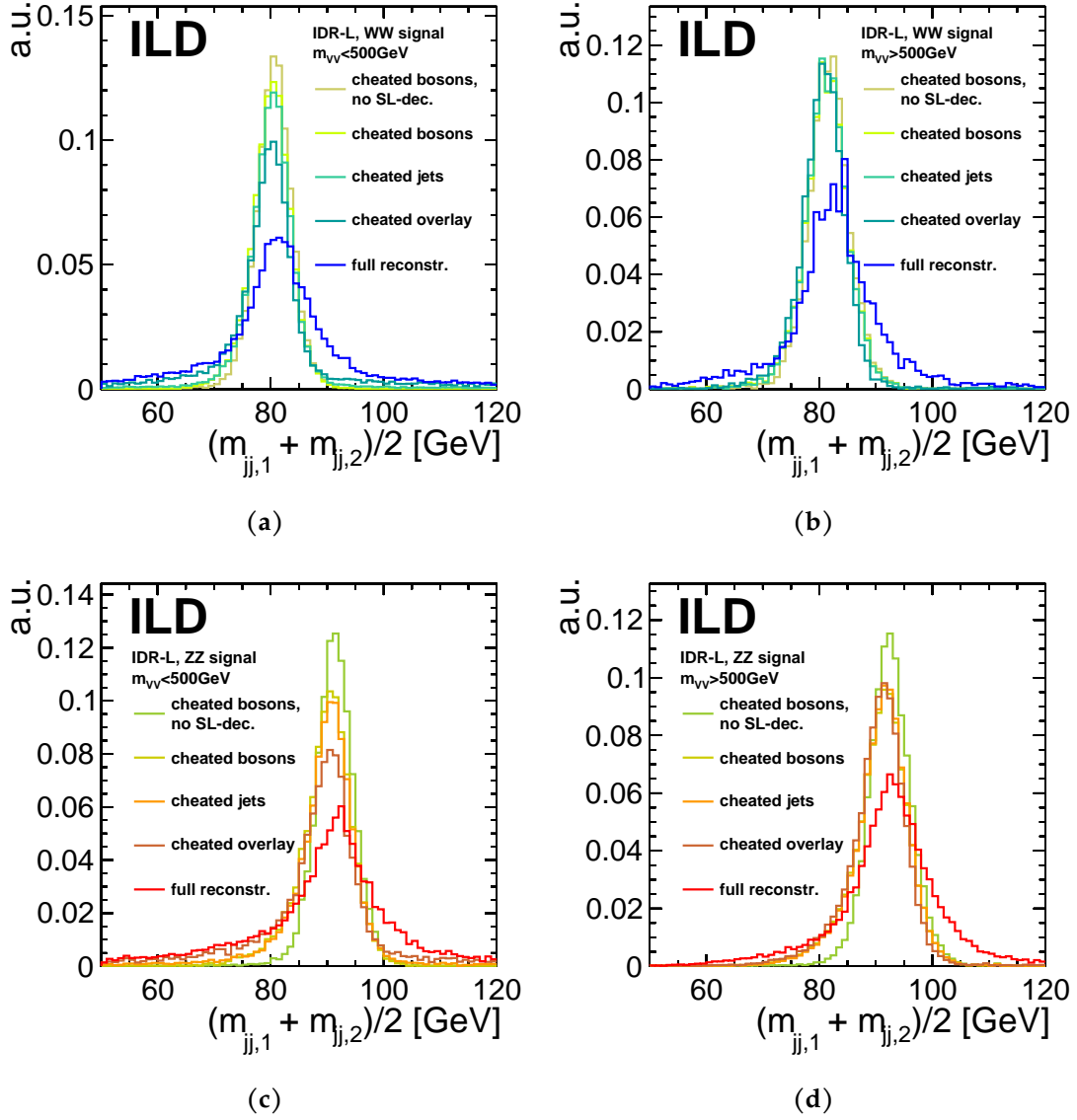


Figure 6.6.: Step-by-step idealizations (table 6.1) of the high-level event reconstruction process show which steps have the largest impact on the reconstructed mass for WW (top) and ZZ (bottom) events, for both kinematic ranges (left: low- m_{VV} , right: high- m_{VV}). Plots here use the large model, plots for the small model are in the appendix (fig. B.7).

6. Separating hadronic decays of boson pairs

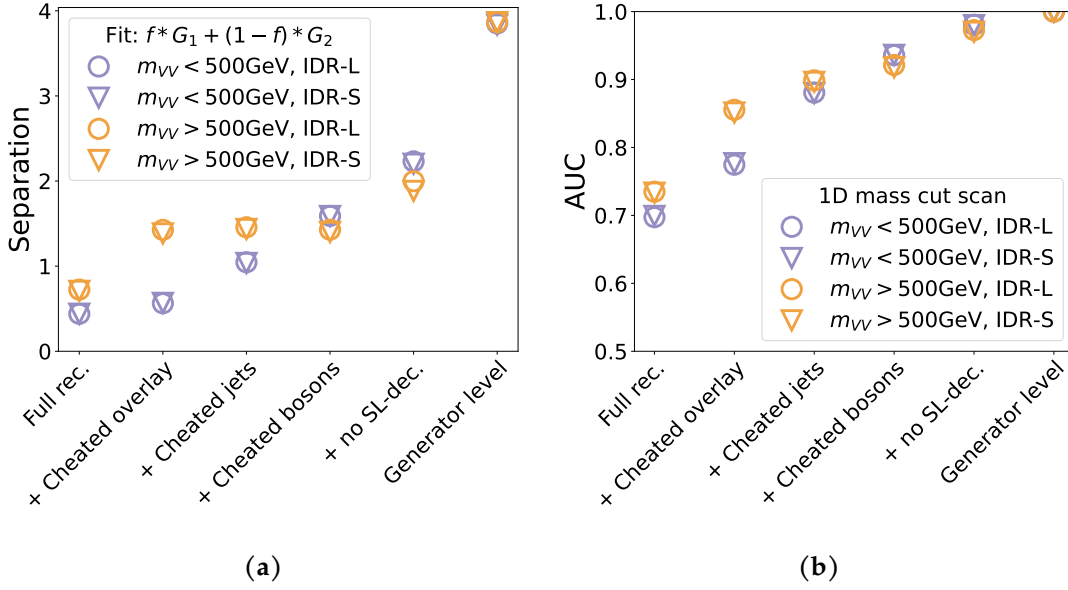


Figure 6.7.: Step-by-step idealizations (table 6.1) of the event reconstruction process show which steps have the largest impact on the two measures for the separation of WW and ZZ events (section 6.2); the Gaussian separation (left) and the area-under-the-curve of the cut scan (right).

reverse (reading figs. 6.7a and 6.7b from right to left), i.e. reading them starting from generator level as the impact that each reconstruction step (table 6.1) has when it is not idealized.

Considering first the Gaussian separation, the detector resolutions and acceptances cause a large change for both kinematic regions, almost halving the separation. At the same time, the separation is still large enough that the WW/ZZ separation efficiency remains almost unaffected, changing the AUC by less than 3%¹.

Semileptonic decays also affect both kinematic regions similarly, decreasing the Gaussian separation by close to 30%. Now the overlap of the distributions also becomes relevant enough to affect the AUC more significantly, decreasing it by 5%. These decays mainly affect the ZZ events (compare figs. 6.6a and 6.6b with figs. 6.6c and 6.6d) since C and especially B mesons are much more common in Z decays compared to W decays [4].

The impact of the two clustering steps - particles to jets and jets to bosons - differs between the two kinematic regions due different boost and angles of the bosons. Clustering the particles to their originating bosons is difficult if the jets have a low boost and are correspondingly spread out and overlapping, as can be the case in the $m_{VV} < 500\text{GeV}$ events. In this kinematic region, both clustering steps have a similar impact on the gaussian separation, and together decrease it by around 65%. The jet clustering turns out to

¹Percentages in this section are relative.

be more detrimental to the separation efficiency, decreasing the AUC by 12% compared to 6% from the clustering of jets to bosons. For the high- m_{VV} events, the two bosons each have a strong boost and are at a larger angle to each other, and both clustering steps show no significant impact on the Gaussian separation while decreasing the AUC in total by only around 5%.

Similarly, the kinematics of the bosons also determine the impact of background particles in the detector on the resolution. These background particles mainly low- p_T hadrons in the very forward regions of the detector. Since bosons are more forward in the high- m_{VV} events (fig. 6.4b), the effect on the resolution is stronger on those events. This is visible both in the Gaussian separation and the AUC. For the low- m_{VV} events, the Gaussian separation decreases by 20% due to background particles in the jets, and for the high- m_{VV} region it is more than double the impact with around 50%. In both cases, the impact of these backgrounds is significant.

6.3.4. Guiding improvements in the event reconstruction

The step-wise idealization identifies two general critical areas of high-level reconstruction: the reconstruction of semileptonic b and c decays in jets and the correct assignment of reconstructed particles to bosons. While this study here itself does not attempt to improve these reconstruction aspects, it can and has guided other studies to look into potential improvements.

Previous studies already started to look into the impact of a potential correction of semileptonic decays in jets at the ILD [180, 205, 210]. These studies either used a generic correction depending on the lepton energy in the jet, or used truth-level information to identify the decays particle. The study here motivated a new set of recent studies that look into the identification and reconstruction of the meson decay vertices in the jets at the ILD, and the corresponding extraction of the neutrino four-momentum [211, 212]. As the above discussion shows, these methods have the potential to improve the WW/ZZ separation by up to 30%.

A correct assignment of particles to bosons requires the removal of background particles, the assignment to jets and then to bosons. The current standard for these methods use iterative jet clustering algorithms and a mass criterion for the assignment to bosons (section 6.1). In addition, some studies employ kinematic fits that make use of knowledge of the event like energy and momentum conservation to correct the jet measurement [212, 213]. Recently, the results and challenges of the LHC have motivated a new look into the reconstruction of jets and hadronically decaying bosons in high-background environments with the help of machine learning techniques [214–217]. These techniques can in some cases surpass the resolution of traditional iterative clustering algorithms [216]. Since the assignment of particles to bosons is responsible for at least a 50% degradation of the WW/ZZ separation, future studies both for the inclusion of kinematic fits and for the use of machine learning techniques promise a significant improvement of the separation of WW and ZZ events.

6.4. Comparing detector models

Recent cost optimisation efforts for the ILC have lead to the proposal of a smaller version of the ILD concept (section 3.3). The smaller model reduces the tracking system radius and applies a stronger magnetic field to recover the tracking performance of the larger model. This section investigates the influence of a change to this smaller detector version.

The most relevant performance difference to this analysis is the change in jet energy resolution (JER). A deterioration of the JER occurs when switching to the smaller detector model. It rises at most by around 0.3% in absolute, which is a relative rise of about 10%.

The distributions for the two detector models show no significant difference for any reconstruction stage and for either dataset (figs. 6.7 and 6.8).

One can expect the strongest difference in the fully idealized case. Only detector resolution effects and additional neutrinos not coming from semi-leptonic decays play a role at that stage. A small difference in the distributions shows up for the high- m_{VV} dataset. This difference is not significant enough to change the diboson separation. In the low- m_{VV} case, the boson mass distributions for the two detector models essentially overlap.

Additional clustering effects and semi-leptonic decays do not change this picture. The resulting smearing dominates the width of the distributions and the detector models show the same results within statistical fluctuations. A switch to the smaller ILD model will not influence the result of the analysis in its current stage.

6.5. Conclusion

A precise measurement of quartic gauge couplings at high center-of-mass energies requires an analysis in the high-statistic hadronic final state. Jets from W and Z bosons need to be distinguished to analyse the W pair and Z pair final states independently.

This study uses the average mass of the two bosons in the final state to investigate the kinematic separation of WW and ZZ final states. A variety of detector and reconstruction effects in the reconstruction determines how well an analysis can reconstruct a hadronically decaying boson.

The relevance of any reconstruction effect depends on the kinematic regime of the boson and its decay jets. A split of the dataset into a high- m_{VV} and a low- m_{VV} region allows studying these effects in two different kinematic regimes. Jet in the high- m_{VV} region are more forward and have higher energies.

Beam-induced backgrounds are forward-oriented and can be misclustered into forward jets. This effect is significant at this high center-of-mass energy and will need removal strategies beyond the standard exclusive jet clustering.

Highly energetic jets are collimated and easy to cluster. The correct clustering of single

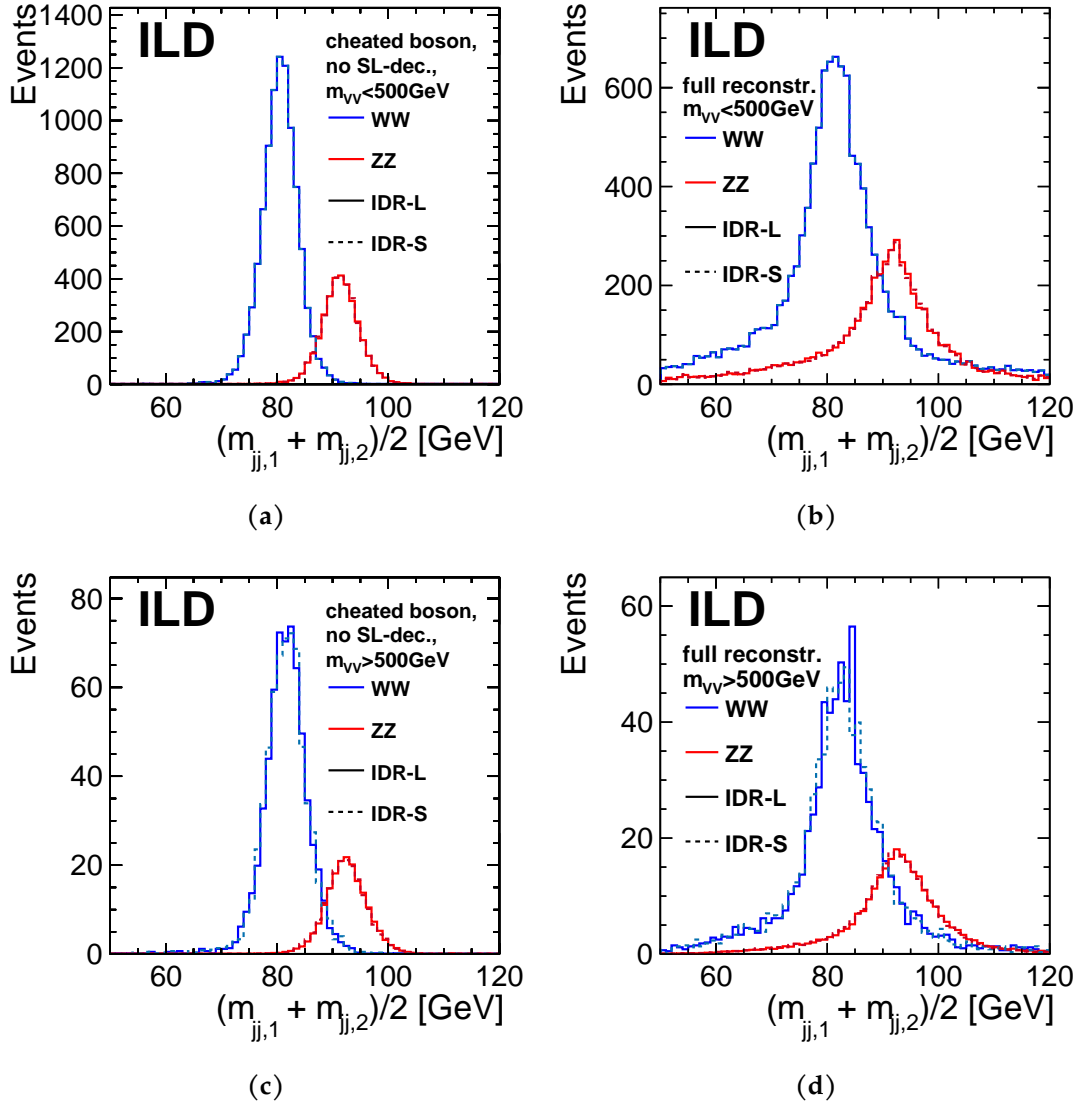


Figure 6.8.: A comparison of a larger (IDR-L) and smaller (IDR-S) model of ILD for both low- m_{VV} (top) and high- m_{VV} (bottom) events shows no significant difference in the performance of both detector models. This holds true both when only considering detector acceptance and resolution (left), and when considering the full analysis of the reconstructed particles (right).

6. Separating hadronic decays of boson pairs

particles becomes more difficult with decreasing boson and jet energy. It starts to limit the reconstruction and will require new approaches to jet clustering, such as recently emerging methods that make use of machine learning techniques.

Semileptonic b and c decays within jets complicate the accurate reconstruction of bosons at any energy. Using the precise final state reconstruction at future e^+e^- colliders, the identification and reconstruction of these decays can in principle allow a reconstruction of the neutrino momentum. The work from this study here motivated a new set of studies to look into the feasibility of such methods at ILD [211, 212].

A comparison of the two variations of ILD design shows no significant influence on the separation in any of the reconstruction steps.

The composition and distribution of the jet constituents in the detector dictate the difficulty of reconstruction. A precise reconstruction of hadronic final states at future colliders is challenging and essential for to the physics program. Progress in different aspects of the jet reconstruction will benefit a large range of measurements, and is worthy more attention.

7. Impact of beam polarisation on electroweak fits

Many studies investigated the importance of beam polarisation for e^+e^- colliders at and beyond the Z -pole (section 4.1). Recent discussions of the high-energy physics community have once again opened this question, with multiple future e^+e^- collider proposals with varying energy, luminosity, and polarisation ranges [1, 68]. Studies for different colliders come to in part contradictory conclusions on the matter [60, 106]. A consistent message on the importance of beam polarisation requires a framework that uses a common and consistent basis of measurements and parameters, on which it can test and compare different collider scenarios.

This study uses a specialized fit framework that can perform simultaneous fit of physical and systematic effects for different polarisation and luminosity options (section 7.1). Such fits extract both process-dependent physical parameters, e.g. Triple Gauge Couplings (TGCs) and fermion pair production parameters, and systematic parameters like the luminosity and beam polarisations (section 7.3). Special attention goes towards including the μ acceptance as a detector systematic effect with free parameters (section 7.4), which previous studies had not considered [60, 157, 170]. Future linear and circular colliders guide the choice of 250 GeV collider scenarios with different polarisations and luminosities (section 7.2).

This study tests both fits to individual final states and simultaneous fit of final states for the different collider scenarios (section 7.5). Results of the fit to μ pair production demonstrate how beam polarisation disentangles parameters of both physical and systematic nature, and how it is crucial to access chiral observables (section 7.6). Fits to semileptonic W pair production further underline these findings, and show that a collider with polarised beams can precisely measure the beam polarisations (section 7.7). A simultaneous fit of these two-fermion and four-fermion final states leads to significant improved measurement of the common systematic effects (section 7.8).

7.1. Assembling electroweak fits

This study aims to compare different scenarios for future e^+e^- colliders by the achievable electroweak precision. Theoretical calculations of sensitivity and statistical precision provide a first indicator of the achievable precisions. Such a purely analytical approach rapidly increases in complexity when the number of parameters of interest increases. A complementary approach - used in this study - is to perform fits to the predicted

7. Impact of beam polarisation on electroweak fits

datasets, and use appropriate statistical methods that extract the uncertainties on the fitted parameters. This study includes a large set of physical and systematic parameters, leading to the choice of fits to differential distribution as the way of determining the parameter precision.

The goal is to compare the impact of polarisation on various physical and systematic parameters, which all need to be part of the fit. This study uses an especially developed fit framework that can simultaneously fit luminosity, polarisations, systematic and physical effects, and include parameter constraints. At the core of the framework is a likelihood minimization that uses the minimizers of the ROOT package Minuit2 [218].

7.1.1. Explanation of the fit on a single polarised dataset

The framework sets up a modified version of the generator-level distributions for the different chiral initial states, by including parameterized physical and systematic effects. It then combines the distributions for the chiral initial states to get the polarised distributions for the different polarisation settings of the beams. Focusing for now on a single polarised dataset, the framework weights the modified chiral distributions according to the polarisation. Finally, it applies global modifications like the luminosity to the polarised distribution to yield the predicted distribution of events.

$$N_{\text{bin}}(\mathcal{D}_{e^-}, \mathcal{D}_{e^+}) = L \times \sum_{\substack{\chi \in \{LR, LL, \\ RL, RR\}}} \left[w_{\text{pol},\chi}(\mathcal{D}_{e^-}, \mathcal{D}_{e^+}) \times \left(\prod_j f_{\chi,j} \right) \times \sigma_{\chi,\text{bin}} \right] \quad (7.1)$$

$$w_{\text{pol},\chi}(\mathcal{D}_{e^-}, \mathcal{D}_{e^+}) = \frac{1}{4} \times \begin{cases} (1 - \mathcal{D}_{e^-})(1 + \mathcal{D}_{e^+}) & \text{for } \chi = LR (e_L^- e_R^+) \\ (1 - \mathcal{D}_{e^-})(1 - \mathcal{D}_{e^+}) & \text{for } \chi = LL (e_L^- e_L^+) \\ (1 + \mathcal{D}_{e^-})(1 - \mathcal{D}_{e^+}) & \text{for } \chi = RL (e_R^- e_L^+) \\ (1 + \mathcal{D}_{e^-})(1 + \mathcal{D}_{e^+}) & \text{for } \chi = RR (e_R^- e_R^+) \end{cases} \quad (7.2)$$

Here, \mathcal{D}_{e^-} and \mathcal{D}_{e^+} are the electron and positron polarisations respectively, the $f_{\chi,j}$ are functions that parameterize the physical and systematic effects (indexed over j) that act on the respective chiral distribution with chirality χ , and $w_{\text{pol},\chi}$ is the polarisation weight of the chiral distribution.

The framework provides two ways to implement physical parameters. One way is to apply a parameter-dependent function $f_{\chi,j}$ to the generator-level distribution. The second way is to completely replace the Monte-Carlo generator-level distribution by a functional description of the differential cross-section. This study makes use of both of these techniques (section 7.3).

Once the framework has assembled the polarised prediction, it can Poisson-fluctuate each bin of the prediction to mimic a measured distribution. A log-likelihood fit of the predicted distribution to such measurement-like distributions yields a prediction of the uncertainties and correlations of the parameters. The fits use a Poissonian log-

likelihood.

$$\begin{aligned}
L_{\text{Poisson}}(\{N_b^{\text{meas}}\} | \{p\}) &= -2 \ln l_{\text{Poisson}}(\{N_b^{\text{meas}}\} | \{p\}) \\
&= -2 \sum_{\text{bins } b} \left[-\ln(N_b^{\text{meas}}!) - N_b^{\text{pred}}(\{p\}) + N_b^{\text{meas}} \ln(N_b^{\text{pred}}(\{p\})) \right]
\end{aligned}
\tag{7.3}$$

A simpler χ^2 minimization would lead to an underestimation of uncertainties when the distributions have bins with expected event numbers close to zero, which e.g. happens in the differential distribution of semileptonic W pair production. In contrast to a χ^2 minimization, there is no general a-priori expectation for which values the log-likelihood L_{Poisson} will take. This means that the log-likelihood approach does not provide a straightforward goodness-of-fit test. If such a test is required e.g. for real measured data, then generator level tests like those performed in this study can provide the expected distribution of L_{Poisson} values. Here, such goodness-of-fit tests are not necessary because the fitted and measured distributions are by design identical within Poisson fluctuations.

Once the fit found the minimum, it numerically determines the Hessian matrix $H_{ij} = \partial^2 L / \partial p_i \partial p_j$ and estimates the covariance matrix as the inverse of the Hessian matrix. The covariance matrix yields the estimates of the uncertainties and correlations of the parameters. Any uncertainties and correlations in this study are averaged results of 300 fits with fluctuated distributions. For each fit, the TMinuit2 framework outputs flags that warn about potential issues in the fit convergence or in the calculation of the Hessian matrix. All results within this study have well-converging fits and show no issues in the calculation of the Hessian matrix.

One notable feature of the log-likelihood formula (eq. (7.3)) is the absence of a covariance matrix that describes common systematic uncertainties of the measured distribution $\{N_b^{\text{meas}}\}$. Any systematic effect that affects multiple bins needs an explicit implementation in the fit with a corresponding set of free parameters.

7.1.2. Fits using multiple polarised datasets

One of the goals of the framework is comparing different scenarios of polarisation and luminosity. When a collider has polarised beams, it can flip the sign of each polarised beam, or even depolarise that beam again. This means that once a collider has a polarised beam, it can run that beam in up to three longitudinal polarisation settings (+, -, 0). A unpolarised beam on the other hand always only has one setting (0). Each combination of the options of the two beams is a potential dataset, for which the collider can decide to assign a fraction of its luminosity.

The formula for the per-bin prediction for a single polarised dataset (eqs. (7.1) and (7.2)) provides a simple extension to implement a polarised scenario with multiple datasets. Each polarised dataset has its own measured distribution. A given bin shares the same

7. Impact of beam polarisation on electroweak fits

chiral prediction $\left(\prod_j f_{\chi,j}\right) \times \sigma_{\chi,\text{bin}}$ amongst the different polarised datasets. Only the polarisation-dependent weights $w_{\text{pol},\chi}$ and the luminosity vary between the predictions for the datasets.

All fits in this study build on the assumption that every polarised beam has fast helicity reversal capabilities (sections 3.1.3 and 3.2.2). As a consequence, any given systematic effect uses the same parameters for all polarised datasets. The luminosity stays a single global parameter, and each polarised dataset receives a factor according to the luminosity fraction that the collider provides to that polarisation combination. Each signed polarisation enters as a single parameter in all datasets that use that polarisation setting. For example, if a collider only has one polarised beam and two corresponding datasets, the unpolarised beam will have the same polarisation parameter in both datasets. If the collider would not have fast helicity reversal, then each polarised dataset would need its own systematic parameters set, including separate luminosity and polarisation parameters.

7.1.3. External constraints

In addition to the Poissonian log-likelihood, the fit can include Gaussian constraints on the fit parameters. These constraints can represent measurements of systematic effects in other detectors, measurements from other final states, results from previous experiments, or uncertainties of theory predictions. Like for the differential distribution, the framework fluctuates the measured values of such constraints for each fit around the true values within their uncertainties.

e^+e^- colliders typically provide measurements of luminosity and polarisation which are independent of the relevant collision data [2] (sections 3.2.1 and 3.2.3). The fits can include such direct input about the parameters in the form of Gaussian constraints.

7.1.4. Nature of the framework

The framework described above is generic in its approach. It is not specific to the process or the dimensionality of the distributions, can implement arbitrary physical and systematic effects, and can test any given polarisation and luminosity scenario. The fits can include multiple processes with separate or overlapping sets of parameters. All electroweak fits of this study use this framework [219–226].

7.2. Choosing collider scenarios

The fit framework can test different collider scenarios and compare the resulting precisions. A collider scenario consists of the center-of-mass energy of the collider, the total luminosity, the choice of beam polarisation with the corresponding sharing of luminosity between polarised datasets, and constraints on polarisation and luminosity. This section describes the motivation and choice of collider scenarios for this study.

Table 7.1.: The polarisation scenarios differ in whether a given beam is polarised, and with that in the amount of dataset which get a share of the luminosity. Collider scenarios with two polarised beams use a luminosity splitting that enhances the fraction of $e_L^- e_R^+$ and $e_R^+ e_L^-$ collisions. This is visible in the increased scenario-specific polarisation weights $w_{LR/RL}$ (eq. (7.4)).

Scenario	(80, 30) ^{w/ o-pol.}	(80, 30)	(80, 0)	(0, 0)
Absolute \mathcal{P}_{e^-} [%]	80 / 0	80	80	0
Absolute \mathcal{P}_{e^+} [%]	30 / 0	30	0	0
Datasets ($\text{sgn}(\mathcal{P}_{e^-}), \text{sgn}(\mathcal{P}_{e^+})$) :	(+, -) : 36 (-, +) : 36	(+, -) : 45 (-, +) : 45	(+, 0) : 50 (-, 0) : 50	(0, 0) : 100
Lumi. sharing [%]	(+, +) : 4 (-, -) : 4 (+, 0) : 4 (-, 0) : 4 (0, +) : 4 (0, -) : 4 (0, 0) : 4	(+, +) : 5 (-, -) : 5		
Pol. weights $w_{LR/RL}$	$1.154 \cdot 1/4$	$1.192 \cdot 1/4$	$1/4$	$1/4$
$1/\sqrt{4} \cdot w_{LR/RL}$	0.931	0.916	1	1

7.2.1. Scenarios inspired by proposed colliders

The comparison of such collider scenarios with different polarisation options exposes the impact of beam polarisation. Such a comparison requires a choice of concrete collider scenarios. Proposed future e^+e^- colliders (section 3.1) guide this choice in this study.

The four most advanced proposed colliders all have an option to run near the ZH threshold around 250 GeV [88, 89, 207, 227]. All fits within this study use distributions for runs at this energy (section 5.3).

The availability of longitudinal beam polarisation varies amongst the proposed colliders. Circular colliders typically do not use longitudinally polarised beams, while linear colliders produce one or both beams with longitudinal polarisation. This landscape motivates the polarisation scenarios in this study (table 7.1). Three options cover the basic scenarios; both beams are unpolarised (“(0/0)”), only the electron beam is polarised with a polarisation of 80% (“(80,0)”), or both beams are polarised with 80% and 30% polarisations for electron and positron beams respectively (“(80,30)”).

A collider with longitudinal polarisation can also depolarise a fraction of the bunches, or can use spin rotators to have fraction of the beam with transversal polarisation [228, 229]. This can improve the control of systematic effects and - in case of transversal polarisation - lead to additional observables. An additional polarisation scenario represents this case, building on the scenario with two polarised beams and allowing both beams

7. Impact of beam polarisation on electroweak fits

to run a fraction of the time in unpolarised mode (“(80/0,30/0)”).

The proposed collider concepts also inspire the luminosity sharing for the scenarios. A CLIC-like 50-50 sharing is the default for the scenario for with one polarised beam. When both beams are polarised, the fits use an ILC-like sharing which gives a larger 45% share to each of two opposite-sign polarised datasets and a 5% share to each of the two same-sign datasets. This sharing is also the basis for the extended (80/0,30/0) scenario, which assumes that the collider runs all possible combinations of signed and unpolarised beams. The luminosity-sharing keeps the 45-to-5 ratio of the opposite-sign to same-sign datasets, and assigns the same fraction to any dataset with unpolarised beams as to the same-sign datasets. As a result, each of the two opposite-sign datasets use 36% of the luminosity, and all other datasets use 4% each.

Each signed polarisation setting of a beam has its own free polarisation parameter in the fit. This emulates an imperfect helicity reversal which can lead to different absolute polarisation values for the different polarisation settings of a beam. The number of polarisation parameters per beam ranges from one for the unpolarised scenario to three for the scenario with two polarised beam that also employs unpolarised beam settings.

All scenarios include independent Gaussian constraints on each polarisation parameter. ILC-studies motivate a relative uncertainty of 0.25% for polarised beams with a polarisation of at least 20% [141, 148]. For the unpolarised beam settings, this study assumes an absolute uncertainty of 0.25%. These constraints neglect any correlation between the measurement of different-sign polarisation settings of the same beam. Future studies can investigate if any such correlations are significant. In addition, the spin transport between polarimeters and IP, as well as depolarising effects at the IP, can lead to biases of the polarimeters compared to the polarisation in the collision. Future studies can look into how well a fit can single out such biases and separate them from physical effects.

Circular colliders have another way to control the polarisation. They can use the transversal field of the bending magnets to ensure unpolarised beams to high precision. A study for the Z threshold scan at LEP arrived at an estimate of the potential residual longitudinal polarisation of around 0.5%, and concluded a negligible impact on electroweak measurements [230]. This study assumes a factor 2 improvement on this uncertainty by applying a polarimeter constraint of 0.25% to unpolarised beams. Future studies can revise this assumption.

The ILC operating scenario motivates the default luminosity of 2 ab^{-1} for all scenarios. Only the unpolarised scenario tests an additional higher-luminosity case of 10 ab^{-1} , corresponding to circular collider scenarios with two interaction points. In each case, a relative Gaussian constraint on the luminosity of 0.3% represents a luminosity measurement in Bhabha events. This constraint is inspired by ILC studies and likely a conservative estimate [125].

The scenarios described above are the basis of this study. Several of the included assumptions may be too conservative, which will affect the different scenarios in unequal

ways. Future studies can choose an updated set of references to revise the assumptions.

7.2.2. Impact of luminosity sharing on event numbers

The choice of luminosity sharing between polarised datasets has one very straightforward impact on the precision. Polarised datasets increase or decrease the total number of observed events for a given chiral initial state. This changes the statistical uncertainty for the chiral states. The corresponding change in statistical uncertainty is relevant when comparing colliders. Here, the focus is on the initial states $e_L^- e_R^+$ (LR) and $e_R^- e_L^+$ (RL). The equation for the total number of events for the initial states explains the change in the statistical uncertainty.

$$\begin{aligned} N_{LR} &= L \left[\sum_{\text{Datasets } D} f_D \frac{1 - \mathcal{P}_{e^-}^D}{2} \frac{1 + \mathcal{P}_{e^+}^D}{2} \right] \sigma_{LR} \equiv L w_{LR} \sigma_{LR} \\ N_{RL} &= L \left[\sum_{\text{Datasets } D} f_D \frac{1 + \mathcal{P}_{e^-}^D}{2} \frac{1 - \mathcal{P}_{e^+}^D}{2} \right] \sigma_{RL} \equiv L w_{RL} \sigma_{RL} \end{aligned} \quad (7.4)$$

Here, f_D is the luminosity fraction for dataset D , and $w_{LR/RL}$ define a pair of scenario-specific polarisation weights¹.

The luminosity sharing in all scenarios is symmetric with respect to a simultaneous sign-change of both beams, leading to equal weights $w_{LR} = w_{RL}$ (table 7.1). A comparison of the polarisation weights shows that only the scenarios with polarisation of both beams have a statistical advantage over the unpolarised scenario. The scenario with only one polarised beam does not see any statistical advantage. This is because polarisation in both beams is required to favor opposite-sign chiral states over same-sign chiral states. In scenarios with two polarised beams, the number of events increases by 15.4% (19.2%) when unpolarised beam settings are (are not) included². This corresponds to a relative decrease in the statistical uncertainty of 6.9% (8.4%). While small, this difference does appear in the results of this study, and is a separate effect of beam polarisation that comes in addition to access to chiral observables.

7.3. Choosing processes, parameters and effects

The basis of the fits is a set of differential distributions, together with a set of parameters describing physical and systematic effects. Both the processes and the parameters need to serve the purposes of the study. This section introduces the two- and four-fermion processes and the corresponding observables for the differential distributions

¹The collider scenario specific polarisation weight $w_{LR/RL}$ differs from the chiral polarisation weight $w_{\text{pol},\chi}$ (eq. (7.2)). While the $w_{\text{pol},\chi}$ describes the pure polarisation factor for one dataset, the $w_{LR/RL}$ describe the average factor of all datasets.

²This increased event number is sometimes rephrased as an increased ‘‘effective’’ luminosity [94].

7. Impact of beam polarisation on electroweak fits

Table 7.2.: Short overview of the processes in this study and which included effects impact them.

	Luminosity & polarisation	TGCs	$f\bar{f}$ parameters	μ acceptance
$e^+e^- \rightarrow \mu^+\mu^-$	×		×	×
$e^+e^- \rightarrow \mu\nu qq$	×	×		×

Table 7.3.: The binning of the differential distributions is the same as in previous studies [60].

Process	$e^+e^- \rightarrow \mu^+\mu^-$	$\mu\nu qq$				
Observables	$\cos \theta_\mu^*$	$\cos \theta_{W^-}$	×	$\cos \theta_\mu^*$	×	ϕ_μ^*
Binning $n_{bins}(x_{min}, x_{max})$	20 (-1, +1)	20 (-1, +1)	×	10 (-1, +1)	×	10 $(-\pi, +\pi)$

in this study (section 7.3.1), and the physical (sections 7.3.2 to 7.3.4) and systematic (section 7.3.5) effects that the fits considers (Overview: table 7.2).

7.3.1. Processes and their differential distributions

The goals of this study set some requirements on the processes that the fits include. Tests of the polarisation measurement require processes with a significant chirality-dependence. For the interplay of that measurement with physical effects, the fit needs to include physical effects that have a well-known dependence of polarisation. And the interplay with a systematic effect is richest when the systematic effect impacts as many included processes as possible.

Taking inspiration from previous studies [60], fermion and W pair production fulfill the requirements of high chirality-dependence and of polarisation-dependent observables (sections 2.1.1 and 2.1.3). This study further restricts itself to also fulfill the criterion of a common systematic effect. One way to guarantee overlapping systematic effects is by using processes with common final state particles. Here, the choice falls on having a μ in the final state. This leads a subset of processes for this study, which consists of μ pair production and semileptonic W pair production with a μ in the final state ($\mu\nu qq$).

With the choice of processes set, the fit needs differential distributions that describe these processes. An optimal choice of observables for these distributions is one that fully describes the kinematics of the respective process.

A single angle fully describes the $2 \rightarrow 2$ process of μ pair production for fixed ISR momentum. That angle is the μ^- production angle $\cos \theta_\mu^*$ in the $\mu^+\mu^-$ rest frame. Fits in this study use a one-dimensional distribution of that angle for each category of that process (fig. 7.1). The categories are the result of a split into high effective center of mass energy events and return-to- Z events, and an additional split of return-to- Z events into forward- and backward boosted events (section 5.3). This results in a total of three

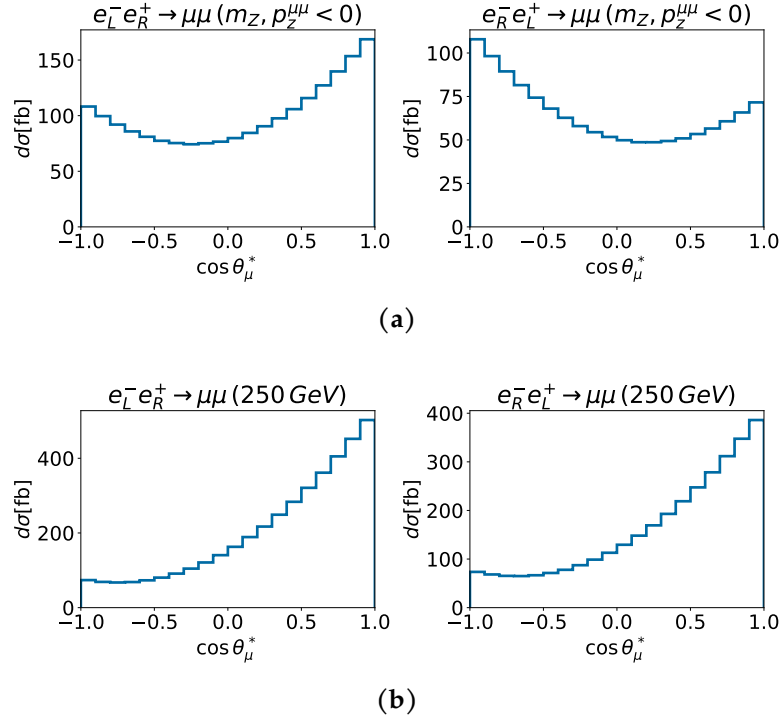


Figure 7.1: 1D differential distributions of the μ production angle in μ pair production demonstrate the energy- and chirality-dependence of the distribution ((a): $\sqrt{s^*} \approx m_Z$, (b): $\sqrt{s^*} \approx 250$ GeV; left: $e_L^- e_R^+$, right: $e_R^- e_L^+$).

categories, each one with its own differential distribution.

The semileptonic W pair production process is a $2 \rightarrow 4$ process and requires five angles for a full kinematic description. Two of those angles are the decay angles of the hadronically decaying W . A measurement of the initial quark charge, while possible [231, 232], is not straightforward, which affects the measurement of the quark angle. This study avoids this issue by restricting itself to a differential distribution in the three remaining angles (fig. 7.2): the W^- production angle $\cos\theta_{W^-}$, and the polar and azimuthal μ angles $\cos\theta_\mu^*$ and ϕ_μ^* in the corresponding W rest frame. The fits split the process into $\mu^+ \nu q q$ and $\mu^- \nu q q$ categories, each with its own distribution, to use the full sensitivity of the angular distribution.

In total, the fits uses three one-dimension μ pair production distributions and two three-dimensional W pair production distributions (table 7.3). This minimal set of distributions fulfills the initial requirements to achieve the goals of this study. A clear step for future studies is to add other processes and observables, and add corresponding effects and parameters. The following sections lay out the current set of effects and parameters that the fits in this study apply to the distributions described here.

7. Impact of beam polarisation on electroweak fits

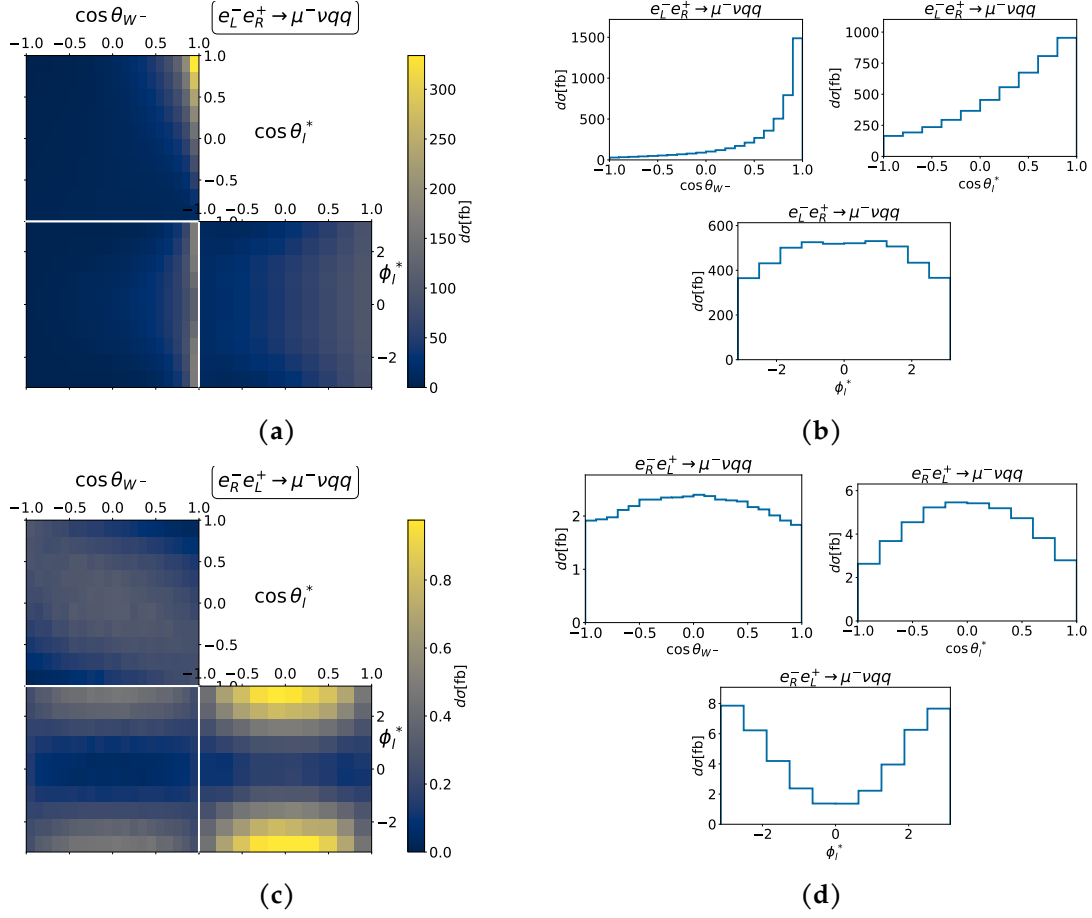


Figure 7.2.: 2D (left) and 1D (right) projections of the 3D differential distributions of chiral states of W pair production reflect that the t -channel dominated $e_L^- e_R^+$ initial state (top) is forward-peaked and that the $e_R^- e_L^+$ initial state (bottom), which contains only s -channel, has a comparatively flat center-peaked shape.

7.3.2. Parameterising fermion pair production

The primary target of $e^+e^- \rightarrow f\bar{f}$ measurements is the extraction of physical parameters such as the ffZ couplings. A study of the interplay between systematic and physical effects requires a parametrisation of the relevant physics.

The paragraphs below introduce a new parametrisation that takes into account a correction due to ISR, and note some special considerations in the implementation of that new parametrisation in the fits.

How ISR distorts the distribution

Fermion pair production (not including Bhabha scattering) is on tree-level a simple s -channel Z/γ exchange process (section 2.1.3). The tree-level formula for fermion pair

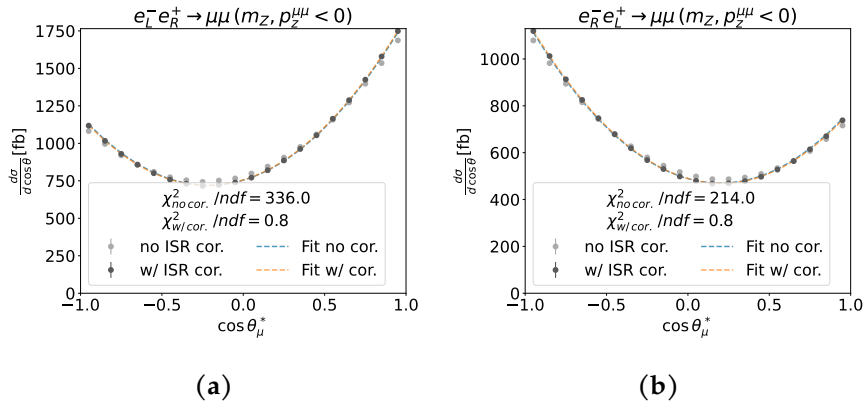


Figure 7.3.: A fit of the tree-level form for fermion pair production (eq. (7.5)) does not describe the used differential distributions for μ pair production in return-to-Z events (“no ISR cor.” & “Fit no cor.”). The reason is a distortion due to ISR; the tree-level form works well when correcting for the true ISR (“w/ ISR cor.” & “Fit w/ cor.”). This is true for both initial states ((a): $e_L^- e_R^+$, (a): $e_R^- e_L^+$).

production contains four terms, describing the combinations of the two allowed initial and final states (eqs. (2.41) and (2.52)).

$$\begin{aligned} \frac{d\sigma_{LR}^f}{d\cos\theta} &= \Sigma_{Ll} (1 + \cos\theta)^2 + \Sigma_{Lr} (1 - \cos\theta)^2 \\ \frac{d\sigma_{RL}^f}{d\cos\theta} &= \Sigma_{Rr} (1 + \cos\theta)^2 + \Sigma_{Rl} (1 - \cos\theta)^2 \end{aligned} \quad (7.5)$$

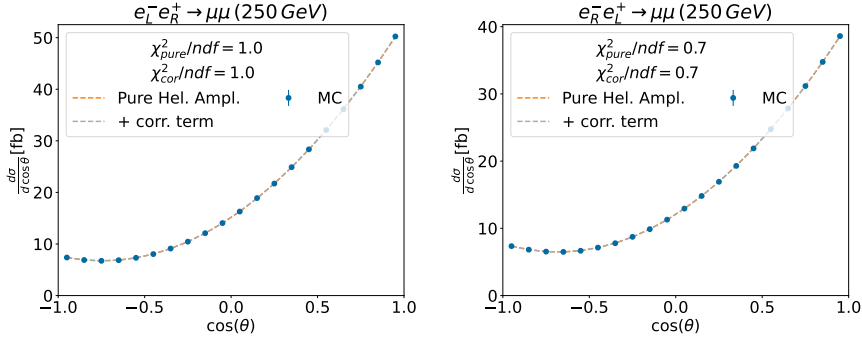
The relevant angle θ is the angle of the fermion wrt. the incoming e^+ in the $f\bar{f}$ rest frame.

While this simple formula describes the high- $\sqrt{s^*}$ dataset well, it does not capture the shape of the differential distribution of the return-to-Z events of μ pair production (fig. 7.3). The only higher-order effect in the MC events is initial-state radiation (section 5.1.1), and the predominance of the mismatch in return-to-Z events hints to a link to the strong ISR in these events.

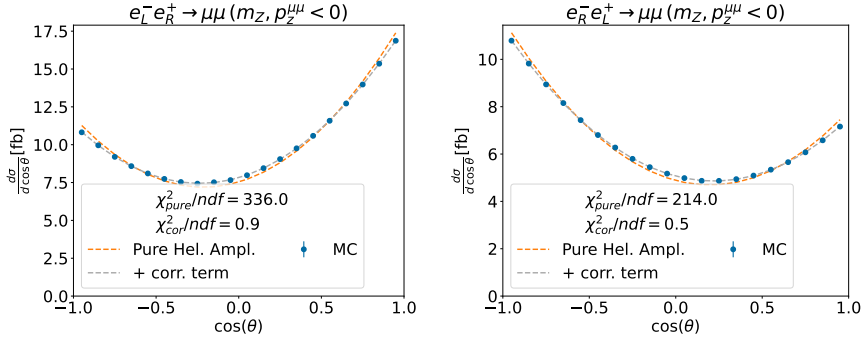
ISR can cause a non-zero momentum of the combined e^+e^- system. This momentum causes a change of the e^+ direction in the $f\bar{f}$ rest frame compared to the e^+ direction in the detector frame. A full correction of this will only be possible in the rare case when the detector measures and identifies the ISR. Otherwise, the unknown change of the e^+ direction leads to a miscalculation of the angle θ and distorts the distribution. A simple generator-level test confirms this: the tree-level formula works well on the angle when using the true e^+ direction after ISR (fig. 7.3).

A simple correction term is sufficient to allow an accurate description of the data even

7. Impact of beam polarisation on electroweak fits



(a) Events with $\sqrt{s^*} \approx \sqrt{s}$



(b) Return-to-Z events ($p_z^{\mu\mu} < 0$).

Figure 7.4.: Fit tests to the two allowed chiral initial states (left: $e^-_L e^+_R$, right: $e^-_R e^+_L$) of μ pair production show that the pure helicity amplitude approach (eq. (7.5), “Pure Hel. Ampl.”) works well for high- $\sqrt{s^*}$ events (a) and that return-to-Z events (b) require an approach with correction terms (eq. (7.6), “+ corr. term”).

with this distortion of the e^+ direction.

$$\begin{aligned} \frac{d\sigma_{LR}^f}{d\cos\theta} &= \Sigma_{LI} (1 + \cos\theta)^2 + \Sigma_{Lr} (1 - \cos\theta)^2 + K_L (1 - 3\cos^2\theta) \\ \frac{d\sigma_{RL}^f}{d\cos\theta} &= \Sigma_{Rr} (1 + \cos\theta)^2 + \Sigma_{RI} (1 - \cos\theta)^2 + K_R (1 - 3\cos^2\theta) \end{aligned} \quad (7.6)$$

Each chiral initial state gets individual correction terms with corresponding parameters K_L and K_R . The correction term frees the otherwise fixed ratio of constant and quadratic $\cos\theta$ terms, without affecting the total cross-section. This more generalized shape accurately describes the shape of $\mu^+\mu^-$ production in the MC events at both $m_{\mu\mu}$ ranges (fig. 7.4).

Restoring known parameters through reparametrisation

The tree-level formula with the correction terms (eq. (7.6)) accurately describes the $\mu^+\mu^-$ distributions. From an experimental point of view, the parameters of that approach turn out to be rather inconvenient. All parameters correlate with normalisation shifts (e.g. luminosity biases) and there is no distinction between chirality-dependent and chirality-independent effects. A reparametrisation resolves these issues and also restores a parameter set similar to that the one used at LEP and SLD [38].

$$\sigma_0^f = \frac{8}{3} (\Sigma_{Ll} + \Sigma_{Lr} + \Sigma_{Rr} + \Sigma_{Rl}) \quad (7.7a)$$

$$A_e = \frac{(\Sigma_{Ll} + \Sigma_{Lr}) - (\Sigma_{Rr} + \Sigma_{Rl})}{\Sigma_{Ll} + \Sigma_{Lr} + \Sigma_{Rr} + \Sigma_{Rl}} \quad (7.7b)$$

$$A_f = \frac{1}{2} \left(\frac{\Sigma_{Ll} - \Sigma_{Lr}}{\Sigma_{Ll} + \Sigma_{Lr}} - \frac{\Sigma_{Rr} - \Sigma_{Rl}}{\Sigma_{Rr} + \Sigma_{Rl}} \right) \quad (7.7c)$$

$$\epsilon_f = \frac{\Sigma_{Ll} - \Sigma_{Lr}}{\Sigma_{Ll} + \Sigma_{Lr}} + \frac{\Sigma_{Rr} - \Sigma_{Rl}}{\Sigma_{Rr} + \Sigma_{Rl}} \quad (7.7d)$$

$$k_0 = \frac{K_L}{\Sigma_{Ll} + \Sigma_{Lr}} + \frac{K_R}{\Sigma_{Rr} + \Sigma_{Rl}} \quad (7.7e)$$

$$\Delta k = \frac{K_L}{\Sigma_{Ll} + \Sigma_{Lr}} - \frac{K_R}{\Sigma_{Rr} + \Sigma_{Rl}} \quad (7.7f)$$

This new parametrisation uses the total cross-section σ_0^f , the electron asymmetry A_e , the final state asymmetry A_f , a new parameter ϵ_f , and the now normalised chirality-symmetric and -asymmetric correction terms k_0 and Δk .

After this reparametrisation, the differential cross-section takes a form that is easy to handle by the fit (detailed derivation: section C.1).

$$\begin{aligned} \frac{d\sigma_{LR}^f}{d\cos\theta} &= \frac{3}{8}\sigma_0^f \frac{1+A_e}{2} \left[\left(1 + \frac{k_0 + \Delta k}{2}\right) + (\epsilon_f + 2A_f) \cos\theta + \left(1 - 3\frac{k_0 + \Delta k}{2}\right) \cos^2\theta \right] \\ \frac{d\sigma_{RL}^f}{d\cos\theta} &= \frac{3}{8}\sigma_0^f \frac{1-A_e}{2} \left[\left(1 + \frac{k_0 - \Delta k}{2}\right) + (\epsilon_f - 2A_f) \cos\theta + \left(1 - 3\frac{k_0 - \Delta k}{2}\right) \cos^2\theta \right] \end{aligned} \quad (7.8)$$

Interpretation of the new parameters

The definition of the new parameters encodes their physical meaning. For the correction parameters k_0 and Δk , their motivation already defines them as corrections for ISR or more general higher-order effects. For the remaining parameters, it is instructive to look at the pure Z -pole case, where the photon contribution to $e^+e^- \rightarrow f\bar{f}$ becomes small compared to the Z -contribution.

7. Impact of beam polarisation on electroweak fits

Table 7.4.: Fits to the chiral distributions of the Monte-Carlo datasets yield specific values of the generalized difermion parameters (eq. (7.8)) for the two mass ranges of μ pair production. Uncertainties arise from the available MC statistics.

*The 250 GeV upper bound also includes few events with higher masses, caused by the beam spectrum of the dataset.

Parameters	$m_{\mu\mu}$ range [GeV]	
	[81, 101]	[180, 250*]
σ_0^μ [fb ⁻¹]	6621.4 ± 1.2	7250.0 ± 1.2
A_e	0.2136 ± 0.0002	0.11251 ± 0.00016
A_μ	0.2028 ± 0.0005	0.03213 ± 0.00017
ϵ_μ	0.0156 ± 0.0005	1.4259 ± 0.0003
k_0	0.0747 ± 0.0006	0.0002 ± 0.0005
Δk	0.0007 ± 0.0007	0.0002 ± 0.0005
A_{FB}^μ	0.03833 ± 0.00016	0.53742 ± 0.00012

Ignoring all photon contributions, the helicity amplitudes assume a simple structure that only depends on a common normalisation S and the chirality-dependent couplings $c_{L/R}^f$ of the fermions to the Z [36].

$$\begin{aligned}
 \Sigma_{LI|SM} &= S * (c_L^e)^2 * (c_L^f)^2, & \Sigma_{Lr|SM} &= S * (c_L^e)^2 * (c_R^f)^2 \\
 \Sigma_{Rr|SM} &= S * (c_R^e)^2 * (c_R^f)^2, & \Sigma_{RI|SM} &= S * (c_R^e)^2 * (c_L^f)^2
 \end{aligned} \tag{7.9}$$

These Z -pole amplitudes enter into the definitions of the generalised parametrisation (eq. (7.7)), and exactly recover the LEP/SLD-definitions [2, 38].

$$\sigma_0^f = \frac{8}{3}S \left((c_L^e)^2 + (c_R^e)^2 \right) \left((c_L^f)^2 + (c_R^f)^2 \right) \quad (7.10a)$$

$$A_e = \frac{\left[(c_L^e)^2 - (c_R^e)^2 \right] \left[(c_L^f)^2 + (c_R^f)^2 \right]}{\left[(c_L^e)^2 + (c_R^e)^2 \right] \left[(c_L^f)^2 + (c_R^f)^2 \right]} = \frac{(c_L^e)^2 - (c_R^e)^2}{(c_L^e)^2 + (c_R^e)^2} \quad (7.10b)$$

$$A_f = \frac{1}{2} \left\{ \frac{(c_L^e)^2 \left[(c_L^f)^2 - (c_R^f)^2 \right]}{(c_L^e)^2 \left[(c_L^f)^2 + (c_R^f)^2 \right]} - \frac{(c_R^e)^2 \left[(c_R^f)^2 - (c_L^f)^2 \right]}{(c_R^e)^2 \left[(c_R^f)^2 + (c_L^f)^2 \right]} \right\} = \frac{(c_L^f)^2 - (c_R^f)^2}{(c_L^f)^2 + (c_R^f)^2} \quad (7.10c)$$

$$\epsilon_f = \frac{(c_L^e)^2 \left[(c_L^f)^2 - (c_R^f)^2 \right]}{(c_L^e)^2 \left[(c_L^f)^2 + (c_R^f)^2 \right]} + \frac{(c_R^e)^2 \left[(c_R^f)^2 - (c_L^f)^2 \right]}{(c_R^e)^2 \left[(c_R^f)^2 + (c_L^f)^2 \right]} = 0 \quad (7.10d)$$

$$(7.10e)$$

The total cross-section contains both the common normalisation S and the normalisation of the couplings. The initial and final fermion asymmetries A_e and A_f quantify the chirality-dependence of the eeZ and ffZ couplings respectively. And the new parameter ϵ_f disappears on the Z pole.

Additional insight comes from the parameter values on the μ pair production datasets. A fit of the new parametrisation (eq. (7.8)) to the chiral distributions of the datasets yields those parameter values (table 7.4). The values confirm that ϵ_μ is small for return-to- Z events, and show that this parameter takes large values for events far away from the Z -pole. This suggests that this parameter describes the influence of γ -exchange in the differential cross-section. For this reason, this study will refer to this parameter as the Z/γ -interference parameter.

The μ pair production parameter values also reiterate that an unpolarised correction term k_0 is only necessary on the return-to- Z dataset, where the ISR energy is large. At both energy ranges, the chirality-asymmetric correction term Δk turns out to be negligible, reflecting the chirality-independence of ISR. The fits of this study still use this parameter, as it can represent any additional chirality-dependent effect in real data that are not present in the Monte Carlo datasets.

The parameter values in this study also come with a caveat. Both μ pair production datasets integrate large mass-ranges of several tens of GeV. Since the parameters are energy-dependent, this integration over energy also means that the parameter values in this study are not values at a fixed energy point. Rather, they are folded with the energy-dependent μ pair production cross-section in the integrated energy range. This complicates a direct comparison of the values here with those from LEP/SLD. Future studies can consider binning the distribution in $m_{\mu\mu}$, which will require that the

7. Impact of beam polarisation on electroweak fits

parametrisation directly considers the energy-dependence of the parameters.

Unpolarised parametrisation

The fits will also test fermion pair production for collider scenarios without beam polarisation. In that scenario, the collider only provides one dataset. That single unpolarised dataset can only measure a single second order polynomial (details: section C.1).

$$\frac{d\sigma_{\text{unpol}}^f}{d\cos\theta} = \frac{1}{4} \frac{3}{8} \sigma_0^f \left[\left(1 + \frac{1}{2}k_0\right) + \frac{8}{3}A_{FB}^f \cos\theta + \left(1 - \frac{3}{2}k_0\right) \cos^2\theta \right] \quad (7.11)$$

This single polynomial contains the polarisation factor $1/4$, and still uses the total cross-section σ_0^f and the chirality-independent correction parameter k_0 . In addition, it introduces the forward-backward asymmetry A_{FB}^f .

A comparison of this unpolarised parametrisation with the polarisation-weighted combination of the general chiral parametrisation gives meaning to these unpolarised parameters (eq. (C.12)). The use of σ_0^f and k_0 is consistent with the general parametrisation up to quadratic corrections in the parameters $\{\mathcal{D}_{e^\pm}, A_e, \Delta k\}$. This study assumes such corrections to be negligible or easy to correct, and uses the same parameters σ_0^f and k_0 for the polarised and unpolarised cases.

The forward-backward asymmetry takes a form that is consistent with the LEP/SLD definition of that parameter [2], and that includes the effective polarisation \mathcal{D}_{eff} (eq. (3.5)).

$$A_{FB}^f = \frac{3}{8} \left(\epsilon_f + 2A_f \frac{\mathcal{D}_{\text{eff}} + A_e}{1 + \mathcal{D}_{\text{eff}}A_e} \right) \stackrel{\mathcal{D}_{\text{eff}} \approx 0}{\approx} \frac{3}{8} (\epsilon_f + 2(\mathcal{D}_{\text{eff}} + A_e)A_f) \quad (7.12)$$

An interpretation of an A_{FB}^f measurement in terms of the chiral parameters requires additional input. From the machine side, the interpretation requires precise polarisation knowledge. A precise calculation of Z/γ -interference parameter ϵ_f reduces A_{FB}^f to the term $4/3 \cdot A_e A_f$. This likely will not pose a problem near the Z -pole where the relative ϵ_μ contribution for the $\mu\mu$ final state makes up only around 15% of A_{FB}^μ (table 7.4). The situation is notably different above the Z -pole, where the Z/γ -interference is strong with e.g. $\epsilon_\mu \approx 1.4$ at 250 GeV. In that case, the $4/3 \cdot A_e A_\mu$ term makes a contribution to A_{FB}^μ that is below the percent level. While polarised colliders can measure ϵ_f directly in $f\bar{f}$ production, unpolarised colliders rely on precise input. Similarly, polarised collider can measure A_e and A_μ directly, while unpolarised colliders require the additional input of A_e from a τ polarisation measurement [2].

Implementation in the fits

The fit framework is designed to apply different effects - physical or systematic - as factors to the chiral cross-section distributions to obtain the full predicted distribution

(eq. (7.1)). Due to technical complications, this approach was not possible for the fermion pair production parameters at the time of implementation. That same technical reasons did not allow shared physical parameters between two- and four-fermion distributions such as ffZ couplings.

An alternative is that the parametrisation (eq. (7.8)) fully replaces the chiral distribution from Monte-Carlo in the fit. The general parametrisation accurately describes the MC distribution (fig. 7.4), and the parametrisation can replace the MC distribution without loss of information.

Unpolarised colliders are a special case, since they have no sensitivity to polarisation values. Fits that consider fermion pair production for unpolarised scenarios include the polarisation exclusively through the polarimeter constraints. The exact value of the polarisations only comes into play in the interpretation of the unpolarised observables.

7.3.3. WW parametrisation

W pair production plays a key role in the beam polarisation measurement [60]. As part of this study, the fits aim to test how the polarisation measurement interplays with measurements of physical effects. Here, the choice of physical effects falls on the primary goals of W pair production measurements at LEP: the total unpolarised cross-section and the charged triple gauge couplings [233]. In addition, the fits can include the left-right asymmetry to test its impact on the measurement. This study does not consider anomalous couplings of the W to fermions and non-SM propagators like additional Z -like bosons. The following paragraphs describe the parameters in this study and their implementation in the fit.

Chiral cross-section parameters

The total chiral cross-sections σ_{LR} and σ_{RL} contain information about the chiral dependence and the total number of expected events. Both of these can be individually relevant for different physical or systematic effects. A transformation into the total cross-section σ_0 and left-right asymmetry A_{LR} separates the chirality-dependent and independent parts, the same way that the fermion pair production uses σ_0^f and A_e (eq. (7.7)).

$$\sigma_0 = \sigma_{LR} + \sigma_{RL}, \quad A_{LR} = \frac{\sigma_{LR} - \sigma_{RL}}{\sigma_{LR} + \sigma_{RL}} \quad (7.13)$$

The fits in this study do not directly use these parameters, and instead use the relative change in σ_0 and the absolute deviation of A_{LR} (details: section C.2).

The measurement of the total cross-section allows a comparison with precise calculations of the integrated SM cross-section. Due to this role as an observable, σ_0 is generally a free parameter in the fits of this study. A fixing of the cross-section here only serves to understand how other observables depend on normalisation information.

7. Impact of beam polarisation on electroweak fits

The fully asymmetric t-channel diagram dominates the left-right asymmetry A_{LR} . A_{LR} also encodes the eeZ coupling in the s-channel diagram at the effective center-of-mass energy $\sqrt{s^*} = m_{WW}$. Fermion pair production will have to measure this coupling with high precision at high energies. Tests of the relevance of left-right asymmetry parameter can demonstrate how important eeZ knowledge is for the triple gauge coupling and polarisation measurements [169].

Triple Gauge Couplings (TGCs)

The fits here build on previous studies (section 4.1) and use the three anomalous couplings of the LEP parametrisation $g_1^Z, \kappa_\gamma, \lambda_\gamma$ (section 2.2.3) to parametrise changes in the chiral differential distributions of W pair production. For this, the fits need a bin-dependent parametrisation of how TGC deviations change the cross-section in each bin. A two-step process makes this possible by first extracting the event-wise impact of TGCs and then transformation it into a bin-wise parametrisation [157].

Starting with the second step, the fit requires a choice of how to parametrise the TGC impact on the cross-section in the bin. TGCs can appear at most quadratically in the differential cross-section (section 2.2.2). A second order polynomial in the three TGC deviations $(\Delta g_1^Z, \Delta \kappa_\gamma, \Delta \lambda_\gamma)$ therefore accurately describes the change of differential chiral cross-section³.

$$\frac{d\sigma_{LR/RL}(\Delta g_1^Z, \Delta \kappa_\gamma, \Delta \lambda_\gamma)}{\sigma_{LR/RL}^{SM}} = 1 + \sum_{c \in \{g_1^Z, \kappa_\gamma, \lambda_\gamma\}} (T_c \Delta c + T_{c^2} \Delta c^2) + \sum_{c_1, c_2, c_1 \neq c_2} T_{c_1 c_2} \Delta c_1 \Delta c_2 \quad (7.14)$$

The coefficients T of the polynomial are bin- and chirality-dependent. Determining all coefficients of the polynomial is possible if the histogram is available for at least nine (well-chosen) points in the $\{\Delta g_1^Z, \Delta \kappa_\gamma, \Delta \lambda_\gamma\}$ space. This requires the first step - the determination of the event-wise TGC impact.

The WHIZARD event generator contains a ‘‘reweighting’’ procedure for exactly this purpose [182, 183]. This procedure reads in the kinematics of an event, and then calculates the squared matrix element for that event both with SM parameter values $|M_{SM}|^2$ and with a given set of non-SM parameter values $|M_{anomalous}|^2$. By calculating the ratio of the non-SM to the SM squared matrix element

$$w_{anomalous} = \frac{|M_{anomalous}|^2}{|M_{SM}|^2} \quad (7.15)$$

the procedure provides event weights $w_{anomalous}$ that quantify the increase or decrease of the probability of that event.

The determination of the polynomial coefficients employs this reweighting procedure

³A previous study has shown that a restriction to only linear terms does not influence the results on 250 GeV ILC data [60], justifying the limitation to dimension-six EFT operators.

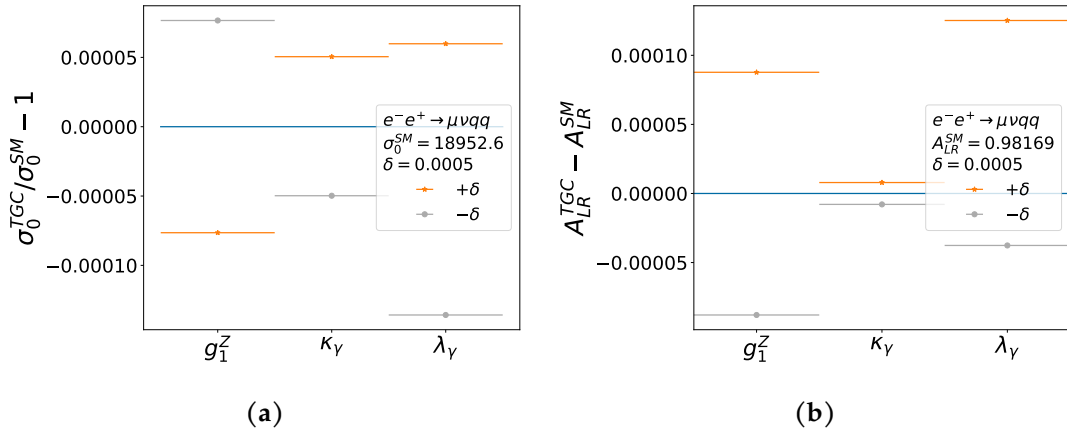


Figure 7.5.: Changes in the Triple Gauge Coupling values change (a) the total unpolarised cross-section σ_0 and (b) the left-right asymmetry A_{LR} of semileptonic W pair production.

for a set of 18 non-SM TGC points in the three parameter space with a common scale $\delta = 5 \cdot 10^{-4}$ (details: section C.3). This scale value plays a minor role since the quadratic polynomial is an exact description of the TGC impact on the differential cross-section. Each of the 18 points yields a histogram with weighted entries, according to the TGC values of that point. The calculation of the nine coefficients of each bin consists of a fit to the bin values at the 18 TGC points.

The electroweak fit applies the polynomial (eq. (7.14)) with the bin-dependent coefficients as factor to the chiral cross-section in each bin. Correlations between the TGCs can in part arise through the bi-linear coefficients $T_{c_1c_2}$. More generally, correlations will arise if the measurement of two effects relies on the same information, be it shape, asymmetry, or normalisation. Negligible $T_{c_1c_2}$ are not a sufficient criterion to exclude correlations between the TGCs.

7.3.4. TGC sensitivity of W pair production

Changes in the TGC values affect the shape and chiral cross-sections of W pair production (figs. 7.5 and 7.7 and section C.4). Knowledge of the impact of the TGCs is the basis for understanding their behaviour in the fit, especially their dependence on beam polarisation.

Beam polarisation aids in the separation of the chiral initial states, beyond the separation from the measured shape. In a polarised measurement each initial state has a dataset where that specific initial state is enhanced and the others reduced. Two advantages arise: the precision of the left-right asymmetry measurement increases, and so does the precision on the shapes of each initial state. This can affect the parameter precision if a parameter is sensitive to the asymmetry or if the sensitivity to the differential

7. Impact of beam polarisation on electroweak fits

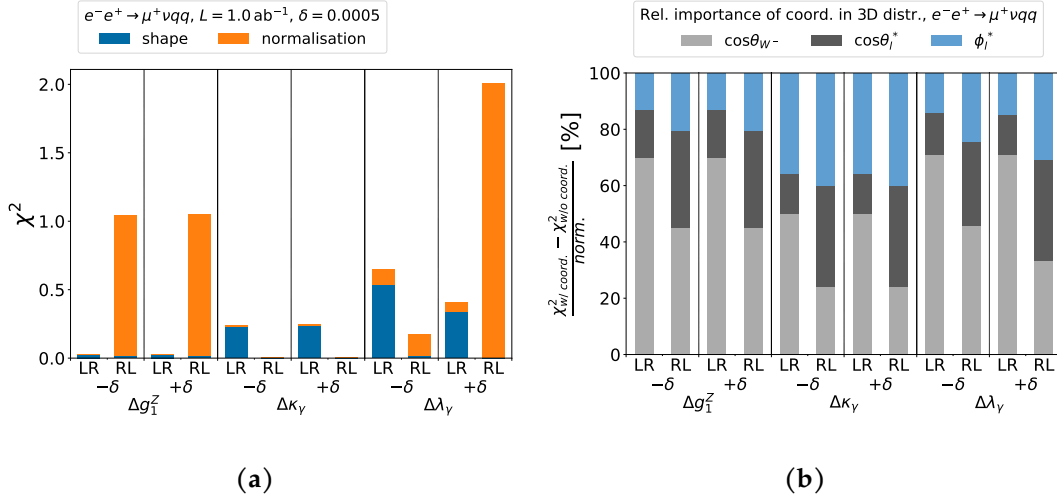


Figure 7.6.: χ^2 checks (eq. (7.16)) of TGC-sensitivity from the overall shape and normalisation (a) show that the most important information is shape in the $e_L^- e_R^+$ initial state and normalisation in $e_R^- e_L^+$. A closer look at the shape sensitivity (b) shows that the W^- production angle is the most important observable. Results shown are for $\mu^+ \nu q q$, results for μ^- are the same.

shape depends on the separation of initial states.

An assessment of the sensitivity of W pair production to the TGCs requires a quantification. Deviations of the TGCs introduce a luminosity-dependent χ^2 on the differential distribution of single chiral initial state with respect to the pure SM distribution.

$$\chi_{LR/RL}^2(g_1^Z, \kappa_\gamma, \lambda_\gamma; L) = \frac{1}{L} \sum_{\text{bins}} \left(\frac{\sigma_{LR/RL}(g_1^Z, \kappa_\gamma, \lambda_\gamma) - \sigma_{LR/RL}^{SM}}{\sqrt{\sigma_{LR/RL}(g_1^Z, \kappa_\gamma, \lambda_\gamma)}} \Big|_{\text{bin}} \right)^2 \quad (7.16)$$

This converts into a measure of the sensitivity to the normalisation of that initial state when the whole differential distribution is a single bin. The difference between the χ^2 of the fully 3D-binned differential distribution and the χ^2 of the normalisation yields the sensitivity to the pure normalisation-independent shape. These quantifiers show whether the sensitivity to a given TGC arises primarily from changes it introduces to the chiral cross-section or to those it introduces in the arbitrarily normalised chiral differential distribution (fig. 7.6a).

When the shape turns out to be more relevant, the question arises which observable plays the biggest role. The previous χ^2 quantifiers cannot answer which coordinate is most important for the shape sensitivity. To address this point, the difference between the χ^2 from the 3D distribution and the χ^2 from the 2D projection without a given observable gives that observables importance (fig. 7.6a).

g_1^Z and λ_γ both draw significant sensitivity from the measurement of $e_R^- e_L^+$ chiral cross-

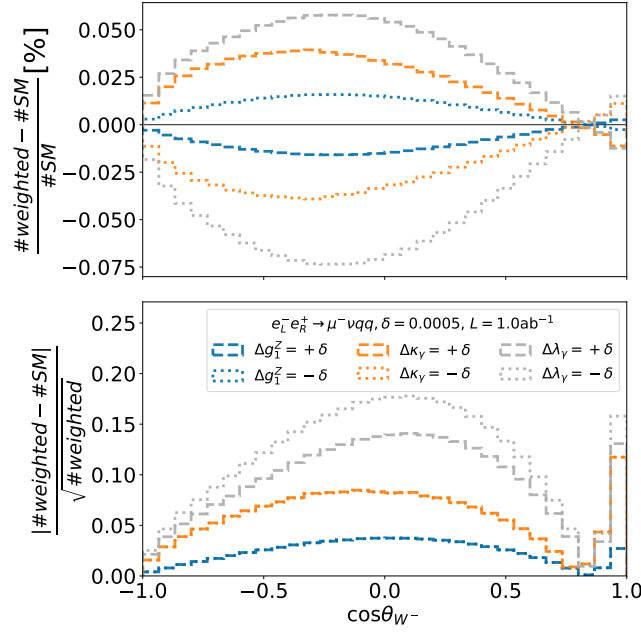


Figure 7.7.: Deviations in the TGC values change the differential distributions of the $\mu^- \nu q q$ final state (top). The significance of that change (bottom) is large for central events with large changes and for forward events with high statistics. For W pair production, the most relevant changes happen on the $\cos \theta_{W^-}$ distribution of the $e_L^- e_R^+$ initial state. The changes are identical for $\mu^+ \bar{\nu} q q$. (Other coordinates and initial states: section C.4)

section. The $e_L^- e_R^+$ cross-section measurement adds only a subdominant contribution in the λ_γ sensitivity. In terms of chiral parameters, the asymmetry measurement A_{LR} determines the uncertainty on the $e_R^- e_L^+$ chiral cross-section, while the normalisation uncertainty plays negligible role.

$$\begin{aligned} \frac{\Delta\sigma_{RL}}{\sigma_{RL}} &= \sqrt{\left(\frac{1}{1-A_{LR}}\Delta A_{LR}\right)^2 + \left(\frac{\Delta\sigma_0}{\sigma_0}\right)^2} \\ &\approx \sqrt{\left(54\frac{\Delta A_{LR}}{A_{LR}}\right)^2 + \left(\frac{\Delta\sigma_0}{\sigma_0}\right)^2} \end{aligned} \quad (7.17)$$

In order to play any significant role, the relative uncertainty of σ_0 has to be 50 times larger than the relative A_{LR} uncertainty.

Significant shape sensitivity in κ_γ and λ_γ comes from the $e_L^- e_R^+$ initial state. This sensitivity relies in both couplings mostly on the $\cos \theta_{W^-}$ observable (fig. 7.7). Any mixing of the $e_R^- e_L^+$ initial state into the $e_L^- e_R^+$ distribution is unlikely to disturb that shape measurement because the $e_L^- e_R^+$ cross-section factor is a factor 100 higher. The chiral separation

7. Impact of beam polarisation on electroweak fits

from beam polarisation will therefore not help in the separation of TGC shape effects.

g_1^Z draws sensitivity from the left-right asymmetry measurement. Beam polarisation increases the A_{LR} precision, which will benefit g_1^Z precision. The κ_γ sensitivity lies almost exclusively in $e_L^- e_R^+$ shape changes. Therefore, as discussed above, beam polarisation does not show an immediate advantage for the pure κ_γ measurement. Sensitivity to λ_γ arises from both the shape and the asymmetry measurements. Beam polarisation will benefit λ_γ precision only if asymmetry information gives the stronger constraint.

The above discussion only considers single TGC sensitivities. It also shows that the sensitivity to the three couplings arises mainly from two types of information in W pair production measurement: the left-right asymmetry and $e_L^- e_R^+ \cos \theta_{W^-}$ shape. All three TGCs cause very similar changes to that $e_L^- e_R^+ \cos \theta_{W^-}$ shape (fig. 7.7). A combined fit of all three TGCs will find less constrained directions in the TGC space (section 7.7.4), where the combined asymmetry and $\cos \theta_{W^-}$ shape changes of the TGCs are small. Such behaviour can cause correlations amongst the TGCs.

7.3.5. Including systematic effects

In addition to the fermion pair production parameters and the WW cross-section and TGC parameters, the fit also includes systematic effects.

Luminosity and beam polarisations are the most basic and important systematic effects that enter practically any measurement at future e^+e^- colliders (eqs. (7.1) and (7.2)). The fit framework foresees these by default as free parameters, and can include Gaussian constraints on them (section 7.1). Values of the luminosity and polarisations and their constraints define the collider scenario (section 7.2). The polarisation values of polarised beams are 80% and 30% for electron and positron beam respectively, and the fits test luminosities of 2 ab^{-1} and 10 ab^{-1} .

Previous studies have sometimes assumed that the absolute polarisation of a beam is the same for both longitudinal polarisation directions [157, 170]. This study completely drops this assumption, and uses separate polarisation parameters for each polarisation setting of a beam, each with an independent Gaussian constraint (section 7.2). A previous study has shown that dropping this assumption does not pose any issue for colliders with two polarised beams [60].

In addition to these, the fit also considers the μ acceptance as an experimental systematic effect. Because the inclusion of this effect is not straightforward, a separate section will describe the implementation in detail (section 7.4).

7.4. Including the muon acceptance

One of the targets of this study is to understand how beam polarisation affects systematic uncertainties (section 4.1). The chirality-independent nature of systematic effects means that a polarised collider can in principle separate them from the chirality-dependent

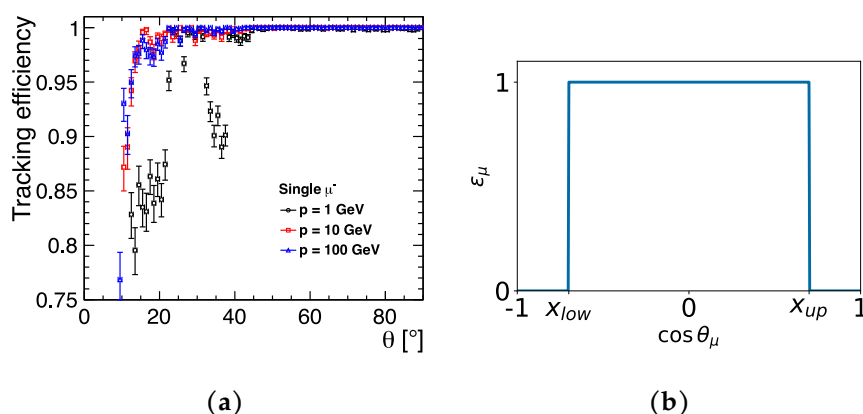


Figure 7.8.: The μ acceptance at future detectors such as SiD promises a high central efficiency and a sharp edge in the forward region (a, copied from [82]). A box-like model (b) serves as a easy-to-implement first approximation to that acceptance.

physical effects simply on the basis of how they affect the different polarised datasets. Tests of this hypothesis require the direct implementation of a specific systematic uncertainty into the fit.

The choice here falls on the μ acceptance. This effect is relevant both for fermion pair production - in the μ pair production final state - and for W pair production - in the semileptonic $\mu\nu q\bar{q}$ final state. LEP measurements of μ pair production quoted the μ acceptance as an important systematic uncertainty [234–236]. Here, a simple box-like model approximates the μ acceptance.

This specific choice serves as a prototype test for including systematic effects directly in the fit. Future studies can use the same approach with other systematic effects and on more final states.

This section motivates and introduces the model (section 7.4.1) and describes the impact on the fitted distributions (section 7.4.2). Symmetries in the μ pair production distribution turn out to be a challenge for this model (section 7.4.3). An implementation into the fit requires a translation of the geometrical model into a model on the differential cross-section (section 7.4.3), a step that also requires verification (sections 7.4.5 and 7.4.6). As a result, the fit can directly extract the μ acceptance from the collision data (section 7.4.7).

7.4.1. A simple muon acceptance model

An implementation of the μ acceptance into the fit first requires a model of that acceptance with corresponding model parameters.

Full simulation studies for possible detectors at future e^+e^- colliders predict a sharp drop of the μ acceptance in the forward region (fig. 7.8a) [82]. A simple “box model” serves as a first approximation to this full-simulation acceptance (fig. 7.8b). The model

7. Impact of beam polarisation on electroweak fits

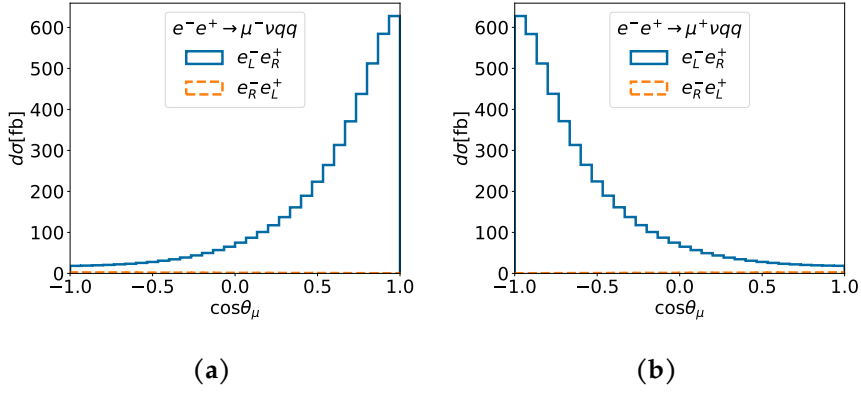


Figure 7.9.: The angular distribution of the μ in the detector frame for semi-leptonic W pair production shows that the majority of μ 's fly in the very-forward (μ^- , a) or very-backward (μ^+ , b) regions of the detector. Contributions from the $e_R^- e_L^+$ initial state are negligible due to the small cross-section.

assumes that the experiment can reconstruct every μ within the two edges (forward and backward), and that any μ outside that range goes undetected. Future detectors such as ILD will place these edges as low as 7° (section 3.3.3).

The values of the two edges fully describe the model. A transformation can separate symmetric and asymmetric behaviour of the box into a width parameter w and a center parameter c , respectively.

$$c = \frac{x_{\text{up}} + x_{\text{low}}}{2}, \quad w = x_{\text{up}} - x_{\text{low}} \quad (7.18)$$

Default values of these parameters are those for both edges at 7° . This study uses the deviations Δc and Δw from the those default values as free parameters.

$$\Delta c = c - c_{7^\circ}, \quad \Delta w = w - w_{7^\circ} \quad (7.19)$$

The approach of fitting the systematic effect fundamentally requires that the given systematic effect has a rather simple shape parametrisation with a reasonable number of parameters. Given the precision discussed in this study, there is no guarantee for that. Future studies can use full simulation to motivate more realistic models, likely with a larger parameter set.

7.4.2. Impact of the muon acceptance on generator-level distributions

The acceptance influences the shape of the fitted differential distributions. Those shape effects and their changes with the parameters determine the behaviour of the acceptance in the fit, and are correspondingly important to understand. A direct application of the model to the MC events gives a first indication of the impact.

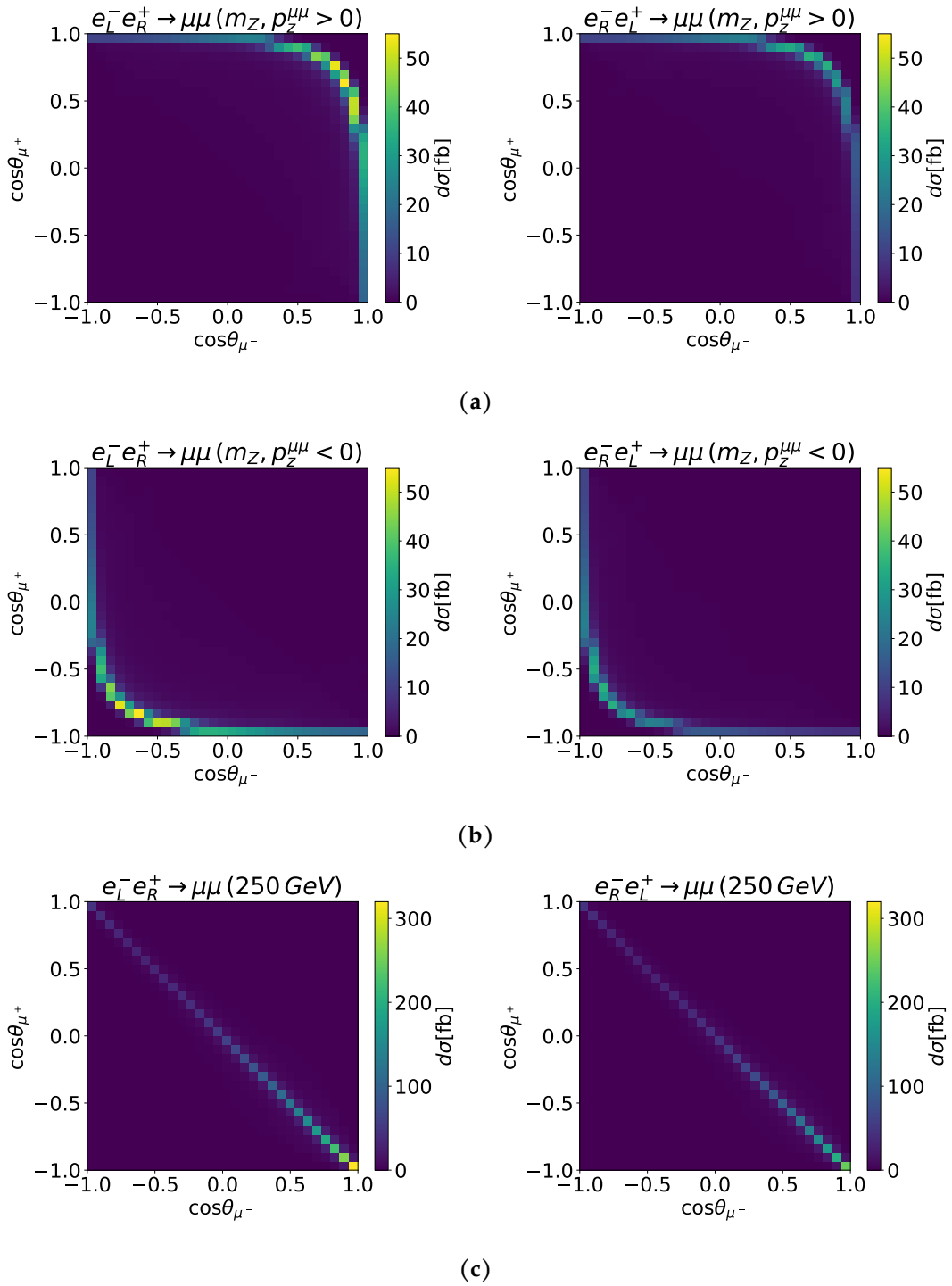


Figure 7.10.: Angular distributions of μ 's in the detector frame show that μ pair production yields either (a,b) two fairly close-by forward or backward muons in return-to-Z events or (c) two back-to-back muons for high- $\sqrt{s^*}$ events (right).

7. Impact of beam polarisation on electroweak fits

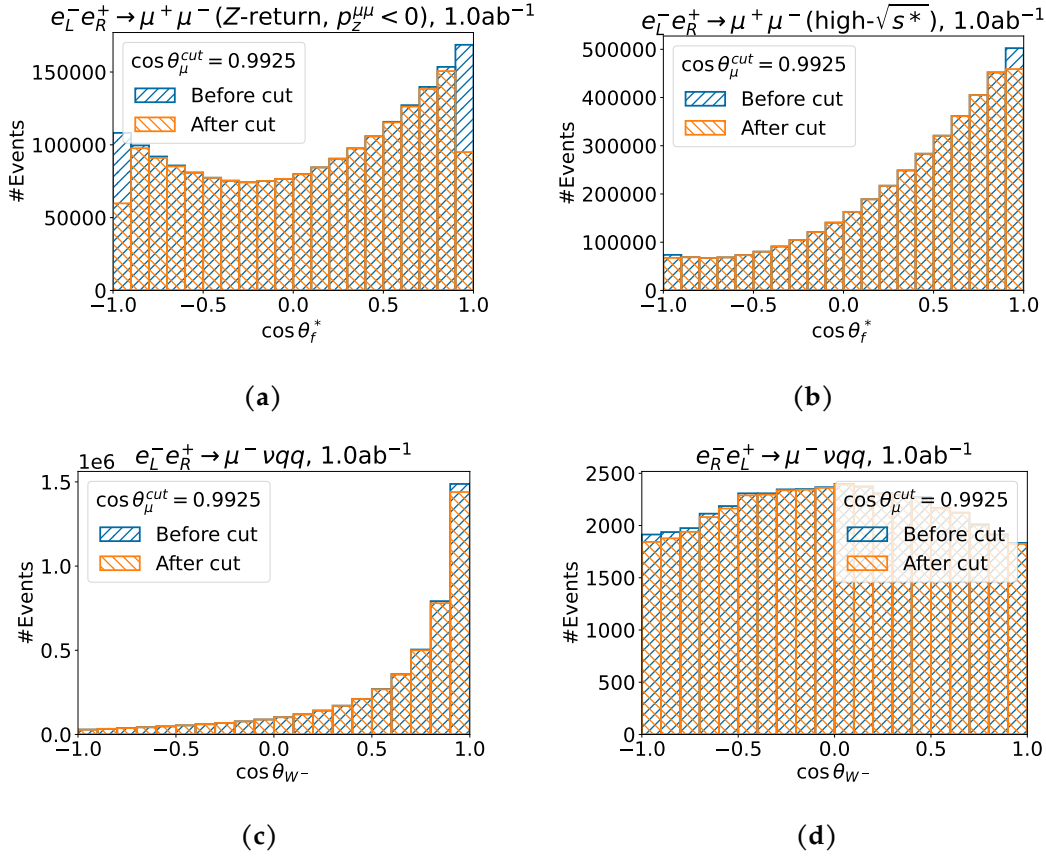


Figure 7.11.: A μ acceptance cut of 7° changes the differential distribution of μ pair production (top) and semileptonic W pair production (bottom, 1D projections of 3D distributions). The impact is non-trivial because the μ angle in the detector frame is not a direct observable of the distributions. Only for high- $\sqrt{s^*}$ μ pair production is the detector frame μ angle almost exactly the angle in the $\mu\mu$ frame. (Distribution for other initial/final states and coordinates in Appendix: figs. C.3 to C.5)

The angle of the μ 's in the detector frame determines the impact of the μ acceptance. All included processes have forward or backward-peaking μ distributions in the detector frame (figs. 7.9 and 7.10). This means that the acceptance will affect a significant number of events in those processes. The μ angle in the detector frame is itself not a direct observable in any of the distributions, so that the impact of the acceptance on the distributions depends on the relation between the observables and the μ angle in the detector frame.

The impact of the acceptance is straightforward on high- $\sqrt{s^*}$ μ pair production events. In these events, the rest frame of the μ pairs corresponds roughly to the detector frame. A very-forward μ acceptance therefore affects only the two bins at the edges of the distribution (fig. 7.11b). For the simple box model, this is a unique signature that is unlikely

to be confused with any physical effect.

Other distributions - return-to-Z μ pair production, and W pair production - do not directly contain the detector frame μ angle in the fitted distributions. The impact on the differential distributions is more complex and affects more bins (figs. 7.11a, 7.11c and 7.11d). Return-to-Z μ pair production sees the strongest impact due to the strong forward (or backward) boost of the di-muon system.

For all processes, more complicated acceptances models will lead to an increased confusion of this systematic effect with physical effects. This can increase the correlations in the corresponding fits.

7.4.3. Implementation challenges in muon pair production

μ pair production exhibits challenges in the direct implementation of the μ acceptance as a fit object. Each of the two mass ranges comes with its own challenge, and both affect the center shift parameter.

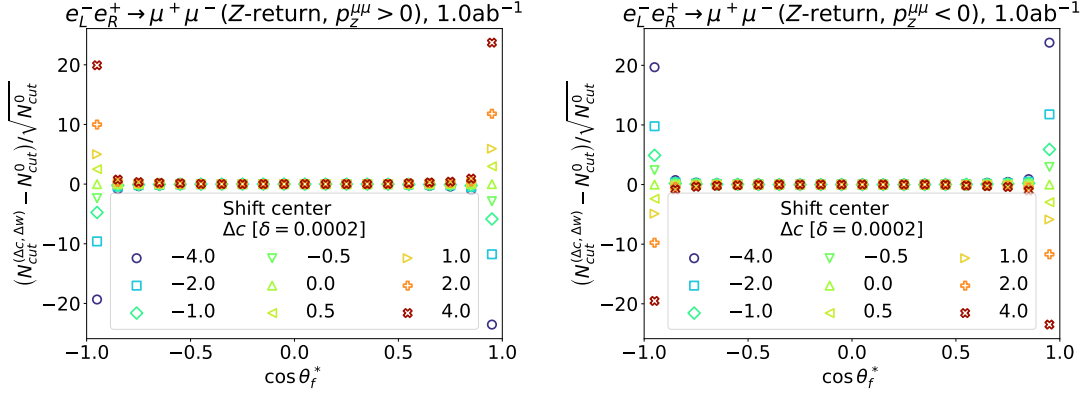
For return-to-Z events, the asymmetric behaviour of forward- and backward-boosted events causes a problem. If the center moves to one side, more events on that side will be within the acceptance, while accordingly more events on the other side are outside the acceptance (compare left and right plot in fig. 7.12a). The differential distribution of $\cos \theta_\mu^*$ is boosted out of the detector frame and into the di-muon frame, making it insensitive to the direction of the di-muon system. Acceptance changes from a shift of the center parameter cancel out on the $\cos \theta_\mu^*$ distribution between forward- and backward-events.

The challenge in high- $\sqrt{s^*}$ events has a different cause. Such events have back-to-back μ 's in the detector rest frame. A successful event reconstruction requires both of these μ 's to be inside the acceptance. Shifts of the center parameter to either side lead to a decreased acceptance on the other side. Any shifts of the center parameter decreases the number of accepted events (fig. 7.12b). High- $\sqrt{s^*}$ events are therefore insensitive to the sign of these shifts, which causes a failure in the covariance matrix estimation.

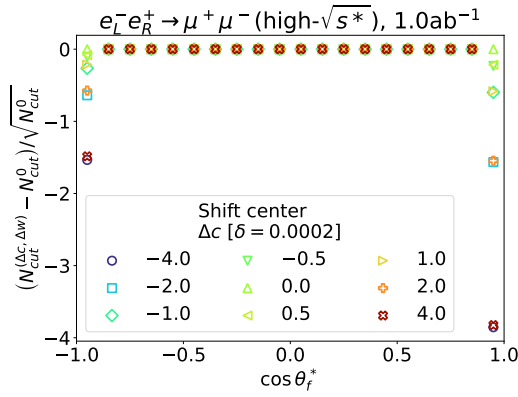
The problem in the return-to-Z events only appears when the fitted distribution does not distinguish forward-produced and backward-produced events. Fits here avoid this by splitting return-to-Z events into the two respective distributions of forward and backward events. The physical parameters of those two split categories remain identical, only systematic effects can affect them in different ways.

In contrast, the sign ambiguity in high- $\sqrt{s^*}$ events is inherent to the back-to-back production in each event. A simple splitting of events can not resolve this issue. Fits here do not attempt to resolve this issue, and instead only use high- $\sqrt{s^*}$ distributions in combination with return-to-Z distributions.

7. Impact of beam polarisation on electroweak fits



(a)



(b)

Figure 7.12.: Changes in the center parameter of the μ acceptance lead to changes of the number of events in each bin, divided here by the statistical uncertainty in the bin to yield the significance, and shown here for (a) the return-to-Z events and (b) the high- $\sqrt{s^*}$ events of μ pair production. The return-to-Z events observe exactly asymmetric-behaviour between forward- and backward-boosted events (compare same markers in left and right of (a)), canceling each other out when not separated. High- $\sqrt{s^*}$ events are insensitive to the sign of the change (compare opposite sign markers in (b)).

7.4.4. Fit-Parametrisation of the muon acceptance

An implementation of the model in the fit requires a fast and simple parametrisation of the impact that the model parameters have on the distribution.

Taking the same general approach as the TGC parametrisation (eq. (7.14)), a bin-dependent second order polynomial in the model parameters Δc and Δw parametrises the acceptance.

$$\frac{d\sigma_{\text{bin}}}{\sigma_{\text{bin}}}(\Delta c, \Delta w) = A_0 + A_c \cdot \Delta c + A_w \cdot \Delta w + A_{c2} \cdot (\Delta c)^2 + A_{w2} \cdot (\Delta w)^2 + A_{cw} \cdot \Delta c \Delta w \quad (7.20)$$

The fit framework applies this polynomial as factor to each bin of the chiral distributions with the corresponding bin-dependent coefficients A . It further ensures reasonable behaviour by restricting the values of that factor to the range between 0 and 1.

In each bin, the polynomial needs to represent the effect of the cut of the MC events. The coefficients are the elements that connect the behaviour of this effect of MC events with the behaviour in the fit. A two-step process determines these coefficients. The first step applies the acceptance model on the MC events with varying values of the model parameters $(\Delta c, \Delta w)$. Each of the tested points leads to a corresponding cross-section value in each bin. The second step fits the coefficients to these points. A selection of eight such tested points with a common scale $\delta = 2 \cdot 10^{-4}$ gives an initial guess of the coefficients by solving the corresponding eight linear equations. Thereafter, a fit to a larger set of points $\{(\Delta c, \Delta w) | \Delta c, \Delta w \in \{-4, -2, -1, -0.5, 0, 0.5, 1, 2, 4\} * \delta\}$ accurately determines the coefficients for each bin. All coefficient-fits yield reasonable χ^2 values within the statistical uncertainty of the MC events.

7.4.5. Validating the parametrisation

There is no inherent guarantee that a second order polynomial is a good approximation of the changes in μ acceptance in a given bin. An application of this technique in the fit requires a validation that the polynomial is a good approximation - i.e. that it differs only negligibly from varying the cut on MC events.

The validation here defines two parameters to assess the relevance of potential mis-modeling. One is the χ^2 of the actual deviation that the parameter shift introduces over all bins.

$$\chi_{\text{shift}}^2 = \sum_{\text{bins}} \left(\frac{N_{\text{cut}}^{(\Delta c, \Delta w)} - N_{\text{cut}}^0}{\sqrt{N_{\text{cut}}^0}} \right)^2 \quad (7.21)$$

Here, $N_{\text{cut}}^{(\Delta c, \Delta w)}$ is the number of Monte-Carlo events after a cut with shifted edges, and N_{cut}^0 the corresponding number of events with the fixed 7° cut. The other validation parameter is the χ^2 of how wrong the parametrisation gets that deviation (in other words,

7. Impact of beam polarisation on electroweak fits

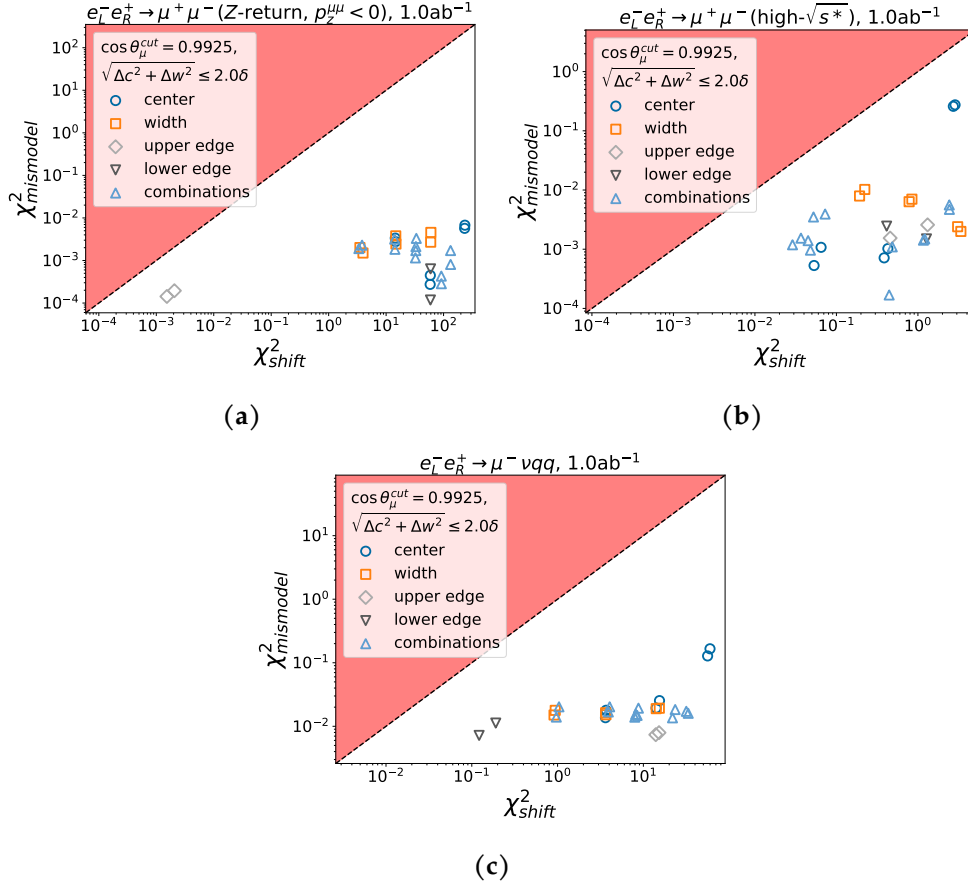


Figure 7.13.: χ^2 tests for (a,b) μ pair production and (c) semileptonic W pair production show that the potential mismodeling by the polynomial parametrisation ($\chi^2_{mismodel}$, eq. (7.22)) of the muon acceptance is negligible compared to the actual impact of changing the acceptance parameters (χ^2_{shift} , eq. (7.21)). Points in or close to the red shaded area signal a mismodeling that is significant compared to the actual impact of the parameter shift on MC events. The appendix contains the full set of plots for all initial states and processes (figs. C.6 to C.8).

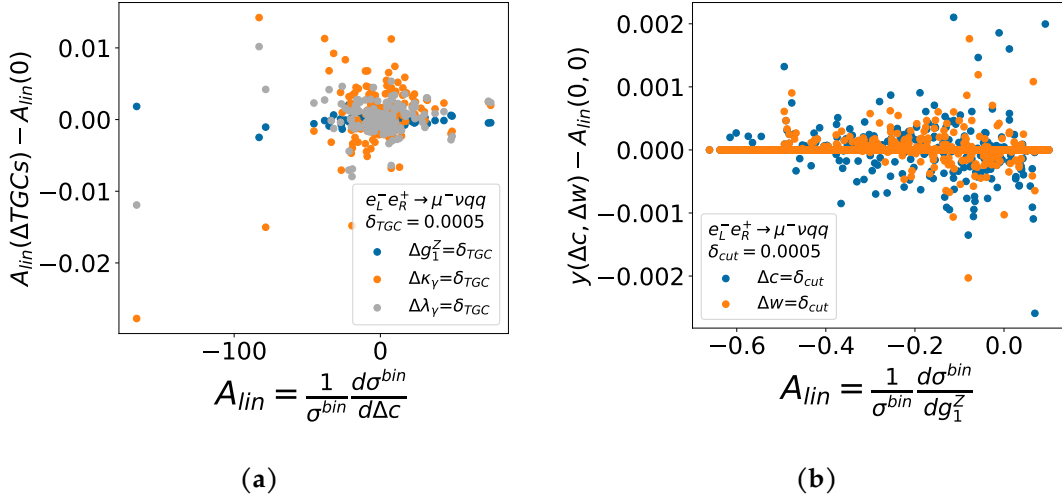


Figure 7.14.: The linear coefficient (y) of the μ acceptance polynomial shows only minimal changes for non-SM TGC values (a), and the linear coefficient of the TGC polynomial shows only minimal changes for varied values of the μ acceptance (b). This confirms that these two effects are largely independent, and that a factorisation is valid.

χ^2 of the artificial bias due to parametrisation), again over all bins.

$$\chi_{mismodel}^2 = \sum_{\text{bins}} \left(\frac{N_{par}^{(\Delta c, \Delta w)} - N_{cut}^{(\Delta c, \Delta w)}}{\sqrt{N_{cut}^{(\Delta c, \Delta w)}}} \right)^2 \quad (7.22)$$

Here, $N_{par}^{(\Delta c, \Delta w)}$ is the number of events that the polynomial parametrisation predicts for a given cut. The parametrisation is valid if the χ^2 of artificial bias $\chi_{mismodel}^2$ is small compared to χ^2 of actual deviation χ_{shift}^2 . Tests of many $(\Delta c, \Delta w)$ points show that the polynomial approach leads to negligible $\chi_{mismodel}^2$ (fig. 7.13). This validates that the fit bin-dependent polynomial is an accurate representation of the μ acceptance model.

7.4.6. Validating the physics-systematics factorisation

The high-statistics very forward region of W pair production shows a strong sensitivity to the TGCs (fig. 7.7). This is also where the μ acceptance takes the strongest effect. The current approach for the μ acceptance implicitly assumes that a change in this acceptance does not significantly change the dependence on the physics for each bin of the differential distribution, and vice versa. Such an assumption of a factorisation of these two effects requires some validation.

A factorisation is valid if the coefficients of the two corresponding polynomials are independent of the parameter values of the respective other effect. Tests of the linear

7. Impact of beam polarisation on electroweak fits

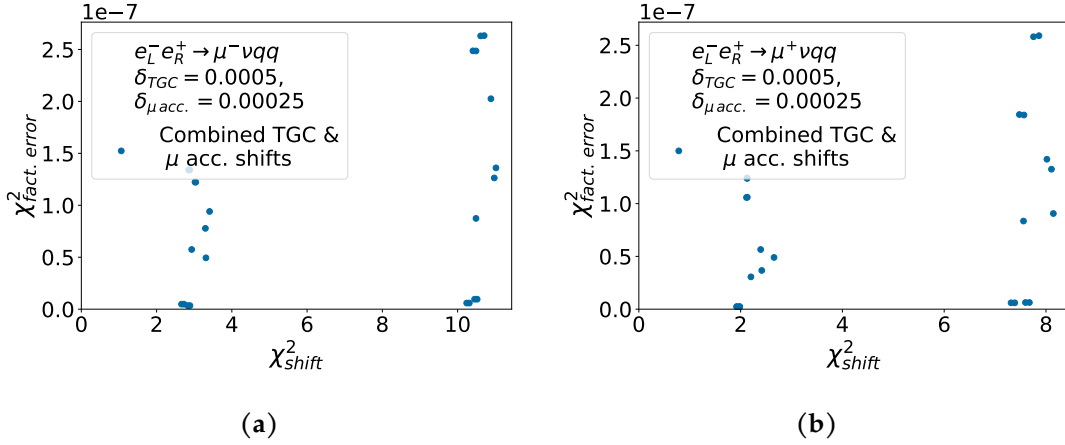


Figure 7.15.: A comparison of the significance of the bias due to factorisation of TGC and μ acceptance ($\chi_{fact.error}^2$, eq. (7.25)) with the significance of the combined shift in both effects (χ_{shift}^2 , eq. (7.24)) shows that the assumption of factorisation causes only negligible biases. Only $e_L^- e_R^+$ is important in this context, since $e_R^- e_L^+$ does not have significant very-forward statistics. ((a): μ^- in the final state, (b): μ^+)

coefficients $A_{lin,x}$ for each parameter x in each given bin

$$A_{lin,x} = \frac{1}{\sigma^{bin}} \frac{d\sigma^{bin}}{dx} \quad (7.23)$$

show that these coefficients change only slightly when the parameter values of the respective other effect vary (fig. 7.14). When one effect deviates, it introduces changes in the linear coefficients of the other effect. The impact on the linear coefficients is small compared to the typical scale of the coefficients, in all cases at or below the percent level.

This can impact the fits when both effects vary at the same time. Similar to the mis-modeling tests (eqs. (7.21) and (7.22)), appropriately designed χ^2 's can quantify the significance of this issue. The first of these χ^2 's assesses the significance of the parameter shift itself over all bins by applying the μ acceptance cut and the TGC weighting directly on the MC events to gain the number of events $N_{not\ factorized}$.

$$\chi_{shift}^2 = \sum_{bins} \left(\frac{N_{not\ factorized}(\Delta c, \Delta w, \Delta g_1^Z, \Delta \kappa_\gamma, \Delta \lambda_\gamma) - N_{not\ factorized}(0)}{\sqrt{N_{not\ factorized}(0)}} \right)^2 \quad (7.24)$$

A second χ^2 quantifies the significance of the bias due to factorisation over all bins by comparing the unfactorised number of events $N_{not\ factorized}$ in the bins to the event num-

Table 7.5.: Simple tests that fit only the μ acceptance on unpolarised distributions ($L = 2 \text{ ab}^{-1}$) show a high precision in the two parameters and negligible correlations.

	$\Delta c [10^{-5}]$	$\Delta w [10^{-5}]$	$\text{cor}(c, w)$
$e^+e^- \rightarrow \mu\mu$			
- return-to-Z	2.1	4.0	$< 10^{-2}$ (abs.)
- return-to-Z and high- $\sqrt{s^*}$	2.1	3.9	$< 10^{-2}$ (abs.)
$e^+e^- \rightarrow \mu^\pm \nu q q$ (charge-separated)	5.4	10.7	$-4 \cdot 10^{-2}$

bers $N_{factorized}$ from the factorized polynomials.

$$\chi_{fact.error}^2 = \sum_{bins} \left(\frac{N_{factorized}(\Delta c, \Delta w, \Delta g_1^Z, \Delta \kappa_\gamma, \Delta \lambda_\gamma) - N_{notfactorized}(\Delta c, \Delta w, \Delta g_1^Z, \Delta \kappa_\gamma, \Delta \lambda_\gamma)}{\sqrt{N_{notfactorized}(\Delta c, \Delta w, \Delta g_1^Z, \Delta \kappa_\gamma, \Delta \lambda_\gamma)}} \right)^2 \quad (7.25)$$

A comparison of these two χ^2 's for many different combined shifts of the μ acceptance and the TGCs shows that the bias due from the factorisation assumption is negligible (fig. 7.15). This validates the factorised approach in this study.

Future studies may seek to avoid the necessity of such factorization checks, which become increasingly more effort with every new effect. A straightforward way that fully avoids that assumption is to fit one common highly-dimensional second order polynomial that encompasses all physical and systematic parameters. Such an approach will increase the computational time effort since the number of terms in a second order polynomial grows like $n^2 + 3n$ with the number of parameters n . This affects both the calculation of the coefficients and the application of the polynomial in the fit. At the same time, the implementation effort does not significantly increase, which makes this approach potentially feasible.

7.4.7. Simple demonstration of a fitted systematic effect

The final step of the inclusion of the μ acceptance in the fit is the implementation into the fitting framework and the test of fits on actual distributions. Since this study is testing the direct inclusion of such a systematic effect for the first time in the context of such fits, this final step serves primarily as a final validation of the approach. In addition, this step provides insight into the interplay of the two acceptance parameters on the distribution of the different processes. For this purpose, the step performs a minimal fit on unpolarised distributions with $L = 2 \text{ ab}^{-1}$ while fixing all other parameters.

The implementation of acceptance parameters into the fit works on both the μ pair production and the semileptonic W pair production events individually. The only restriction is that high- $\sqrt{s^*}$ μ pair production events cannot extract parameters in individual fits due to the symmetry issue described above (section 7.4.3).

7. Impact of beam polarisation on electroweak fits

Table 7.6.: Overview of the different fit setups and which final states and parameter sets they use. The study tests fit setups first with the individual final states (“Two-fermion” and “Four-fermion”) and with both simultaneously (“Combined”).

		Two-fermion	Four-fermion	Combined
Final states	$\mu^+\mu^-$ (return-to-Z)	x		x
	$\mu^+\mu^-$ (high- $\sqrt{s^*}$)	x		x
	$\mu\nu qq$		x	x
Parameters	Luminosity [1]*	x	x	x
[# parameters]	Polarisations [2-6]*	x	x	x
(*: w/ constraint)	μ acceptance [2]	x	x	x
	$f\bar{f}$ parameters [12]	x		x
	TGCs [3]		x	x
	WW cross-sections [2-4]		x	x

The very-forward return-to-Z μ pair production events provide the highest precision of the μ acceptance parameters (table 7.5). Adding high- $\sqrt{s^*}$ events does not improve the precision. Semileptonic W pair production yields uncertainties that are around a factor 2.5 larger than with μ pair production.

All tested scenarios yield negligible correlations between the two parameters. The fit extracts both detector edges equally well due to symmetry of W pair production and return-to-Z μ pair production events (figs. 7.9 and 7.10).

In isolation, the fit can extract the acceptance parameters with high precision and negligible correlation. The interplay of acceptance changes and other physical or systematic effects can change this picture. Addressing this question requires a combined fit with other effects.

7.5. Fits in this study

The previous sections outlined the different building blocks of the fits in this study, including the fit framework itself (section 7.1), the polarisation and luminosity scenarios (section 7.2), the differential distributions (section 7.3.1) and the physical (sections 7.3.2 to 7.3.4) and systematic (sections 7.3.5 and 7.4) effects. These building blocks assemble into different fit setups (table 7.6), which this section presents as an introduction to the results in the following sections.

A fit setup here is a set of final state distributions and fitted parameters. This study first tests two fit setups corresponding to the two final states in this study: $\mu^+\mu^-$ and $\mu\nu qq$. These individual final state fits are the basis for the study of the third fit setup, which then uses both final states at the same time. Each fit setup tests all the different collider scenarios (section 7.2). All three setups include the general systematic effects:

the luminosity, the polarisation, and the μ acceptance. The setups that include the $\mu^+\mu^-$ final state always use both the return-to-Z and the high- $\sqrt{s^*}$ distributions, and use the corresponding set of μ pair production parameters. Setups with the $\mu\nu q\bar{q}$ include the TGC and WW cross-section parameters.

A basic understanding of the fits to the individual final states is necessary to fully understand the combined fit. For this purpose, both individual fit setups investigate how beam polarisation affects the measurement of the systematic and relevant physical parameters. In the $\mu^+\mu^-$ setup (section 7.6), this includes a focus on the issue of translating an unpolarised measurement to constraints on polarised parameters. For the $\mu\nu q\bar{q}$ setup (section 7.7), the impact of beam polarisation on the polarisation measurement itself comes into a stronger focus, and special attention goes to how and why the TGC precision changes with beam polarisation. Both setups also for the first time include the μ acceptance as a parameterised detector effect, and the setups can investigate the impact of this effect on the other parameters in the different collider scenarios. Finally, the combined setup (section 7.8) tests which advantage arise from a simultaneous fit for both systematic and physical parameters. This provides a baseline and guidance for future studies to further broaden these fits, and crucially builds on the conclusions from the individual fits.

7.6. Two-fermion fits: Chiral disentangling with beam polarisation

SLD experience has shown the great impact of beam polarisation on fermion pair production measurements [2]. This makes fermion pair production a prime candidate to study the impact of beam polarisation at future e^+e^- colliders. Here, the fits use only the μ pair production channel in order to focus on μ -related experimental systematics. The fits include the $\cos\theta_\mu^*$ distributions of both the return-to-Z and the high- $\sqrt{s^*}$ datasets (sections 5.3 and 7.3.1), and extracts the fermion pair production parameters for both mass ranges (section 7.3.2) as well as the systematic effects of luminosity and polarisation (section 7.3.5) and the μ acceptance (section 7.4). Primary outputs of the fits are the uncertainties (fig. 7.16) and correlations (fig. 7.17) for the different collider scenarios (section 7.2). Besides the default setting with all parameters (bars in fig. 7.16), the fits also test scenarios that fix the parameters of one of the systematic effects (markers in fig. 7.27) to test the influence of the corresponding systematic uncertainties.

The fit results reflect the advantages of access to chiral observables with beam polarisation (section 7.6.1) and the additional effort that unpolarised colliders must make to extract chiral asymmetries (section 7.6.2), and demonstrate that unpolarised colliders need a high experimental and theoretical precision to keep up with polarised results (section 7.6.3). A comparison of the chiral asymmetry precision from the fits to those of dedicated Z-pole run studies reiterate the increased sensitivity with polarised beams, and show that studies of return-to-Z events provide significant improvements over current precisions (section 7.6.4). Finally, the conclusions on the interplay of beam polari-

7. Impact of beam polarisation on electroweak fits

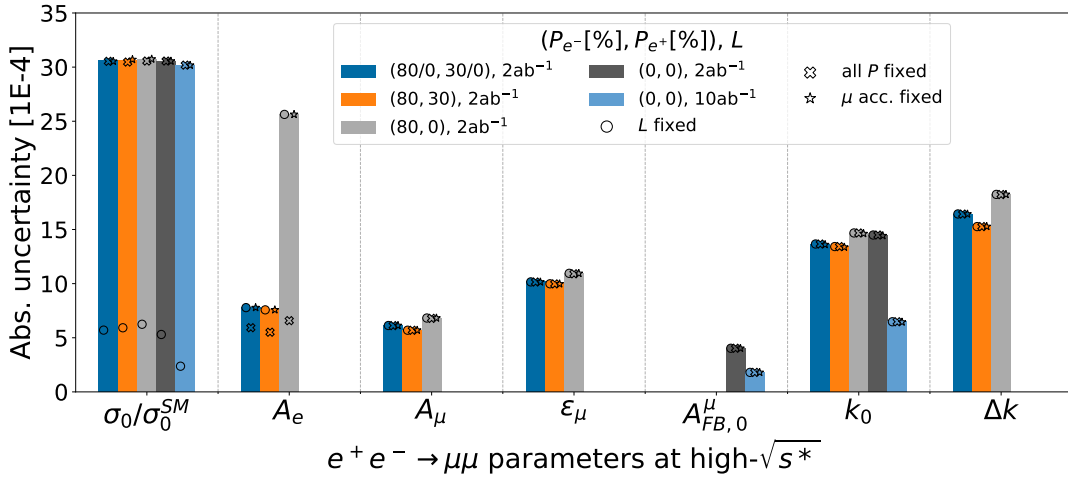
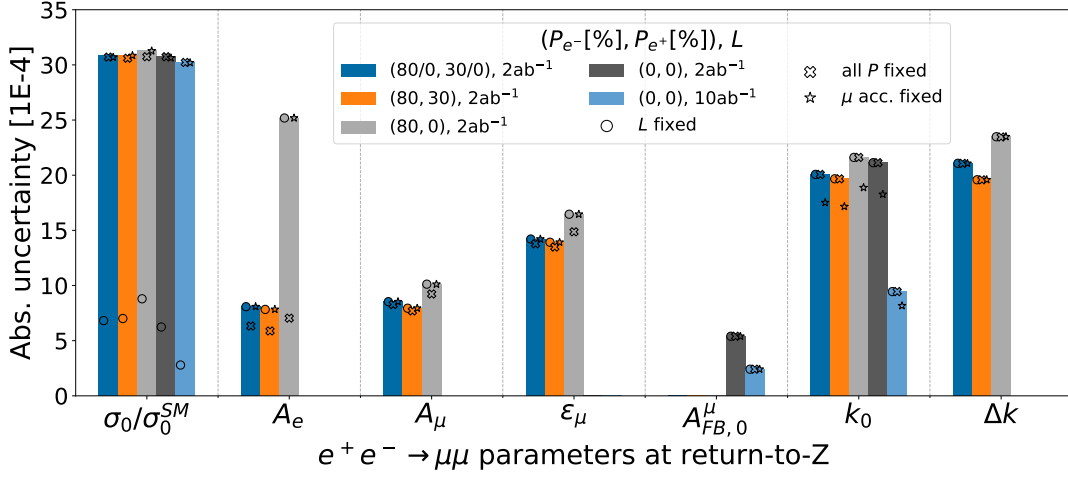
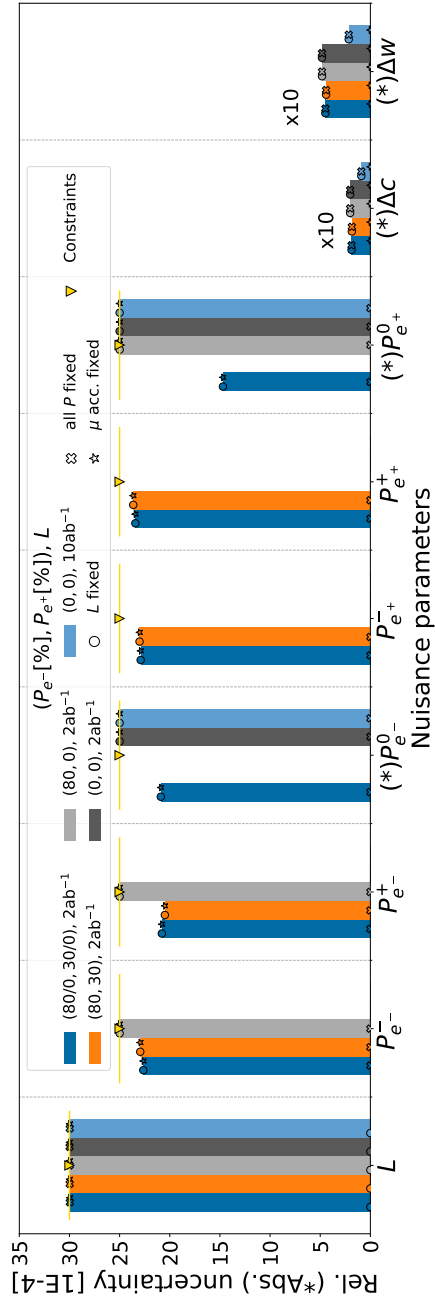


Figure 7.16: Uncertainties of two-fermion production parameter at (a) $\sqrt{s^*} \approx m_Z$ and (b) $\sqrt{s^*} \approx 250 \text{ GeV}$, and (c) systematic parameters for the fit to μ pair production in different collider scenarios (section 7.2). Uncertainties on physical parameters are absolute, those on systematic parameters are relative unless specified otherwise. Only polarised colliders can measure all physical parameters. (Tables with uncertainty numbers in appendix: tables C.2 to C.5)



(c)

Figure 7.16.: (cont.)

7. Impact of beam polarisation on electroweak fits

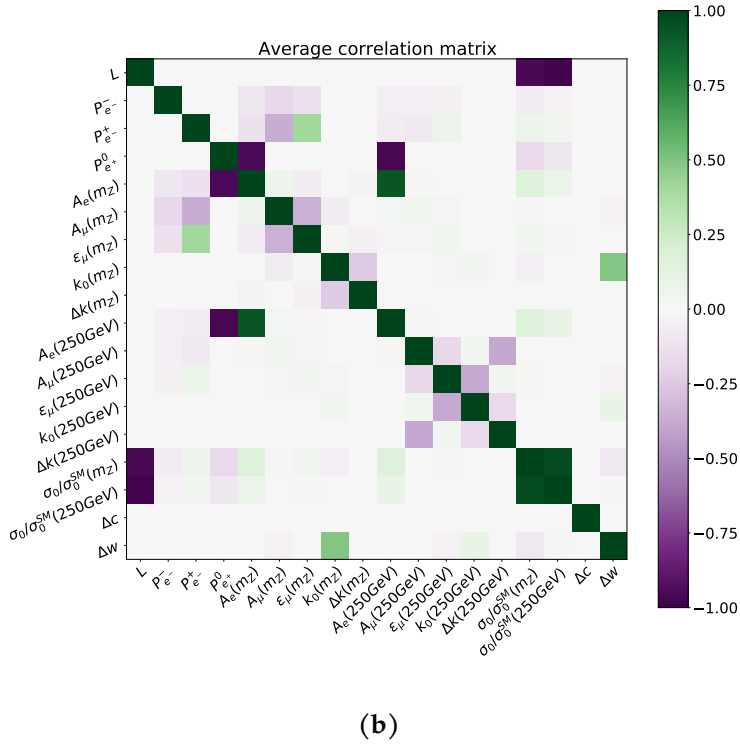
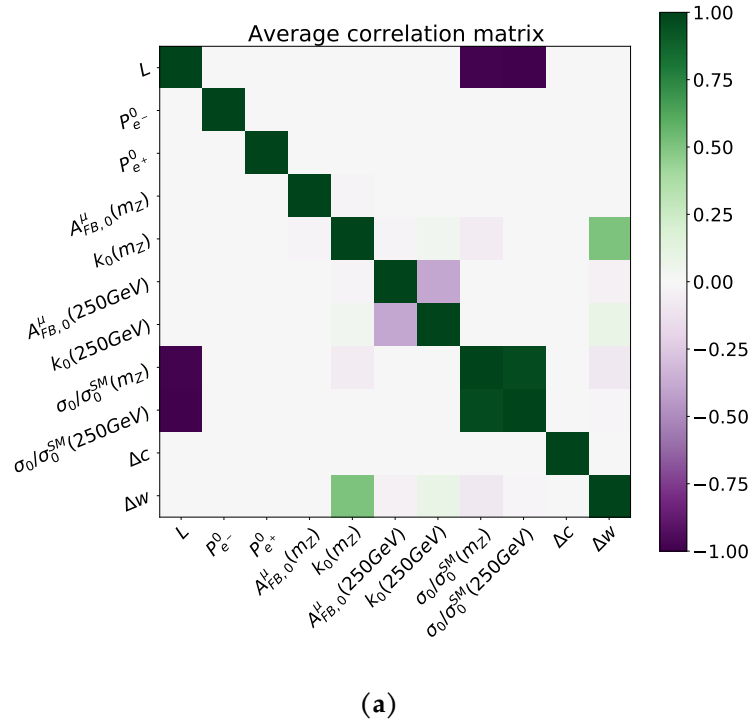
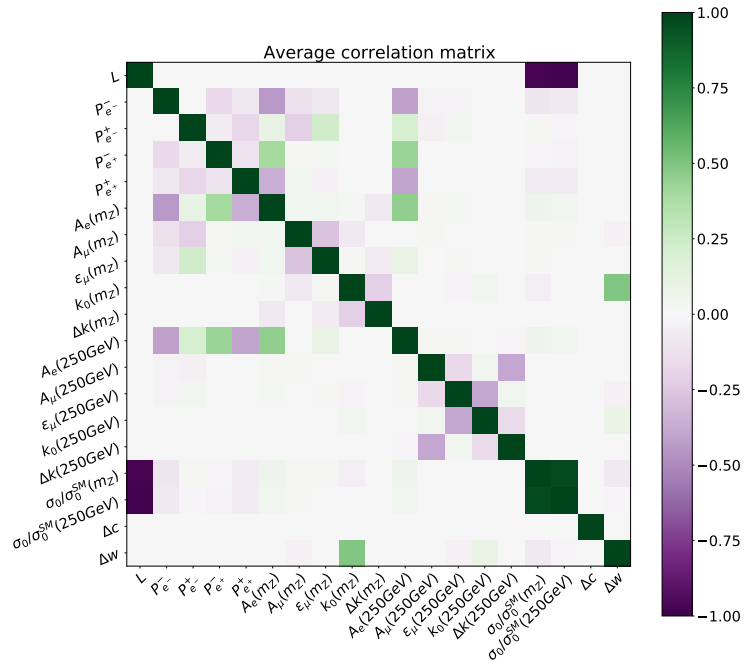
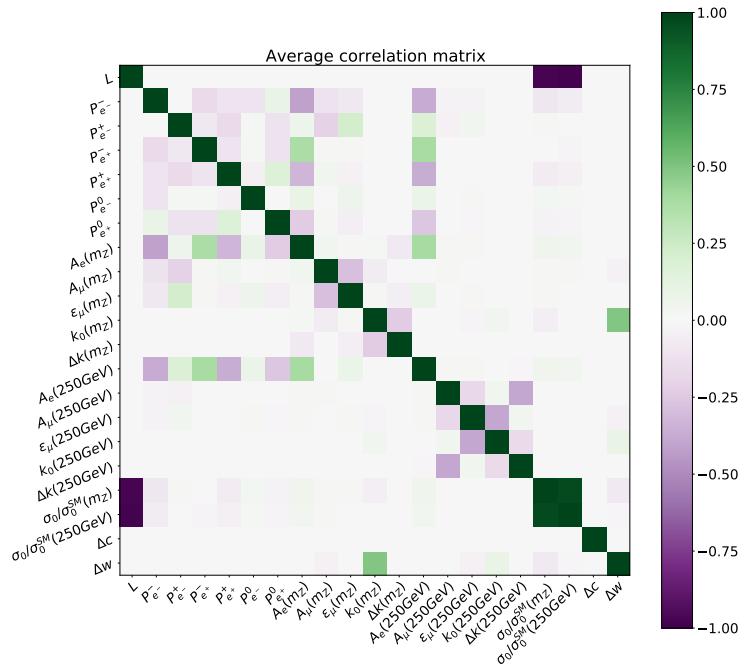


Figure 7.17.: Visualisation of the correlation matrices of the (a) (0,0), (b) (80,0), (c) (80,30), and (d) (80/0,30/0) default scenarios (section 7.2) with $L = 2 \text{ ab}^{-1}$ for the fit to μ pair production. Significant correlations of physical effects with systematic ones happen through the electron asymmetry, total cross-sections and the unpolarised correction parameter k_0 . (Duplicates with numbers in appendix: fig. C.9)

7.6. Two-fermion fits: Chiral disentangling with beam polarisation



(c)



(d)

Figure 7.17.: (cont.)

sation and experimental systematics turn out rather weak due to the only small impact of the μ acceptance on the parameter precisions (section 7.6.5).

7.6.1. Access to chiral information with beam polarisation

Colliders with longitudinally polarised beams can get direct access to the chiral behaviour of collisions taking data with reversed polarisation directions. The exact consequences of polarizing one or both beams depend on the physical process in question. Here, uncertainties and correlations for the different scenarios show the benefits of polarised beams in the μ pair production channel (bars in fig. 7.16, and fig. 7.17).

A collider without beam polarisation can only access unpolarised observables (section 7.3.2). Precisions on these observables are in the range of 10^{-4} to 10^{-3} ((0,0) scenarios in figs. 7.16a and 7.16b). The luminosity uncertainty fully determines the unpolarised cross-section precision (circles compared to bars in figs. 7.16a and 7.16b). Constraints of chiral parameters will require additional assumptions (eq. (7.12) and section 7.6.2). An increased luminosity only increases the precision on the two unpolarised shape parameters and does not facilitate access to the chiral structure of the interaction.

Electron polarisation enables access to all chiral parameters. A collider with one polarised beam can set constraints on all chiral parameters with an uncertainty in the range of 10^{-3} ((80,0) scenario in figs. 7.16a and 7.16b). The luminosity uncertainty still limits the precision on the unpolarised cross-section, as both have identical effects on a given process. This single beam polarisation scenario sees a remaining ambiguity of the electron asymmetry A_e and polarisations (A_e - $\mathcal{D}_{e^+}^0$ correlation in fig. 7.17b). As a consequence, the polarimeter precision determines A_e precision (crosses compared to bars in figs. 7.16a and 7.16b) and polarisation biases directly translate to A_e biases. A measurement of the polarisation in other final states like W pair production is necessary to increase the polarisation precision and help detect biases. This is only possible for runs above the W production threshold, e.g. at 250 GeV. Due to that same ambiguity, collision data from μ pair production in this scenario does not set constraints on polarisations beyond the polarimeter precision ((80,0) scenario in fig. 7.16c).

An additional non-zero positron polarisation removes the ambiguity with A_e ((80,30) scenario in figs. 7.16a and 7.16b, and fig. 7.17c). All chiral parameters benefit from the polarisation of the second beam, beyond the increase in statistics (see section 7.2.2). Each beam polarisation affects multiple datasets, which allows the collision data to constrain all beam polarisations ((80,30) scenario in fig. 7.16c).

Such a scenario with both beams polarised can include also unpolarised beam settings ((80/0,30/0) scenario in fig. 7.16). The polarisation precision remains stable in that case despite each of the individual beam polarisations having now a smaller share of the luminosity. Collision data can even constrain the polarisation of the unpolarised beam settings, which is not possible in any other tested scenario with unpolarised beam settings (fig. 7.16c). Of the physical observables, only the correction parameter Δk shows a small negative impact beyond lower event numbers.

7.6. Two-fermion fits: Chiral disentangling with beam polarisation

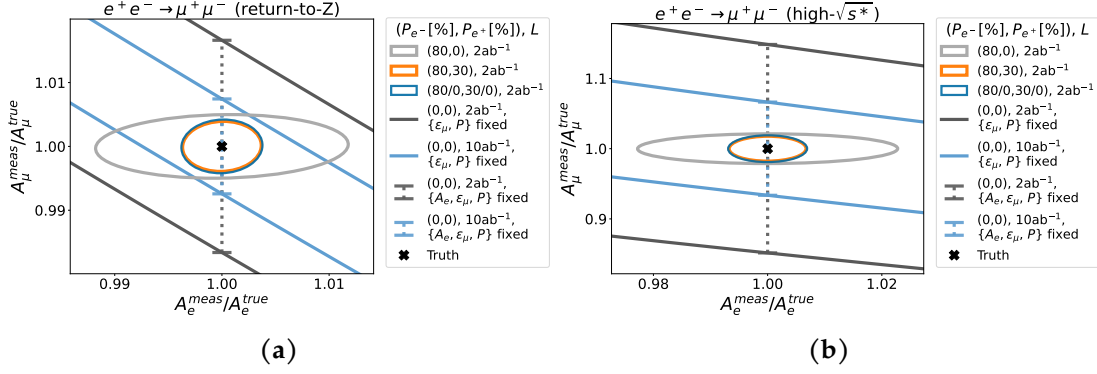


Figure 7.18.: Comparisons of relative $\{A_e, A_\mu\}$ limits from (a) return-to-Z events and (b) high- $\sqrt{s^*}$ events for different collider scenarios demonstrate the benefit of access to chiral observables with beam polarisation. Unpolarised scenarios use A_{FB} and need to make assumptions on a subset of parameters to set limits.

The discussion above shows how each added polarisation setting benefits the collider. Measurements with electron beam polarisation have direct chiral access and do not rely on assumptions for the underlying chiral parameters. Positron polarisation further removes ambiguities and reduces correlations, allowing also a measurement of the polarisations in collision data. The effort of polarizing the beams shows clear advantages for this process.

7.6.2. Translating unpolarised measurements to chiral parameters

The asymmetry parameters A_e and A_μ of μ pair production are sensitive to the effective Weinberg angle (eq. (2.45)). Constraints in the $\{A_e, A_\mu\}$ plane are a precision tests of the SM predictions, and deviations can hint at new BSM physics.

Polarised colliders directly constrain all directions in this plane. The scenario with two polarised beams again shows the significant advantage that A_e decouples from the polarisations ((80, 30) and (80/0, 30/0) in fig. 7.18), whereas for a collider with only one polarised beam the polarimeter precision dictates the A_e uncertainty ((80, 0) in fig. 7.18). A comparison with the unpolarised scenarios ((0, 0) in fig. 7.18) is not straightforward because the unpolarised case is not directly sensitive to the individual A_e and A_μ .

An unpolarised collider constrains only a direction in this plane with the use of the unpolarised asymmetry A_{FB} . The definition of A_{FB}^μ defines this $\{A_e, A_\mu\}$ direction (section 7.3.2).

$$A_{FB}^\mu = \frac{3}{8} (\epsilon_\mu + 2A_e A_\mu) \quad (7.26)$$

This simplified equation assumes that the polarisations are exactly zero. The influence of polarisation uncertainties is explored separately below (section 7.6.3). The comparisons here further assumes precise knowledge of the Z/γ -interference parameter ϵ_μ in

7. Impact of beam polarisation on electroweak fits

the unpolarised case. In practice this means assuming that ϵ_μ takes its SM value and the theory can calculate that value precisely. As seen later on (section 7.6.3 and fig. 7.19), the required knowledge of ϵ_μ must be on the level of 10^{-4} . An unpolarised collider can still use τ polarisation to measure A_e [2]. To take this into account, the comparisons also consider an optimistic case for the unpolarised scenarios that assumes perfect A_e knowledge (dashed line (0,0) in fig. 7.18), in addition to the unpolarised scenarios without any additional A_e knowledge (full line (0,0) in fig. 7.18). The comparison assumes that the τ polarisation technique is also applicable in return-to-Z events.

The constraining power of the unpolarised observable A_{FB}^μ depends on values of A_e and A_μ . A polarised collider has a sensitivity that is roughly \mathcal{D}_{eff}/A_e higher than the sensitivity for the unpolarised collider from A_{FB}^μ alone [161]. This formula yields (for $\mathcal{D}_{eff} \approx 0.89$) a factor of roughly 4 for return-to-Z events and roughly 8 for high-energy events. For return-to-Z events, a luminosity increase of a factor 5 can bring the uncertainty of the unpolarised collider to a comparable level with the polarised scenarios. The small value of A_e at high energies means that there is only a very low A_μ -sensitivity from A_{FB}^μ . Even the most optimistic case for an unpolarised collider (e.g. A_e perfectly known from τ polarisation) remains significantly worse than the polarised measurement. An unpolarised collider with 10 ab^{-1} can only set limits which are three times worse than any polarised collider. This is particularly troubling since the main target of high-energy collisions are these high energy events. An inclusion of other relevant systematic effects can influence this comparison, and will need further studies in the future.

Overall, the unpolarised measurement shows two disadvantages compared to a polarised one. First, the translation of A_{FB}^μ to the chiral parameters $\{A_e, A_\mu, \epsilon_\mu\}$ is ambiguous and requires additional input. And second, even under the assumption of perfect knowledge of A_e and ϵ_μ , that same translation degrades the sensitivity to A_μ . Both of these observations will hold true for other (non- e) $f\bar{f}$ final states.

7.6.3. Polarisation and theory knowledge in the forward-backward asymmetry interpretation

The discussion above (section 7.6.2) focused on the role of the electron asymmetry in the interpretation of A_{FB}^μ . An interpretation of A_{FB}^μ in terms of A_μ also requires input on the exact values of the effective polarisation $\mathcal{D}_{eff} = (\mathcal{D}_{e^+} - \mathcal{D}_{e^-}) / (1 - \mathcal{D}_{e^+}\mathcal{D}_{e^-})$ and the Z/γ -interference parameter ϵ_μ (eq. (7.12)).

$$A_\mu = \left(\frac{3}{4}A_{FB}^\mu - \frac{1}{2}\epsilon_\mu \right) \frac{1 + \mathcal{D}_{eff}A_e}{\mathcal{D}_{eff} + A_e} \quad (7.27)$$

A_{FB}^μ , A_e , and \mathcal{D}_{eff} are experimental inputs in that interpretation. An unpolarised collider can not independently measure ϵ_μ , meaning that theoretical calculations must provide

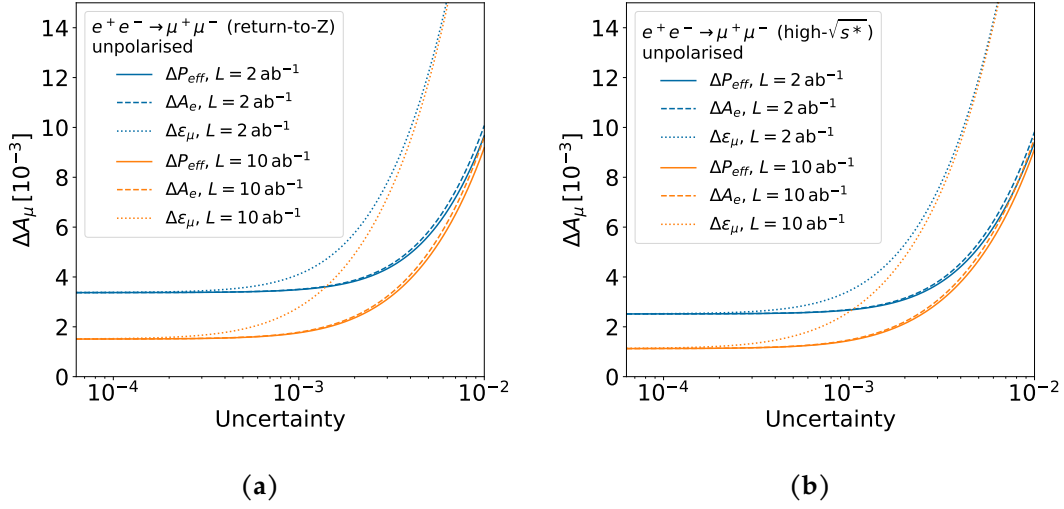


Figure 7.19: Dependence of absolute A_μ uncertainty from unpolarised A_{FB} measurements in (a) return-to- Z events and (b) high- $\sqrt{s^*}$ events on the absolute uncertainty of the polarisation, electron asymmetry and Z/γ -interference term. An undisturbed A_μ measurement requires better than 10^{-3} precision on A_e and the effective polarisation \mathcal{P}_{eff} and 10^{-4} precision on ϵ_μ .

ϵ_μ . Those four quantities determine the uncertainty on A_μ .

$$\Delta A_\mu = \frac{1}{A_e} \sqrt{\left(\frac{3}{4} \Delta A_{FB}^\mu\right)^2 + \left(\frac{1}{2} \Delta \epsilon_\mu\right)^2 + \left(A_\mu (1 - A_e^2) \Delta \mathcal{P}_{\text{eff}}\right)^2 + \left(A_\mu \Delta A_e\right)^2} \quad (7.28)$$

Precision in the effective polarisation has roughly the same importance as precise A_e input (fig. 7.19). An unpolarised collider can not measure the polarisation values from collision events and relies on polarimetry to confirm that the longitudinal polarisation is vanishing. This was the case at LEP, where the longitudinal polarisation was measured with sufficient precision to not influence the interpretation of A_{FB}^μ (section 7.2.1). An undisturbed interpretation of A_{FB}^μ in terms of A_μ requires a knowledge of \mathcal{P}_{eff} at same level as the expected A_μ precision. Future unpolarised measurements will likely require a polarimeter precision at or below the 10^{-3} level. A precision of this level is challenging if it only relies on polarimeters, which will deliver a precision at or above 10^{-3} [237].

The precision requirement on ϵ_μ is significantly stronger than that on A_e and \mathcal{P}_{eff} . In order to avoid a significant impact on the A_μ uncertainty, theoretical calculations must achieve a precision on ϵ_μ at the few 10^{-4} level.

Both the required polarimeter precision and the theoretical precision are challenges for this measurement at an unpolarised collider, and need careful consideration in detailed studies.

7. Impact of beam polarisation on electroweak fits

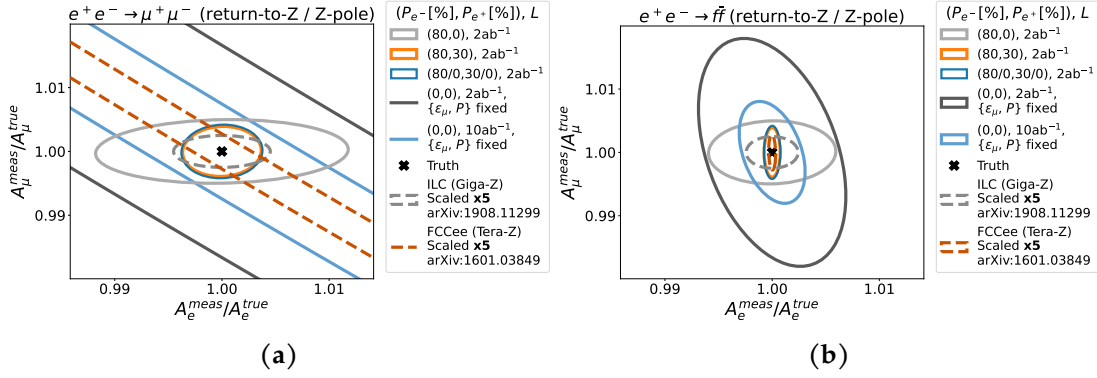


Figure 7.20.: Comparison of relative $\{A_e, A_\mu\}$ limits from return-to-Z events from different collider scenarios (same as fig. 7.18a), and from external predictions from full Z-pole runs of future colliders [88, 122], either (a) from $e^+e^- \rightarrow \mu^+\mu^-$ alone or (b) including all fermion pair production measurements. Z-pole run uncertainties are scaled up for visibility, and show roughly an order-of-magnitude improvement over return-to-Z results.

Table 7.7.: A straightforward difference of collider scenarios is the number of observed events. Shown here are estimated numbers of $e^+e^- \rightarrow \mu^+\mu^-$ events with $Q^2 \approx m_Z$ in fits from this study, from SLD [159] and LEP1 [233], and for different future collider runs [88, 122]. The fit results (“Fit”) use $L = 2 \text{ ab}^{-1}$, “ e^+ & e^- polarised” refers to a polarisation of $(\mathcal{P}_{e^-}, \mathcal{P}_{e^+}) = (80\%, 30\%)$.

	SLD	LEP1	Fit 250 GeV e^+ & e^- polarised	Fit 250 GeV unpolarised	ILC Giga-Z	FCC-ee Tera-Z
$\mu^+\mu^-$ ($Q^2 \approx m_Z$) events	$2.2 \cdot 10^4$	$5.7 \cdot 10^5$	$3.9 \cdot 10^6$	$3.3 \cdot 10^6$	$1.6 \cdot 10^8$	$1.5 \cdot 10^{11}$

7.6.4. Comparison to dedicated Z-pole runs

Both linear and circular future e^+e^- collider concepts provide options to perform dedicated Z-pole runs [88, 122]. At the same time, return-to-Z events are an opportunity to measure the Z-pole couplings without the need to run directly on the Z-pole. The question arises how the precisions from return-to-Z events compare to dedicated Z-pole runs of past and future e^+e^- colliders. Here it becomes important that the A_e measurement relies mainly on other fermion pair production measurements, which are not a direct part of the fit. Comparisons therefore will focus on A_μ , and estimate the impact of other including other final states on the A_μ uncertainty.

The results in the paragraphs below show that a measurement with return-to-Z events increases the A_μ precision by an order of magnitude, and that dedicated Z-pole runs of future e^+e^- colliders add another order of magnitude. They reiterate that access to both A_e and A_μ is significantly easier with polarised beams, reducing the luminosity needs. Meanwhile, the reduced dataset of an unpolarised collider will require more

assumptions in the interpretation of the measurement.

Impact of other $f\bar{f}$ final states

Past and future e^+e^- collider studies have also included other $f\bar{f}$ final states in measurement of A_e . A comparison with such studies needs an estimation of the impact of these additional final states.

The addition of other $f\bar{f}$ final states impacts the A_e precision in two ways. First, it increases the available statistics for the direct A_e measurement at polarised colliders. And second, it adds the independent measurement of A_e through τ polarisation. The expected A_e precision from τ polarisation is not an explicit part of this study. An extrapolation of the relative A_e uncertainty from LEP to increased numbers of $\tau\tau$ events serves a simple estimate here. The LEP measurement was statistically limited, and no systematics enter that extrapolation [233].

Additional visible Z decays for a polarised A_e measurement only translates to increased precision if the statistical uncertainty is dominant. The fits show that this is only the case in the scenario with two polarised beams. In that case it is justified to scale the A_e precision from the $\mu^+\mu^-$ measurement, because the polarisation precision will also increase with the increased number of events. The scaling results in a relative A_e uncertainty of approximately 0.08% which agrees with dedicated ILC studies on return-to- Z events [238].

Due to the Z decay branching ratios, an A_e measurement from τ polarisation has a factor $\Gamma_{Z\rightarrow\mu\mu}/\Gamma_{Z\rightarrow\text{visible}} = 3.4\%/80\%$ fewer statistics than a polarised measurement of A_e in all visible final states. LEP achieved an absolute (relative) A_e precision of 0.49% (3.3%) with $5.7 \cdot 10^5$ $\tau\tau$ events, corresponding to $1.4 \cdot 10^7$ visible Z decays [233]. SLD, with only $5.3 \cdot 10^5$ visible Z decays and a polarised electron beam, achieved an absolute (relative) precision of 0.21% (1.4%) [233]. When correcting for the different luminosity, the uncertainty of the A_e measurement from τ polarisation is a factor 12 higher than the uncertainty from the measurement with beam polarisation. An A_e measurement from τ polarisation therefore only contributes significantly to the overall A_e precision if both beams are unpolarised or if the beam polarisation uncertainty on A_e is an order of magnitude larger than the statistical uncertainty. All scenarios considered in this comparison - independent of polarisation - include the estimated independent A_e measurement from τ polarisation.

The fitted scenarios on return-to- Z events also include this measurement, and also for this range it is the only A_e measurement for unpolarised scenarios. This inherently assumes that the τ polarisation measurement remains undisturbed by a strong forward-boost of τ pair. Future studies will be necessary to further investigate this assumption.

The fits observe that the A_e precision in the scenario with only electron polarisation is limited by beam polarisation measurement (section 7.6.1). In that case, the τ polarisation measurement becomes the leading determinant of A_e in a measurement of all $f\bar{f}$ final states (compare (80,0) in fig. 7.20a and fig. 7.20b). The absolute A_e uncertainty

7. Impact of beam polarisation on electroweak fits

from τ polarisation in that case is $1.5 \cdot 10^{-3}$ compared to the polarimeter-limited uncertainty of $2.5 \cdot 10^{-3}$ from the measurement in collision data. Realistically, additional four-fermion final states increase the polarisation precision at high energies, potentially decreasing the importance of the τ polarisation measurement again. Future studies can include the τ polarisation measurement directly in the fit, especially if at least one beam is unpolarised.

Expected A_μ uncertainty from basic principles

A comparison of the A_μ precision from other studies of past and future colliders requires an understanding of the expected precision differences between the different colliders and studies.

Two factors primarily drive the differences in A_μ precision of e^+e^- colliders: the available number of events and the sensitivity of the available observables. Future facilities expect an orders-of-magnitude increase in the available statistics wrt. previous large scale e^+e^- colliders (table 7.7). An e^+e^- collider with longitudinally polarised beams additionally gains direct sensitivity to A_μ through the left-right forward-backward asymmetry [161]. The expected uncertainty of A_μ is anti-proportional to these two factors.

$$\frac{1}{\Delta A_\mu} \propto \sqrt{N_{\mu^+\mu^-}} \cdot \begin{cases} \mathcal{P}_{\text{eff}} = \frac{|\mathcal{P}_{e^+}| + |\mathcal{P}_{e^-}|}{1 + |\mathcal{P}_{e^+}| + |\mathcal{P}_{e^-}|} & \text{if any beam polarised} \\ A_e & \text{if both beams unpolarised} \end{cases} \quad (7.29)$$

The effective polarisation \mathcal{P}_{eff} is approximately 0.89 and 0.75 for polarisations of $(\mathcal{P}_{e^-}, \mathcal{P}_{e^+}) = (80\%, 30\%)$ and $(75\%, 0\%)$, respectively, and the electron-asymmetry value A_e is 0.2136 in the return-to-Z MC dataset and 0.1515 ± 0.0019 from SLD and LEP [2]. While the difference in \mathcal{P}_{eff} is a physically real difference, the different A_e values are an artifact of the $m_{\mu\mu}$ -integration over the Z peak (section 5.3).

The values of the μ pair production parameters also determine how sensitive an unpolarised dataset is to A_{FB}^μ , and subsequently to A_μ . This expresses itself first in the sensitivity of the data to the forward-backward asymmetry.

$$A_{FB} = \frac{N_F - N_B}{N_F + N_B} \quad (7.30)$$

$$\Rightarrow \Delta A_{FB} = \frac{1}{\sqrt{N_F + N_B}} \frac{2\sqrt{N_F N_B}}{N_F + N_B} \quad (7.31)$$

$$\Rightarrow \frac{\Delta A_{FB}}{A_{FB}} = \frac{1}{\sqrt{N_{\text{total}}}} \frac{\sqrt{1 - A_{FB}^2}}{A_{FB}} \quad (7.32)$$

With a given forward-backward asymmetry measurement, the values of the chiral parameters A_e and A_μ also influence the interpretation of A_{FB}^μ in terms of A_μ . The estimation of the impact of the μ pair production parameters becomes simple when assuming

that the only significant uncertainty arises from A_{FB}^μ , as was the case at LEP [2].

$$\frac{\Delta A_\mu}{A_\mu} \left(\{ \Delta A_e, \Delta \epsilon_\mu, \Delta \mathcal{D}_{\text{eff}} \} \rightarrow 0 \right) \stackrel{\text{eq. (7.28)}}{=} \frac{A_{FB}^\mu}{\frac{3}{4} A_e A_\mu} \frac{\Delta A_{FB}^\mu}{A_{FB}^\mu} = \frac{1}{\sqrt{N_{\text{total}}}} \frac{\sqrt{1 - A_{FB}^{\mu 2}}}{\frac{3}{4} A_e A_\mu} \quad (7.33)$$

When comparing two unpolarised scenarios that worked on datasets with different chiral parameter values, the ratio of relative uncertainties depends on the factor $\sqrt{1 - A_{FB}^{\mu 2}} / (\frac{3}{4} A_e A_\mu)$. That factor is 30.8 for the LEP/SLD parameter values, and 58.1 for the return-to-Z dataset parameter values of this study. This decreases the A_μ uncertainties from the unpolarised fits in this study by a factor 1.89, compared to the uncertainties from LEP and the dedicated future collider Z pole run studies. From a physical point of view, the reason for the seemingly improved precision in the fits of this study is that the asymmetries of the dataset in this study are larger than those measured at LEP (table 7.4). This difference is a consequence of the $m_{\mu\mu}$ -integration of the parameters in this study (section 5.3), and leads to an increased sensitivity.

In addition to the measurement technique and the parameter values, experimental realities like the acceptance and additional systematic uncertainties impact the achievable A_μ precision.

The detector acceptance has two kinds of impact; the decreased event number and a sensitivity decrease from regions outside the acceptance. Considerations here directly build on the number of observed $\mu^+ \mu^-$ events, which already takes the event loss from events outside the acceptance into account.

The sensitivity of forward-backward asymmetries (both unpolarised and left-right) to A_μ decreases when the acceptance decreases. Both of these asymmetries correspond to ratios of the term linear in $\cos \theta$ to the $(1 - \cos^2 \theta)$ term of the differential cross-section (eq. (7.8)). The integrals of each of those terms yield the dependence of the sensitivity on the (symmetric) angular acceptance edge.

$$\frac{\Delta A_\mu (\cos \theta_{\text{cut}})}{\Delta A_\mu (1)} = \frac{3}{4} \frac{\cos^3 \theta_{\text{cut}}/3 + \cos \theta_{\text{cut}}}{\cos^2 \theta_{\text{cut}}} \quad (7.34)$$

Analyses of SLD and OPAL had μ acceptance edges of 0.9 and 0.95 in $\cos \theta$, respectively [159, 236], with future collider studies assuming similar or better acceptances. This leads to only slight sensitivity decreases of factors 0.945 and 0.974 for SLD and OPAL, respectively. The μ acceptance therefore changes the sensitivity in a negligible way when the acceptance varies between 0.9 and 1 in $\cos \theta$.

Systematic uncertainties did not play a dominant role in SLD or LEP measurements of A_μ [159, 236]. The fits also do not observe dominant systematic uncertainties on A_μ (fig. 7.16a). In contrast to those, the studies for dedicated Z pole runs of both ILC and FCC-ee predict that systematic uncertainties will dominate. The A_μ precision at an ILC GigaZ run will likely depend on the polarisation precision, which is slightly

7. Impact of beam polarisation on electroweak fits

worse than the statistical uncertainty [122]. FCC-ee predictions consider the center-of-mass energy measurement to be the dominant source of uncertainty, surpassing the statistical uncertainty by a factor 3 [88]. The fits here do not consider such center-of-mass energy uncertainties, and these uncertainties were negligible at LEP. A comparison of the uncertainties needs to keep these additional systematic effects in mind, since they will break the otherwise simple scaling laws (eqs. (7.29), (7.33) and (7.34)).

The principle drivers of the A_μ precision are the event numbers and the sensitivity advantage of polarised colliders. A second important difference is that the return-to-Z events here differ in the asymmetry parameter values from LEP/SLD values, which changes the sensitivity of the unpolarised colliders by the ratio of the $(A_e \cdot A_\mu)$ products.

A_μ uncertainties reflect expected behaviour

The theoretical behaviour of the A_μ uncertainty is well-defined, showing the advantages of increased luminosity and beam polarisation. Both past collider results and prediction for future colliders follow these trends, as will be seen below. The results underline the usefulness of polarised beams and the power of both return-to-Z and dedicated Z-pole measurements.

Previous e^+e^- collider experiments at LEP and SLD provide a first insight into behaviour of uncertainty in real experiments. SLD directly measured A_μ with a result of $A_\mu = 0.142 \pm 0.015$, corresponding to a relative precision of approximately 10.6% [233]. LEP did not measure A_μ directly and instead provided measurements of the electron asymmetry $A_e = 0.1498 \pm 0.0049$ from τ polarisation and of the μ forward-backward asymmetry $A_{FB}^\mu = 0.0169 \pm 0.0013$ [233]. These two LEP measurements transform into a precision on A_μ (eq. (7.26)), assuming exact knowledge of the Z/γ -interference parameter ϵ_μ . A cross-check of LEP and SLD results shows $\epsilon_\mu \approx 0$ within the uncertainties, justifying this assumption and confirming the negligible γ contribution on the Z-pole. With this, LEP results provide a corresponding relative uncertainty of $\Delta A_\mu \approx 7.9\%$ with negligible polarisation uncertainties [230]. The statistically limited A_{FB}^μ precision dominates that uncertainty.

The combination of a factor 26 lower event numbers at SLD and the polarisation gain (eq. (7.29)) from the polarised SLC beams lead to comparable A_μ precisions from LEP and SLD.

$$\frac{\Delta A_\mu(\text{SLD})}{\Delta A_\mu(\text{LEP})} = \sqrt{\frac{N_{\text{LEP}}}{N_{\text{SLD}}}} \frac{A_e}{\mathcal{P}_{\text{eff,SLD}}} \approx \sqrt{26} \cdot 0.152 \cdot \frac{1 + 0 \cdot 0.75}{0.75 + 0} \approx 1.03 \quad (7.35)$$

This confirms that the A_μ precision is primarily a function of the number of Z events and the effective polarisation.

A comparison of previous colliders with the fit results must also consider differences in selection efficiency and input asymmetry values. The fits yield a relative A_μ uncertainty of around 0.4% for scenarios with two polarised beams and $L = 2 \text{ ab}^{-1}$. This

marks a factor 25 increase of precision compared to SLD, which is a combination of the increased number of events and the increased polarisation of both beams. An unpolarised fit with $L = 2 \text{ ab}^{-1}$, under the same assumptions as LEP, ignoring the A_e uncertainty and using the Monte-Carlo ϵ_μ value, arrives at a 1.8% relative uncertainty on A_μ . This factor 4.4 precision increase of the unpolarised fit result wrt. LEP is around a factor 2 larger than expected from the pure increase of number of events. The factor 2 corresponds to the different values of A_e , A_μ and A_{FB}^μ between this fit and LEP, which increases the sensitivity (eq. (7.33)). Both cases demonstrate that return-to-Z events from a 250 GeV machine alone can lead to a significant improvement of the A_μ precision, up to an order of magnitude with polarised beams.

Both the FCC-ee and the ILC can perform dedicated Z-pole runs [88, 122]. An ILC “GigaZ” run will achieve a 0.05% relative A_μ precision [122]. This marks a precision increase of a factor 8 wrt. the 250 GeV polarised fit results on return-to-Z events (ILC compared to (80,30) in fig. 7.2ob), which agrees with the increased number of events. An FCC-ee “TeraZ” run is in same situation as LEP and could only measure A_μ through the combination of A_e and A_{FB}^μ measurements. Previous studies on electroweak measurements at FCC-ee predict a precision on A_{FB}^μ of approximately $9.5 \cdot 10^{-6}$, which includes considerations of systematic uncertainties [88]. Translating this in the same way as the LEP results, an FCC-ee TeraZ achieves a relative A_μ precision of around 0.05%, comparable to the ILC GigaZ (FCC-ee compared to ILC in fig. 7.2ob). The Z-pole A_μ relative precision from such a unpolarised TeraZ run is a factor 36 better than results from return-to-Z events at a high luminosity unpolarised 250 GeV collider (FCC-ee compared to (0,0) in fig. 7.2ob), or a factor 108 when systematics are negligible. The luminosity difference alone predicts a factor 213, which leaves a factor 2 difference. Again here, the different input asymmetry values cause the remaining factor 2.

Z-pole runs of both polarised linear and unpolarised high-luminosity circular colliders lead to the best precisions in this comparison. This takes into account that an unpolarised machine does not get direct access to A_μ and needs to work under an increased set of assumptions. Specifically, unpolarised colliders cannot directly measure the Z/γ -interference parameter ϵ_μ . The interpretation of the measurements relies on precise and accurate predictions of that term in the same order of magnitude as the expected A_μ precision (section 7.6.3). An FCC-ee with an A_μ relative precision goal of 0.05% will require a knowledge of ϵ_μ at or below the 10^{-5} absolute level.

Keeping in mind that the MC dataset and the formula in this study use only tree-level diagrams, there is another way to interpret this. For an unbiased interpretation of an unpolarised A_{FB}^μ measurement, the calculation of higher order corrections needs to have a precision below 10^{-5} . A polarised measurement on the other hand sets that precision requirement at the level of the A_μ precision, which is only at the level of a few 10^{-4} . In addition, as seen for ϵ_μ , the polarised measurement can directly measure the higher order corrections for an experimental cross-check of the theory calculation.

The above discussion shows that the differences of precisions for different past and

7. Impact of beam polarisation on electroweak fits

future colliders reflect the theoretical behaviour. They demonstrate that even a 250 GeV collider can increase the A_μ precision by one order-of-magnitude over the current precision, and dedicated Z-pole runs of future e^+e^- colliders add another order-of-magnitude. In all cases, an unpolarised collider needs at least an order-of-magnitude more luminosity to compete with the direct chiral access at a polarised collider.

7.6.5. Small impact of muon acceptance

The fully muonic final state is the prime candidate for testing the influence of the μ acceptance. Simple reasoning (section 7.2) lead to the possibility that the impact of systematic uncertainties reduces with beam polarisation. The fits include the μ acceptance to perform a first test of this hypothesis. By comparing the results with fix and free parameters of the acceptance model (bars compared to stars in fig. 7.16), the fits can extract the relative impact of this systematic uncertainty.

The only affected fermion pair production parameter is unpolarised correction parameter k_0 of the return-to-Z events (fig. 7.16a). Only this parameter leads to a change in the differential distribution which is similar to the change provoked by varying the μ acceptance, i.e. it is most relevant in the forward region and still has a non-vanishing impact in more central bins. All scenarios show relative impact of approximately 14%, independently of the luminosity or polarisation setup.

Changes with the polarisation (beyond statistical differences) are neither expected nor observed, since k_0 is by design chirality-independent. This means that no strong statement on the interaction of polarisation and systematics is possible, since the considered systematic effect turns out to not play any significant role on chirality-dependent parameters.

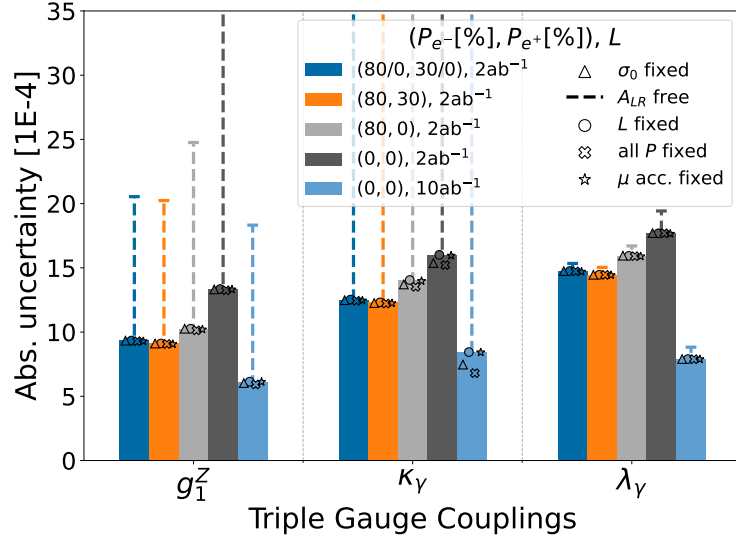
At the same time, it is remarkable to note that the chirality-dependent correction parameter Δk does not correlate with the μ acceptance. This is despite the fact that Δk and k_0 induce very similar shape changes. The Δk parameter stays unaffected by the systematic exactly because of its chirality-dependence, which a polarised collider can separate well from the chirality-independence of the μ acceptance. In that way, the fit does manage to demonstrate the power of chiral observables at a polarised collider.

That same pattern is also likely to hold up for more complex μ acceptance models. While correlations of the systematic effect with the chirality-independent parameters ($\sigma_0^\mu, A_{FB}^\mu, \epsilon_\mu, k_0$) can increase, it is unlikely that any correlation of the chirality-independent acceptance with the chirality-depend parameters ($A_e, A_\mu, \Delta k$) appears.

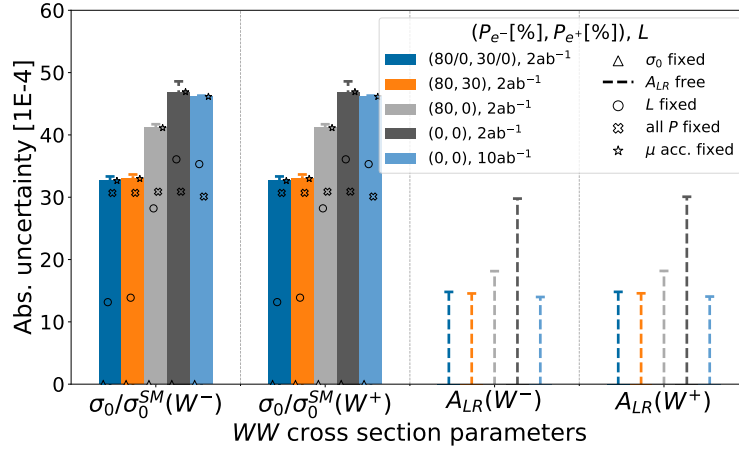
7.7. Four-fermion fits: Polarisation measurement in the presence of physical parameters

W pair production has a strong chirality-dependence, leading to a strong dependence on the beam polarisation. As a consequence, the set of available polarisations at a collider

7.7. Four-fermion fits: Polarisation measurement in the presence of physical parameters



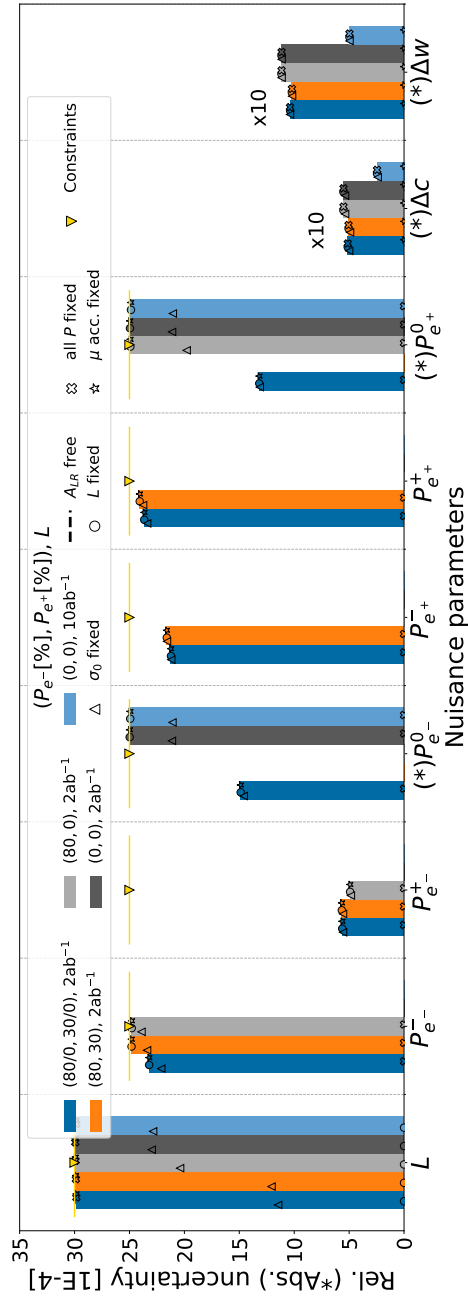
(a)



(b)

Figure 7.21.: Uncertainties on (a) TGCs, (b) cross-section parameters, and (c) systematic parameters from fits to semileptonic W pair production in different collider scenarios (section 7.2). Uncertainties on physical parameters are absolute, those on systematic parameters are relative unless specified otherwise. Polarised beams significantly improve the precision on all physical parameters and the beam polarisations. (Tables with uncertainty numbers in appendix: tables C.6 to C.11)

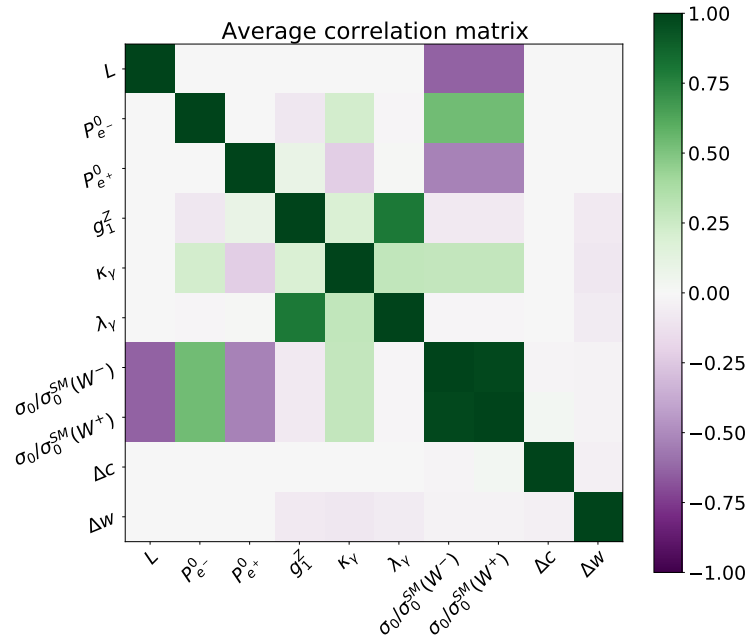
7. Impact of beam polarisation on electroweak fits



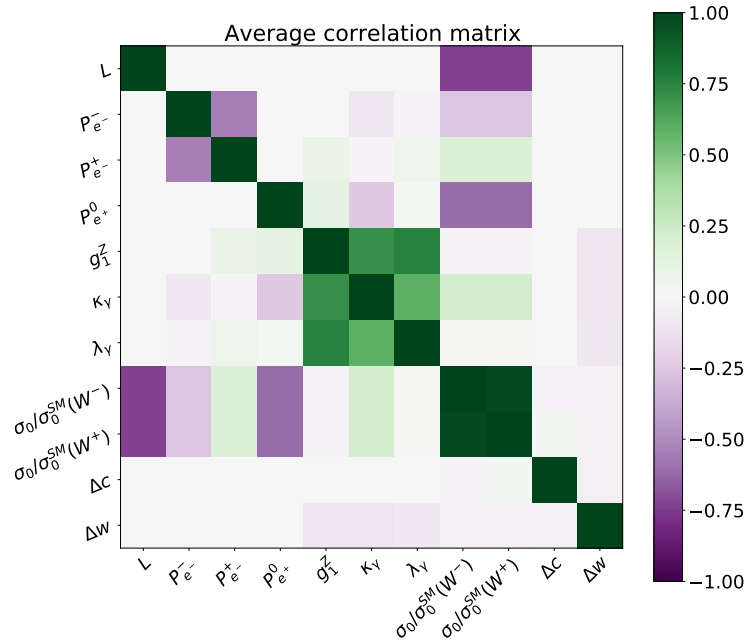
(c)

Figure 7.21.: (cont.)

7.7. Four-fermion fits: Polarisation measurement in the presence of physical parameters



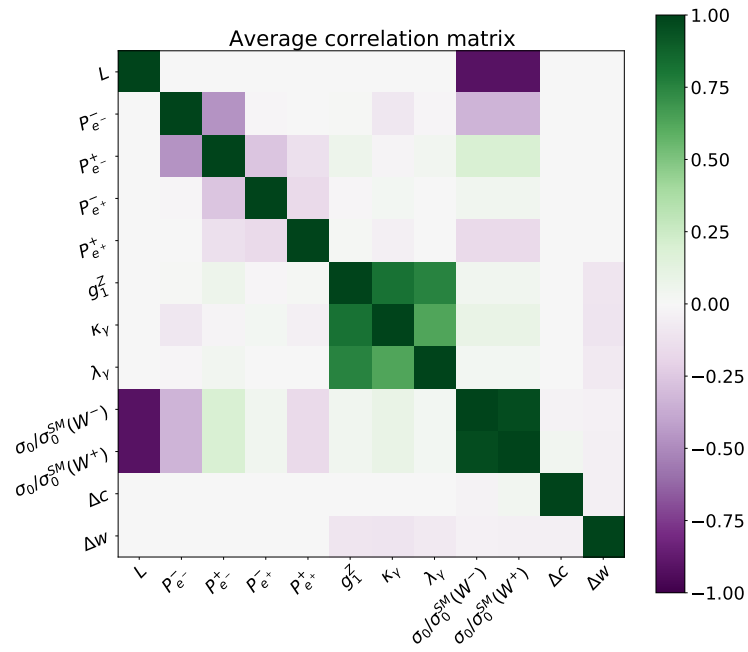
(a)



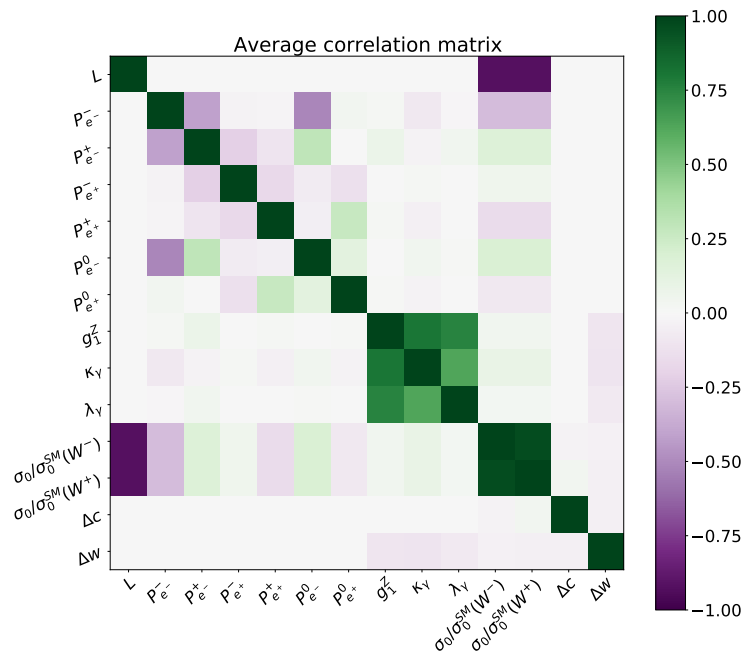
(b)

Figure 7.22.: Visualisation of the correlation matrices of the (a) (0,0), (b) (80,0), (c) (80,30), and (d) (80/0,30/0) default scenarios (section 7.2) with $L = 2 \text{ ab}^{-1}$ for the fit to semileptonic W pair production. The TGCs show strong correlations amongst each other in polarised scenarios, and generally low correlations with systematic effects. (Duplicates with numbers in appendix: fig. C.10)

7. Impact of beam polarisation on electroweak fits



(c)



(d)

Figure 7.22.: (cont.)

will significantly affect all measurements in this channel. In addition, the W pair can arise from vector boson self-coupling vertices which are of high interest for searches of BSM physics.

Here, fits to semileptonic W pair production in the $\mu\nu qq$ channel give insight into the different aspects of the impact of beam polarisation on physical and systematic parameters, and the interplay between them. These fits use the three-dimensional distributions of the W^- production angle and the two decay angles of the leptonically decaying W for the charge-separated $\mu^+\nu qq$ and $\mu^-\nu qq$ final states (sections 5.3 and 7.3.1). The standard set of free parameters in the fits contains the three Triple Gauge Couplings (TGCs, section 7.3.3), the total unpolarised cross-section, the μ acceptance parameters (section 7.4), as well as luminosity and polarisations with corresponding constraints (section 7.3.5). Primary outputs of the fits are the uncertainties (fig. 7.21) and correlations (fig. 7.22) for the different collider scenarios (section 7.2). In addition to the default parameter set (bars in fig. 7.21, and fig. 7.22), the fits also test scenarios in which either fix or additionally fit different parameters (markers in fig. 7.21).

The fit results show that one of the most significant gains from polarised beams is the measurement of the polarisations themselves (section 7.7.1). They also demonstrate the additional access to chiral observables (section 7.7.3), here in the form of the left-right asymmetry, and the importance of that information for the measurement of electroweak parameters such as the TGCs (section 7.7.4). Like in the μ pair production case, the μ acceptance systematic turns out to not limit the W pair production measurement (section 7.7.5).

7.7.1. Polarisation measurement gains from additional datasets

W pair production is one of the key channels for the measurement of the polarisations [144, 145, 237]. As the μ pair production fits have already shown (section 7.6.1), this measurement qualitatively and quantitatively improves with the availability of polarised beams (bars in fig. 7.21c). This section first considers only the polarisation parameters, later sections will discuss the impact on correlations with physical parameters.

The availability of polarised beams leads to multiple datasets with different polarisation settings. These datasets need to share the luminosity between each other. An optimised luminosity splitting between the polarised datasets can cause an increase in expected number of $e_L^- e_R^+$ and $e_R^- e_L^+$ events (table 7.1). In addition, polarised beams can reduce the correlation between the polarisation parameters. The statistical advantage from slightly higher event numbers turns out to be negligible compared to the qualitative impact of having multiple datasets.

For an unpolarised collider setup, the polarimeter precision fully determines the precision on both beam polarisations ($(0,0)$ scenarios in fig. 7.21c). No further information is available from collision data. An unpolarised circular collider can additionally use the depolarisation in the dipole magnets to ensure that the polarisation is close to zero below the percent level (section 7.2). This is not possible at a linear collider. In either

7. Impact of beam polarisation on electroweak fits

case, the high-precision physics goals of these colliders demand also a high-precision polarisation measurement for unpolarised beams.

A polarised electron beam leads to additional information on the electron polarisations beyond the pure polarimeter measurement $((80,0)$ scenario in fig. 7.21c). While the precision on the negative-sign polarisation \mathcal{P}_e^- increases only by a few percent, the precision on the positive-sign polarisation \mathcal{P}_e^+ increases by a factor five compared to the polarimeter precision. A dedicated analysis of this scenario follows below (section 7.7.2) and shows that this is due to the large left-right asymmetry, which introduces a difference in the polarisation sensitivities. The positron polarisation measurement still fully relies on polarimeter precision.

The step to a collider with two polarised beams brings additional qualitative advantages $((80,30)$ scenario in fig. 7.21c). Each of the now multiple positron polarisations observes an improved precision compared to the polarimeters. In other words, a collider with two polarised beams can measure all polarisations. This yields another important advantage for the polarisation measurement: a bias in the polarimeters can no longer fully translate into a bias in polarisation measurements. The independent polarisation measurements from collision data and from the polarimeters can cross-check each other in this scenario [60].

Colliders with polarised beams can also use unpolarised or transversally polarised beam settings, which results in a larger number of datasets (section 7.2). This introduces a disadvantage in terms of increasing opposite-sign longitudinally polarised collisions, and potential advantages in the polarisation measurement from the increased number of datasets and in the measurement of CP-sensitive observables [111]. The fits show that such a scenario measures the polarisations of all beam settings - including the unpolarised beam settings - with much higher precision than polarimeters alone $((80/0,30/0)$ in fig. 7.21c). Compared to the polarised scenario without these unpolarised datasets, the precision improves slightly on all polarisations despite the decrease in statistics for these beam settings. This only works if the collider includes datasets that combine the longitudinally unpolarised beam settings of one beam with the longitudinally polarised settings of the other beam. As the fits demonstrate, a collider with two polarised beams can dedicate a fraction of the luminosity to unpolarised or transversally polarised beam settings without negatively impacting the polarisation precision. In addition, the increased redundancy from the larger number of datasets provides a further improvement in the control of polarisation biases.

These results confirm that polarised datasets significantly increase the precision of the polarisation measurement. They further show that a collider with two polarised beams in this context also benefits from adding unpolarised or transversally polarised beam settings.

7.7.2. Polarisation measurement with one polarised beam

The fit with only e^- polarisation ((80,0) scenario in fig. 7.21c) finds a measurement of the positive-sign e^- polarisation $\mathcal{D}_{e^-}^+$ at the level of $5 \cdot 10^{-4}$, while the precision negative-sign e^- polarisation $\mathcal{D}_{e^-}^-$ and the e^+ polarisation $\mathcal{D}_{e^+}^0$ do not show any improvement beyond the polarimeter constraint. A similar pattern is also visible in the case of two polarised beams ((80,30) scenario in fig. 7.21c), and previous studies also observed a similar behaviour for an ILC with two polarised beams [60, 157]. An analytic approach to the polarisation measurement with one polarised beam can explain this behaviour (detailed calculations in appendix: section C.8).

A collider with only e^- polarisation measures two datasets corresponding to the directions of the e^- polarisation. It accordingly measures a number of events N^+ for the positive-sign polarisation setting and a number of events N^- for the negative-sign polarisation setting. If the measurement includes the differential distribution, then the different differential shapes of the different initial states allow a measurement of the number of events for each one of the initial states in each of the datasets. In the case of W pair production there are two allowed initial states $e_L^- e_R^+$ (short: L) and $e_R^- e_L^+$ (short: R), and the collider can measure four integrated chiral event numbers $\{N_L^+, N_R^+, N_L^-, N_R^-\}$. Those event numbers are functions of the polarisations in the corresponding dataset, the left-right asymmetry A_{LR} and the unpolarised event number $N_0 = L \cdot \sigma_0$.

$$\begin{aligned}
 N_L^+ &= \frac{1}{8} (1 - \mathcal{D}_{e^-}^+) (1 + \mathcal{D}_{e^+}^0) (1 + A_{LR}) N_0 \\
 N_R^+ &= \frac{1}{8} (1 + \mathcal{D}_{e^-}^+) (1 - \mathcal{D}_{e^+}^0) (1 - A_{LR}) N_0 \\
 N_L^- &= \frac{1}{8} (1 - \mathcal{D}_{e^-}^-) (1 + \mathcal{D}_{e^+}^0) (1 + A_{LR}) N_0 \\
 N_R^- &= \frac{1}{8} (1 + \mathcal{D}_{e^-}^-) (1 - \mathcal{D}_{e^+}^0) (1 - A_{LR}) N_0
 \end{aligned} \tag{7.36}$$

If A_{LR} is a fixed parameter, then these formulas for the event numbers are a system of four equations with four unknowns $(\mathcal{D}_{e^-}^+, \mathcal{D}_{e^-}^-, \mathcal{D}_{e^+}^0, N_0)$. This system has a unique solution.

$$\mathcal{D}_{e^-}^+ = \frac{N_L^+ (N_R^- - 2N_R^+) + N_R^+ N_L^-}{N_R^+ N_L^- - N_L^+ N_R^-} \tag{7.37}$$

$$\mathcal{D}_{e^-}^- = \frac{N_R^- (N_L^+ - 2N_L^-) + N_L^- N_R^+}{N_L^+ N_R^- - N_R^- N_L^+} \tag{7.38}$$

$$\mathcal{D}_{e^+}^0 = \frac{(1 - A_{LR}) (N_L^- - N_L^+) + (1 + A_{LR}) (N_R^- - N_R^+)}{(1 - A_{LR}) (N_L^- - N_L^+) - (1 + A_{LR}) (N_R^- - N_R^+)} \tag{7.39}$$

$$N_0 = 2 (N_L^+ N_R^- - N_R^+ N_L^-) \frac{(1 + A_{LR}) (N_R^+ - N_R^-) - (1 - A_{LR}) (N_L^+ - N_L^-)}{(1 - A_{LR}^2) (N_L^+ - N_L^-) (N_R^+ - N_R^-)} \tag{7.40}$$

7. Impact of beam polarisation on electroweak fits

This set of equations is the basis of the polarisation measurement at a collider with one polarised beam with W pair production events.

A prediction for the expected polarisation uncertainties is possible by means of simple Gaussian error propagation (section C.8). Here the calculation of a first estimate will assume independent Poisson uncertainties ($\Delta N = \sqrt{N}$) for each of the four event numbers, and the discussion of that estimate will revisit this assumption.

The evaluation of the Gaussian error propagation at the central values of the polarisations

$$\begin{aligned}\mathcal{D}_{e^+}^+ &= \mathcal{D}_{e^-} > 0 \\ \mathcal{D}_{e^-}^- &= -\mathcal{D}_{e^-} < 0 \\ \mathcal{D}_{e^+}^0 &= 0\end{aligned}\tag{7.41}$$

yields an analytic formula for the expected polarisation uncertainties.

$$\Delta \mathcal{D}_{e^+}^+ = \frac{1}{\sqrt{N_0}} \sqrt{\frac{1 - \mathcal{D}_{e^-}^2}{\mathcal{D}_{e^-}^2} \sqrt{\frac{(1 + \mathcal{D}_{e^-})^2}{1 + A_{LR}} + \frac{(1 - \mathcal{D}_{e^-})^2}{1 - A_{LR}}}}\tag{7.42}$$

$$\Delta \mathcal{D}_{e^-}^- = \frac{1}{\sqrt{N_0}} \sqrt{\frac{1 - \mathcal{D}_{e^-}^2}{\mathcal{D}_{e^-}^2} \sqrt{\frac{(1 - \mathcal{D}_{e^-})^2}{1 + A_{LR}} + \frac{(1 + \mathcal{D}_{e^-})^2}{1 - A_{LR}}}}\tag{7.43}$$

$$\Delta \mathcal{D}_{e^+}^0 = \frac{1}{\sqrt{N_0}} \frac{1}{|\mathcal{D}_{e^-}|} \sqrt{\frac{1}{1 + A_{LR}} + \frac{1}{1 - A_{LR}}}\tag{7.44}$$

The formulas for uncertainties of the two e^- polarisations contain polarisation factors $(1 \pm \mathcal{D}_{e^-})^2$ which are suppressed or enhanced by asymmetry factors $(1 \pm A_{LR})$. For the positive-sign polarisation, the asymmetry factor $(1 + A_{LR})$ suppresses the larger polarisation factor $(1 + \mathcal{D}_{e^-})^2$, whereas for the negative-sign polarisation the asymmetry factor $(1 - A_{LR})$ enhances that polarisation factor. This is the reason why the measurement has a much better precision on the positive-sign e^- polarisation.

The uncertainty formulas also allow a quantitative prediction using the specific numbers for the polarisation ($\mathcal{D}_{e^-} = 80\%$), the luminosity ($L = 2 \text{ ab}^{-1}$), the left-right asymmetry ($A_{LR} \approx 0.98$) and the unpolarised cross-section ($\sigma_0 \approx 18953 \text{ fb}$).

$$\begin{aligned}\Delta \mathcal{D}_{e^-}^+ &\approx 9.75 \cdot 10^{-5} \quad \Rightarrow \quad \left| \frac{\Delta \mathcal{D}_{e^-}^+}{\mathcal{D}_{e^-}^+} \right| \approx 1.22 \cdot 10^{-4} \\ \Delta \mathcal{D}_{e^-}^- &\approx 6.53 \cdot 10^{-4} \quad \Rightarrow \quad \left| \frac{\Delta \mathcal{D}_{e^-}^-}{\mathcal{D}_{e^-}^-} \right| \approx 8.16 \cdot 10^{-4} \\ \Delta \mathcal{D}_{e^+}^0 &\approx 1.44 \cdot 10^{-3}\end{aligned}\tag{7.45}$$

Those numbers follow the general trend that both negative-sign e^- polarisation and the e^+ polarisation have a significantly worse precision than the positive e^- polarisation. Compared to the corresponding fit results ((80,0) scenario in fig. 7.21c), the prediction

here is consistently too optimistic. While the fit finds a precise \mathcal{D}_{e^-} measurement with a precision of around $5 \cdot 10^{-4}$, both \mathcal{D}_{e^-} and $\mathcal{D}_{e^+}^0$ do not show any measurement beyond the polarimeter precision.

This discrepancy turns out to be due to the simplistic assumption that each of the four event numbers $\{N_L^+, N_R^+, N_L^-, N_R^-\}$ has an independent Poissonian uncertainty. In reality, for each of the two datasets the measurement of the $e_L^- e_R^+$ event number contains the $e_R^- e_L^+$ events as backgrounds and vice versa.

The impact of this additional uncertainty becomes clear when looking at the case of a highly-polarised e^- beam ($\mathcal{D}_{e^-} \gtrsim 90\%$). In that case, the event numbers for each of the two chiral state differ greatly between the two datasets.

$$\begin{aligned} \frac{N_L^-}{N_L^+} &= \frac{1 - \mathcal{D}_{e^-}}{1 - \mathcal{D}_{e^+}} \gtrsim 10 \\ \frac{N_R^+}{N_R^-} &= \frac{1 + \mathcal{D}_{e^+}}{1 + \mathcal{D}_{e^-}} \gtrsim 10 \\ \Rightarrow \rho &= \frac{N_L^+ N_R^-}{N_R^+ N_L^-} \ll 1 \end{aligned} \quad (7.46)$$

This allows a Taylor expansion in the small ratio ρ of the formula for the e^- polarisations (eq. (7.37)). Neglecting any terms that contain ρ (details: section C.8), the two e^- polarisations take a simple form.

$$\begin{aligned} \mathcal{D}_{e^+} &\approx 1 - 2 \frac{N_L^+}{N_L^-} \\ \mathcal{D}_{e^-} &\approx - \left(1 - 2 \frac{N_R^-}{N_R^+} \right) \end{aligned} \quad (7.47)$$

These simplified forms, assuming only a high degree of e^- polarisation, are the first part of why the first prediction (eq. (7.45)) for the polarisation uncertainties strongly underestimated the \mathcal{D}_{e^-} uncertainty. The second relevant point is the large A_{LR} value. Due to this large asymmetry, the measurement of the $e_L^- e_R^+$ initial state is almost free of $e_R^- e_L^+$ background while the measurement of the $e_R^- e_L^+$ initial state struggles with an overwhelming $e_L^- e_R^+$ background. According to the approximated e^- polarisation formulas (eq. (7.47)), the measurement of the positive-sign polarisation relies mainly on $e_L^- e_R^+$ events and will see very little disturbance from background. On the other hand, the measurement of the negative-sign polarisation relies on mainly on $e_R^- e_L^+$, and the high $e_L^- e_R^+$ background will strongly disturb this measurement.

A similar approximation is possible for the e^+ polarisation (section C.8).

$$\mathcal{D}_{e^+}^0 \approx \frac{1 - \frac{1+A_{LR}}{1-A_{LR}} \frac{N_R^-}{N_L^+}}{1 + \frac{1+A_{LR}}{1-A_{LR}} \frac{N_R^-}{N_L^+}} \quad (7.48)$$

7. Impact of beam polarisation on electroweak fits

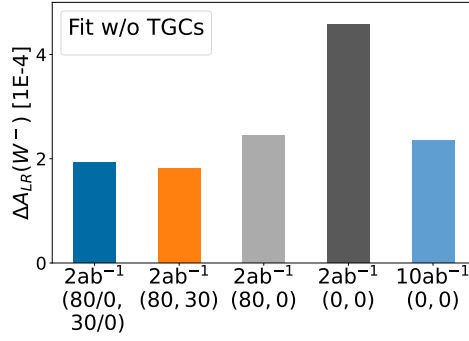


Figure 7.23: A_{LR} uncertainties of the fits with a change to the default parameters so that the TGCs are fixed and the A_{LR} is free. This tests the precision on A_{LR} , which in the fit with the default parameter set is part of the TGC measurement (section 7.7.4). The direct access to chiral behaviour of gives polarised colliders a significantly better handle of the asymmetry information.

It turns out that the measurement of the positron polarisation requires precision in the measurement of both initial states. Like for \mathcal{D}_{e^-} , the disturbance of the measurement of the $e_R^- e_L^+$ initial state due to the high $e_L^- e_R^+$ background deteriorates the $\mathcal{D}_{e^+}^0$ precision.

Summarizing that discussion for the scenario with only e^- polarisation, two consequences of the large A_{LR} value explain the difference between the precise \mathcal{D}_{e^+} measurement and the much less precise \mathcal{D}_{e^-} and $\mathcal{D}_{e^+}^0$ measurements. The first, reflected in the Gaussian error propagation (eq. (7.42)), is the much larger statistics for the $e_L^- e_R^+$ initial state. The second, not included in the Gaussian error propagation, is the large $e_L^- e_R^+$ background that disturbs the $e_R^- e_L^+$ measurement.

Since the weak interaction causes a general preference for $e_L^- e_R^+$ events, this precision difference between the settings of the e^- polarisation is unavoidable in the polarisation measurement from collision data. This adds emphasis to the polarimeters. If the polarimeters measure the difference between the settings of the same beam with high precision, then the high precision from collision data on only one of the two settings can be sufficient.

7.7.3. Roles of asymmetry and normalisation information in W pair production

Turning the focus now to the physical parameters, the simplest physical parameters are the chiral cross-sections of the two allowed initial states. The fit can implement these in the form of the summed total cross-section σ_0 and the left-right asymmetry A_{LR} (eq. (7.13)). Theory calculations calculate their SM values with high-precision [239], and any deviation from those values will indicate new physics. For this reason, the summed total cross-section σ_0 is usually an observable in itself, parametrising the total normalisation. In contrast, the left-right asymmetry A_{LR} is usually not a direct observable. Instead, other parameters in the fit make use of the left-right asymmetry in the

measured cross-sections, making the asymmetry indirectly a free parameter.

The σ_0 measurement is already part of the fits. In the collider scenario with two polarised beams, the luminosity measurement fully determines the normalisation uncertainty (circles compared to bars in fig. 7.21b). The beam polarisation uncertainty contributes significantly when only one or neither beam is polarised (crosses compared to bars in fig. 7.21b). Resulting from these limitations, the relative uncertainty on the total cross-section ranges from $3 \cdot 10^{-3}$ for scenarios with two polarised beams to around $4.5 \cdot 10^{-3}$ for the unpolarised cases. Only an improved determination of the respective dominating systematic effect - the luminosity or the polarisations - can increase the σ_0 precisions.

If physically motivated, the fits can also assume the unpolarised cross-section as known (triangles in fig. 7.21). In that case, the normalisation information will contribute to the measurement of other effects. The fits for that case show that the luminosity and polarisation measurements benefit from the additional normalisation information.

This observed interplay of the normalisation measurement and beam polarisation traces back to the large asymmetry value in W pair production (details: section C.9). Due to the overwhelming dominance of the $e_L^- e_R^+$ initial state, the measurement of these events yields the most stringent limits on the polarisation. These stringent limits can significantly soften or even fall away when there is a specific direction in the parameter space that includes the polarisation and keeps the expected number of events constant. If the cross-section is a free parameter with an absolute deviation $\Delta\sigma_0$, there is a free direction $\mathcal{D}_{e^-} = \mathcal{D}_{e^+} + \frac{\Delta\sigma_0}{\sigma_0 + \Delta\sigma_0} \approx \mathcal{D}_{e^+} + \frac{\Delta\sigma_0}{\sigma_0}$. When the cross-section is fixed and the polarisation measurement can use the normalisation information, this free direction transforms into a semi-free direction where $\mathcal{D}_{e^-} = \mathcal{D}_{e^+}$. It is semi-free because both polarimeters constrain that direction, leading to a combined polarimeter constraint that is a factor $\sqrt{2}$ better. This scenario is rather academic, since the total cross-section is typically a free fit parameter.

The μ acceptance is the only tested systematic effect that cannot benefit from the normalisation information, and instead seems to fully rely on differential information. A more elaborate and realistic implementation of acceptance can have a stronger interplay with normalisation information.

In contrast to σ_0 , the left-right asymmetry is usually not a free parameter in the fit. As a later section will show (section 7.7.4), the TGC extraction is highly sensitive to this asymmetry. For the fit, this means that the free TGC parameters can already almost freely vary the left-right asymmetry of the prediction almost, making an additional A_{LR} parameter redundant. Since the left-right asymmetry is only one part of the TGC measurement, it can be instructive to still look at this part in isolation and see how the left-right asymmetry measurement changes with polarisation. This is possible by diverging from the default parameter set, fixing the TGC parameters and instead using the left-right asymmetries of the two final states $\mu^+ \nu q \bar{q}$ and $\mu^- \nu q \bar{q}$ as free parameters (fig. 7.23).

A template fit of a superposition of the two allowed initial states to the differential

distribution of even a single datasets can in principle measure each individual chiral cross-section, and with that the left-right asymmetry A_{LR} . This method does not work for the μ pair production fit, where a single dataset is not directly sensitive to A_{LR} due to the common differential shape of the two initial states (section 7.3.2). In that case, the asymmetry measurement requires beam polarisation. This problem does not occur when the different chiral initial states have functionally different differential distributions, which avoids ambiguities in a superposition of these differential distributions. Such is the case for W pair production, where the $e_L^- e_R^+$ initial state can interact through a t-channel ν exchange that is unavailable to the $e_R^- e_L^+$ initial state. Due to this additional process for the $e_L^- e_R^+$ initial state, the two chiral initial states result in different differential distributions, and an extraction of their relative contributions is possible.

For the same luminosity, an unpolarised collider delivers around a factor two higher uncertainty than a collider with two polarised beams ((0,0) compared to (80,30) in fig. 7.23). The reason is that the unpolarised collider fully relies on the differential distribution measurement of a single dataset. Increasing the unpolarised luminosity by around a factor five can almost recover the A_{LR} precision from a collider with two polarised beams. If the electron beam is polarised, then a polarisation of the positron beam only makes a small difference in this context. This is a noticeable contrast to the μ pair production fit (section 7.6.1), where the addition of e^+ polarisation removes a strong correlation between the electron asymmetry A_e (equivalent to A_{LR}) and the e^+ polarisation. In the μ pair production case, the fit cannot directly measure A_e on a single dataset, and the A_e measurement fully relies on the differences between the polarised datasets. In W pair production, each individual dataset is sensitive to A_{LR} , and the A_{LR} measurement is less reliant on the differences between the polarised datasets.

The beam polarisation parameters themselves show no interplay with the asymmetry measurement. Only the statistical uncertainty and the availability of chiral observables through beam polarisations determine the asymmetry precision. Studies of the theoretical calculations suggest that also the theoretical uncertainty on the SM values of the chiral cross-sections will be negligible [239].

The availability of beam polarisation is the most important factor for the precision on the measured left-right asymmetry. For the parameters that make use of the left-right asymmetry information in the fit, this will mean an improved measurement with beam polarisation.

7.7.4. Impact of polarised beams on the TGC measurement

W pair production, besides being one of the main channels for polarisation measurement, is also relevant for a large range of potential extensions to the SM. This raises the question whether measurements of physical and systematic effects can disturb each other, and - more generally - how polarised beams affect the physics precision. Here, the fits test this by including the three Triple Gauge Coupling (TGC) parameters of LEP parametrisation (section 2.2.3).

Table 7.8.: TGCs uncertainties from fit in different collider scenarios (section 7.2) with simultaneous extraction of the three TGCs with $L = 2 \text{ ab}^{-1}$ show an order-of-magnitude improvement over the single-parameter precisions from LEP [3]. Results from a simultaneous extraction with all LEP experiments are not available.

	LEP	(0, 0)	(80, 0)	(80, 30)	(80/0, 30/0)
$\Delta g_1^Z [10^{-3}]$	19	1.33	1.02	0.91	0.93
$\Delta \kappa_\gamma [10^{-3}]$	42	1.60	1.40	1.23	1.25
$\Delta \lambda_\gamma [10^{-3}]$	19	1.76	1.59	1.44	1.47

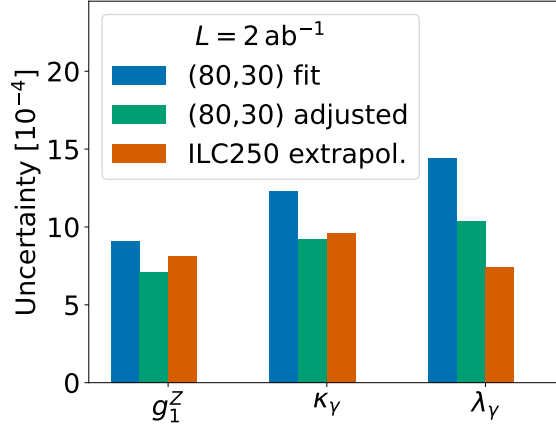


Figure 7.24.: Comparison of the TGC uncertainties from the fit scenario with two polarised beams (“(80,30) fit”, section 7.2) and from a study that extrapolates higher-energy ILC full simulation-studies to the 250 GeV stage [60]. The ILC studies use the same angular distributions as the fits, and include the $WW \rightarrow evqq$ process and systematic uncertainties, which require an adjustment of the fit uncertainties for comparability (“(80,30) adjust”). Even after the adjustment, the fit prediction for λ_γ differs visible from the ILC study.

The fits observe uncertainties on the TGCs of around $1 - 2 \cdot 10^{-3}$ for 2 ab^{-1} (fig. 7.21a and table 7.8). This marks an order of magnitude improvement over current precision from LEP experiments [3], and a factor three to an order of magnitude improvement over current precision from LHC experiments [166–168] (see section 4.2.1). It is a comparable precision to what is predicted for the HL-LHC [169].

For the scenario ILC-like scenario with two polarised beams it is possible to compare the TGC precisions from the fit with dedicated ILC studies (fig. 7.24). A previous study extrapolated the full-simulation results for TGC measurements at the 500 GeV and 1 TeV stages of the ILC to the 250 GeV stage [60]⁴. The higher-energy full simulation studies

⁴The reference also includes an extrapolation that uses additional extrapolation that adds the fully hadronic final state, hadronic angles, and optimal observables. This is not included in the numbers quoted here, which refer to Table 2.4 in the published version of the reference.

7. Impact of beam polarisation on electroweak fits

used the same angular distributions as the fit here and additionally included the process $WW \rightarrow evqq$ [157, 170]. In addition, the extrapolation assumes a systematic uncertainty from selection efficiencies of $3 \cdot 10^{-4}$ for g_1^Z and κ_γ , and $2 \cdot 10^{-4}$ for λ_γ . An adjustment of the fit uncertainties scales the uncertainties down by a factor $\sqrt{2}$ for the additional final state and add the systematic uncertainty in quadrature, which simplifies the comparison. Comparing the adjusted fit uncertainties to the ILC extrapolation, the uncertainties for g_1^Z and κ_γ are slightly lower for the fit, while the fit uncertainty for λ_γ is a factor 1.4 than predicted by the extrapolation. The discrepancy is likely due to the correlations amongst the TGCs in the fit (fig. 7.22c), which an extrapolation cannot capture.

A comparison of the TGC uncertainties for the different fit scenarios show that the TGC precision increases with beam polarisation. This precision increase varies between the TGCs. From an unpolarised scenario to a scenario with two polarised beams at the same luminosity, the uncertainties decrease by factors 1.5, 1.3 and 1.2 for g_1^Z , κ_γ and λ_γ respectively.

The fits observe only mild correlations of the TGCs with nuisance parameters (fig. 7.22). Only κ_γ slightly correlates with the polarisations when one or no beam is unpolarised, and more so for increased luminosity. An addition of unpolarised datasets to the scenario with two polarised beams does not increase the TGC precisions since the polarisation uncertainty is not an issue in that case. Uncertainties in the μ acceptance do not influence the TGC precision at all (stars compared to bars in fig. 7.21a). A simultaneous measurement of TGCs and systematic effects - notably polarisations - seems unproblematic.

Understanding the varying precisions and the exact impact of beam polarisation requires a closer look at the sensitivities to the TGCs.

Role of an improved asymmetry measurement

Initial sensitivity checks show that precise knowledge of the left-right asymmetry and the shape of the distribution of the $e_L^- e_R^+$ initial state will be crucial for the TGC measurement, and the knowledge of the overall normalisation is unlikely to play a role (section 7.3.4). The fit results reflect these initial findings.

No benefit comes from normalisation information, which can be seen from the absence of any improvements when fixing the total cross-section parameters (compare triangles and bars in fig. 7.21a). In contrast, the left-right asymmetry of the measured distributions is crucial for the TGC precision. This becomes visible when fit uses both the left-right asymmetry A_{LR} and the TGCs as free parameters at the same time, so that the asymmetry information is fully absorbed in the A_{LR} parameter (lines compared to bars in fig. 7.25a). The g_1^Z precision decreases by more than a factor 2 and the κ_γ precision by more than a factor 5. This loss of asymmetry information for the TGC determination also changes the uncertainty ratio between unpolarised scenario and the various polarised scenarios (fig. 7.25b). λ_γ is the only exception, as it shows almost no dependence on chiral information. An unpolarised measurement shows a stronger reliance on

7.7. Four-fermion fits: Polarisation measurement in the presence of physical parameters

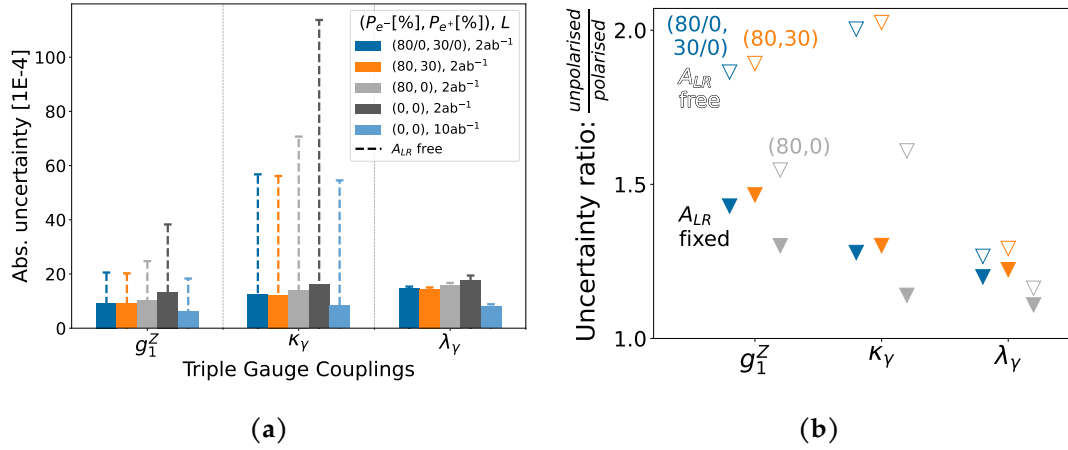


Figure 7.25: A comparison of the TGC uncertainties (a) from the fits with a free or fixed A_{LR} parameter shows that a limited knowledge of the left-right asymmetry - modeled through A_{LR} as free parameter - can deteriorate the TGC precision drastically, most notably for κ_γ . This affects the unpolarised measurement stronger than any measurement with polarised beams, as is visible in the uncertainty ratio (b) of the $(0,0)$ scenario to the various polarised scenarios.

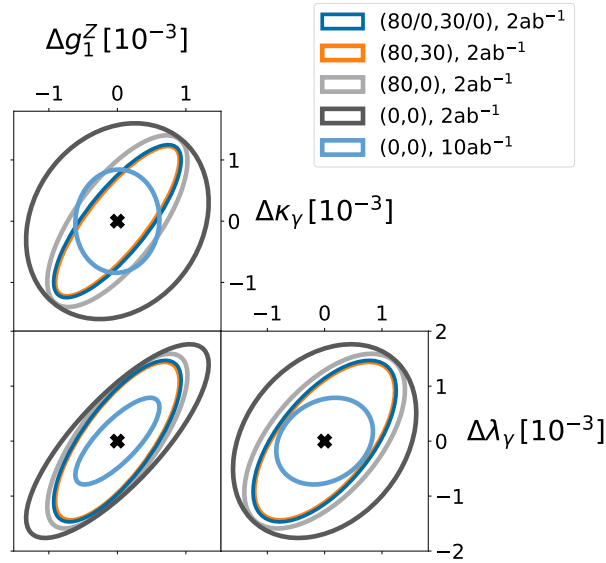


Figure 7.26: 2D-confidence ellipses of the TGC parameters in the fits with the default parameter set show that beam polarisation improves the TGC precision in one specific direction. The ellipses assume Gaussian uncertainties for all parameters (problematic for λ_γ as seen in figs. 7.5 and 7.6).

the asymmetry knowledge than a polarised one, and any limitations on that knowledge affect the unpolarised scenario the most.

The presence of non-zero polarisation increases the precision on the left-right asymmetry precision (section 7.7.3). An improved left-right asymmetry measurement only affects the direction of the TGC space that is sensitive to that information, and when that sensitivity is as at least as good as the sensitivity from the shape measurement. In contrast to the asymmetry measurement, the shape measurement for the $e_L^- e_R^+$ initial state is not likely to improve with the availability of polarised beams since the $e_L^- e_R^+$ cross-section is dominant and the $e_R^- e_L^+$ background negligible. The only expected precision increase for the shape measurement is the modest increase in statistics from the optimised luminosity sharing when both beams are polarised (section 7.2.2).

The full impact of additional polarisation on the TGC measurement is visible in the 2D projections of the three-dimensional TGC uncertainty ellipse (fig. 7.26). A comparison of the collider scenarios in those projections shows that one specific direction in the TGC space benefits the most from polarised beams. That direction is the one where g_1^Z and λ_γ increase at the same time as κ_γ decreases. The magnitude of the increase or decrease is not the same for the three couplings; the changes in g_1^Z and κ_γ are much stronger than the change in λ_γ . Looking back at the initial sensitivity checks (fig. 7.5b), changes in κ_γ have a minimal impact on A_{LR} while increases in g_1^Z and λ_γ lead to an asymmetry increase around twice the TGC increase. The relevant direction therefore significantly changes the left-right asymmetry. At the same time, an increase in g_1^Z causes a change in the differential distribution of the $e_L^- e_R^+$ initial state that has the opposite sign to the changes that increases in κ_γ and λ_γ produce (fig. 7.7). This means that shape measurement of the $e_L^- e_R^+$ initial state has a reduced sensitivity to the relevant direction in the TGC space. Summarizing these observations, additional beam polarisation benefits the measurement of the direction of the TGC space where asymmetry information has a significantly higher restrictive power than shape information.

If an asymmetry measurement is not available at all, then the uncertainties in the above described direction will increase until the point where any of the shape measurements show sensitivity. In that case a measurement of the shape of the $e_R^- e_L^+$ initial state starts to become relevant. This can explain why a lack of asymmetry knowledge affects the unpolarised scenario the most ((0,0) in fig. 7.25), since the polarised scenarios measure datasets with an improved signal-to-background ratio for each initial state.

The shape measurement of the $e_L^- e_R^+$ initial state is not particularly sensitive to the specific direction of the TGC space described above. Other directions in the TGC space cause larger changes in that shape, so that the shape measurement can set the most stringent limits. For those directions, additional processes like single- W production can improve the precision.

Since two different kinds of information - A_{LR} and the shape of the $e_L^- e_R^+$ initial state - determine the measurement of the TGC parameter space, the uncertainty will not necessarily be the same in every direction of the TGC space. This explains the final corre-

lations that the fits observe between the three TGCs.

One way an unpolarised collider can make up for the less precise asymmetry measurement is by increasing the luminosity. A higher luminosity also leads to higher precision in $e_L^- e_R^+$ -shape measurement, which the presence of beam polarisation alone can not be achieved. The drawback of an unpolarised high-luminosity run is that the polarimeter precision becomes more critical. This is visible most notably for κ_γ in the unpolarised scenario with $L = 10 \text{ ab}^{-1}$, where the limited polarisation knowledge is responsible for almost 20% of the κ_γ uncertainty (compare crosses and bars in fig. 7.21a).

The discussion here demonstrates that an initial understanding of the impact of physical parameters like the TGCs on the observables is crucial for understanding the final uncertainties and correlation. At the same time, the complex behaviour of the uncertainty ellipse shows that a combined fit of the physical parameters is necessary to uncover all correlations between parameters, and to make a reliable prediction.

ffZ-couplings disturbing the asymmetry measurement

The left-right asymmetry measurement in W pair production is a major driver of the TGC uncertainty.

This left-right asymmetry is a combination of the 100% asymmetry of t-channel and the asymmetry of eeZ coupling in the s-channel. The left-handed nature of the SM $SU(2)_L$ gauge symmetry does not allow W pair production through a t-channel exchange with an $e_R^- e_L^+$ initial state, since that would require a coupling of right-handed fermions to W bosons. A change to the t-channel asymmetry is only possible by breaking that fundamental principle. In contrast, the left-right asymmetry of the s-channel diagram has a non-trivial value from the eeZ coupling, and receives both radiative corrections and potentially corrections from non-vanishing higher-order SMEFT-operators. This can introduce uncertainties in the asymmetry.

Predictions for the HL-LHC observe a strong dependence of TGC precision on qqZ couplings (fig. 40,41 in [169]) - equivalent to the eeZ coupling at an e^+e^- collider. The predictions show that the measurement of g_1^Z and κ_γ at the HL-LHC will suffer strongly when the qqZ couplings are treated as free parameters, while λ_γ remains essentially unaffected. This is consistent with the behaviour of the fit here, where the λ_γ precision is robust against the loss of asymmetry information.

The fermion pair production measurement at a future e^+e^- collider can extract the value of the ffZ couplings at different relevant energies. This includes both the electron and quark couplings to the Z , which will be unique and precise inputs to the W production measurements at e^+e^- and pp colliders respectively. Direct access to the left-right asymmetry with polarised colliders holds a special importance in this context since it provides the single most precise ffZ coupling measurement. The current fit does not provide an answer to the question of which precision in the coupling is necessary, or how to translate the A_{LR} precision from fermion pair production to the asymmetry precision on W pair production. A combined fit of two- and four-fermion couplings, e.g. in

the form of common EFT operators, can resolve both of those issues. This task remains open to future studies.

7.7.5. Negligible role of muon acceptance in W pair production

The fits also explicitly include the μ acceptance as a fitable systematic effect in two-parameter “box model” (section 7.4), with the goal to see how the influence of the systematic effect changes with the presence or absence of beam polarisation.

In the current setup, the fits observe a slight correlation of the acceptance width Δw with TGC parameters (fig. 7.22). This effect proves negligible, as none of the uncertainties improve when the fits fix the μ acceptance parameters (stars compared to bars in fig. 7.21a).

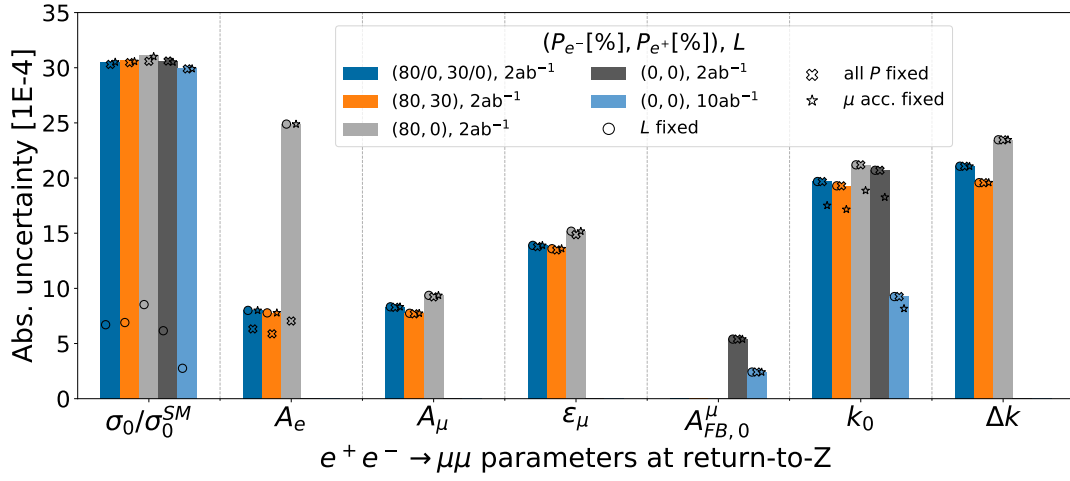
One of the goals of including the μ acceptance explicitly in the fit is to assess whether beam polarisation can separate such systematic effect from the physics of interest. The minimal impact of the μ acceptance does not allow any such conclusions.

A main cause may be the assumption of the simplified “box model” for the μ acceptance (section 7.4.1). This assumption leads to a unique signature of the model parameters which the fits easily separate from physical parameters. A more complex and realistic model can take more details into account, e.g. the slope of the acceptance edge. This will introduce a larger variety of changes on the differential distribution, potentially leading to more pronounced correlations with physical parameters.

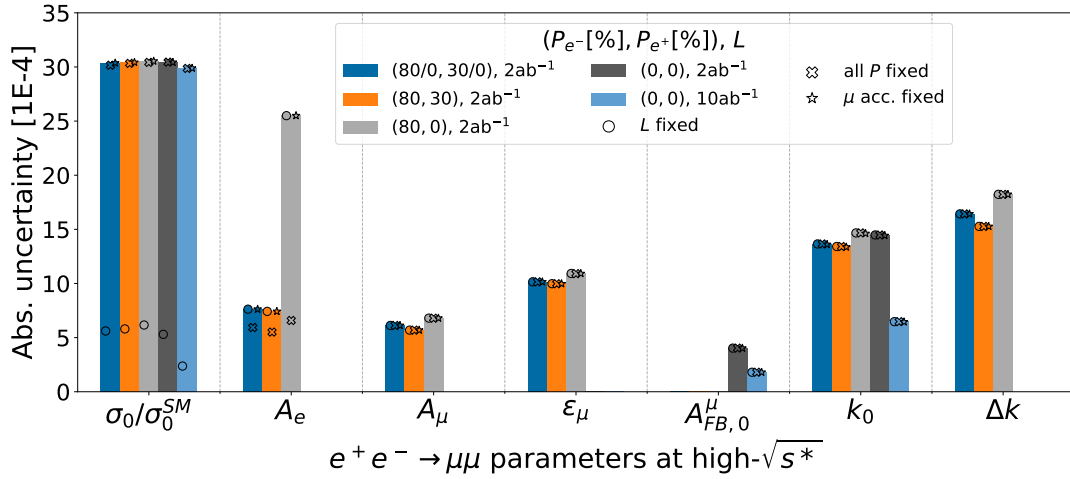
There remains the possibility that all relevant differential systematic effects have differential shape effects that distinguish them significantly from the differential shape effects of the TGCs. If that turns out to be true, then a TGC fit on differential distributions that directly includes models for those systematic effects will minimize the corresponding systematic uncertainties to a negligible level. While non-zero beam polarisation is not necessarily crucial for this case, it can aid in separating the differential behaviour of the effects. A previous study for the TGC extraction at the 500 GeV stage of the ILC found that selection efficiencies and background modeling can lead to a significant contribution of around $1 \cdot 10^{-3}$ to the TGC uncertainty [157]. Both of these effects are differential in nature, and a direct modeling in the fit will reduce their impact. This can be a specific target for future studies.

7.8. Combining two- and four-fermion fits

The discussions of the individual fits set the basis for understanding the behaviour of a combined fit of the two processes. This combined fit uses the default parameter sets of both individual fits, and simultaneously fits them to the differential distributions (section 7.3.1) of both μ pair production and semileptonic W pair production. In the combined parameter set, only the systematic effects - luminosity, polarisation, and μ acceptance - are common to both processes. The physical parameters are separate for



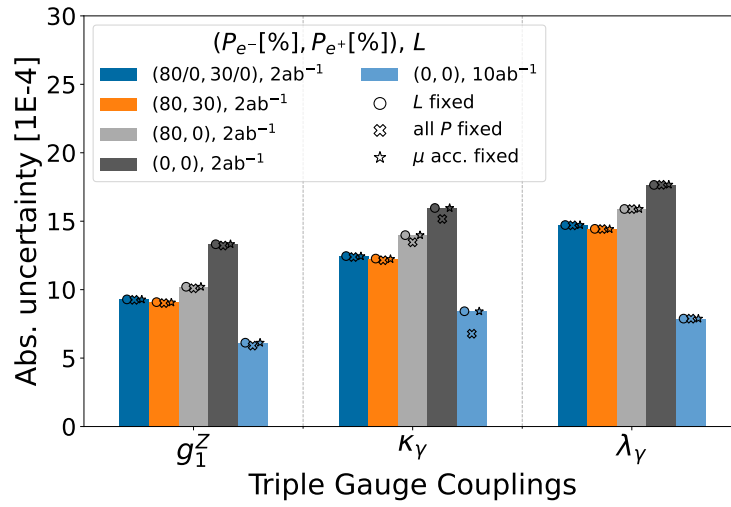
(a)



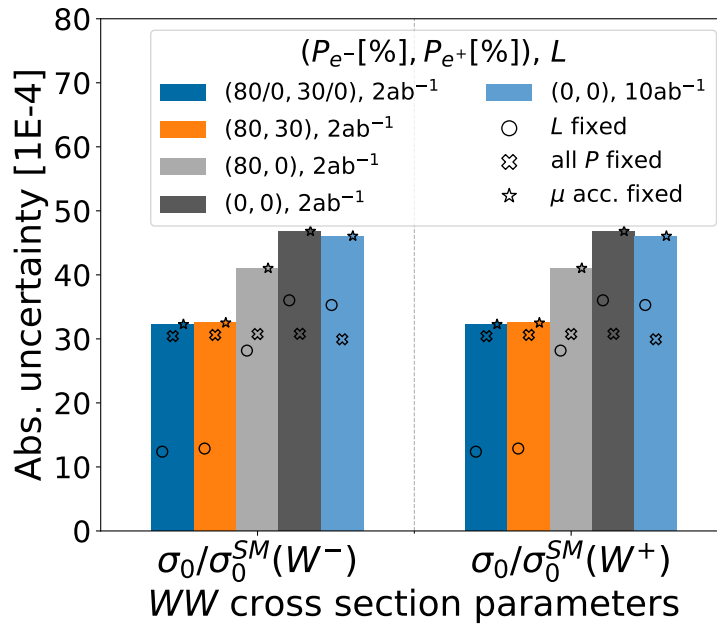
(b)

Figure 7.27.: Uncertainties of (a,b) two-fermion parameters, (c,d) W pair production parameters, and (e) systematic parameters for the combined fit in different collider scenarios (section 7.2). Uncertainties on physical parameters are absolute, those on systematic parameters are relative unless specified otherwise. Only the systematic parameters significantly improve compared to the individual fits, resulting in minor improvements of systematics-limited physical parameter precisions. (Tables with uncertainty numbers below and in appendix: tables 7.9 and C.12 to C.15)

7. Impact of beam polarisation on electroweak fits

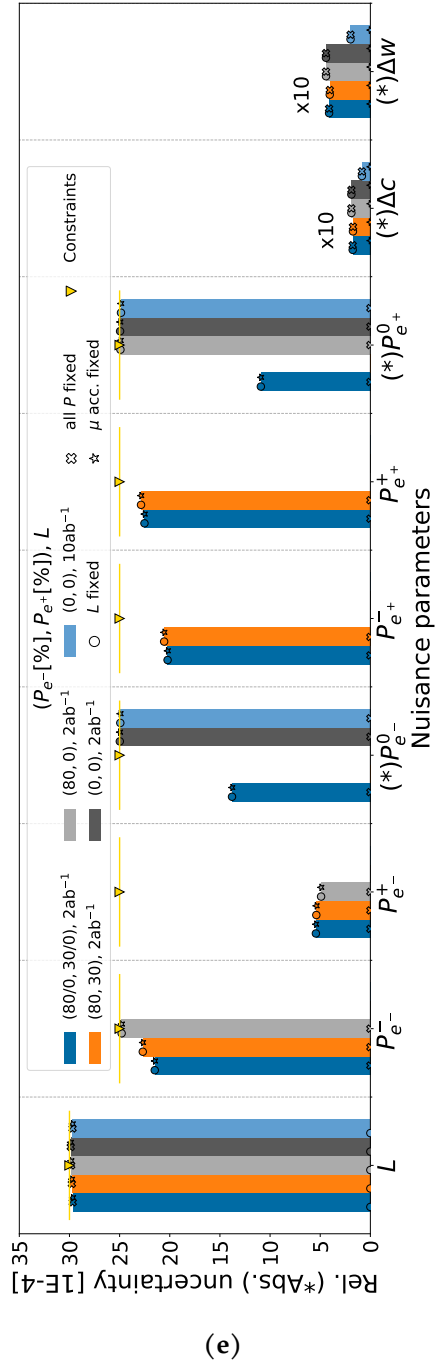


(c)

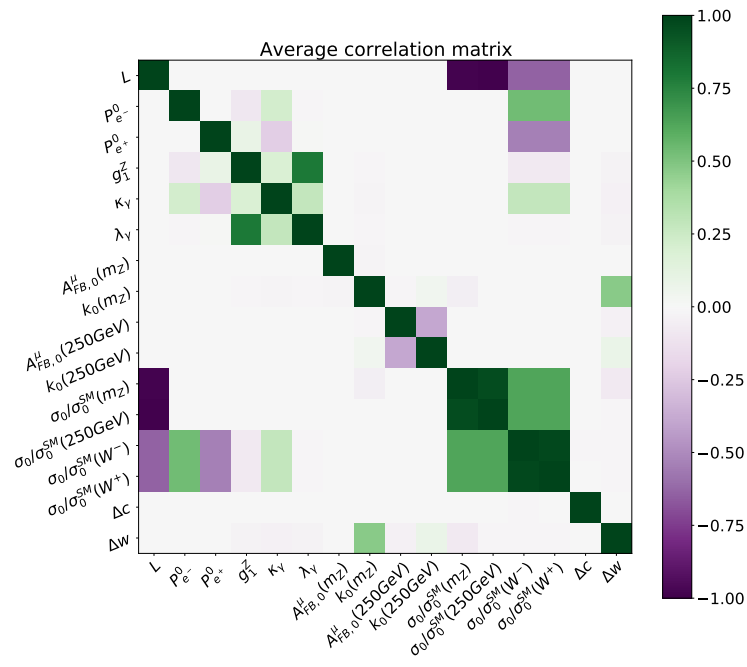


(d)

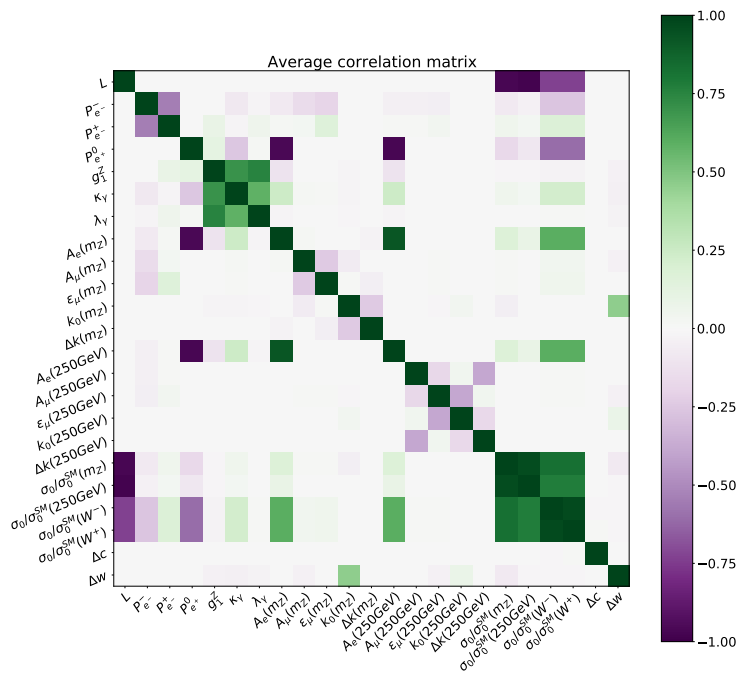
Figure 7.27.: (cont.)



7. Impact of beam polarisation on electroweak fits

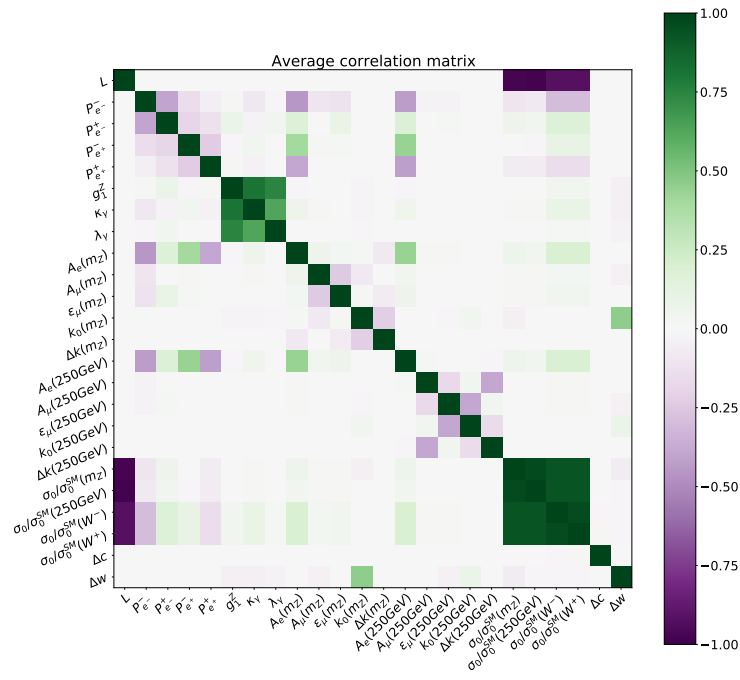


(a)

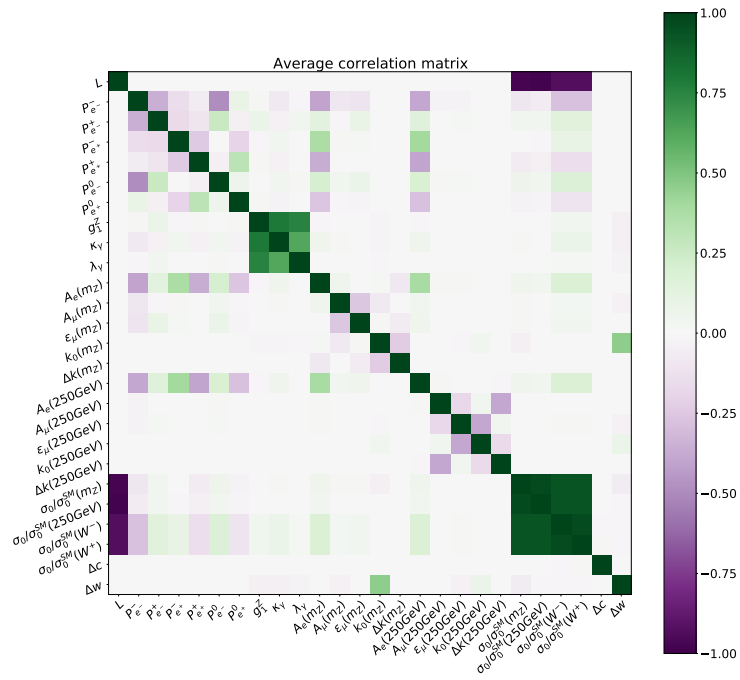


(b)

Figure 7.28: Visualisation of the correlation matrices of the (a) (0,0), (b) (80,0), (c) (80,30), and (d) (80/0,30/0) default scenarios (section 7.2) with $L = 2 \text{ ab}^{-1}$ for the combined fit. Only the correlations of systematic effects significantly change compared to the individual fits. (Duplicates with numbers in appendix: fig. C.11)



(c)



(d)

Figure 7.28.: (cont.)

each process, with the fermion pair production parameters (section 7.3.2) on the μ pair production process, and the chiral cross-section parameters and TGCs (section 7.3.3) on the semileptonic W pair production process. Like for the individual fits, the primary output of the fits are the uncertainties (fig. 7.27) and correlations (fig. 7.28) for the different collider scenarios (section 7.2). In addition to the default parameter set (bars in fig. 7.27), the fits also test scenarios that fix the parameters of one of the systematic effects (markers in fig. 7.27) to test the influence of the corresponding systematic uncertainties. The above discussions of the fits to the individual processes (sections 7.6 and 7.7) already describe a majority of the effects in the combined fit, and this section will focus on consequences specific to the combination of these fits. This includes the direct improvements for the systematic effects (section 7.8.1), subsequent indirect improvements for the physical effects (section 7.8.2), and a discussion of the final uncertainties in this study (section 7.8.3).

7.8.1. Direct improvements for systematic effects

A combination of the two processes can lead to a direct improvement of the precision on the shared parameters, and to a subsequent indirect improvement of other parameters that correlate with the subset of shared parameters. The improvements are visible in the ratio of the uncertainty from the combined fit to the uncertainty of the two individual fits (fig. 7.29). In the current implementation, only systematic effects are common to both final states, and the combination of final states only directly improves the measurement of these common systematics.

Collision data aids in the polarisation measurement when at least one beam is polarised, as seen in the individual fits (sections 7.6.1 and 7.7.1). Unpolarised scenarios consequently do not see any improvement in the polarisation precision from the combination ($(0,0)$ in fig. 7.29). If one beam is polarised, then only the W pair production measurement can provide sensitivity to the polarisations ($(80,0)$ in fig. 7.29).

In the scenarios with two polarised beams ($(80,30)$ and $(80/0,30/0)$ in fig. 7.29), the combination leads to a polarisation precisions that are significantly better than the fits that only use μ pair production (filled markers in fig. 7.29), and that slightly improve over the results of the W pair production fits (hollow markers in fig. 7.29). The W pair production measurement delivers the most precise determination of a single polarisation, with a $\mathcal{P}_{e^-}^+$ precision up to five times better than from μ pair production. The μ pair production measurement complements this with sensitivity to the polarisation which the W pair production measurement does not constrain, improving especially the precision on $\mathcal{P}_{e^-}^-$ and $\mathcal{P}_{e^+}^+$ by up to 10% relative to the polarimeter constraint.

The polarisation setting of the collider is irrelevant for the μ acceptance measurement, since such detector effects do not depend on the chirality of the colliding particles. For the μ acceptance measurement, the combination leads to a strong improvement over the results of the W pair production fits, and a slight improvement over the μ pair production fits. The large amount of forward μ 's in the μ pair production process dominates

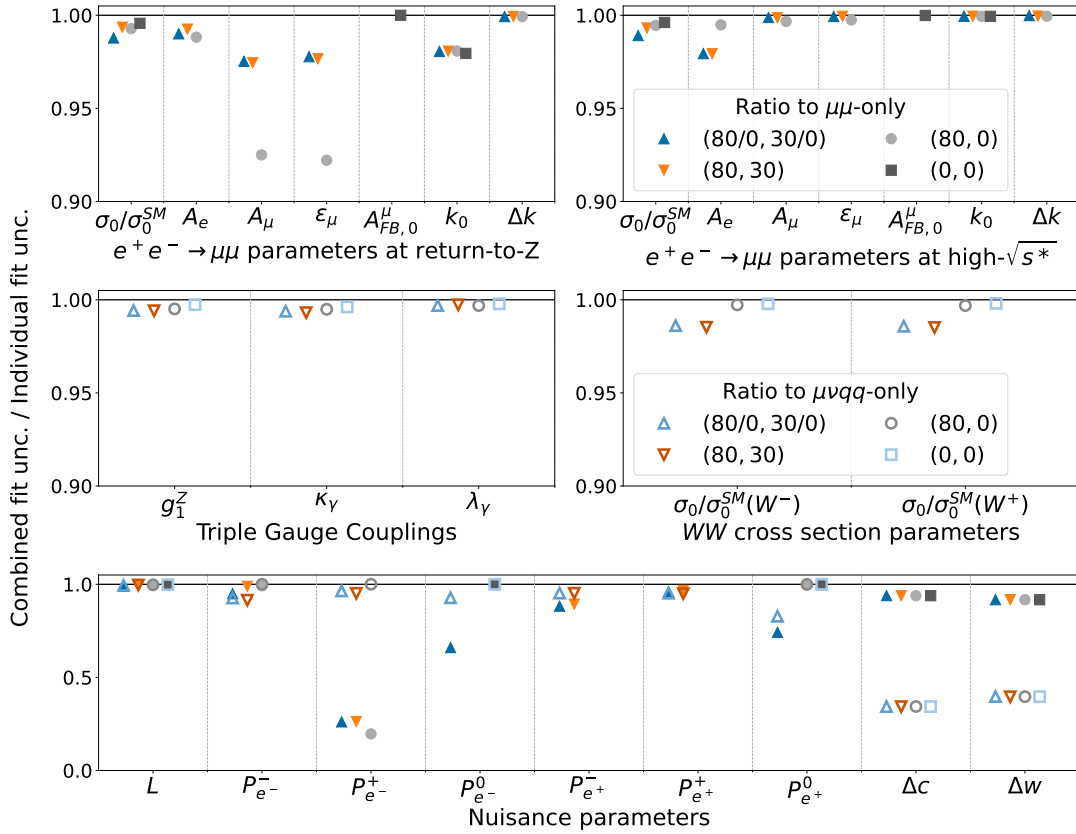


Figure 7.29.: A combined fit of the $\mu^+\mu^-$ and $\mu\nu q\bar{q}$ final states improves the common systematic uncertainties, and through that also leads to improvements on the systematics-limited uncertainties of physical parameters. Results here use $L = 2 \text{ ab}^{-1}$.

this measurement, and yields a precision three times better than the W pair production measurement. Since the parameters of the μ acceptance correlate with the physical parameters in the μ pair production measurement (section 7.6.5), the additional measurement from semileptonic W pair production is an important cross-check to avoid biases in the μ pair production parameters.

The total cross-section is a free parameter for both included final processes, so that neither of them provides additional input to the luminosity measurement.

For the shared systematic parameters, the combination of processes means that a measurement of a given parameter in one process directly benefits the measurements in the other process. When both processes provide input to a systematic effect, then the combination both improves the overall precision and cross-checks the two measurements for consistency.

7.8.2. Indirect improvements for physical effects

The current implementation of the two considered process does not include any shared physical parameters. In that context, physical effects can only indirectly benefit from the combination through a reduction of the systematic uncertainties.

For example, the μ acceptance measurement significantly interferes with the k_0 parameter measurement of return-to-Z events (section 7.6.5). As described above, the measurement of this chirality-independent parameter improves in same way for all collider scenarios (top left in fig. 7.29). The improved precision on the μ acceptance from the additional μ 's in the semileptonic W pair production process leads to a relative precision improvement on k_0 of around 2 – 3%.

In the μ pair production fit, limited knowledge of the polarisations contributes to the uncertainties on A_e in both mass ranges, as well as on A_μ and ϵ_μ on return-to-Z events (section 7.6.1). The improved polarisation measurements in the combined fit for the scenarios with at least one polarised beam lead to corresponding improvements on the uncertainties of those μ pair production parameters (top in fig. 7.29). A scenario without beam polarisation cannot measure the polarisations in the collision data.

If only one beam is polarised ((80, 0) in fig. 7.29), then the μ pair production measurement does not provide any input to the polarisation measurement and the corresponding systematic uncertainties on A_e , A_μ , and ϵ_μ are the largest. This gives importance to the additional polarisation precision from W pair production events. Since this scenario does not measure all polarisations significantly better than the polarimeter, not all parameters benefit in the same way. While the polarisation precision almost fully determines the A_e precision, the A_e precision only improves by up to 2% relative to the μ pair production fit (full markers in top of fig. 7.29). This is because the precision on the positron polarisation does not improve, which is the polarisation most relevant for the A_e precision (section 7.6.1). On the other hand, the precision on A_μ and ϵ_μ in return-to-Z events improves by 7 – 8% relative to the μ pair production fit, showing that the e^- polarisations play a more significant role for these parameters.

The precision increase is generally smaller if both beams are polarised ((80, 30) and (80/0, 30/0) in fig. 7.29) because a collider with two polarised beams already measures the polarisation in μ pair production alone. For the return-to-Z events, the precision on A_μ and ϵ_μ improves by 2 – 3% and the precision on A_e by 1 – 2% relative to the μ pair production fit. The exception is A_e in the high energy events, the precision for which increases by 2 – 3% relative to the μ pair production fit due to the improved polarisation. This shows the importance of the combined polarisation measurement also for the scenario with two polarised beams, where the processes individually already measure the polarisations.

The improved polarisation measurement of the scenarios with two polarised beams also slightly benefits the WW unpolarised cross-section measurement (middle right in fig. 7.29), leading to a relative improvement of 1 – 2%. That measurement relies on a precise determination of the $e_L^- e_R^+$ chiral cross-section (section 7.7.3). Only a collider with

two polarised beams can measure the relevant polarisations $\mathcal{D}_{e^-}^-$ and $\mathcal{D}_{e^+}^+$ in collision data.

The combination also minimally improves the TGC precision at a relative level at or below a percent (middle left in fig. 7.29). Also here the benefit is larger for the scenario with two polarised beams, indicating that the cause is the improved polarisation precision.

In all cases, the scenario with two polarised beams shows two essential benefits. First, the systematic uncertainty cause the least disturbance in the measurement of the physical effects. And second, where polarisation uncertainties are dominant, a collider with two polarised beams benefits most from the measurement of polarisation in collision data of different processes.

Minimizing the impact of systematic uncertainties will take on a new role when processes use common physical parameters. Systematic uncertainties can propagate between processes when the physical parameters overlap. This will lead to even more pronounced differences between polarised and unpolarised beams.

7.8.3. Final precisions and limitations of this study

The combined fit provides the final precisions on all parameters in this study (table 7.9). Since the primary focus of this study is the setup of framework to study how beam polarisation affects the precision, these results do not represent a final comprehensive prediction for parameter precisions of any specific collider. Any comparison to current precisions or other studies must consider the constraints of the framework of this study.

Fit results here indicate absolute precisions on TGCs of around $1-2 \cdot 10^{-3}$, and fermion pair production parameter absolute precisions ranging from $5 \cdot 10^{-4}$ for statistically limited parameters to $3 \cdot 10^{-3}$ for systematically limited ones. As described in the discussions on the individual fits (sections 7.6 and 7.7), this represents an order-of-magnitude improvement of the precision on all included parameters over current precisions from LEP and SLD [2, 3]. That is also the case for the Z-pole fermion pair production parameters, for which return-to-Z events offer an opportunity of a measurement without a dedicated Z-pole run. If future experiments find need for even more precise Z-pole studies, dedicated Z-pole runs can provide another order-of-magnitude improvement [88, 122]. All of these fit results rely on a set of imperfect assumptions, which will require future studies to investigate in detail.

One major drawback of the fit results is that they ignore the majority of experimental realities. The fits use generator-level distributions and do not consider selection efficiencies, backgrounds, detector resolutions and high-level analysis uncertainties.

For the measurement of μ pair production, LEP and SLD results show that these experimental uncertainties play only a subdominant role [2]. Selection efficiencies and purities are typically significantly above 90% in this simple final state, and the detectors measure μ 's with great precision.

The much more complicated final state of semileptonic W pair production is likely

7. Impact of beam polarisation on electroweak fits

Table 7.9.: Absolute uncertainties of the combined fits of μ pair production and semileptonic W pair production with the default parameter set for the different collider scenarios at $L = 2 \text{ ab}^{-1}$.

Parameter	True value	Abs. uncertainties [10^{-4}]			
		(0,0)	(80,0)	(80,30)	(80/0,30/0)
$\sigma_0^f/\sigma_0^{f,SM} _{Z\text{-pole}}$	1	30.5	32.0	30.5	30.4
$A_e _{Z\text{-pole}}$	0.2136	–	25.0	7.8	8.0
$A_\mu _{Z\text{-pole}}$	0.2028	–	9.4	7.7	8.3
$\epsilon_\mu _{Z\text{-pole}}$	0.0158	–	15.2	13.6	13.9
$A_{FB}^\mu _{Z\text{-pole}}$	0.0384	5.4	–	–	–
$k_0 _{Z\text{-pole}}$	0.0747	20.7	21.2	19.3	19.7
$\Delta k _{Z\text{-pole}}$	0.0006	–	23.5	19.6	21.1
$\sigma_0^f/\sigma_0^{f,SM} _{250\text{GeV}}$	1	30.3	30.5	30.3	30.2
$A_e _{250\text{GeV}}$	0.1125	–	25.5	7.4	7.6
$A_\mu _{250\text{GeV}}$	0.0322	–	6.8	5.7	6.1
$\epsilon_\mu _{250\text{GeV}}$	1.4260	–	10.9	10.0	10.2
$A_{FB}^\mu _{250\text{GeV}}$	0.5375	4.0	–	–	–
$k_0 _{250\text{GeV}}$	0.0003	14.5	14.6	13.4	13.6
$\Delta k _{250\text{GeV}}$	0.0003	–	18.2	15.3	16.4
Δg_1^Z	0	13.3	10.2	9.0	9.3
$\Delta \kappa_\gamma$	0	15.9	13.9	12.2	12.4
$\Delta \lambda_\gamma$	0	17.6	15.8	14.4	14.7
$\sigma_0/\sigma_0^{SM}(W^-)$	1	46.6	40.9	32.4	32.1
$\sigma_0/\sigma_0^{SM}(W^+)$	1	46.6	40.9	32.4	32.1
$L [\text{ab}^{-1}]$	2	60	60	60	60
\mathcal{D}_{e^-}	0.8	–	19.8	18.1	17.2
\mathcal{D}_{e^+}	0.8	–	3.9	4.3	4.3
$\mathcal{D}_{e^-}^0$	0.0	25.0	–	–	13.8
$\mathcal{D}_{e^+}^-$	0.3	–	–	6.2	6.1
$\mathcal{D}_{e^+}^+$	0.3	–	–	6.9	6.8
$\mathcal{D}_{e^+}^0$	0.0	25.0	25.0	–	10.9
Δc	0.0	0.19	0.19	0.17	0.18
$\Delta \tau$	0.0	0.44	0.44	0.40	0.41

to suffer more from experimental effects. It requires a stricter event selection due to the large set of final states with similar signatures. This typically results in selection efficiencies of around 50% and purities of around 80%, which also affect the shape of the differential distributions [157]. The global component of these efficiencies and purities lead to straightforward scalings of the statistical uncertainties [60]. Since the shape measurements is an important input to the TGC measurement (section 7.3.4), shape-dependent efficiencies and purities can change correlations and uncertainties between the TGCs. Jet energy and angular resolutions can also affect the shape measurement and cause additional systematic uncertainties.

There are also more fundamental reasons why a comparison of fit results of this study with those of other studies is not straightforward.

For the TGC extraction the fit only considers semileptonic W pair production with a μ in the final state. Previous full simulation studies have additionally included the $evqq$ final state and tried to kinematically select an WW intermediate state [157, 170]. Another way to produce this final state is through t-channel Z exchange with the subsequent radiation of a singular W . A previous study found that this single- W production can potentially reduce the uncertainties by more than a factor two [60]. The kinematic cuts of the full simulation studies aim to separate WW and single- W production from each other. Remaining irreducible single- W contributions in the $evqq$ final state can change the TGC-dependence compared to the $\mu\nu qq$ final state. This means that a comparison with those full simulation studies is not as straightforward as a simple scaling of the TGC uncertainties in this study.

For comparisons with the μ pair production result, the exact parameter definition and values complicate the picture. The fits use a special parametrisation (eqs. (7.7) and (7.8)) which differs from the LEP- and SLD-parametrisations [2]. In addition, this study does not consider the energy-dependence of the parameters within each μ pair production dataset (section 7.3.2). This entails a different set of parameter values (table 7.4), which also determines the sensitivity of the differential distributions to those parameters (section 7.6.4). A precise comparison of such differing parametrisations requires a parameter transformation and needs to take parameter correlations into account.

With these imperfections in mind, the fit results suggest significant improvements over current precisions, and can motivate future studies with increasing realism to provide more thorough predictions.

7.9. Conclusions

This goal of this study is to address the question of how beam polarisation influences the determination of physical and systematic effects at future e^+e^- collider, in both qualitative and quantitative fashion. It expands on a large set of previous studies (for example [38, 60, 145, 240]), and draws the focus on how the effort of polarising a beam changes

7. Impact of beam polarisation on electroweak fits

the landscape of measurements and precisions.

This study builds on a dedicated fit framework (section 7.1) which can fit physical and systematic effects for different polarisation and luminosity options (section 7.2) of an e^+e^- collider. The fits here serve as a proof-of-principle for this framework. For this purpose, they limit themselves to the 250 GeV stage of an e^+e^- collider and to differential distributions of the $\mu^+\mu^-$ and $\mu\nu qq$ final states. The parameter set (sections 7.3 and 7.4) includes the common systematic effects of luminosity and polarisations with corresponding constraints, and the μ acceptance as experimental systematic effect. Relevant physical effects here are fermion pair production parameters on $\mu^+\mu^-$ and triple gauge couplings (TGCs) on $\mu\nu qq$. For fermion pair production, the fit uses a special differential shape parametrisation that includes parameters that correct for effects of initial state radiation. The parametrisation of the TGCs uses WHIZARD to extract the impact on the differential distribution.

One of the most important systematic effects in electroweak precision measurements is the beam polarisation itself. The collision data is sensitive to the exact polarisation, which potentially allows a measurement of those polarisations from the collision data [139]. A collider can measure all polarisations if the number of measurements of chiral cross-sections surpasses the combined number of polarisation and cross-section observables. Depending on the definition of the set of observables, this can be the case for a collider with only one polarised beam. Polarising both beams of the collider guarantees sufficient redundancy. Fit results reflect these ideas both for two-fermion and four-fermion final state measurements, showing that a collider with one polarised beam can measure a subset of the polarisations from collision data, and that this extends to all polarisations when both beams are polarised (section 7.8.1). The fits find that such a polarised collider with two polarised beams can even gain additional redundancy by including unpolarised beam settings in the polarisation combinations.

Fit results also demonstrate that a polarisation measurement from collision data requires a significant chiral asymmetry of the final state (section 7.7.2). For that reason, W pair production - with an asymmetry close to one - provides a much stronger polarisation constraint than μ pair production. The value of the left-right asymmetry of a process also determines which polarisations that process can effectively constrain. A combination of processes with different asymmetry values provides constraints on all polarisations. This puts a new emphasis on measurements with return-to- Z events in high energy stages where the polarisation measurement can use W pair production data.

The fit directly includes a simple model for the μ acceptance with two model parameters (section 7.4) that the fit can extract from the differential distributions. This allows the study of how beam polarisation affects experimental systematic uncertainties. Here, the μ acceptance turns out to play minimal role for the two considered final states (sections 7.6.5 and 7.7.5). The only observed impact in μ pair production affects a chirality-independent parameter. The μ acceptance does not affect any chirality-dependent observables. This demonstrates how a polarised collider can access chiral observables

which are largely unaffected by experimental systematics.

Beam polarisation also shows clear advantages for a measurement of physical parameters in two- and four-fermion final states. Unpolarised measurements cannot access chiral observables, and can only access such observables through final states helicity measurements or with additional assumptions. Both final states in the fit provide concrete examples of this benefit. Without beam polarisation, a collider can only measure half of the fermion pair production observables directly in all final states (section 7.6.1). A collider with polarised beams achieves a factor 4 – 8 better precision in the final state asymmetry A_μ than an unpolarised collider (section 7.6.2). The TGC precision also sees a qualitative benefit from beam polarisation (section 7.7.4). A precise determination of the left-right asymmetry of W pair production is essential for restraining the TGCs. Beam polarisation leads to an improved measurement of that asymmetry because polarised collider can directly access this observable. That same asymmetry measurement will likely also benefit from the improved eeZ coupling measurement at a polarised collider.

Positron polarisation plays a non-trivial role in this. As seen already for polarisation measurement, positron polarisation adds redundancy that removes correlations and ambiguities. The most striking example is the ambiguity of polarisations and the electron asymmetry A_e ; positron polarisation removes this ambiguity and with it the systematic limit on the physical parameter (section 7.6.1).

An unpolarised collider can in many cases catch up with the precision of a polarised collider by increasing the luminosity by a factor of five. At the same time, an increased luminosity cannot resolve fundamental differences between unpolarised and polarised collider. Measurements of chiral observables are significantly more challenging with an unpolarised collider.

7.9.1. Recommendations for future studies

Future studies can consider expanding on this work, or ask themselves where to go with it. For them, the following paragraphs give an overview of lessons from this study and recommendation for future ones.

A large part of the time to perform this study went into setting up the fitting framework. The framework, based on ROOTs TMinuit2 minimization [218], ended up being fairly specific to the task of this study, and does not have a particularly intuitive interface or core. Future studies will likely benefit from using the RooFit framework instead, which is designed for likelihood fits to data. RooFit has some crucial advantages like extensive documentation, a Python-implementation, and straightforward ways to implement arbitrary fit functions.

The conclusions of this study also suffer from the limited scope of the fit setup. Here, some concrete recommendation are possible that will make the fit more complete and realistic.

- **Common EFT + SM parameter set:**

The fit does currently not model any common physical parameters of the final states. This turns out particularly problematic for the common eeZ vertex (section 7.7.4). A common set of EFT and SM parameters can resolve this issue. It will further provide a consistent treatment of physical parameters, in contrast to the very different approaches of the current fit to TGCs and fermion pair production parameters. The implementation can follow the same path as the current TGC implementation. Some technical issues, which now are resolved, prohibited this study from using such an approach.

- **Including other final states:**

Both the TGCs and some difermion parameters (e.g. A_e) find major constraints in other final states that the fit did not include. Main candidates are single- W production ($evqq$) for the TGCs and other fermion pair production final states for A_e . Previous studies have used both of these before and seen significant impacts on TGC and polarisation precisions [60]. Special attention may go in including τ pair production, which can include the measurement of τ polarisation directly in the fit.

- **Including hadronic decay angles:**

Previous studies of TGC measurements at e^+e^- colliders have shown that the decay angles of the hadronically decaying W can increase the precisions by around 10% even with imperfect charge measurements [241]. This is because the decay angles contain information about the W helicities [160]. Including these angles is also going to open up the possibility to including fully hadronic W pair production and quark pair production. Doing so will require a treatment of charge confusion in the fit.

- **Including backgrounds:**

The current implementation does not consider backgrounds in the differential distribution. Guided by full simulation analysis, the fit can include backgrounds as part of the fitted distribution. This can be especially important for return-to- Z measurements, for which previous studies predict an overwhelming eeZ background [109]. Notably, the fit can provide statistically sound results by including the impact of the physical and systematic parameters on the backgrounds.

- **Expanding the systematic effects:**

The current fit results do not reflect a better control of systematic effect when beams are polarised. A possible explanation is that the implemented effect is too simple, affects too few bins, and correspondingly easily separated from other effects. This is also reflected in the very minimal impact that the μ acceptance has on the measurement of the physical parameters. A fit that includes additional and more detailed systematic effects will be able to give more concrete statements on

the matter. Full simulation detector studies can motivate the shape of such effects. The implementation can use the same approach as the one for the μ acceptance.

- **Consider correlated polarimeter measurements:**

The current implementation employs polarimeter constraints on each polarisation independently. This assumes that systematic uncertainties of the individual polarisation measurements are uncorrelated. While this assumption is reasonable for the two separate beams, the measurements of the different signed polarisations of the same beam are measured by the same detectors. This means that the polarimeter measurements on the two signed polarisations of the same beam can have correlated uncertainties.

The fit results also raise some questions with respect to the analysis of the considered final states. These require dedicated studies, or can become part of future expansions of this study.

- **Which precision on the eeZ vertex does the TGC measurement require?**

The TGC measurement in W pair production relies heavily on the asymmetry information (section 7.7.4). Uncertainties on the eeZ vertex will disturb that information. Which precision on the eeZ vertex is needed? What happens when including single- W events in the TGC fit?

- **Is it possible to measure τ polarisation in return-to- Z events?**

A measurement of τ polarisation in return-to- Z events might provide an important cross-check of the A_e measurement when at least one beam is unpolarised (section 7.6.4). The feasibility of this measurement in the forward-boosted topology of return-to- Z events is an open question.

- **Is it useful to bin the fermion pair production in m_{ff} ?**

The energy-dependence of the fermion pair production parameters is well-understood [2]. So far, future e^+e^- collider studies on return-to- Z events did not consider a binning in the fermion pair mass to capture this dependence.

The current implementation of the fit lays the groundwork for studying such combined fits. When adding more realism and completeness, the fit will allow more reliable and comprehensive conclusions to guide the discussion on the future of particle physics.

8. Conclusion

Future e^+e^- colliders will run at energies between the Z pole and TeV scales, and produce orders-of-magnitude more events than the previous e^+e^- machines. This will lead to unprecedented statistical precision on physical parameter. The question quickly becomes which other effects can interfere with that precision and how the machine can prepare for those.

Two studies here shed light on which effects limit the electroweak precision at future e^+e^- colliders.

A first part of this study (chapter 6) considers the kinematic separation of hadronic W and Z decays in the context of a vector boson scattering search. The results show that detector resolution, beam backgrounds and high level analysis effects all can hinder the electroweak precision. This motivates future studies to look into possible improvements in the analysis techniques, like reconstructing semi-leptonic decays, improved beam background removal, and improved clustering techniques. Details of the detector model do not show an impact in this analysis, other analyses come to varying conclusions depending on the signal [123].

A second approach here (chapter 7) is a study of electroweak fits using generator level distributions of two- and four-fermion production, and largely ignoring detector and analysis systematics. The results of that study demonstrate that electroweak precision requires precise knowledge of systematic effects like beam polarisation, luminosity, and detector acceptances. They further show that differential distributions cannot always separate physical effects, or physical from systematic effects, leaving open directions in the parameter space.

Limitations from combination of detector resolution and acceptance, high level analysis methods, systematic uncertainties and correlated parameters will bring new and unforeseen challenges to electroweak measurements. The design of future e^+e^- colliders and detectors is a crucial step to tackle these challenges.

As the test of electroweak fits in this study show, equipping the machine with beam polarisation can help electroweak precision. The most important impact of polarised beams is the direct access to chiral observables, which distinguish different physical effects and largely go unharmed by systematic uncertainties. A collider with polarised beams also use the collision data to measure the polarisations - a crucial systematic uncertainty in the highly chirality-dependent electroweak sector. Here, colliders with two polarised beams have a clear advantage because the larger number of polarisation combination distinguishes the behaviour of the polarisations from any physical effects. This study finds that future e^+e^- colliders can achieve precisions in the range of 10^{-4} to

8. Conclusion

10^{-3} for both two-fermion and four-fermion parameters. It will be a major experimental challenge to keep all experimental effects under control at a similar precision. Beam polarisation will significantly alleviate a part of this challenge.

This study shows that there the choice of collider, running plan and detector design all have complex impacts on the precision of electroweak measurements. By shedding light on some of these aspects, the author hopes to constructively contribute to the ongoing discussion about the next big collider project. In such a highly political discussion, it is essential to know which trade-offs each choice represents, and to always keep the goal in mind: to reveal the gaps in our understanding of the most fundamental principles of nature.

References

- [1] European Strategy Group. *2020 Update of the European Strategy for Particle Physics*. Tech. rep. Geneva, 2020. DOI: 10.17181/ESU2020.
- [2] “Precision electroweak measurements on the Z resonance”. In: *Physics Reports* 427.5 (2006), pp. 257–454. ISSN: 0370-1573. DOI: <https://doi.org/10.1016/j.physrep.2005.12.006>. URL: <https://www.sciencedirect.com/science/article/pii/S0370157305005119>.
- [3] “Electroweak measurements in electron–positron collisions at W-boson-pair energies at LEP”. In: *Physics Reports* 532.4 (2013). Electroweak Measurements in Electron-Positron Collisions at W-Boson-Pair Energies at LEP, pp. 119–244. ISSN: 0370-1573. DOI: <https://doi.org/10.1016/j.physrep.2013.07.004>. URL: <https://www.sciencedirect.com/science/article/pii/S0370157313002706>.
- [4] P.A. Zyla et al. “Review of Particle Physics”. In: *PTEP* 2020.8 (2020), p. 083C01. DOI: 10.1093/ptep/ptaa104.
- [5] Abdus Salam and J. C. Ward. “Weak and electromagnetic interactions”. In: *Il Nuovo Cimento (1955-1965)* 11.4 (Feb. 1959), pp. 568–577. ISSN: 1827-6121. DOI: 10.1007/BF02726525. URL: <https://doi.org/10.1007/BF02726525>.
- [6] Sheldon L. Glashow. “Partial-symmetries of weak interactions”. In: *Nuclear Physics* 22.4 (1961), pp. 579–588. ISSN: 0029-5582. DOI: [https://doi.org/10.1016/0029-5582\(61\)90469-2](https://doi.org/10.1016/0029-5582(61)90469-2). URL: <https://www.sciencedirect.com/science/article/pii/0029558261904692>.
- [7] Steven Weinberg. “A Model of Leptons”. In: *Phys. Rev. Lett.* 19 (21 Nov. 1967), pp. 1264–1266. DOI: 10.1103/PhysRevLett.19.1264. URL: <https://link.aps.org/doi/10.1103/PhysRevLett.19.1264>.
- [8] H. Fritzsch, M. Gell-Mann, and H. Leutwyler. “Advantages of the color octet gluon picture”. In: *Physics Letters B* 47.4 (1973), pp. 365–368. ISSN: 0370-2693. DOI: [https://doi.org/10.1016/0370-2693\(73\)90625-4](https://doi.org/10.1016/0370-2693(73)90625-4). URL: <https://www.sciencedirect.com/science/article/pii/0370269373906254>.
- [9] F. Englert and R. Brout. “Broken Symmetry and the Mass of Gauge Vector Mesons”. In: *Phys. Rev. Lett.* 13 (9 Aug. 1964), pp. 321–323. DOI: 10.1103/PhysRevLett.13.321. URL: <https://link.aps.org/doi/10.1103/PhysRevLett.13.321>.

8. Conclusion

- [10] G. S. Guralnik, C. R. Hagen, and T. W. B. Kibble. “Global Conservation Laws and Massless Particles”. In: *Phys. Rev. Lett.* 13 (20 Nov. 1964), pp. 585–587. DOI: 10.1103/PhysRevLett.13.585. URL: <https://link.aps.org/doi/10.1103/PhysRevLett.13.585>.
- [11] Peter W. Higgs. “Broken Symmetries and the Masses of Gauge Bosons”. In: *Phys. Rev. Lett.* 13 (16 Oct. 1964), pp. 508–509. DOI: 10.1103/PhysRevLett.13.508. URL: <https://link.aps.org/doi/10.1103/PhysRevLett.13.508>.
- [12] P.W. Higgs. “Broken symmetries, massless particles and gauge fields”. In: *Physics Letters* 12.2 (1964), pp. 132–133. ISSN: 0031-9163. DOI: [https://doi.org/10.1016/0031-9163\(64\)91136-9](https://doi.org/10.1016/0031-9163(64)91136-9). URL: <https://www.sciencedirect.com/science/article/pii/0031916364911369>.
- [13] Peter W. Higgs. “Spontaneous Symmetry Breakdown without Massless Bosons”. In: *Phys. Rev.* 145 (4 May 1966), pp. 1156–1163. DOI: 10.1103/PhysRev.145.1156. URL: <https://link.aps.org/doi/10.1103/PhysRev.145.1156>.
- [14] Paul Adrien Maurice Dirac and Ralph Howard Fowler. “The quantum theory of the electron”. In: *Proceedings of the Royal Society of London. Series A, Containing Papers of a Mathematical and Physical Character* 117.778 (1928), pp. 610–624. DOI: 10.1098/rspa.1928.0023. eprint: <https://royalsocietypublishing.org/doi/pdf/10.1098/rspa.1928.0023>. URL: <https://royalsocietypublishing.org/doi/abs/10.1098/rspa.1928.0023>.
- [15] T. D. Lee and C. N. Yang. “Question of Parity Conservation in Weak Interactions”. In: *Phys. Rev.* 104 (1 Oct. 1956), pp. 254–258. DOI: 10.1103/PhysRev.104.254. URL: <https://link.aps.org/doi/10.1103/PhysRev.104.254>.
- [16] C. S. Wu et al. “Experimental Test of Parity Conservation in Beta Decay”. In: *Phys. Rev.* 105 (4 Feb. 1957), pp. 1413–1415. DOI: 10.1103/PhysRev.105.1413. URL: <https://link.aps.org/doi/10.1103/PhysRev.105.1413>.
- [17] G. Aad et al. “Observation of a new particle in the search for the Standard Model Higgs boson with the ATLAS detector at the LHC”. In: *Physics Letters B* 716.1 (2012), pp. 1–29. ISSN: 0370-2693. DOI: <https://doi.org/10.1016/j.physletb.2012.08.020>. URL: <https://www.sciencedirect.com/science/article/pii/S037026931200857X>.
- [18] S. Chatrchyan et al. “Observation of a new boson at a mass of 125 GeV with the CMS experiment at the LHC”. In: *Physics Letters B* 716.1 (2012), pp. 30–61. ISSN: 0370-2693. DOI: <https://doi.org/10.1016/j.physletb.2012.08.021>. URL: <https://www.sciencedirect.com/science/article/pii/S0370269312008581>.
- [19] A.M. Sirunyan et al. “Measurement and interpretation of differential cross sections for Higgs boson production at s=13TeV”. In: *Physics Letters B* 792 (2019), pp. 369–396. ISSN: 0370-2693. DOI: <https://doi.org/10.1016/j.physletb.2019.03.011>.

- 2019.03.059. URL: <https://www.sciencedirect.com/science/article/pii/S037026931930228X>.
- [20] Combined measurements of Higgs boson production and decay using up to 139 fb^{-1} of proton-proton collision data at $\sqrt{s} = 13\text{ TeV}$ collected with the ATLAS experiment. Tech. rep. All figures including auxiliary figures are available at <https://atlas.web.cern.ch/Atlas/GROUPS/PHYSICS/CONFNOTES/ATLAS-CONF-2021-053>. Geneva: CERN, Nov. 2021. URL: <http://cds.cern.ch/record/2789544>.
- [21] M. Gell-Mann. "A schematic model of baryons and mesons". In: *Physics Letters* 8.3 (1964), pp. 214–215. ISSN: 0031-9163. DOI: [https://doi.org/10.1016/S0031-9163\(64\)92001-3](https://doi.org/10.1016/S0031-9163(64)92001-3). URL: <https://www.sciencedirect.com/science/article/pii/S0031916364920013>.
- [22] G Zweig. "An SU_3 model for strong interaction symmetry and its breaking; Version 2". In: (Feb. 1964). Version 1 is CERN preprint 8182/TH.401, Jan. 17, 1964, 80 p. URL: <http://cds.cern.ch/record/570209>.
- [23] O. Biebel. "Experimental tests of the strong interaction and its energy dependence in electron-positron annihilation". In: *Physics Reports* 340.3 (2001), pp. 165–289. ISSN: 0370-1573. DOI: [https://doi.org/10.1016/S0370-1573\(00\)00072-7](https://doi.org/10.1016/S0370-1573(00)00072-7). URL: <https://www.sciencedirect.com/science/article/pii/S0370157300000727>.
- [24] Reinhard Alkofer. "Confinement & Chiral Symmetry Breaking: The fundamental problems of hadron physics". In: *Nuclear Physics B - Proceedings Supplements* 195 (2009). Proceedings of the 47th Internationale Universitätswochen für Theoretische Physik, pp. 261–266. ISSN: 0920-5632. DOI: <https://doi.org/10.1016/j.nuclphysbps.2009.10.018>. URL: <https://www.sciencedirect.com/science/article/pii/S0920563209007397>.
- [25] Gunnar S. Bali et al. "Static potentials and glueball masses from QCD simulations with Wilson sea quarks". In: *Phys. Rev. D* 62 (5 July 2000), p. 054503. DOI: 10.1103/PhysRevD.62.054503. URL: <https://link.aps.org/doi/10.1103/PhysRevD.62.054503>.
- [26] David J. Gross and Frank Wilczek. "Ultraviolet Behavior of Non-Abelian Gauge Theories". In: *Phys. Rev. Lett.* 30 (26 June 1973), pp. 1343–1346. DOI: 10.1103/PhysRevLett.30.1343. URL: <https://link.aps.org/doi/10.1103/PhysRevLett.30.1343>.
- [27] H. David Politzer. "Reliable Perturbative Results for Strong Interactions?" In: *Phys. Rev. Lett.* 30 (26 June 1973), pp. 1346–1349. DOI: 10.1103/PhysRevLett.30.1346. URL: <https://link.aps.org/doi/10.1103/PhysRevLett.30.1346>.
- [28] James D. Bjorken and Stanley J. Brodsky. "Statistical Model for Electron-Positron Annihilation into Hadrons". In: *Phys. Rev. D* 1 (5 Mar. 1970), pp. 1416–1420. DOI: 10.1103/PhysRevD.1.1416. URL: <https://link.aps.org/doi/10.1103/PhysRevD.1.1416>.

8. Conclusion

- [29] G. Hanson et al. “Evidence for Jet Structure in Hadron Production by e^+e^- Annihilation”. In: *Phys. Rev. Lett.* 35 (24 Dec. 1975), pp. 1609–1612. DOI: 10.1103/PhysRevLett.35.1609. URL: <https://link.aps.org/doi/10.1103/PhysRevLett.35.1609>.
- [30] The ALEPH collaboration. *ALEPH archived webpage - Event Displays*. July 7, 2022. URL: <https://aleph.web.cern.ch/aleph/aleph/newpub/dali-displays.html>.
- [31] Stefano Moretti, Leif Lönnblad, and Torbjörn Sjöstrand. “New and old jet clustering algorithms for electron-positron events”. In: *Journal of High Energy Physics* 1998.08 (Aug. 1998), pp. 001–001. DOI: 10.1088/1126-6708/1998/08/001. URL: <https://doi.org/10.1088/1126-6708/1998/08/001>.
- [32] Ryan Atkin. “Review of jet reconstruction algorithms”. In: *Journal of Physics: Conference Series* 645 (Oct. 2015), p. 012008. DOI: 10.1088/1742-6596/645/1/012008. URL: <https://doi.org/10.1088/1742-6596/645/1/012008>.
- [33] M. Boronat et al. “Jet reconstruction at high-energy electron-positron colliders”. In: *The European Physical Journal C* 78.2 (Feb. 2018), p. 144. ISSN: 1434-6052. DOI: 10.1140/epjc/s10052-018-5594-6. URL: <https://doi.org/10.1140/epjc/s10052-018-5594-6>.
- [34] S. Catani et al. “Longitudinally-invariant k_{\perp} -clustering algorithms for hadron-hadron collisions”. In: *Nuclear Physics B* 406.1 (1993), pp. 187–224. ISSN: 0550-3213. DOI: [https://doi.org/10.1016/0550-3213\(93\)90166-M](https://doi.org/10.1016/0550-3213(93)90166-M). URL: <https://www.sciencedirect.com/science/article/pii/055032139390166M>.
- [35] S. Catani et al. “New clustering algorithm for multijet cross sections in $e+e-$ annihilation”. In: *Physics Letters B* 269.3 (1991), pp. 432–438. ISSN: 0370-2693. DOI: [https://doi.org/10.1016/0370-2693\(91\)90196-W](https://doi.org/10.1016/0370-2693(91)90196-W). URL: <https://www.sciencedirect.com/science/article/pii/037026939190196W>.
- [36] Mark Thomson. *Modern Particle Physics*. Cambridge University Press, 2013. DOI: 10.1017/CB09781139525367.
- [37] Jorge M. R. Crispim Romão and João Silva. “A resource for signs and Feynman diagrams of the Standard Model”. In: *International Journal of Modern Physics A* 27.26 (Oct. 2012), p. 1230025. DOI: 10.1142/s0217751x12300256. URL: <https://doi.org/10.1142/s0217751x12300256>.
- [38] Morris L. Swartz. “Physics with polarized electron beams”. In: *Conf. Proc. C* 8708101 (1987). Ed. by Eileen C. Brennan, pp. 83–131. URL: <https://www-public.slac.stanford.edu/sciDoc/docMeta.aspx?slacPubNumber=SLAC-PUB-4656>.
- [39] M. Böhm and W. Hollik. “Radiative corrections to polarized $e-e+$ annihilation in the standard electroweak model”. In: *Nuclear Physics B* 204.1 (1982), pp. 45–77. ISSN: 0550-3213. DOI: [https://doi.org/10.1016/0550-3213\(82\)90421-7](https://doi.org/10.1016/0550-3213(82)90421-7). URL: <https://www.sciencedirect.com/science/article/pii/0550321382904217>.

- [40] Marek Karliner et al. “Radiative return capabilities of a high-energy, high-luminosity e^+e^- collider”. In: *Phys. Rev. D* 92 (3 Aug. 2015), p. 035010. DOI: 10.1103/PhysRevD.92.035010. URL: <https://link.aps.org/doi/10.1103/PhysRevD.92.035010>.
- [41] Tomio Kobayashi. “Experimental verification of the standard model of particle physics”. en. In: *Proc Jpn Acad Ser B Phys Biol Sci* 97.5 (2021), pp. 211–235. DOI: 10.2183/pjab.97.013.
- [42] Björn Garbrecht. “Why is there more matter than antimatter? Computational methods for leptogenesis and electroweak baryogenesis”. In: *Progress in Particle and Nuclear Physics* 110 (2020), p. 103727. ISSN: 0146-6410. DOI: <https://doi.org/10.1016/j.pnpnp.2019.103727>. URL: <https://www.sciencedirect.com/science/article/pii/S0146641019300626>.
- [43] Katherine Garrett and Gintaras Duda. “Dark Matter: A Primer”. In: *Advances in Astronomy* 2011 (Dec. 2010), p. 968283. ISSN: 1687-7969. DOI: 10.1155/2011/968283. URL: <https://doi.org/10.1155/2011/968283>.
- [44] Bing-Lin Young. “A survey of dark matter and related topics in cosmology”. In: *Frontiers of Physics* 12.2 (Oct. 2016), p. 121201. ISSN: 2095-0470. DOI: 10.1007/s11467-016-0583-4. URL: <https://doi.org/10.1007/s11467-016-0583-4>.
- [45] K. G. Begeman. “HI rotation curves of spiral galaxies. I. NGC 3198.” In: *AAP* 223 (Oct. 1989), pp. 47–60. URL: <https://ui.adsabs.harvard.edu/abs/1989A&A...223...47B>.
- [46] D. Walsh, R. F. Carswell, and R. J. Weymann. “0957+561 A, B: twin quasistellar objects or gravitational lens?” In: *Nature* 279 (May 1979), pp. 381–384. DOI: 10.1038/279381a0.
- [47] Roger Lynds and Vahe Petrosian. “Luminous Arcs in Clusters of Galaxies”. In: *ApJ* 336 (Jan. 1989), p. 1. DOI: 10.1086/166989.
- [48] Anton G. Bergmann, Vahe Petrosian, and Roger Lynds. “Gravitational Lens Models of Arcs in Clusters”. In: *ApJ* 350 (Feb. 1990), p. 23. DOI: 10.1086/168359.
- [49] N. Jarosik et al. “Seven-Year Wilkinson Microwave Anisotropy Probe (WMAP) Observations: Sky Maps, Systematic Errors, and Basic Results”. In: *The Astrophysical Journal Supplement Series* 192.2 (Jan. 2011), p. 14. DOI: 10.1088/0067-0049/192/2/14. URL: <https://doi.org/10.1088/0067-0049/192/2/14>.
- [50] Marc Schumann. “Direct detection of WIMP dark matter: concepts and status”. In: *Journal of Physics G: Nuclear and Particle Physics* 46.10 (Aug. 2019), p. 103003. DOI: 10.1088/1361-6471/ab2ea5. URL: <https://doi.org/10.1088/1361-6471/ab2ea5>.
- [51] Leszek Roszkowski. “Particle dark matter — A theorist’s perspective”. In: *Pramana* 62.2 (Feb. 2004), pp. 389–401. ISSN: 0973-7111. DOI: 10.1007/BF02705097. URL: <https://doi.org/10.1007/BF02705097>.

8. Conclusion

- [52] Ilaria Brivio and Michael Trott. “The standard model as an effective field theory”. In: *Physics Reports* 793 (2019). The standard model as an effective field theory, pp. 1–98. ISSN: 0370-1573. DOI: <https://doi.org/10.1016/j.physrep.2018.11.002>. URL: <https://www.sciencedirect.com/science/article/pii/S0370157318303223>.
- [53] W. Buchmüller and D. Wyler. “Effective lagrangian analysis of new interactions and flavour conservation”. In: *Nuclear Physics B* 268.3 (1986), pp. 621–653. ISSN: 0550-3213. DOI: [https://doi.org/10.1016/0550-3213\(86\)90262-2](https://doi.org/10.1016/0550-3213(86)90262-2). URL: <https://www.sciencedirect.com/science/article/pii/0550321386902622>.
- [54] K. Hagiwara et al. “Low energy effects of new interactions in the electroweak boson sector”. In: *Phys. Rev. D* 48 (5 Sept. 1993), pp. 2182–2203. DOI: 10.1103/PhysRevD.48.2182. URL: <https://link.aps.org/doi/10.1103/PhysRevD.48.2182>.
- [55] Andrew Kobach. “Baryon number, lepton number, and operator dimension in the Standard Model”. In: *Physics Letters B* 758 (2016), pp. 455–457. ISSN: 0370-2693. DOI: <https://doi.org/10.1016/j.physletb.2016.05.050>. URL: <https://www.sciencedirect.com/science/article/pii/S0370269316301976>.
- [56] B. Grzadkowski et al. “Dimension-six terms in the Standard Model Lagrangian”. In: *Journal of High Energy Physics* 2010.10 (Oct. 2010), p. 85. ISSN: 1029-8479. DOI: 10.1007/JHEP10(2010)085. URL: [https://doi.org/10.1007/JHEP10\(2010\)085](https://doi.org/10.1007/JHEP10(2010)085).
- [57] Markus Diehl, Otto Nachtmann, and Felix Nagel. “Triple gauge couplings in polarized $e^-e^+ \rightarrow W^-W^+$ and their measurement using optimal observables”. In: *Eur. Phys. J. C* 27 (2003), pp. 375–397. DOI: 10.1140/epjc/s2002-01096-y. arXiv: hep-ph/0209229.
- [58] George J Gounaris et al. “Triple gauge boson couplings”. In: (1996). DOI: 10.5170/CERN-1996-001-V-1.525. URL: <http://cds.cern.ch/record/293937>.
- [59] Christian Fleper et al. “Scattering of W and Z bosons at high-energy lepton colliders”. In: *The European Physical Journal C* 77.2 (Feb. 2017). ISSN: 1434-6052. DOI: 10.1140/epjc/s10052-017-4656-5. URL: <http://dx.doi.org/10.1140/epjc/s10052-017-4656-5>.
- [60] Robert Karl. “From the Machine-Detector Interface to Electroweak Precision Measurements at the ILC — Beam-Gas Background, Beam Polarization and Triple Gauge Couplings”. Dissertation, Universität Hamburg, 2019. Dissertation. Hamburg: Universität Hamburg, 2019, p. 330. DOI: 10.3204/PUBDB-2019-03013. URL: <https://bib-pubdb1.desy.de/record/424633>.
- [61] K. J. F. Gaemers and G. J. Gounaris. “Polarization amplitudes for $e^+e^- \rightarrow W^+W^-$ and $e^+e^- \rightarrow ZZ$ ”. In: *Zeitschrift für Physik C Particles and Fields* 1.3 (Sept. 1979), pp. 259–268. ISSN: 1431-5858. DOI: 10.1007/BF01440226. URL: <https://doi.org/10.1007/BF01440226>.

- [62] K. Hagiwara et al. “Probing the weak boson sector in $e+e\rightarrow W+W-$ ”. In: *Nuclear Physics B* 282 (1987), pp. 253–307. ISSN: 0550-3213. DOI: [https://doi.org/10.1016/0550-3213\(87\)90685-7](https://doi.org/10.1016/0550-3213(87)90685-7). URL: <https://www.sciencedirect.com/science/article/pii/0550321387906857>.
- [63] M. Bilenky et al. “Trilinear couplings among the electroweak vector bosons and their determination at LEP2”. In: *Nuclear Physics B* 409.1 (1993), pp. 22–68. ISSN: 0550-3213. DOI: [https://doi.org/10.1016/0550-3213\(93\)90445-U](https://doi.org/10.1016/0550-3213(93)90445-U). URL: <https://www.sciencedirect.com/science/article/pii/055032139390445U>.
- [64] E.N Argyres et al. “Trilinear gauge boson couplings in the MSSM”. In: *Physics Letters B* 383.1 (1996), pp. 63–77. ISSN: 0370-2693. DOI: [https://doi.org/10.1016/0370-2693\(96\)00696-X](https://doi.org/10.1016/0370-2693(96)00696-X). URL: <https://www.sciencedirect.com/science/article/pii/037026939600696X>.
- [65] A. Arhrib, J.-L. Kneur, and G. Moultaka. “MSSM radiative contributions to the $WW\gamma$ and WWZ form factors”. In: *Physics Letters B* 376.1 (1996), pp. 127–135. ISSN: 0370-2693. DOI: [https://doi.org/10.1016/0370-2693\(96\)00191-8](https://doi.org/10.1016/0370-2693(96)00191-8). URL: <https://www.sciencedirect.com/science/article/pii/0370269396001918>.
- [66] Enrico Bertuzzo et al. “Constraints from triple gauge couplings on vectorlike leptons”. In: *Phys. Rev. D* 96 (3 Aug. 2017), p. 035035. DOI: 10.1103/PhysRevD.96.035035. URL: <https://link.aps.org/doi/10.1103/PhysRevD.96.035035>.
- [67] Jorge de Blas et al. “Global SMEFT Fits at Future Colliders”. In: *2022 Snowmass Summer Study*. June 2022. arXiv: 2206.08326 [hep-ph].
- [68] European Strategy for Particle Physics Preparatory Group. *Physics Briefing Book*. 2020. arXiv: 1910.11775 [hep-ex].
- [69] J. de Blas et al. *The CLIC potential for new physics*. CERN Yellow Reports: Monographs. 282 pages, 128 Figures, 55 Tables and 732 citations. Editors: J. de Blas, R. Franceschini, F. Riva, P. Roloff, U. Schnoor, M. Spannowsky, J. D. Wells, A. Wulzer and J. Zupan. Version published in CERN Yellow Report Monographs. Geneva: CERN, Dec. 2018. DOI: 10.23731/CYRM-2018-003. URL: <http://cds.cern.ch/record/2650541>.
- [70] Kerstin Tackmann. *Higgs Measurements*. Tech. rep. Geneva: CERN, Oct. 2021. URL: <https://cds.cern.ch/record/2784115>.
- [71] *Snowmass White Paper Contribution: Physics with the Phase-2 ATLAS and CMS Detectors*. Tech. rep. All figures including auxiliary figures are available at <https://atlas.web.cern.ch/Atlas/GROUPS/PHYSICS/PUBNOTES/ATL-PHYS-PUB-2022-018>. Geneva: CERN, Apr. 2022. URL: <http://cds.cern.ch/record/2805993>.
- [72] Tim Barklow et al. “Improved Formalism for Precision Higgs Coupling Fits”. In: *Phys. Rev. D* 97.5 (2018), p. 053003. DOI: 10.1103/PhysRevD.97.053003. arXiv: 1708.08912 [hep-ph].

8. Conclusion

- [73] Keisuke Fujii et al. “Physics Case for the 250 GeV Stage of the International Linear Collider”. In: (Oct. 2017). arXiv: 1710.07621 [hep-ex].
- [74] Shin-ichi Kawada. “ILC Higgs physics potential”. In: *PoS EPS-HEP2021* (2022), p. 611. DOI: 10.22323/1.398.0611.
- [75] Roman Pöschl. “Top and heavy quark studies at linear colliders”. In: *PoS EPS-HEP2021* (2022), p. 491. DOI: 10.22323/1.398.0491.
- [76] Jürgen Reuter. “The BSM Physics Case of the ILC”. In: *International Workshop on Future Linear Colliders*. Feb. 2016. arXiv: 1602.08352 [hep-ph].
- [77] J. de Blas et al. “Higgs Boson Studies at Future Particle Colliders”. In: *JHEP* 01 (2020), p. 139. DOI: 10.1007/JHEP01(2020)139. arXiv: 1905.03764 [hep-ph].
- [78] “The International Linear Collider Technical Design Report - Volume 1: Executive Summary”. In: (June 2013). Ed. by Ties Behnke et al. arXiv: 1306.6327 [physics.acc-ph].
- [79] “The International Linear Collider Technical Design Report - Volume 2: Physics”. In: (June 2013). Ed. by Howard Baer et al. arXiv: 1306.6352 [hep-ph].
- [80] Chris Adolphsen et al. *The International Linear Collider Technical Design Report*. Tech. rep. Comments: See also <http://www.linearcollider.org/ILC/TDR>. The full list of signatories is inside the Report. Geneva, June 2013. arXiv: 1306.6353. URL: <https://cds.cern.ch/record/1541315>.
- [81] “The International Linear Collider Technical Design Report - Volume 3.II: Accelerator Baseline Design”. In: (June 2013). Ed. by Chris Adolphsen et al. arXiv: 1306.6328 [physics.acc-ph].
- [82] Ties Behnke et al. *The International Linear Collider Technical Design Report - Volume 4: Detectors*. 2013. arXiv: 1306.6329 [physics.ins-det].
- [83] Philip Bambade et al. “The International Linear Collider: A Global Project”. In: (2019). DOI: 10.3204/PUBDB-2019-01998. arXiv: 1903.01629. URL: <https://bib-pubdb1.desy.de/record/421408>.
- [84] M Aicheler et al. *A Multi-TeV Linear Collider Based on CLIC Technology: CLIC Conceptual Design Report*. CERN Yellow Reports: Monographs. Geneva: CERN, 2012. DOI: 10.5170/CERN-2012-007. URL: <https://cds.cern.ch/record/1500095>.
- [85] Lucie Linssen et al. *Physics and Detectors at CLIC: CLIC Conceptual Design Report*. Ed. by Lucie Linssen. CERN Yellow Reports: Monographs. Comments: 257 p, published as CERN Yellow Report CERN-2012-003. Geneva: CERN, 2012. DOI: 10.5170/CERN-2012-003. URL: <https://cds.cern.ch/record/1425915>.
- [86] P. Lebrun et al. *The CLIC programme: Towards a staged e^+e^- linear collider exploring the terascale: CLIC conceptual design report*. CERN Yellow Reports: Monographs. Comments: 84 pages, published as CERN Yellow Report. Geneva: CERN, 2012. DOI: 10.5170/CERN-2012-005. URL: <https://cds.cern.ch/record/1475225>.

- [87] Michelangelo Mangano et al. *FCC Physics Opportunities: Future Circular Collider Conceptual Design Report Volume 1. Future Circular Collider*. Tech. rep. Geneva: CERN, Dec. 2018. DOI: 10.1140/epjc/s10052-019-6904-3. URL: <http://cds.cern.ch/record/2651294>.
- [88] A. Abada et al. “FCC-ee: The Lepton Collider”. In: *The European Physical Journal Special Topics* 228.2 (June 2019), pp. 261–623. ISSN: 1951-6401. DOI: 10.1140/epjst/e2019-900045-4. URL: <https://doi.org/10.1140/epjst/e2019-900045-4>.
- [89] The CEPC Study Group. *CEPC Conceptual Design Report: Volume 1 - Accelerator*. 2018. arXiv: 1809.00285 [physics.acc-ph].
- [90] Mingyi Dong et al. “CEPC Conceptual Design Report: Volume 2 - Physics & Detector”. In: (Nov. 2018). Ed. by João Barreiro Guimarães da Costa et al. arXiv: 1811.10545 [hep-ex].
- [91] Matthew Sands. “The Physics of Electron Storage Rings: An Introduction”. In: *Conf. Proc. C 6906161* (1969), pp. 257–411. URL: <https://www.osti.gov/biblio/4064201>.
- [92] M. Tigner. “A possible apparatus for electron clashing-beam experiments”. In: *Nuovo Cimento (1955-1965)* 37.3 (June 1965), pp. 1228–1231. ISSN: 1827-6121. DOI: 10.1007/BF02773204. URL: <https://doi.org/10.1007/BF02773204>.
- [93] B. Richter. “Very high energy electron-positron colliding beams for the study of weak interactions”. In: *Nuclear Instruments and Methods* 136.1 (1976), pp. 47–60. ISSN: 0029-554X. DOI: [https://doi.org/10.1016/0029-554X\(76\)90396-7](https://doi.org/10.1016/0029-554X(76)90396-7). URL: <https://www.sciencedirect.com/science/article/pii/0029554X76903967>.
- [94] G. Moortgat-Pick et al. “Polarized positrons and electrons at the linear collider”. In: *Physics Reports* 460.4 (2008), pp. 131–243. ISSN: 0370-1573. DOI: <https://doi.org/10.1016/j.physrep.2007.12.003>. URL: <https://www.sciencedirect.com/science/article/pii/S0370157308000136>.
- [95] Ken-ichi Hikasa. “Transverse-polarization effects in e^+e^- collisions: The role of chiral symmetry”. In: *Phys. Rev. D* 33 (11 June 1986), pp. 3203–3223. DOI: 10.1103/PhysRevD.33.3203. URL: <https://link.aps.org/doi/10.1103/PhysRevD.33.3203>.
- [96] M. Woods. “The Polarized electron beam for the SLAC linear collider”. In: *12th International Symposium on High-energy Spin Physics (SPIN 96)*. Oct. 1996, pp. 623–627. arXiv: hep-ex/9611006.
- [97] V. Gharibyan and K. P. Schuler. “HERA transverse polarimeter absolute scale and error by rise time calibration”. In: *NATO Sci. Ser. II* 111 (2003). Ed. by E. Steffens and R. Shanidze, p. 149. arXiv: hep-ex/0310045.

8. Conclusion

- [98] K. C. Moffeit. “Spin physics with polarized electrons at the SLC”. In: *9th International Symposium on High-energy Spin Physics*. Nov. 1990. URL: <https://www.osti.gov/biblio/6326449-spin-physics-polarized-electrons-slc-stanford-linear-collider>.
- [99] U. Fano. “Spin Orientation of Photoelectrons Ejected by Circularly Polarized Light”. In: *Phys. Rev.* 178 (1 Feb. 1969), pp. 131–136. DOI: 10.1103/PhysRev.178.131. URL: <https://link.aps.org/doi/10.1103/PhysRev.178.131>.
- [100] R. Alley et al. “The Stanford Linear Accelerator polarized electron source”. In: *Nucl. Instrum. Meth. A* 365 (1995), pp. 1–27. DOI: 10.1016/0168-9002(95)00450-5.
- [101] A. A. Sokolov and I. M. Ternov. “On The Spin And Polarization Effects In The Theory Of Synchrotron Radiation”. In: *4th International Conference on High-Energy Accelerators*. 1963, pp. 1271–1275. URL: <https://inspirehep.net/literature/918891>.
- [102] H. D. Bremer et al. *Beam Polarization At Petra*. Tech. rep. DESY M-82-26. 1982, p. 4. URL: <https://bib-pubdb1.desy.de/record/224384>.
- [103] Blanka Sobloher. “Polarisation and Polarimetry at HERA”. In: (Jan. 2012). arXiv: 1201.3836 [physics.ins-det].
- [104] L. Arnaudon et al. “Accurate determination of the LEP beam energy by resonant depolarization”. In: *Zeitschrift für Physik C Particles and Fields* 66.1 (Mar. 1995), pp. 45–62. ISSN: 1431-5858. DOI: 10.1007/BF01496579. URL: <https://doi.org/10.1007/BF01496579>.
- [105] J. D. Jackson. “On understanding spin-flip synchrotron radiation and the transverse polarization of electrons in storage rings”. In: *Rev. Mod. Phys.* 48 (3 July 1976), pp. 417–433. DOI: 10.1103/RevModPhys.48.417. URL: <https://link.aps.org/doi/10.1103/RevModPhys.48.417>.
- [106] Alain Blondel et al. *FCC-ee: Your Questions Answered*. 2019. arXiv: 1906.02693 [hep-ph].
- [107] Alain Blondel and Eliana Gianfelice. “The challenges of beam polarization and keV-scale centre-of-mass energy calibration at the FCC-ee”. In: *Eur. Phys. J. Plus* 136.11 (2021), p. 1103. DOI: 10.1140/epjp/s13360-021-02038-y.
- [108] Guy Wilkinson. “Requirements for polarization measurements (talk at 2d FCC Polarization Workshop)”. 2022. URL: <https://indico.cern.ch/event/1181966/contributions/5041437/>.
- [109] Klaus Monig. “The Use of positron polarization for precision measurements”. In: (Dec. 2000). Ed. by Ties Behnke et al., pp. 1346–1352. URL: <http://flc.desy.de/lcnotes/notes/LC-PHSM-2000-059.ps.gz>.

- [110] Gudrid A. Moortgat-Pick and Herbert M. Steiner. “Physics opportunities with polarized e^- and e^+ beams at TESLA”. In: *Eur. Phys. J. direct* 3.1 (2001). Ed. by Ties Behnke et al., p. 6. DOI: 10.1007/s1010501c0006. arXiv: hep-ph/0106155.
- [111] Keisuke Fujii et al. “The role of positron polarization for the initial 250 GeV stage of the International Linear Collider”. In: (Jan. 2018). arXiv: 1801.02840 [hep-ph].
- [112] Kenji Abe et al. “High-Precision Measurement of the Left-Right Z Boson Cross-Section Asymmetry”. In: *Phys. Rev. Lett.* 84 (26 June 2000), pp. 5945–5949. DOI: 10.1103/PhysRevLett.84.5945. URL: <https://link.aps.org/doi/10.1103/PhysRevLett.84.5945>.
- [113] C. Y. Prescott. “Polarized e^-e^+ Physics in Linear Colliders”. In: *Experientia Suppl.* 38 (1981). Ed. by C. Joseph and Jacques Soffer, p. 0034. URL: <https://slac.stanford.edu/pubs/slacpubs/2500/slac-pub-2649.pdf>.
- [114] Moritz Habermehl, Mikael Berggren, and Jenny List. “WIMP Dark Matter at the International Linear Collider”. In: *Phys. Rev. D* 101.7 (2020), p. 075053. DOI: 10.1103/PhysRevD.101.075053. arXiv: 2001.03011 [hep-ex].
- [115] Jakob Beyer and Jenny List. “Interplay of Beam Polarisation and Systematic Uncertainties in Electroweak Precision Measurements at Future e^+e^- Colliders”. In: *24th International Symposium on Spin Physics*. Feb. 2022. arXiv: 2202.07385 [hep-ph].
- [116] Adrian Vogel. “Beam-induced backgrounds in detectors at the ILC”. Other thesis. Aug. 2008. DOI: 10.3204/DESY-THESIS-2008-036.
- [117] Moritz Habermehl. “Dark Matter at the International Linear Collider”. Dissertation, Universität Hamburg, 2018. Dissertation. Hamburg: Universität Hamburg, 2018, p. 253. DOI: 10.3204/PUBDB-2018-05723. URL: <https://bib-pubdb1.desy.de/record/417605>.
- [118] Kollassery Swathi Sasikumar, Jenny List, and Carl Mikael Berggren. “Hadron production in photon photon processes and BSM signatures with small mass differences”. In: International Conference for Linear Colliders, Strassbourg (France), 23 Oct 2017 - 27 Oct 2017. Oct. 23, 2017. DOI: 10.3204/PUBDB-2017-13722. URL: <https://bib-pubdb1.desy.de/record/398111>.
- [119] Ichiro Adachi et al. “The International Linear Collider: Report to Snowmass 2021”. In: (Mar. 2022). arXiv: 2203.07622 [physics.acc-ph].
- [120] Eldwan Brianne. “Time development of hadronic showers in a Highly Granular Analog Hadron Calorimeter”. Dissertation, Universität Hamburg, 2018. Dissertation. Hamburg: Universität Hamburg, 2018, p. 259. DOI: 10.3204/PUBDB-2018-02769. URL: <https://bib-pubdb1.desy.de/record/408316>.

8. Conclusion

- [121] Lyn Evans and Shinichiro Michizono. “The International Linear Collider Machine Staging Report 2017”. In: (Nov. 2017). arXiv: 1711.00568 [physics.acc-ph].
- [122] Keisuke Fujii et al. *Tests of the Standard Model at the International Linear Collider*. 2019. arXiv: 1908.11299 [hep-ex].
- [123] Halina Abramowicz et al. “International Large Detector: Interim Design Report”. In: (Mar. 2020). arXiv: 2003.01116 [physics.ins-det].
- [124] M. Breidenbach et al. “Updating the SiD Detector concept”. In: (Oct. 2021). arXiv: 2110.09965 [physics.ins-det].
- [125] I Božović Jelisavčić et al. “Luminosity measurement at ILC”. In: *Journal of Instrumentation* 8.08 (Aug. 2013), P08012–P08012. ISSN: 1748-0221. DOI: 10.1088/1748-0221/8/08/p08012. URL: <http://dx.doi.org/10.1088/1748-0221/8/08/P08012>.
- [126] *Z Physics at LEP1: CERN, Geneva, Switzerland 20 - 21 Feb, 8 - 9 May and 4 - 5 Sep 1989. Workshop on Z Physics at LEP1*. Coordinated and supervised by G. Altarelli. CERN. Geneva: CERN, 1989. DOI: 10.5170/CERN-1989-008-V-1. URL: <https://cds.cern.ch/record/116932>.
- [127] S. Dittmaier and Klaus Monig, eds. *Electroweak precision data and the Higgs mass. Proceedings, Workshop, Zeuthen, Germany, February 28-March 1, 2003*. Mini-Workshop on Electroweak Precision Data and the Higgs Mass, Zeuthen (Germany), 28 Feb 2003 - 1 Mar 2003. Feb. 28, 2003. URL: <https://bib-pubdb1.desy.de/record/308213>.
- [128] Felix Dietrich et al. “Status of the undulator-based ILC positron source”. In: *International Workshop on Future Linear Colliders*. Feb. 2019. arXiv: 1902.07744 [physics.acc-ph].
- [129] V. E. Balakin and A. A. Mikhailichenko. “Conversion system for obtaining highly polarized electrons and positrons”. In: (1979).
- [130] V. E. Balakin and A. A. Mikhailichenko. “Conversion System of Vlepp (Linear Electron - Positron Collider) to Obtain Polarized Beams. (Talk, in Russian)”. In: *7th All Union Conference on Charged Particle Accelerators*. 1980, pp. 302–307.
- [131] Sabine Riemann et al. “Updated status of the undulator-based ILC positron source”. In: *International Workshop on Future Linear Colliders*. Feb. 2020. arXiv: 2002.10919 [physics.acc-ph].
- [132] S. Riemann et al. “The Design of Spin-Rotator with a Possibility of Helicity Switching for Polarized Positron at the ILC”. In: *Conf. Proc. C 1205201* (2012). Ed. by Vic Suller, pp. 1813–1815. URL: <https://accelconf.web.cern.ch/ipac2012/papers/tuppr003.pdf>.

- [133] H. Nagoshi et al. "A design of an electron driven positron source for the international linear collider". In: *Nuclear Instruments and Methods in Physics Research Section A: Accelerators, Spectrometers, Detectors and Associated Equipment* 953 (2020), p. 163134. ISSN: 0168-9002. DOI: <https://doi.org/10.1016/j.nima.2019.163134>. URL: <https://www.sciencedirect.com/science/article/pii/S016890021931455X>.
- [134] Wei Gai et al. *Report on the ILC Positron Source*. Tech. rep. 2018, p. 78. DOI: 10.3204/PUBDB-2019-00651. URL: <https://bib-pubdb1.desy.de/record/418711>.
- [135] J. E. Clendenin et al. "SLC POSITRON SOURCE STARTUP". In: *14th International Linear Accelerator Conference*. Sept. 1988.
- [136] E. Reuter et al. "Mechanical design and development of a high power target system for the SLC positron source". In: *Conference Record of the 1991 IEEE Particle Accelerator Conference*. 1991, 1999–2001 vol.3. DOI: 10.1109/PAC.1991.164849.
- [137] A. Variola. "Advanced positron sources". In: *Nuclear Instruments and Methods in Physics Research Section A: Accelerators, Spectrometers, Detectors and Associated Equipment* 740 (2014). Proceedings of the first European Advanced Accelerator Concepts Workshop 2013, pp. 21–26. ISSN: 0168-9002. DOI: <https://doi.org/10.1016/j.nima.2013.10.051>. URL: <https://www.sciencedirect.com/science/article/pii/S0168900213014320>.
- [138] Markus Diehl, Otto Nachtmann, and Felix Nagel. "Probing triple gauge couplings with transverse beam polarisation in $e^+ e^- \rightarrow W^+ W^-$ ". In: *Eur. Phys. J. C* 32 (2003), pp. 17–27. DOI: 10.1140/epjc/s2003-01339-5. arXiv: hep-ph/0306247.
- [139] Alain Blondel. "A scheme to measure the polarization asymmetry at the z pole in LEP". In: *Physics Letters B* 202.1 (1988), pp. 145–148. ISSN: 0370-2693. DOI: [https://doi.org/10.1016/0370-2693\(88\)90869-6](https://doi.org/10.1016/0370-2693(88)90869-6). URL: <https://www.sciencedirect.com/science/article/pii/0370269388908696>.
- [140] S Boogert et al. "Polarimeters and energy spectrometers for the ILC Beam Delivery System". In: *Journal of Instrumentation* 4.10 (Oct. 2009), P10015–P10015. DOI: 10.1088/1748-0221/4/10/p10015. URL: <https://doi.org/10.1088/1748-0221/4/10/p10015>.
- [141] Annika Vauth and Jenny List. "Beam Polarization at the ILC: Physics Case and Realization". In: *International Journal of Modern Physics: Conference Series* 40 (2016), p. 1660003. DOI: 10.1142/S201019451660003X. eprint: <https://doi.org/10.1142/S201019451660003X>. URL: <https://doi.org/10.1142/S201019451660003X>.
- [142] M Beckmann et al. "Spin transport and polarimetry in the beam delivery system of the international linear collider". In: *Journal of Instrumentation* 9.07 (July 2014), P07003–P07003. DOI: 10.1088/1748-0221/9/07/p07003. URL: <https://doi.org/10.1088/1748-0221/9/07/p07003>.

8. Conclusion

- [143] Robert Karl and Jenny List. “Polarimetry at the ILC”. In: *International Workshop on Future Linear Colliders*. Mar. 2017. arXiv: 1703.00214 [hep-ex].
- [144] K. Mönig. “Polarisation Measurements With Annihilation Data”. In: *LCWS-2004 (Paris)*. Hamburg: DESY, 2004. URL: <http://flc.desy.de/lcnotes/notes/LC-PHSM-2004-012.ps.gz>.
- [145] A. Rosca. “Measurement of the beam polarization at the ILC using $e + e - \rightarrow W + W - \rightarrow qq\ell\nu$ data”. In: *3rd Linear Collider Forum*. Hamburg: DESY, 2013, pp. 159–167. URL: <http://flc.desy.de/lcnotes/notes/LC-REP-2013-009.pdf>.
- [146] B. Aurand et al. “Executive Summary of the Workshop on Polarization and Beam Energy Measurements at the ILC”. In: (Aug. 2008). arXiv: 0808.1638 [physics.acc-ph].
- [147] Jenny List, Annika Vauth, and Benedikt Vormwald. “A Quartz Cherenkov Detector for Compton-Polarimetry at Future e^+e^- Colliders”. In: *Journal of Instrumentation* 10.05 (2015), P05014. ISSN: 1751-8822. DOI: 10.1088/1748-0221/10/05/P05014. arXiv: 1502.06955. URL: <https://bib-pubdb1.desy.de/record/221054>.
- [148] C. Helebrant, D. Käfer, and J. List. *Precision Polarimetry at the International Linear Collider*. 2008. arXiv: 0809.4485 [physics.ins-det].
- [149] Nils Feege and DESY. “Low-energetic Hadron Interactions in a Highly Granular Calorimeter”. Universität Hamburg, Diss., 2011. Dr. Hamburg: Universität Hamburg, 2011. URL: <https://bib-pubdb1.desy.de/record/94643>.
- [150] M.A. Thomson. “Particle flow calorimetry and the PandoraPFA algorithm”. In: *Nuclear Instruments and Methods in Physics Research Section A: Accelerators, Spectrometers, Detectors and Associated Equipment* 611.1 (2009), pp. 25–40. ISSN: 0168-9002. DOI: <https://doi.org/10.1016/j.nima.2009.09.009>. URL: <https://www.sciencedirect.com/science/article/pii/S0168900209017264>.
- [151] J S Marshall and M A Thomson. “The Pandora Particle Flow Algorithm”. In: (Aug. 2013). Comments: Proceedings of CHEF2013 - Calorimetry for the High Energy Frontier. arXiv: 1308.4537. URL: <https://cds.cern.ch/record/1593234>.
- [152] Toshinori Abe et al. “The International Large Detector: Letter of Intent”. In: (Feb. 2010). DOI: 10.2172/975166. arXiv: 1006.3396 [hep-ex].
- [153] Carl Mikael Berggren. “Overall ILD dimensions and the ILD tracker”. In: *ECFA-Linear Collider Workshop 2016, Santander (Spain), 30 May 2016 - 5 Jun 2016*. May 30, 2016. URL: <https://bib-pubdb1.desy.de/record/316017>.
- [154] Mikael Berggren. *SGV 3.0 - a fast detector simulation*. 2012. arXiv: 1203.0217 [physics.ins-det].
- [155] V. Khachatryan et al. “Jet energy scale and resolution in the CMS experiment in pp collisions at 8 TeV”. In: *Journal of Instrumentation* 12.02 (Feb. 2017), P02014–P02014. DOI: 10.1088/1748-0221/12/02/p02014. URL: <https://doi.org/10.1088/1748-0221/12/02/p02014>.

- [156] G. Aad et al. “Jet energy scale and resolution measured in proton–proton collisions at $\sqrt{s} = 13$ TeV with the ATLAS detector”. In: *The European Physical Journal C* 81.8 (Aug. 2021), p. 689. ISSN: 1434-6052. DOI: 10.1140/epjc/s10052-021-09402-3. URL: <https://doi.org/10.1140/epjc/s10052-021-09402-3>.
- [157] I. Marchesini and DESY. “Triple Gauge Couplings and Polarization at the ILC and Leakage in a Highly Granular Calorimeter”. Hamburg University, Diss., 2011. Dr. Hamburg: Hamburg University, 2011. URL: <https://bib-pubdb1.desy.de/record/94888>.
- [158] Aliakbar Ebrahimi. “Jet Energy Measurements at ILC: Calorimeter DAQ Requirements and Application in Higgs Boson Mass Measurements”. Dissertation, Universität Hamburg, 2017. Dissertation. Hamburg: Universität Hamburg, 2017, p. 205. DOI: 10.3204/PUBDB-2017-11891. URL: <https://bib-pubdb1.desy.de/record/394104>.
- [159] Koya Abe et al. “Improved Direct Measurement of Leptonic Coupling Asymmetries with Polarized Z Bosons”. In: *Phys. Rev. Lett.* 86 (7 Feb. 2001), pp. 1162–1166. DOI: 10.1103/PhysRevLett.86.1162. URL: <https://link.aps.org/doi/10.1103/PhysRevLett.86.1162>.
- [160] T. Barklow. “Experimental W boson physics at future e+ e- linear colliders”. In: *Workshop on Physics and Experiments with Linear Colliders*. Apr. 1992, pp. 0423–450. URL: <https://www.osti.gov/biblio/5083924>.
- [161] Richard Hawkings and Klaus Monig. “Electroweak and CP violation physics at a linear collider Z factory”. In: *Eur. Phys. J. direct* 1.1 (1999), p. 8. DOI: 10.1007/s1010599c0008. arXiv: hep-ex/9910022.
- [162] Dmitry Vladimirovich Onoprienko. “Precise Measurement of the Left-Right Asymmetry in Z Boson Production by e^+e^- Collisions: Electron Beam Polarization Measurement with the Quartz Fiber Calorimeter”. PhD thesis. Tennessee U., 2000. URL: <https://www.slac.stanford.edu/pubs/slacreports/reports15/slac-r-556a.pdf>.
- [163] M. Bilenky et al. “The potential of a new linear collider for the measurement of the trilinear couplings among the electroweak vector bosons”. In: *Nuclear Physics B* 419.2 (1994), pp. 240–253. ISSN: 0550-3213. DOI: [https://doi.org/10.1016/0550-3213\(94\)90041-8](https://doi.org/10.1016/0550-3213(94)90041-8). URL: <https://www.sciencedirect.com/science/article/pii/0550321394900418>.
- [164] Matt Herndon. *Limits on anomalous triple and quartic gauge couplings*. 2020. URL: <https://twiki.cern.ch/twiki/bin/view/CMSPublic/PhysicsResultsSMPaTGC> (visited on 03/22/2022).

8. Conclusion

- [165] S. Schael et al. “Improved measurement of the triple gauge-boson couplings γWW and ZWW in e^+e^- collisions”. In: *Physics Letters B* 614.1 (2005), pp. 7–26. ISSN: 0370-2693. DOI: <https://doi.org/10.1016/j.physletb.2005.03.058>. URL: <https://www.sciencedirect.com/science/article/pii/S0370269305004120>.
- [166] M. Aaboud et al. “Measurement of $WW/WZ \rightarrow \ell\nu qq'$ production with the hadronically decaying boson reconstructed as one or two jets in pp collisions at $\sqrt{s} = 8\text{TeV}$ with ATLAS, and constraints on anomalous gauge couplings”. In: *The European Physical Journal C* 77.8 (Aug. 2017). ISSN: 1434-6052. DOI: 10.1140/epjc/s10052-017-5084-2. URL: <http://dx.doi.org/10.1140/epjc/s10052-017-5084-2>.
- [167] A. M. Sirunyan et al. “ W^+W^- boson pair production in proton-proton collisions at $\sqrt{s} = 13\text{TeV}$ ”. In: *Physical Review D* 102.9 (Nov. 2020). ISSN: 2470-0029. DOI: 10.1103/physrevd.102.092001. URL: <http://dx.doi.org/10.1103/PhysRevD.102.092001>.
- [168] A.M. Sirunyan et al. “Search for anomalous couplings in boosted $WW/ZZ \rightarrow \ell\nu q\bar{q}$ production in proton–proton collisions at $\sqrt{s} = 8\text{TeV}$ ”. In: *Physics Letters B* 772 (Sept. 2017), pp. 21–42. ISSN: 0370-2693. DOI: 10.1016/j.physletb.2017.06.009. URL: <http://dx.doi.org/10.1016/j.physletb.2017.06.009>.
- [169] P. Azzi et al. *Standard Model Physics at the HL-LHC and HE-LHC*. 2019. arXiv: 1902.04070 [hep-ph].
- [170] Aura Rosca. “Measurement of the charged triple gauge boson couplings at the ILC”. In: *Nuclear and Particle Physics Proceedings* 273-275 (2016). 37th International Conference on High Energy Physics (ICHEP), pp. 2226–2231. ISSN: 2405-6014. DOI: <https://doi.org/10.1016/j.nuclphysbps.2015.09.362>. URL: <https://www.sciencedirect.com/science/article/pii/S2405601415008512>.
- [171] A. A. Billur et al. “Model-independent limits for anomalous triple gauge bosons $W^+W^-\gamma$ couplings at the CLIC”. In: *The European Physical Journal Plus* 136.6 (June 2021), p. 697. ISSN: 2190-5444. DOI: 10.1140/epjp/s13360-021-01684-6. URL: <https://doi.org/10.1140/epjp/s13360-021-01684-6>.
- [172] W. Menges. “A study of charged current triple gauge couplings at TESLA”. In: (Jan. 2001). Ed. by Ties Behnke et al., pp. 1635–1669. URL: <http://flc.desy.de/lcnotes/notes/LC-PHSM-2001-022.ps.gz>.
- [173] Wolfgang Kilian et al. “High-energy vector boson scattering after the Higgs boson discovery”. In: *Phys. Rev. D* 91 (9 May 2015), p. 096007. DOI: 10.1103/PhysRevD.91.096007. URL: <https://link.aps.org/doi/10.1103/PhysRevD.91.096007>.

- [174] A. M. Sirunyan et al. “Observation of Electroweak Production of Same-Sign W Boson Pairs in the Two Jet and Two Same-Sign Lepton Final State in Proton-Proton Collisions at $\sqrt{s} = 13$ TeV”. In: *Phys. Rev. Lett.* 120 (8 Feb. 2018), p. 081801. doi: 10.1103/PhysRevLett.120.081801. URL: <https://link.aps.org/doi/10.1103/PhysRevLett.120.081801>.
- [175] M. Aaboud et al. “Measurement of $W^\pm W^\pm$ vector-boson scattering and limits on anomalous quartic gauge couplings with the ATLAS detector”. In: *Phys. Rev. D* 96 (1 July 2017), p. 012007. doi: 10.1103/PhysRevD.96.012007. URL: <https://link.aps.org/doi/10.1103/PhysRevD.96.012007>.
- [176] M. Baak et al. “Working Group Report: Precision Study of Electroweak Interactions”. In: *Community Summer Study 2013: Snowmass on the Mississippi*. Oct. 2013. arXiv: 1310.6708 [hep-ph].
- [177] Genesis Perez, Marco Sekulla, and Dieter Zeppenfeld. “Anomalous quartic gauge couplings and unitarization for the vector boson scattering process $pp \rightarrow W^+ W^+ jj X \rightarrow \ell^+ \nu_\ell \ell^+ \nu_\ell jj X$ ”. In: *The European Physical Journal C* 78.9 (Sept. 2018), p. 759. ISSN: 1434-6052. doi: 10.1140/epjc/s10052-018-6230-1. URL: <https://doi.org/10.1140/epjc/s10052-018-6230-1>.
- [178] P. Krstonic et al. “Experimental studies of strong electroweak symmetry breaking in gauge boson scattering and three gauge boson production”. In: *eConf C050318* (2005). Ed. by JoAnne L. Hewett, p. 0310. arXiv: hep-ph/0508179.
- [179] R. Chierici, S. Rosati, and M. Kobel. “Strong electroweak symmetry breaking signals in WW scattering at Tesla”. In: *AIP Conf. Proc.* 578.1 (2001). Ed. by Ties Behnke et al., pp. 544–549. doi: 10.1063/1.1394378.
- [180] Jakob Beyer. “Measuring Vector Boson Scattering at the future International Linear Collider”. Masterarbeit, Technische Universität Dresden, 2018. Masterarbeit. Technische Universität Dresden, 2018, p. 90. doi: 10.3204/PUBDB-2018-05085. URL: <https://bib-pubdb1.desy.de/record/416692>.
- [181] Mikael Berggren. “Generating the full SM at linear colliders”. In: *PoS ICHEP2020* (2021), p. 903. doi: 10.22323/1.390.0903.
- [182] Wolfgang Kilian, Thorsten Ohl, and Jürgen Reuter. “WHIZARD—simulating multi-particle processes at LHC and ILC”. In: *The European Physical Journal C* 71.9 (Sept. 2011). ISSN: 1434-6052. doi: 10.1140/epjc/s10052-011-1742-y. URL: <http://dx.doi.org/10.1140/epjc/s10052-011-1742-y>.
- [183] Mauro Moretti, Thorsten Ohl, and Jürgen Reuter. “O’Mega: An Optimizing matrix element generator”. In: (Feb. 2001). Ed. by Ties Behnke et al., pp. 1981–2009. arXiv: hep-ph/0102195.
- [184] Steve Aplin et al. “LCIO: A persistency framework and event data model for HEP”. In: *2012 IEEE Nuclear Science Symposium and Medical Imaging Conference Record (NSS/MIC)*. 2012, pp. 2075–2079. doi: 10.1109/NSSMIC.2012.6551478.

8. Conclusion

- [185] Daniel Schulte. “Beam-Beam Simulations with GUINEA-PIG”. In: (Mar. 1999). URL: <http://cds.cern.ch/record/382453>.
- [186] Thorsten Ohl. “circe Version 1.02: beam spectra for simulating linear collider physics”. In: *Computer Physics Communications* 101.3 (1997), pp. 269–288. ISSN: 0010-4655. DOI: [https://doi.org/10.1016/S0010-4655\(96\)00167-1](https://doi.org/10.1016/S0010-4655(96)00167-1). URL: <https://www.sciencedirect.com/science/article/pii/S0010465596001671>.
- [187] Pascal Stienemeier et al. “WHIZARD 3.0: Status and News”. In: *International Workshop on Future Linear Colliders*. Apr. 2021. arXiv: 2104.11141 [hep-ph].
- [188] S. Jadach et al. “The τ decay library TAUOLA, version 2.4”. In: *Computer Physics Communications* 76.3 (1993), pp. 361–380. ISSN: 0010-4655. DOI: [https://doi.org/10.1016/0010-4655\(93\)90061-G](https://doi.org/10.1016/0010-4655(93)90061-G). URL: <https://www.sciencedirect.com/science/article/pii/001046559390061G>.
- [189] M. Chrzaszcz et al. *TAUOLA of tau lepton decays— framework for hadronic currents, matrix elements and anomalous decays*. 2017. arXiv: 1609.04617 [hep-ph].
- [190] Torbjörn Sjöstrand, Stephen Mrenna, and Peter Skands. “PYTHIA 6.4 physics and manual”. In: *Journal of High Energy Physics* 2006.05 (May 2006), pp. 026–026. ISSN: 1029-8479. DOI: [10.1088/1126-6708/2006/05/026](https://doi.org/10.1088/1126-6708/2006/05/026). URL: <http://dx.doi.org/10.1088/1126-6708/2006/05/026>.
- [191] Armin Böhrer. “Inclusive particle production in hadronic decays of the Z boson at LEP I”. In: *Physics Reports* 291.3 (1997), pp. 107–217. ISSN: 0370-1573. DOI: [https://doi.org/10.1016/S0370-1573\(97\)00015-X](https://doi.org/10.1016/S0370-1573(97)00015-X). URL: <https://www.sciencedirect.com/science/article/pii/S037015739700015X>.
- [192] Remi Ete. “The ILD Software Tools and Detector Performance”. In: *PoS ICHEP2020* (2021), p. 909. DOI: [10.22323/1.390.0909](https://doi.org/10.22323/1.390.0909).
- [193] F. Gaede. “Marlin and LCCD—Software tools for the ILC”. In: *Nuclear Instruments and Methods in Physics Research Section A: Accelerators, Spectrometers, Detectors and Associated Equipment* 559.1 (2006). Proceedings of the X International Workshop on Advanced Computing and Analysis Techniques in Physics Research, pp. 177–180. ISSN: 0168-9002. DOI: <https://doi.org/10.1016/j.nima.2005.11.138>. URL: <https://www.sciencedirect.com/science/article/pii/S0168900205022643>.
- [194] M Frank et al. “DD4hep: A Detector Description Toolkit for High Energy Physics Experiments”. In: *Journal of Physics: Conference Series* 513.2 (June 2014), p. 022010. DOI: [10.1088/1742-6596/513/2/022010](https://doi.org/10.1088/1742-6596/513/2/022010). URL: <https://doi.org/10.1088/1742-6596/513/2/022010>.
- [195] Markus Frank et al. *AIDASoft/DD4hep: v01-20*. Version v01-20. Jan. 2022. DOI: [10.5281/zenodo.5886851](https://doi.org/10.5281/zenodo.5886851). URL: <https://doi.org/10.5281/zenodo.5886851>.

- [196] S. Agostinelli et al. “Geant4 - a simulation toolkit”. In: *Nuclear Instruments and Methods in Physics Research Section A: Accelerators, Spectrometers, Detectors and Associated Equipment* 506.3 (2003), pp. 250–303. ISSN: 0168-9002. DOI: [https://doi.org/10.1016/S0168-9002\(03\)01368-8](https://doi.org/10.1016/S0168-9002(03)01368-8). URL: <https://www.sciencedirect.com/science/article/pii/S0168900203013688>.
- [197] Frank Gaede et al. “Track reconstruction at the ILC: the ILD tracking software”. In: *Journal of Physics: Conference Series* 513.2 (June 2014), p. 022011. DOI: 10.1088/1742-6596/513/2/022011. URL: <https://doi.org/10.1088/1742-6596/513/2/022011>.
- [198] J. S. Marshall and M. A. Thomson. “The Pandora software development kit for pattern recognition”. In: *The European Physical Journal C* 75.9 (Sept. 2015), p. 439. DOI: 10.1140/epjc/s10052-015-3659-3. URL: <https://doi.org/10.1140/epjc/s10052-015-3659-3>.
- [199] Taikan Suehara and Tomohiko Tanabe. “LCFIPlus: A framework for jet analysis in linear collider studies”. In: *Nuclear Instruments and Methods in Physics Research Section A: Accelerators, Spectrometers, Detectors and Associated Equipment* 808 (2016), pp. 109–116. ISSN: 0168-9002. DOI: <https://doi.org/10.1016/j.nima.2015.11.054>. URL: <https://www.sciencedirect.com/science/article/pii/S0168900215014199>.
- [200] Carl Mikael Berggren. “Truth information : RecoMCTruthLinker and TrueJet”. In: ILD Benchmarking Days, Arlington, TX (USA), 19 Oct 2018 - 21 Oct 2018. Oct. 19, 2018. DOI: 10.3204/PUBDB-2018-05111. URL: <https://bib-pubdb1.desy.de/record/416718>.
- [201] Domènec Espriu and Brian Yencho. “Longitudinal WW scattering in light of the “Higgs boson” discovery”. In: *Phys. Rev. D* 87 (5 Mar. 2013), p. 055017. DOI: 10.1103/PhysRevD.87.055017. URL: <https://link.aps.org/doi/10.1103/PhysRevD.87.055017>.
- [202] Kingman Cheung, Cheng-Wei Chiang, and Tzu-Chiang Yuan. “Partially strong WW scattering”. In: *Phys. Rev. D* 78 (5 Sept. 2008), p. 051701. DOI: 10.1103/PhysRevD.78.051701. URL: <https://link.aps.org/doi/10.1103/PhysRevD.78.051701>.
- [203] Benjamin W. Lee, C. Quigg, and H. B. Thacker. “Weak interactions at very high energies: The role of the Higgs-boson mass”. In: *Phys. Rev. D* 16 (5 Sept. 1977), pp. 1519–1531. DOI: 10.1103/PhysRevD.16.1519. URL: <https://link.aps.org/doi/10.1103/PhysRevD.16.1519>.
- [204] Benjamin W. Lee, C. Quigg, and H. B. Thacker. “Strength of Weak Interactions at Very High Energies and the Higgs Boson Mass”. In: *Phys. Rev. Lett.* 38 (16 Apr. 1977), pp. 883–885. DOI: 10.1103/PhysRevLett.38.883. URL: <https://link.aps.org/doi/10.1103/PhysRevLett.38.883>.

8. Conclusion

- [205] Jakob Beyer and Jenny List. “ILD benchmark: Quartic Gauge Couplings”. In: (Feb. 2020). arXiv: 2002.10830 [hep-ex].
- [206] Jakob Beyer. *ILDbench_QGC : Code of the VBS analysis*. https://github.com/ILDAnaSoft/ILDbench_QGC/tree/master/FinalStateAnalysis. 2022.
- [207] T. Barklow et al. *ILC Operating Scenarios*. 2015. arXiv: 1506.07830 [hep-ex].
- [208] Matteo Cacciari, Gavin P. Salam, and Gregory Soyez. “FastJet User Manual”. In: *Eur. Phys. J. C* 72 (2012), p. 1896. doi: 10.1140/epjc/s10052-012-1896-2. arXiv: 1111.6097 [hep-ph].
- [209] Stephen D. Ellis and Davison E. Soper. “Successive combination jet algorithm for hadron collisions”. In: *Phys. Rev. D* 48 (7 Oct. 1993), pp. 3160–3166. doi: 10.1103/PhysRevD.48.3160. URL: <https://link.aps.org/doi/10.1103/PhysRevD.48.3160>.
- [210] Claude Fabienne Duerig. “Measuring the Higgs Self-coupling at the International Linear Collider”. Universität Hamburg, Diss., 2016. Dr. Hamburg: Universität Hamburg, 2016, p. 246. doi: 10.3204/PUBDB-2016-04283. URL: <https://bib-pubdb1.desy.de/record/310520>.
- [211] Yasser Radkhorrani and Jenny List. “Conceptual aspects for the improvement of the reconstruction of b - and c -jets at e^+e^- Higgs Factories with ParticleFlow detectors”. In: *International Workshop on Future Linear Colliders*. May 2021. arXiv: 2105.08480 [hep-ex].
- [212] Yasser Radkhorrani and Jenny List. “Kinematic fitting for ParticleFlow Detectors at Future Higgs Factories”. In: *PoS PANIC2021* (2022), p. 398. doi: 10.22323/1.380.0398. arXiv: 2111.14775 [hep-ex].
- [213] Moritz Beckmann, Benno List, and Jenny List. “Treatment of Photon Radiation in Kinematic Fits at Future e^+e^- Colliders”. In: *Nucl. Instrum. Meth. A* 624 (2010), pp. 184–191. doi: 10.1016/j.nima.2010.08.107. arXiv: 1006.0436 [hep-ex].
- [214] Gilles Louppe et al. “QCD-aware recursive neural networks for jet physics”. In: *Journal of High Energy Physics* 2019.1 (Jan. 2019), p. 57. ISSN: 1029-8479. doi: 10.1007/JHEP01(2019)057. URL: [https://doi.org/10.1007/JHEP01\(2019\)057](https://doi.org/10.1007/JHEP01(2019)057).
- [215] Jonathan Shlomi et al. “Secondary vertex finding in jets with neural networks”. In: *Eur. Phys. J. C* 81.6 (2021), p. 540. doi: 10.1140/epjc/s10052-021-09342-y. arXiv: 2008.02831 [hep-ex].
- [216] Xiangyang Ju and Benjamin Nachman. “Supervised jet clustering with graph neural networks for Lorentz boosted bosons”. In: *Phys. Rev. D* 102 (7 Oct. 2020), p. 075014. doi: 10.1103/PhysRevD.102.075014. URL: <https://link.aps.org/doi/10.1103/PhysRevD.102.075014>.
- [217] Kyle Cranmer et al. “Reframing Jet Physics with New Computational Methods”. In: *EPJ Web Conf.* 251 (2021), p. 03059. doi: 10.1051/epjconf/202125103059. arXiv: 2105.10512 [hep-ph].

- [218] Fons Rademakers et al. *root-project/root: v6.20/06*. Version v6-20-06. June 2020. DOI: 10.5281/zenodo.3895852. URL: <https://doi.org/10.5281/zenodo.3895852>.
- [219] Jakob Beyer. *PrEW - Precision Electro-Weak fits*. <https://github.com/beyerja/PrEW>. 2022.
- [220] Jakob Beyer. *PrEWUtils - Utensils to use PrEW with ease*. <https://github.com/beyerja/PrEWUtils>. 2022.
- [221] Jakob Beyer. *PrEWRunExample - Fitting example for PrEW*. <https://github.com/beyerja/PrEWRunExample>. 2022.
- [222] Jakob Beyer. *PrEWMultiSetupTest - Testing a large number of setups with PrEW*. <https://github.com/beyerja/PrEWMultiSetupTest>. 2022.
- [223] Jakob Beyer. *PrEWSampleProduction*. <https://github.com/beyerja/PrEWSampleProduction>. 2022.
- [224] Jakob Beyer. *PrEWSystematicsValidation*. <https://github.com/beyerja/PrEWSystematicsValidation>. 2022.
- [225] Jakob Beyer. *PrEWRescanChecks*. <https://github.com/beyerja/PrEWRescanChecks>. 2022.
- [226] Jakob Beyer. *PrEWShapeChecks*. <https://github.com/beyerja/PrEWShapeChecks>. 2022.
- [227] M J Boland et al. *Updated baseline for a staged Compact Linear Collider*. CERN Yellow Reports: Monographs. Comments: 57 pages, 27 figures, 12 tables. Geneva: CERN, Aug. 2016. DOI: 10.5170/CERN-2016-004. URL: <https://cds.cern.ch/record/2210892>.
- [228] Jean Buon and Klaus Steffen. “Hera variable-energy “mini” spin rotator and head-on ep collision scheme with choice of electron helicity”. In: *Nuclear Instruments and Methods in Physics Research Section A: Accelerators, Spectrometers, Detectors and Associated Equipment* 245.2 (1986), pp. 248–261. ISSN: 0168-9002. DOI: [https://doi.org/10.1016/0168-9002\(86\)91257-X](https://doi.org/10.1016/0168-9002(86)91257-X). URL: <https://www.sciencedirect.com/science/article/pii/016890028691257X>.
- [229] E. Gianfelice and DESY. “First Polarisation Studies at HERA with 3 Spin Rotators”. In: *DESY-HERA-Report* (2003). URL: <https://bib-pubdb1.desy.de/record/139209>.
- [230] A Blondel. *Systematic Uncertainties on LEP Electroweak observables Due to Unknown Residual Longitudinal Beam Polarization*. Tech. rep. Geneva: CERN, 1995. URL: <https://cds.cern.ch/record/806152>.
- [231] S. Bilokin, R. Pöschl, and F. Richard. “Measurement of b quark EW couplings at ILC”. In: (Sept. 2017). arXiv: 1709.04289 [hep-ex].

8. Conclusion

- [232] A. Irlles, R. Pöschl, and F. Richard. “Production and measurement of $e^+e^- \rightarrow c\bar{c}$ signatures at the 250 GeV ILC”. In: *International Workshop on Future Linear Colliders*. Feb. 2020. arXiv: 2002.05805 [hep-ex].
- [233] “A Combination of preliminary electroweak measurements and constraints on the standard model”. In: (Dec. 2003). arXiv: hep-ex/0312023.
- [234] The ALEPH Collaboration. “Measurement of the Z resonance parameters at LEP”. In: *The European Physical Journal C - Particles and Fields* 14.1 (May 2000), pp. 1–50. ISSN: 1434-6052. DOI: 10.1007/s100520000319. URL: <https://doi.org/10.1007/s100520000319>.
- [235] The L3 Collaboration. “Measurements of cross sections and forward-backward asymmetries at the Z resonance and determination of electroweak parameters”. In: *The European Physical Journal C - Particles and Fields* 16.1 (Aug. 2000), pp. 1–40. ISSN: 1434-6052. DOI: 10.1007/s100520050001. URL: <https://doi.org/10.1007/s100520050001>.
- [236] G. Abbiendi et al. “Precise determination of the Z resonance parameters at LEP: “Zedometry””. In: *The European Physical Journal C* 19.4 (Mar. 2001), pp. 587–651. ISSN: 1434-6052. DOI: 10.1007/s100520100627. URL: <http://dx.doi.org/10.1007/s100520100627>.
- [237] B. Aurand et al. *Beam Polarization at the ILC: the Physics Impact and the Accelerator Solutions*. 2009. arXiv: 0903.2959 [physics.acc-ph].
- [238] Takayuki Ueno. “A simulation study on measurement of the polarization asymmetry A_{LR} using the initial state radiation at the ILC with center-of-mass energy of 250 GeV”. Master thesis. Tohoku University, Department of Physics, 2018. URL: http://lambda.phys.tohoku.ac.jp/gppu/news/20190208QE1/students/ueno2019/thesis_ueno.pdf.
- [239] A. Denner et al. “corrections to : first numerical results from RacoonWW”. In: *Physics Letters B* 475.1-2 (Feb. 2000), pp. 127–134. ISSN: 0370-2693. DOI: 10.1016/S0370-2693(00)00059-9. URL: [http://dx.doi.org/10.1016/S0370-2693\(00\)00059-9](http://dx.doi.org/10.1016/S0370-2693(00)00059-9).
- [240] Michael E. Peskin. “Theory of e^+e^- collisions at very high-energy”. In: *Conf. Proc. C 8708101* (1987). Ed. by Eileen C. Brennan, pp. 1–45. URL: <https://www.slac.stanford.edu/pubs/slacpubs/4500/slac-pub-4601.pdf>.
- [241] T. Barklow et al. “Anomalous Gauge Boson Couplings”. In: *arXiv e-prints*, hep-ph/9611454 (Nov. 1996), hep-ph/9611454. arXiv: hep-ph/9611454 [hep-ph].

Appendix

A. Datasets

A.1. Uncertainties on fractional cross-sections

The chapter describing the datasets (chapter 5) quotes uncertainties on the cross-sections for the processes in this study (tables 5.1 and 5.2). These cross-sections are all fractional, meaning that they represent a subset of the full Monte-Carlo sample for the given process, which defines a “category” of that process. For each category, the fractional cross-section σ_{cat} is the result of the product of the fraction of MC events in that category and the total cross-section.

$$\sigma_{\text{cat}} = \frac{N_{\text{cat}}}{N_{\text{tot}}} \sigma_{\text{tot}} \quad (\text{A.1})$$

The total number of MC events itself is the sum of the events in the category N_{cat} and events outside the category N_{other} .

$$N_{\text{tot}} = N_{\text{cat}} + N_{\text{other}} \quad (\text{A.2})$$

The uncertainty of the fractional cross-section is therefore the composition of the uncertainties on the three independent quantities σ_{tot} , N_{cat} and N_{other} .

Using the partial derivatives

$$\frac{\partial \sigma_{\text{cat}}}{\partial \sigma_{\text{tot}}} = \frac{N_{\text{cat}}}{N_{\text{tot}}}, \quad \frac{\partial \sigma_{\text{cat}}}{\partial N_{\text{cat}}} = \frac{\sigma_{\text{tot}}}{N_{\text{tot}}^2} (N_{\text{tot}} - N_{\text{cat}}), \quad \frac{\partial \sigma_{\text{cat}}}{\partial N_{\text{other}}} = -\frac{\sigma_{\text{tot}}}{N_{\text{tot}}^2} N_{\text{cat}} \quad (\text{A.3})$$

and the Poisson uncertainty on the MC events $\Delta N = \sqrt{N}$, the uncertainty formula for σ_{cat} reduces to two terms.

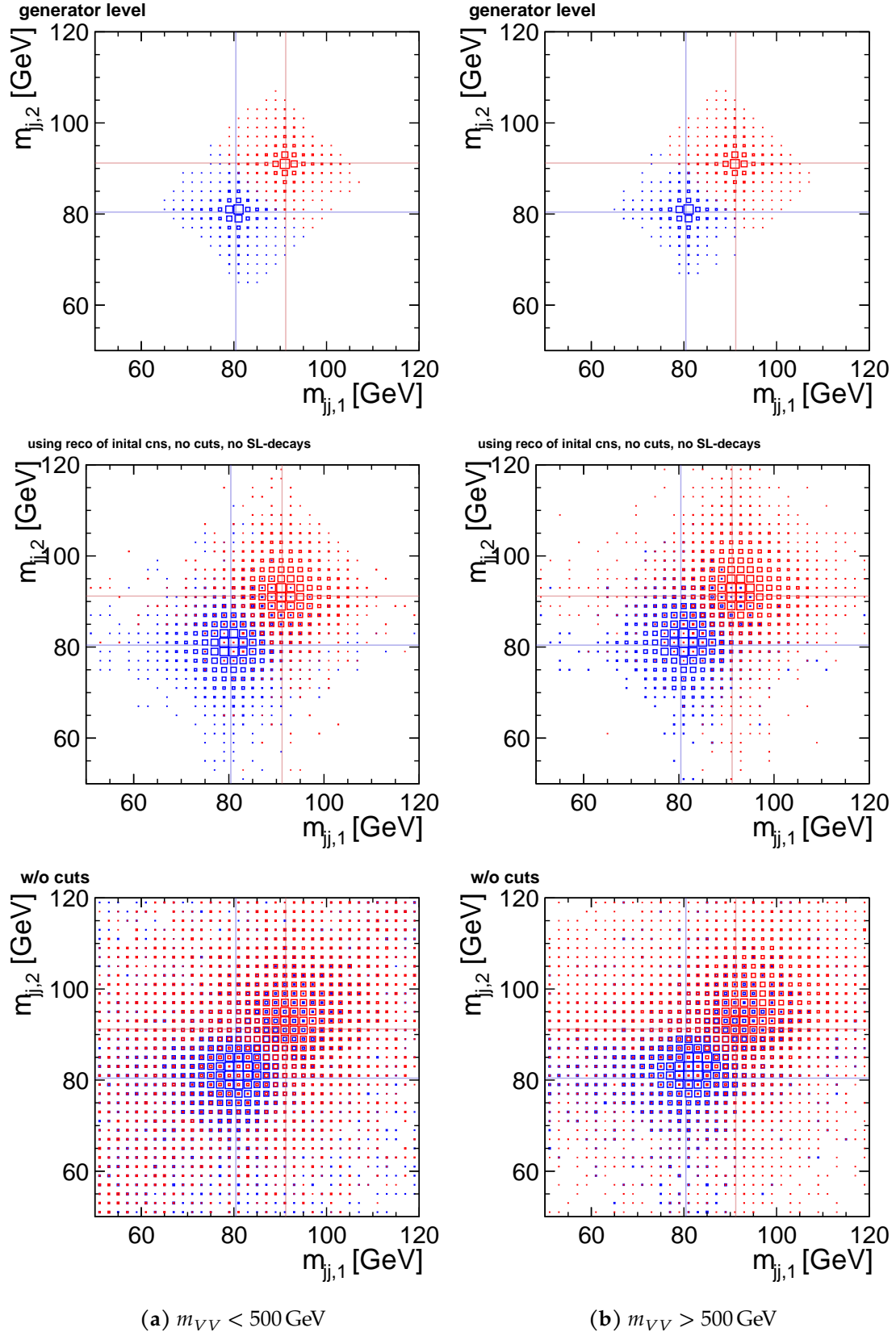
$$\begin{aligned} \Delta \sigma_{\text{cat}} &= \sqrt{\left(\frac{\partial \sigma_{\text{cat}}}{\partial \sigma_{\text{tot}}} \right)^2 (\Delta \sigma_{\text{tot}})^2 + \left(\frac{\partial \sigma_{\text{cat}}}{\partial N_{\text{cat}}} \right)^2 (\Delta N_{\text{cat}})^2 + \left(\frac{\partial \sigma_{\text{cat}}}{\partial N_{\text{other}}} \right)^2 (\Delta N_{\text{other}})^2} \\ &= \sqrt{\left(\frac{N_{\text{cat}}}{N_{\text{tot}}} \Delta \sigma_{\text{tot}} \right)^2 + \left(\frac{\sigma_{\text{tot}}}{N_{\text{tot}}^2} \right)^2 \left[(N_{\text{tot}} - N_{\text{cat}})^2 N_{\text{cat}} + N_{\text{cat}}^2 (N_{\text{tot}} - N_{\text{cat}}) \right]} \quad (\text{A.4}) \\ &= \sqrt{\left(\frac{N_{\text{cat}}}{N_{\text{tot}}} \Delta \sigma_{\text{tot}} \right)^2 + \left(\frac{\sigma_{\text{tot}}}{N_{\text{tot}}^2} \sqrt{N_{\text{tot}}^2 N_{\text{cat}} - N_{\text{tot}} N_{\text{cat}}^2} \right)^2} \\ &=: \sqrt{\Delta_{\text{ME}}^2 + \Delta_{\text{MC}}^2} \end{aligned}$$

The first term Δ_{ME} describes the uncertainty from the calculation of the total cross-section from the phase-space integration of the matrix element, and the second term Δ_{MC} describes the uncertainty from the Poisson fluctuation in the fraction $N_{\text{cat}}/N_{\text{tot}}$. In this study, the WHIZARD phase-space integration gives the value $\Delta \sigma_{\text{tot}}$.

B. Separating hadronic decays of boson pairs

B.1. Mass distributions

This section presents the two-dimensional mass distributions (fig. B.1) and corresponding one-dimensional $(m_{V1} + m_{V2}) / 2$ projections (fig. B.2) for the large ILD model for three of the idealization steps (see section 6.3).



a-4 **Figure B.1.:** 2D mass distributions of true WW (blue) and ZZ (red) events for (a) the low- m_{VV} and (b) the high- m_{VV} events in the large ILD model for three stages: (top) generator level, (middle) no semileptonic decays and idealized assignment to boson, and (bottom) full reconstruction.

B. Separating hadronic decays of boson pairs

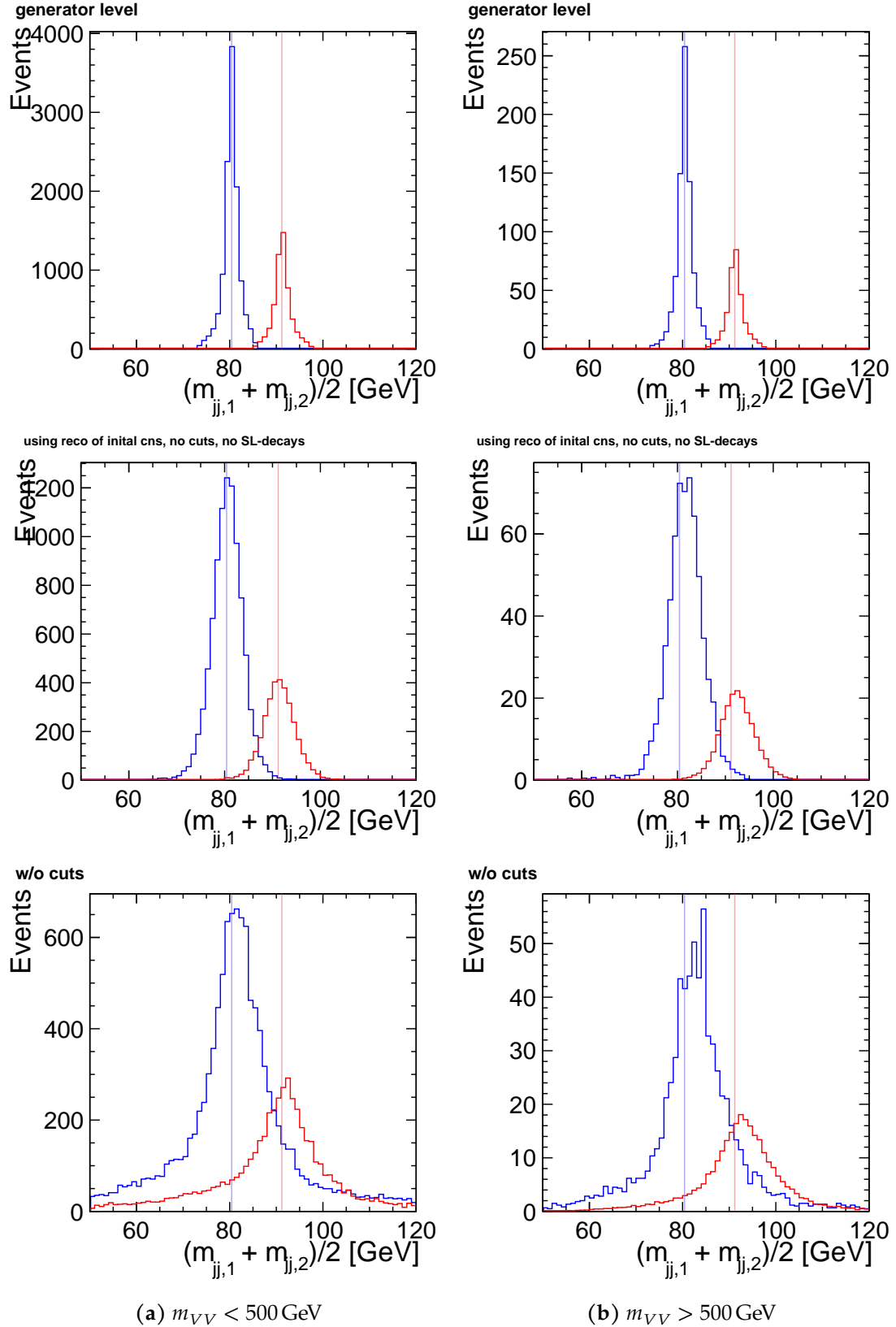
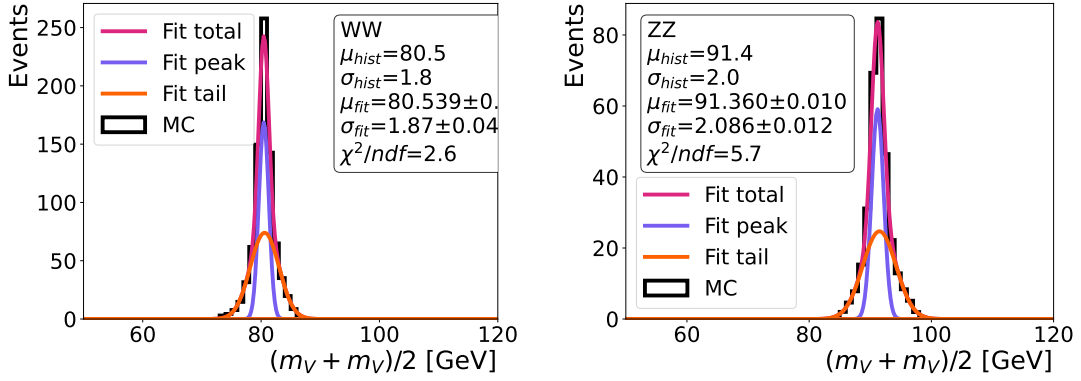


Figure B.2.: 1D mass projections of true WW (blue) and ZZ (red) events for (a) the low- m_{VV} and (b) the high- m_{VV} events in the large ILD model for three stages: (top) generator level, (middle) no semileptonic decays and idealized assignment to boson, and (bottom) full reconstruction. a-5

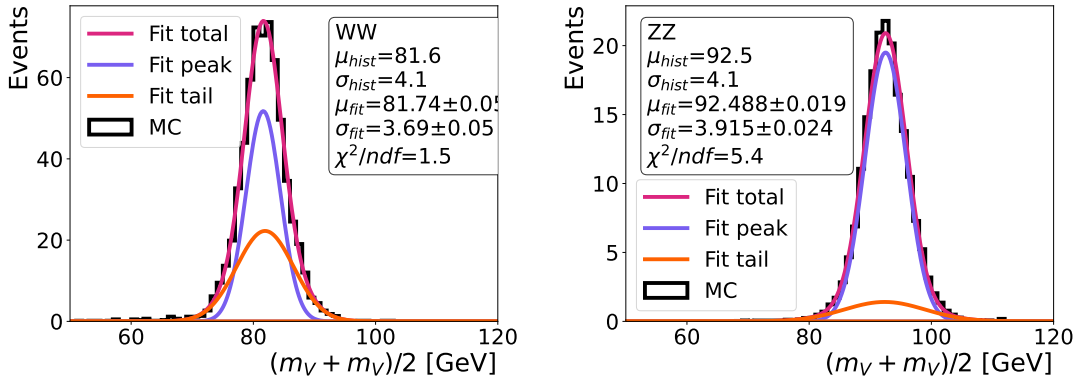
B.2. Complete set of fits to mass distributions

This section presents the full set of fits of two gaussians to the WW and ZZ one-dimensional mass projections (figs. B.3 to B.6) as described in the main body of this work (section 6.2).

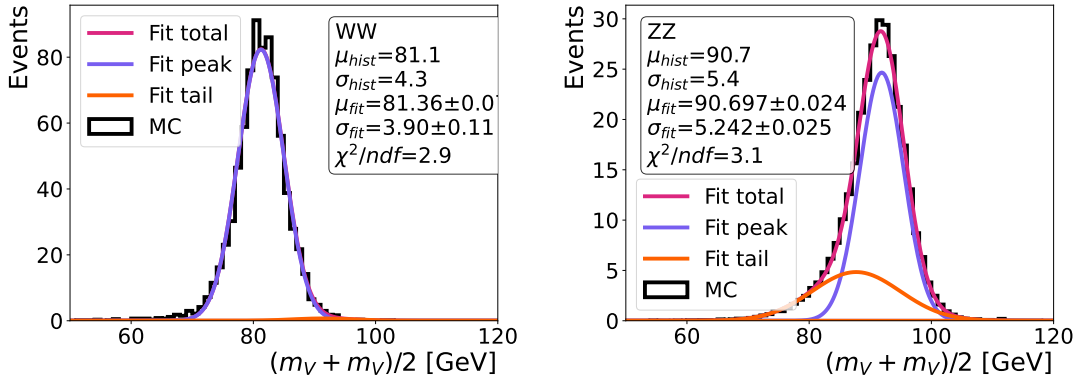
B. Separating hadronic decays of boson pairs



(a) IDR-L, $m_{VV} > 500$ GeV, generator level

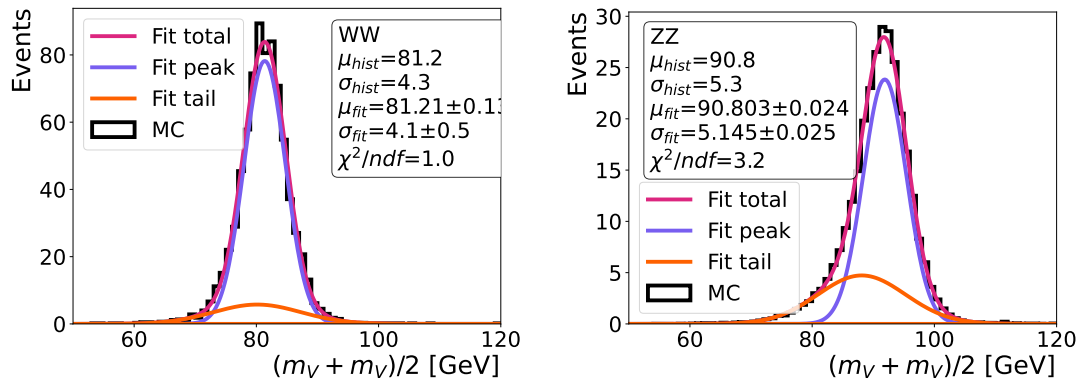


(b) IDR-L, $m_{VV} > 500$ GeV, cheated bosons, no SL-dec.

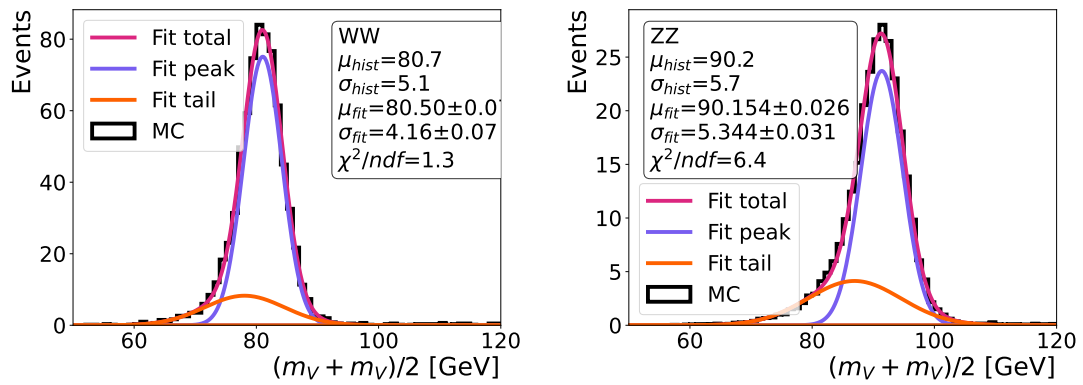


(c) IDR-L, $m_{VV} > 500$ GeV, cheated bosons

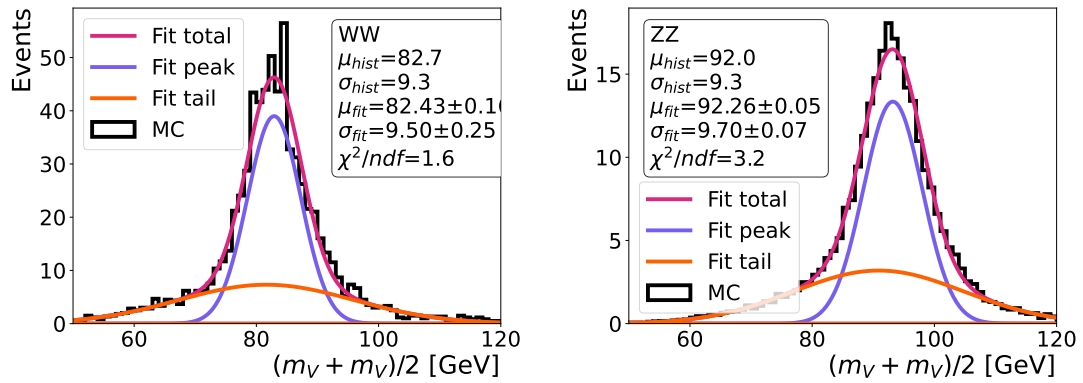
Figure B.3.: Fits of the sum of two Gaussians to the WW and ZZ mass distributions for the IDR-L model and the $m_{VV} > 500$ GeV events at the different idealization steps (see table 6.1).



(d) IDR-L, $m_{VV} > 500$ GeV, cheated jets



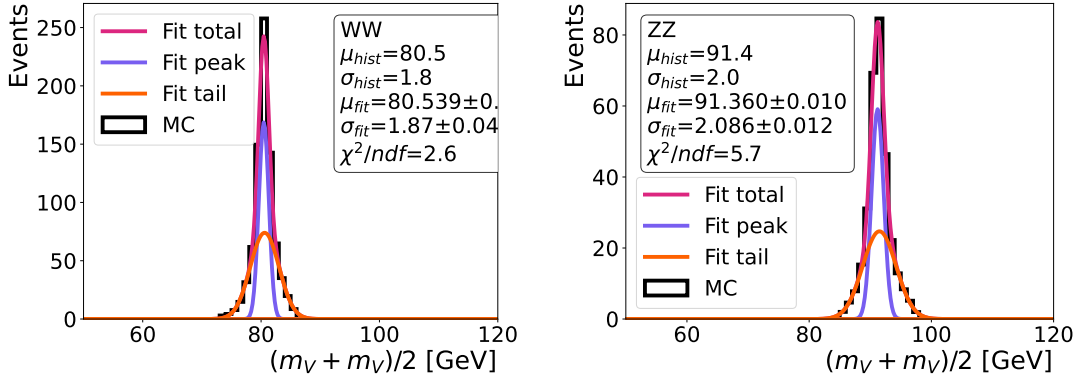
(e) IDR-L, $m_{VV} > 500$ GeV, cheated overlay



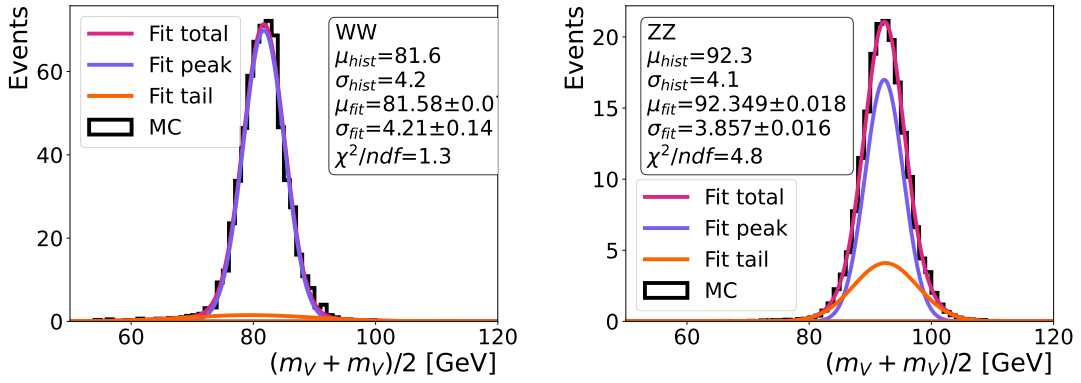
(f) IDR-L, $m_{VV} > 500$ GeV, full reconstruction

Figure B.3.: (cont.)

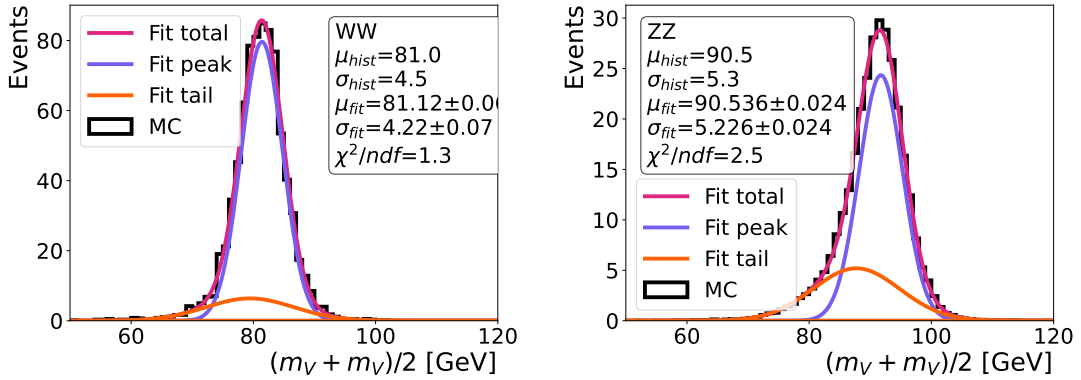
B. Separating hadronic decays of boson pairs



(a) IDR-S, $m_{VV} > 500$ GeV, generator level

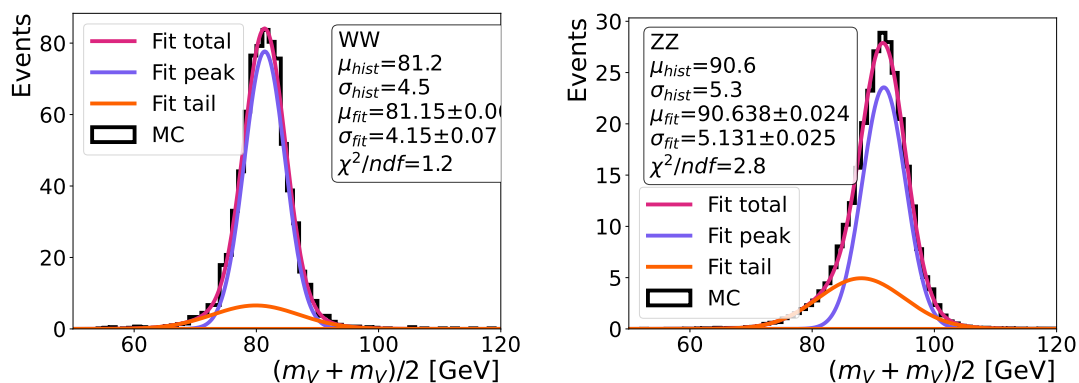


(b) IDR-S, $m_{VV} > 500$ GeV, cheated bosons, no SL-dec.

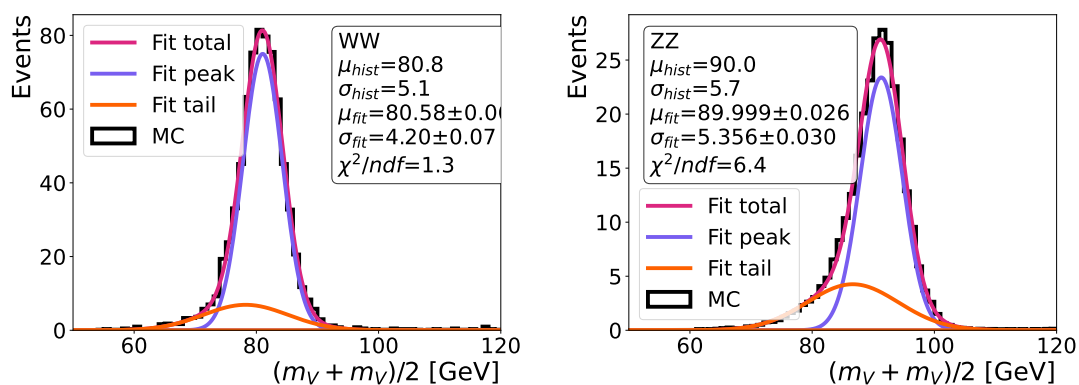


(c) IDR-S, $m_{VV} > 500$ GeV, cheated bosons

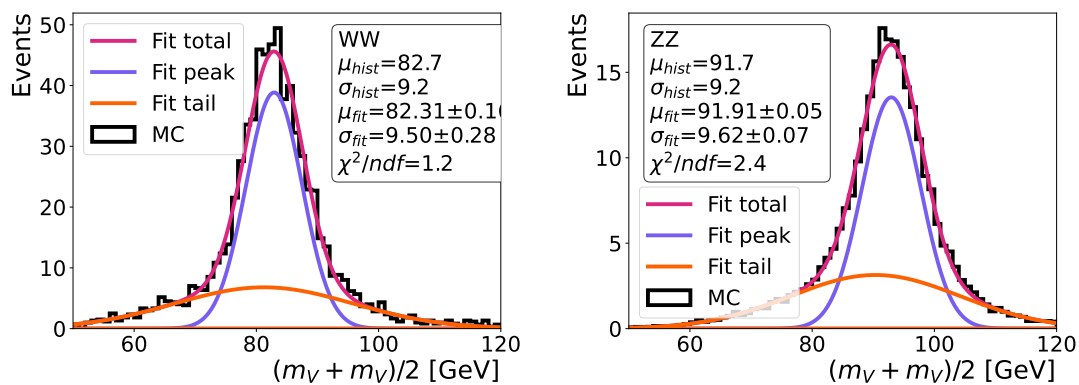
Figure B.4.: Fits of the sum of two Gaussians to the WW and ZZ mass distributions for the IDR-S model and the $m_{VV} > 500$ GeV events at the different idealization steps (see table 6.1).



(d) IDR-S, $m_{VV} > 500$ GeV, cheated jets



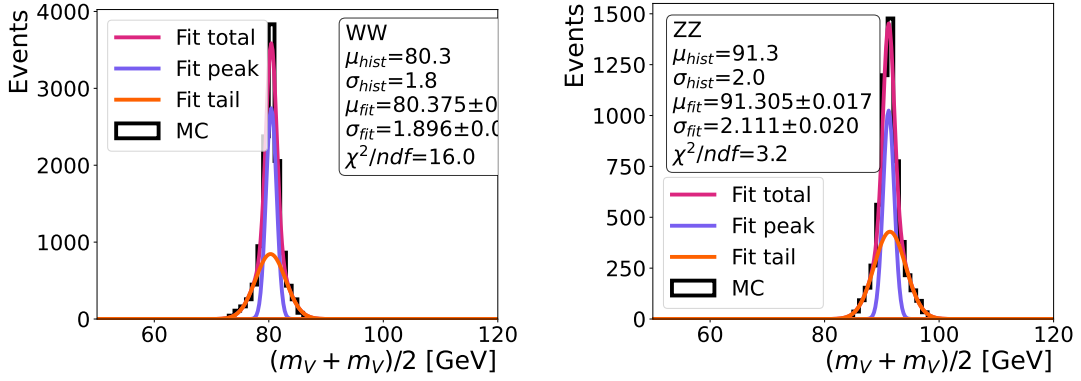
(e) IDR-S, $m_{VV} > 500$ GeV, cheated overlay



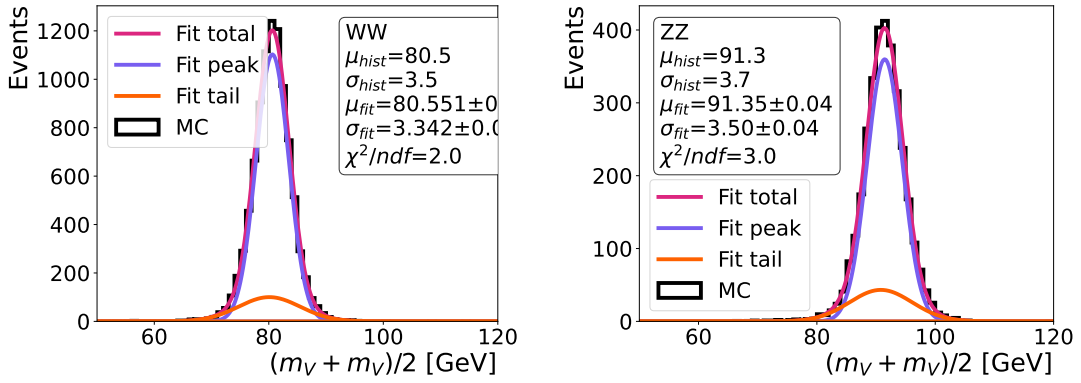
(f) IDR-S, $m_{VV} > 500$ GeV, full reconstruction

Figure B.4.: (cont.)

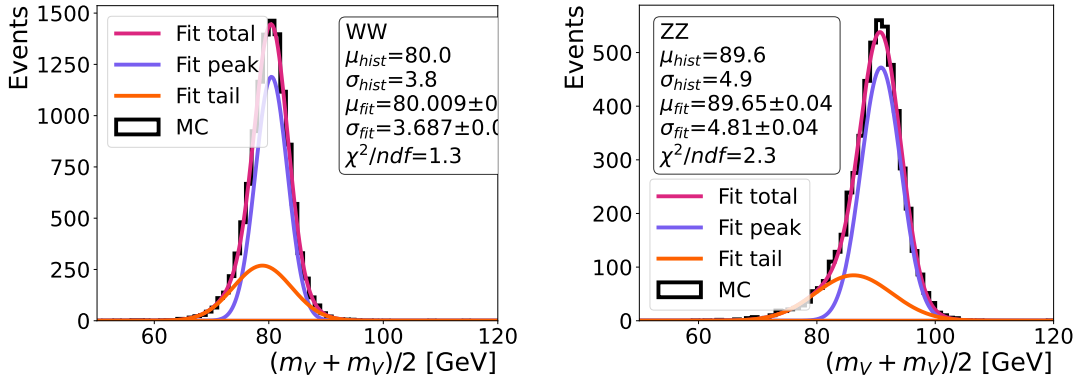
B. Separating hadronic decays of boson pairs



(a) IDR-L, $m_{VV} < 500$ GeV, generator level

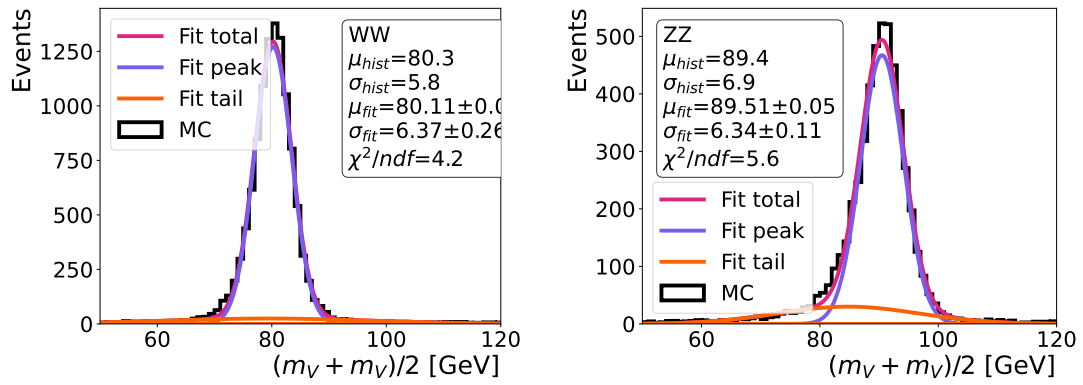


(b) IDR-L, $m_{VV} < 500$ GeV, cheated bosons, no SL-dec.

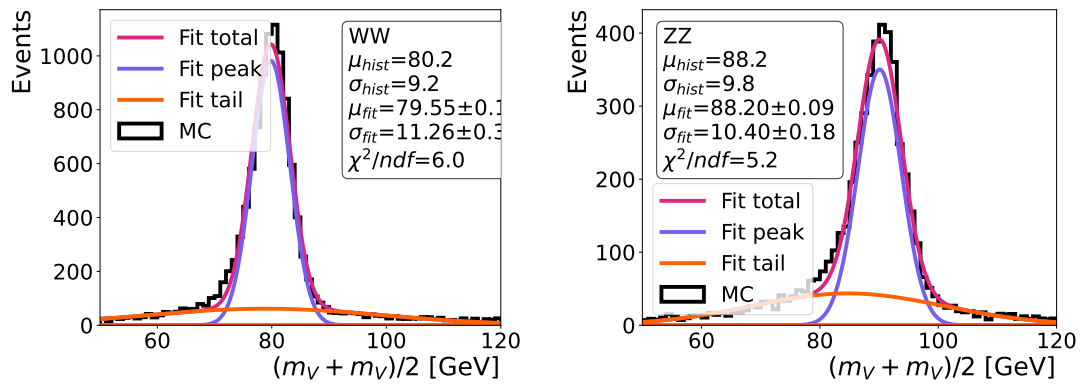


(c) IDR-L, $m_{VV} < 500$ GeV, cheated bosons

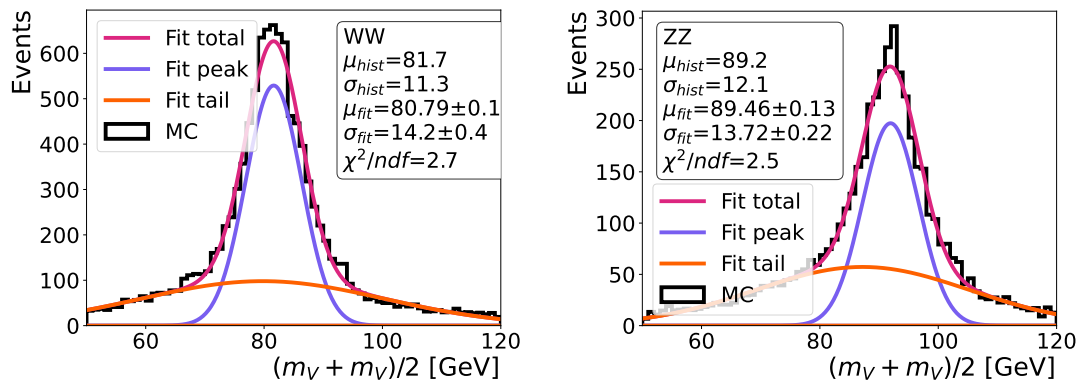
Figure B.5.: Fits of the sum of two Gaussians to the WW and ZZ mass distributions for the IDR-L model and the $m_{VV} < 500$ GeV events at the different idealization steps (see table 6.1).



(d) IDR-L, $m_{VV} < 500$ GeV, cheated jets



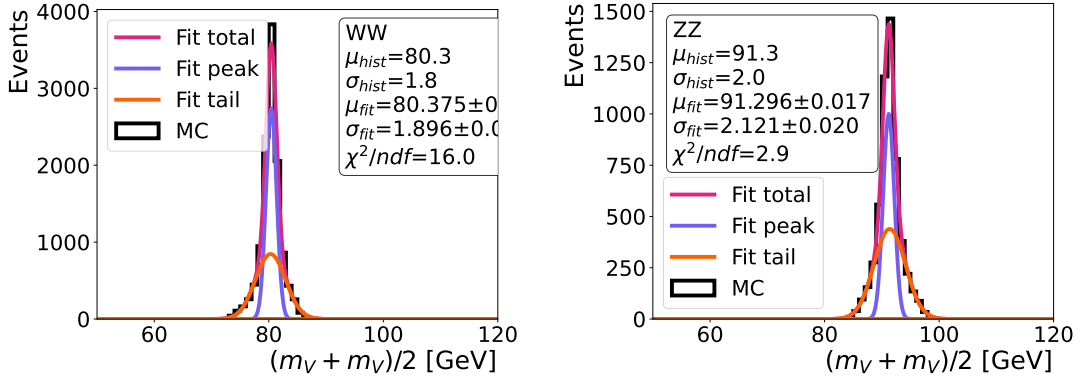
(e) IDR-L, $m_{VV} < 500$ GeV, cheated overlay



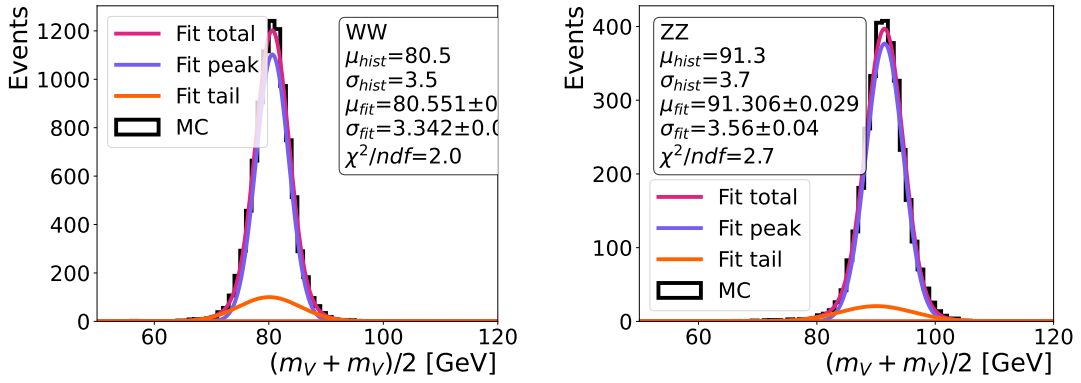
(f) IDR-L, $m_{VV} < 500$ GeV, full reconstruction

Figure B.5.: (cont.)

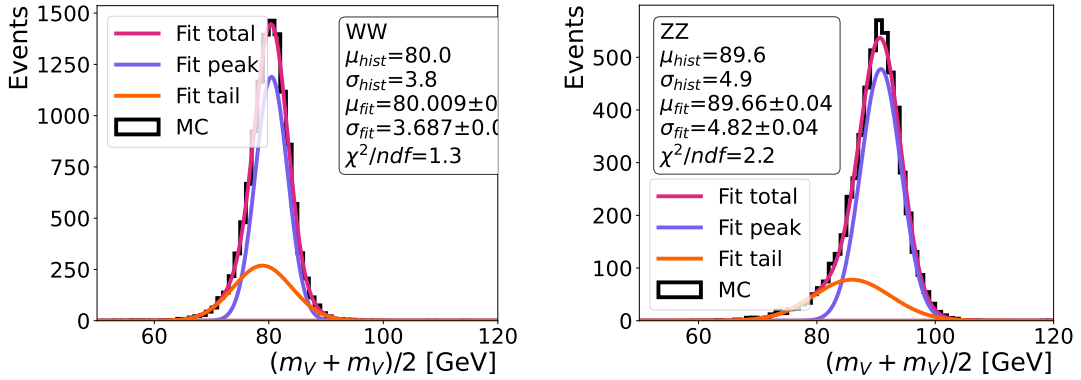
B. Separating hadronic decays of boson pairs



(a) IDR-S, $m_{VV} < 500$ GeV, generator level

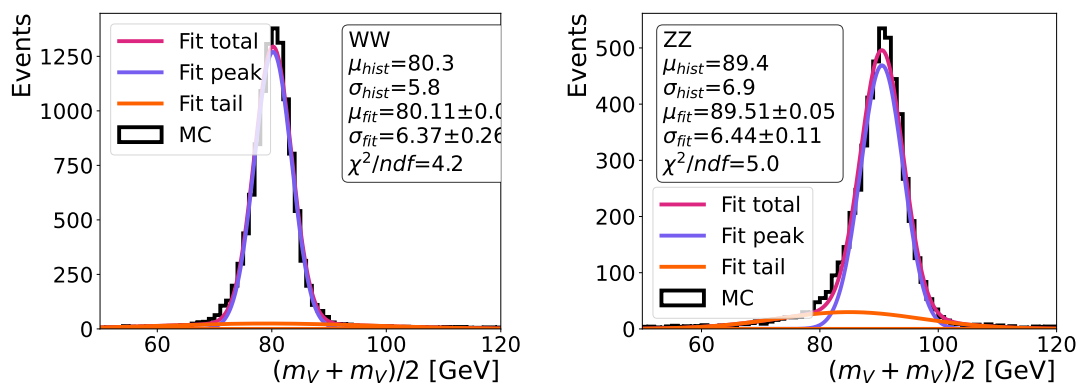


(b) IDR-S, $m_{VV} < 500$ GeV, cheated bosons, no SL-dec.

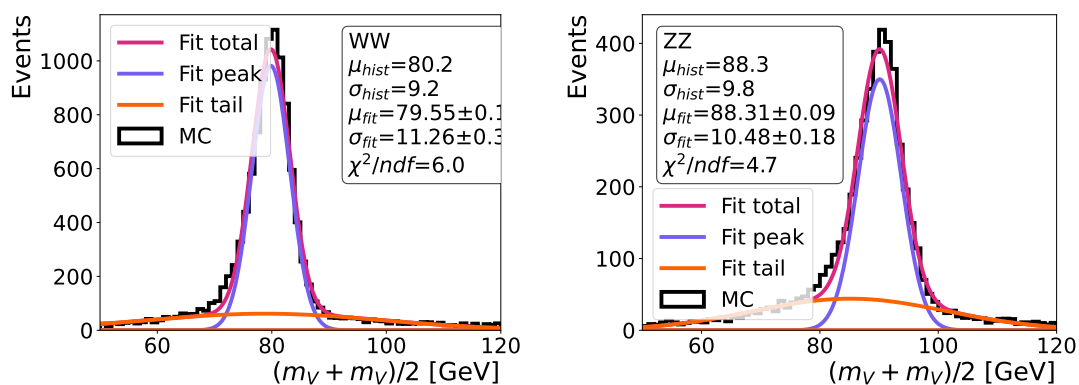


(c) IDR-S, $m_{VV} < 500$ GeV, cheated bosons

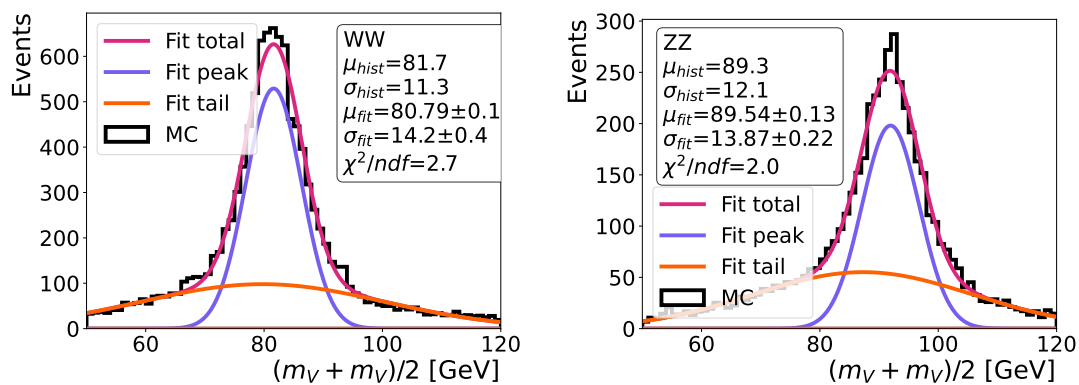
Figure B.6.: Fits of the sum of two Gaussians to the WW and ZZ mass distributions for the IDR-S model and the $m_{VV} < 500$ GeV events at the different idealization steps (see table 6.1).



(d) IDR-S, $m_{VV} < 500$ GeV, cheated jets



(e) IDR-S, $m_{VV} < 500$ GeV, cheated overlay



(f) IDR-S, $m_{VV} < 500$ GeV, full reconstruction

Figure B.6.: (cont.)

B.3. Idealization steps in the small ILD model

This section presents the idealization step plots (fig. B.7) for the small detector models. Corresponding plots for the large model are in the main text (fig. 6.6).

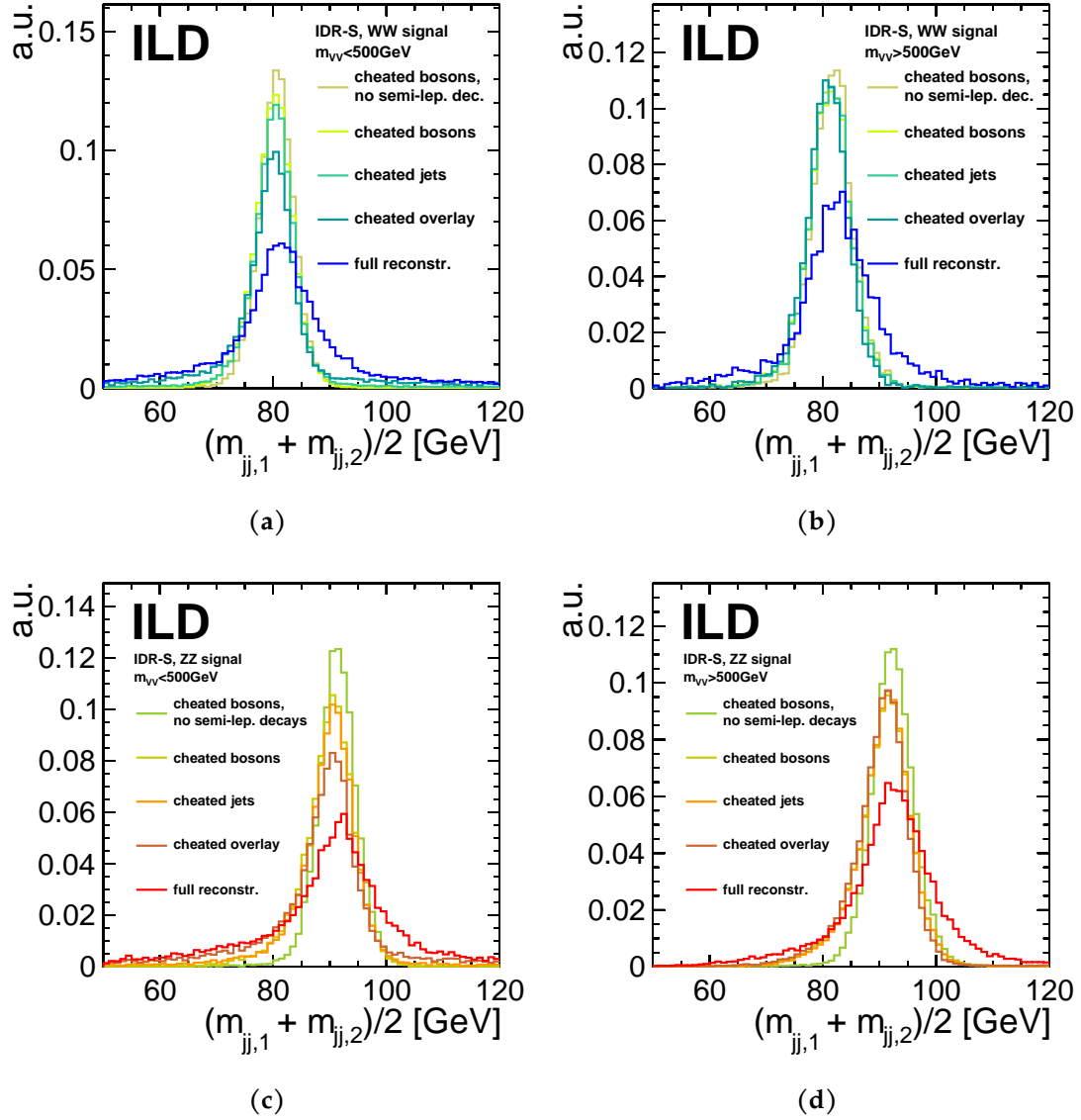


Figure B.7.: Step-by-step idealizations of the event reconstruction process for the mass distributions of WW (top) and ZZ (bottom) events, for both kinematic ranges (left: low- m_{VV} , right: high- m_{VV}), here for the small detector model (for large model: fig. 6.6).

B.4. ROC curves for the idealization steps

This section presents the receiver-operator-curves (ROC, fig. B.8) for the scan of the cut in the one-dimensional mass projections. The area under each ROC curve gives the AUC values, which is one of the quantifiers in this study (section 6.2 and fig. 6.7).

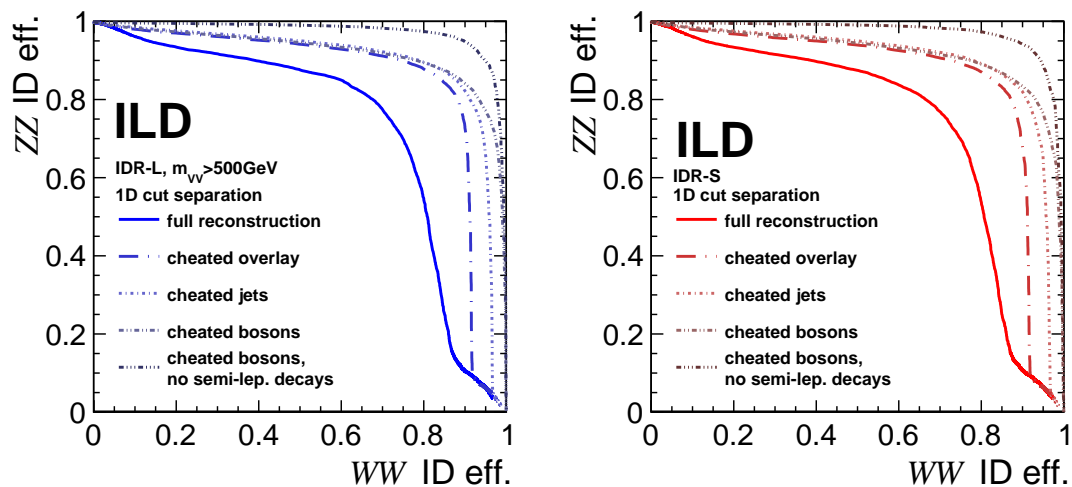
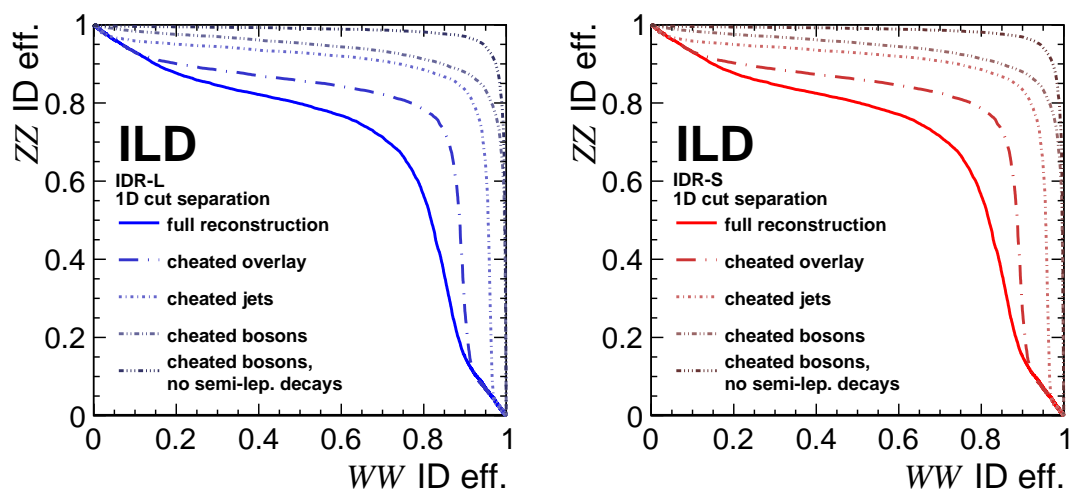
(a) $m_{VV} > 500$ GeV(b) $m_{VV} < 500$ GeV

Figure B.8.: Varying a 1D-cut in the di-boson mass projections (figs. 6.6 and B.7) yields a ROC-curve, and the area under such curves quantifies the separation of the distributions (fig. 6.7b). The curves here show the distributions for (a) $m_{VV} > 500$ GeV and (b) $m_{VV} < 500$ GeV events, with the (left) large and (right) small ILD model. Previously published in [205].

C. Impact of beam polarisation on electroweak fits

C.1. Detailed derivation of the 2f parametrisation

This section describes the derivation of the new fermion pair production parametrisation (eq. (7.8)) in detail, including the unpolarised form and the properties of that parametrisation.

Restoring known parameters through reparametrisation

The helicity amplitude approach with the correction terms (eq. (7.6))

$$\begin{aligned}\frac{d\sigma_{LR}^f}{d\cos\theta} &= \Sigma_{Ll} (1 + \cos\theta)^2 + \Sigma_{Lr} (1 - \cos\theta)^2 + K_L (1 - 3\cos^2\theta) \\ \frac{d\sigma_{RL}^f}{d\cos\theta} &= \Sigma_{Rr} (1 + \cos\theta)^2 + \Sigma_{Rl} (1 - \cos\theta)^2 + K_R (1 - 3\cos^2\theta)\end{aligned}\tag{C.1}$$

accurately describes the $\mu^+\mu^-$ distributions. From an experimental point of view, the parameters of that approach turn out inconvenient. All parameters correlate with normalisation shifts (e.g. luminosity) and there is no distinction between chirality dependent and chirality independent effects. A reparametrisation mitigates both of these issues, and also restore the parameter set used at LEP and SLD [38].

The first step in the reparametrisation isolates the overall normalisation of each chiral cross-section.

$$\begin{aligned}\frac{d\sigma_{LR}^f}{d\cos\theta} &= (\Sigma_{Ll} + \Sigma_{Lr}) \left[\frac{\Sigma_{Ll}}{\Sigma_{Ll} + \Sigma_{Lr}} (1 + \cos\theta)^2 + \frac{\Sigma_{Lr}}{\Sigma_{Ll} + \Sigma_{Lr}} (1 - \cos\theta)^2 + \frac{K_L}{\Sigma_{Ll} + \Sigma_{Lr}} (1 - 3\cos^2\theta) \right] \\ \frac{d\sigma_{RL}^f}{d\cos\theta} &= (\Sigma_{Rr} + \Sigma_{Rl}) \left[\frac{\Sigma_{Rr}}{\Sigma_{Rr} + \Sigma_{Rl}} (1 + \cos\theta)^2 + \frac{\Sigma_{Rl}}{\Sigma_{Rr} + \Sigma_{Rl}} (1 - \cos\theta)^2 + \frac{K_R}{\Sigma_{Rr} + \Sigma_{Rl}} (1 - 3\cos^2\theta) \right]\end{aligned}\tag{C.2}$$

This motivates the choice for the lower case k 's, splitting them into chirality-dependent and -independent parts.

$$k_0 = \frac{K_L}{\Sigma_{Ll} + \Sigma_{Lr}} + \frac{K_R}{\Sigma_{Rr} + \Sigma_{Rl}}, \quad \Delta k = \frac{K_L}{\Sigma_{Ll} + \Sigma_{Lr}} - \frac{K_R}{\Sigma_{Rr} + \Sigma_{Rl}}\tag{C.3}$$

The normalisation reparameterises into a global normalisation (correlating e.g. with the luminosity) and a normalisation asymmetry (correlating e.g. with the polarisations).

$$\sigma_0^f = \frac{8}{3} (\Sigma_{Ll} + \Sigma_{Lr} + \Sigma_{Rr} + \Sigma_{Rl}) \quad (\text{C.4a})$$

$$A_e = \frac{(\Sigma_{Ll} + \Sigma_{Lr}) - (\Sigma_{Rr} + \Sigma_{Rl})}{\Sigma_{Ll} + \Sigma_{Lr} + \Sigma_{Rr} + \Sigma_{Rl}} \quad (\text{C.4b})$$

The factor $\frac{8}{3}$ results from the integral over $(1 \pm \cos \theta)^2$.

An application of these reparametrisations together with an expansion of the $(1 \pm \cos \theta)^2$ terms leads to a new form that only contains specific combinations of the helicity amplitudes in the linear term.

$$\begin{aligned} \frac{d\sigma_{LR}^f}{d \cos \theta} &= \frac{8}{3} \sigma_0^f \frac{1 + A_e}{2} \left[(1 + \cos^2 \theta) + 2 \frac{\Sigma_{Ll} - \Sigma_{Lr}}{\Sigma_{Ll} + \Sigma_{Lr}} \cos \theta + \frac{k_0 + \Delta k}{2} (1 - 3 \cos^2 \theta) \right] \\ \frac{d\sigma_{RL}^f}{d \cos \theta} &= \frac{8}{3} \sigma_0^f \frac{1 - A_e}{2} \left[(1 + \cos^2 \theta) + 2 \frac{\Sigma_{Rr} - \Sigma_{Rl}}{\Sigma_{Rr} + \Sigma_{Rl}} \cos \theta + \frac{k_0 - \Delta k}{2} (1 - 3 \cos^2 \theta) \right] \end{aligned} \quad (\text{C.5})$$

The linear coefficients again combine into a summed and an asymmetric term.

$$\epsilon_f = \frac{\Sigma_{Ll} - \Sigma_{Lr}}{\Sigma_{Ll} + \Sigma_{Lr}} + \frac{\Sigma_{Rr} - \Sigma_{Rl}}{\Sigma_{Rr} + \Sigma_{Rl}} \quad (\text{C.6a})$$

$$A_f = \frac{1}{2} \left(\frac{\Sigma_{Ll} - \Sigma_{Lr}}{\Sigma_{Ll} + \Sigma_{Lr}} - \frac{\Sigma_{Rr} - \Sigma_{Rl}}{\Sigma_{Rr} + \Sigma_{Rl}} \right) \quad (\text{C.6b})$$

The parameter ϵ_f is given named that way because it vanishes in the SM Z-pole case (eq. (7.10a)).

All the reparametrisations together yield the new generalised parametrisation approach.

$$\begin{aligned} \frac{d\sigma_{LR}^f}{d \cos \theta} &= \frac{3}{8} \sigma_0^f \frac{1 + A_e}{2} \left[\left(1 + \frac{k_0 + \Delta k}{2} \right) + (\epsilon_f + 2A_f) \cos \theta + \left(1 - 3 \frac{k_0 + \Delta k}{2} \right) \cos^2 \theta \right] \\ \frac{d\sigma_{RL}^f}{d \cos \theta} &= \frac{3}{8} \sigma_0^f \frac{1 - A_e}{2} \left[\left(1 + \frac{k_0 - \Delta k}{2} \right) + (\epsilon_f - 2A_f) \cos \theta + \left(1 - 3 \frac{k_0 - \Delta k}{2} \right) \cos^2 \theta \right] \end{aligned} \quad (\text{C.7})$$

The parameters σ_0^f , A_e and A_f are fully consistent with the parameters of the same notation used by LEP and SLD (eq. (7.10a)).

Helicity amplitudes in new parametrisation

A comparison of the initial and final form of the new parametrisation (eqs. (C.1) and (C.7)) directly yields how the helicity amplitudes relate to the new parameter set.

$$\Sigma_{Ll} = \frac{3}{8}\sigma_0^f \frac{1+A_e}{2} \frac{1}{2} \left(1 + \frac{1}{2} [\epsilon_f + 2A_f] \right) \quad (\text{C.8a})$$

$$\Sigma_{Lr} = \frac{3}{8}\sigma_0^f \frac{1+A_e}{2} \frac{1}{2} \left(1 - \frac{1}{2} [\epsilon_f + 2A_f] \right) \quad (\text{C.8b})$$

$$\Sigma_{Rr} = \frac{3}{8}\sigma_0^f \frac{1-A_e}{2} \frac{1}{2} \left(1 + \frac{1}{2} [\epsilon_f - 2A_f] \right) \quad (\text{C.8c})$$

$$\Sigma_{Rl} = \frac{3}{8}\sigma_0^f \frac{1-A_e}{2} \frac{1}{2} \left(1 - \frac{1}{2} [\epsilon_f - 2A_f] \right) \quad (\text{C.8d})$$

A single dataset measurement

The discussion so far considered directly the pure chiral initial states. When taking data at an e^+e^- collider, the measured distribution of a given dataset is combination of these initial states. The polarisations \mathcal{D}_{e^\pm} in that dataset determine the weights of the initial states.

$$\begin{aligned} \frac{d\sigma_{\text{pol}}^f}{d\cos\theta}(\mathcal{D}_{e^-}, \mathcal{D}_{e^+}) &= \frac{1}{4}(1-\mathcal{D}_{e^-})(1+\mathcal{D}_{e^+}) \frac{d\sigma_{LR}^f}{d\cos\theta} + \frac{1}{4}(1+\mathcal{D}_{e^-})(1-\mathcal{D}_{e^+}) \frac{d\sigma_{RL}^f}{d\cos\theta} \\ &= \frac{3}{8}\sigma_0^f \frac{1}{4} \\ &\quad \times [(1 - \mathcal{D}_{e^-}\mathcal{D}_{e^+} + A_e(\mathcal{D}_{e^+} - \mathcal{D}_{e^-})) (1 + \cos^2\theta) + \\ &\quad (\epsilon_f(1 - \mathcal{D}_{e^-}\mathcal{D}_{e^+} + A_e(\mathcal{D}_{e^+} - \mathcal{D}_{e^-})) + 2A_f\{\mathcal{D}_{e^+} - \mathcal{D}_{e^-} + A_e(1 - \mathcal{D}_{e^-}\mathcal{D}_{e^+})\}) \cos\theta + \\ &\quad \left(\frac{k_0}{2}\{1 - \mathcal{D}_{e^-}\mathcal{D}_{e^+} + A_e(\mathcal{D}_{e^+} - \mathcal{D}_{e^-})\} + \frac{\Delta k}{2}\{\mathcal{D}_{e^+} - \mathcal{D}_{e^-} + A_e(1 - \mathcal{D}_{e^-}\mathcal{D}_{e^+})\} \right) \\ &\quad \times (1 - 3\cos^2\theta)] \end{aligned} \quad (\text{C.9})$$

This form includes two common factors that are combinations of the polarisations and the electron asymmetry. Drawing out one of these factors simplifies the equation.

$$\begin{aligned}
& \frac{d\sigma_{\text{pol}}^f}{d\cos\theta}(\mathcal{D}_{e^-}, \mathcal{D}_{e^+}) \\
&= \frac{13}{48}\sigma_0^f(1 - \mathcal{D}_{e^-}\mathcal{D}_{e^+} + A_e(\mathcal{D}_{e^+} - \mathcal{D}_{e^-})) \\
&\quad \times \left[(1 + \cos^2\theta) + \left(\epsilon_f + 2A_f \frac{\mathcal{D}_{e^+} - \mathcal{D}_{e^-} + A_e(1 - \mathcal{D}_{e^-}\mathcal{D}_{e^+})}{1 - \mathcal{D}_{e^-}\mathcal{D}_{e^+} + A_e(\mathcal{D}_{e^+} - \mathcal{D}_{e^-})} \right) \cos\theta + \right. \\
&\quad \left. \left(\frac{k_0}{2} + \frac{\Delta k}{2} \frac{\mathcal{D}_{e^+} - \mathcal{D}_{e^-} + A_e(1 - \mathcal{D}_{e^-}\mathcal{D}_{e^+})}{1 - \mathcal{D}_{e^-}\mathcal{D}_{e^+} + A_e(\mathcal{D}_{e^+} - \mathcal{D}_{e^-})} \right) \times (1 - 3\cos^2\theta) \right] \\
&= \frac{13}{48}\sigma_0^f(1 - \mathcal{D}_{e^-}\mathcal{D}_{e^+} + A_e(\mathcal{D}_{e^+} - \mathcal{D}_{e^-})) \\
&\quad \times \left[(1 + \cos^2\theta) + \left(\epsilon_f + 2A_f \frac{\frac{\mathcal{D}_{e^+} - \mathcal{D}_{e^-}}{1 + \mathcal{D}_{e^+}\mathcal{D}_{e^-}} + A_e}{1 + \frac{\mathcal{D}_{e^+} - \mathcal{D}_{e^-}}{1 + \mathcal{D}_{e^+}\mathcal{D}_{e^-}} A_e} \right) \cos\theta + \right. \\
&\quad \left. \left(\frac{k_0}{2} + \frac{\Delta k}{2} \frac{\frac{\mathcal{D}_{e^+} - \mathcal{D}_{e^-}}{1 + \mathcal{D}_{e^+}\mathcal{D}_{e^-}} + A_e}{1 + \frac{\mathcal{D}_{e^+} - \mathcal{D}_{e^-}}{1 + \mathcal{D}_{e^+}\mathcal{D}_{e^-}} A_e} \right) \times (1 - 3\cos^2\theta) \right]
\end{aligned} \tag{C.10}$$

The last step contains the effective polarisation \mathcal{D}_{eff} .

$$\mathcal{D}_{\text{eff}} = \frac{\mathcal{D}_{e^+} - \mathcal{D}_{e^-}}{1 + \mathcal{D}_{e^+}\mathcal{D}_{e^-}} \tag{C.11}$$

A single dataset can therefore measure only a single second order polynomial with coefficients that are a combination of the fermion pair production parameters and the polarisations.

$$\begin{aligned}
& \frac{d\sigma_{\text{pol}}^f}{d\cos\theta}(\mathcal{D}_{e^-}, \mathcal{D}_{e^+}) \\
&= \frac{13}{48}\sigma_0^f(1 - \mathcal{D}_{e^-}\mathcal{D}_{e^+} + A_e(\mathcal{D}_{e^+} - \mathcal{D}_{e^-})) \\
&\quad \times \left[(1 + \cos^2\theta) + \left(\epsilon_f + 2A_f \frac{\mathcal{D}_{\text{eff}} + A_e}{1 + \mathcal{D}_{\text{eff}}A_e} \right) \cos\theta + \left(\frac{k_0}{2} + \frac{\Delta k}{2} \frac{\mathcal{D}_{\text{eff}} + A_e}{1 + \mathcal{D}_{\text{eff}}A_e} \right) \times (1 - 3\cos^2\theta) \right]
\end{aligned} \tag{C.12}$$

The unpolarised parametrisation

An unpolarised collider measures only a single dataset with $\mathcal{D}_{e^\pm} \approx 0$ and correspondingly $\mathcal{D}_{\text{eff}} \approx 0$. It only measures a single second order polynomial (eq. (C.12)) and it cannot distinguish all eight parameters that appear in that polynomial. To still allow a

measurement, the unpolarised scenario requires the definition of a set of three unpolarised parameters $\{\tilde{\sigma}_0^f, \tilde{k}_0, A_{FB}^f\}$, including the forward-backward asymmetry A_{FB}^f .

$$\frac{d\sigma_{\text{unpol}}^f}{d\cos\theta} = \frac{1}{4} \frac{3}{8} \tilde{\sigma}_0^f \left[(1 + \cos^2\theta) + \frac{8}{3} A_{FB}^f \cos\theta + \frac{\tilde{k}_0}{2} (1 - 3\cos^2\theta) \right] \quad (\text{C.13})$$

A comparison with the full formula for a single dataset yields the composition of these unpolarised parameters.

$$\begin{aligned} \tilde{\sigma}_0^f &= \sigma_0^f (1 - \mathcal{P}_{e^-} \mathcal{P}_{e^+} + A_e (\mathcal{P}_{e^+} - \mathcal{P}_{e^-})) \\ \tilde{k}_0 &= k_0 + \Delta k \frac{\mathcal{P}_{\text{eff}} + A_e}{1 + \mathcal{P}_{\text{eff}} A_e} \\ A_{FB}^f &= \frac{3}{8} \left(\epsilon_f + 2A_f \frac{\mathcal{P}_{\text{eff}} + A_e}{1 + \mathcal{P}_{\text{eff}} A_e} \right) \end{aligned} \quad (\text{C.14})$$

The small value of the polarisation allows some approximations that ignore non-linear polarisation terms.

$$\begin{aligned} (1 - \mathcal{P}_{e^-} \mathcal{P}_{e^+} + A_e (\mathcal{P}_{e^+} - \mathcal{P}_{e^-})) &\approx (1 - A_e (\mathcal{P}_{e^+} - \mathcal{P}_{e^-})) \\ \frac{\mathcal{P}_{\text{eff}} + A_e}{1 + \mathcal{P}_{\text{eff}} A_e} &\approx \mathcal{P}_{\text{eff}} (1 - A_e^2) + A_e \end{aligned} \quad (\text{C.15})$$

In addition, A_e is of order 10^{-1} (table 7.4). This allows an additional approximation that ignores any terms quadratic in A_e or mixed in the polarisation and A_e .

$$\begin{aligned} (1 - \mathcal{P}_{e^-} \mathcal{P}_{e^+} + A_e (\mathcal{P}_{e^+} - \mathcal{P}_{e^-})) &\approx 1 \\ \frac{\mathcal{P}_{\text{eff}} + A_e}{1 + \mathcal{P}_{\text{eff}} A_e} &\approx \mathcal{P}_{\text{eff}} + A_e \end{aligned} \quad (\text{C.16})$$

This is a rather crude approximation. In practice, the actual value of A_e will mainly be important in the suppression of the polarisation uncertainties in the mixed term. Only the terms linear in the polarisation (and not suppressed by A_e) and the terms linear in A_e will present a significant uncertainty. At the same time, known non-zero polarisations value do not pose a problem due to the straightforward linear correction.

Another approximation is possible because of the negligible value of Δk (table 7.4). This parameter only appears in mixed terms with A_e and the polarisations, which are correspondingly negligible as well.

Assuming these approximations (eq. (C.16)) as valid, the unpolarised parameters $\tilde{\sigma}_0^f$ and \tilde{k}_0 identify with the parameters σ_0^f and k_0 of the chiral parametrisation, and the forward-backward asymmetry takes a simple form.

$$\begin{aligned}
 \tilde{\sigma}_0^f &\approx \sigma_0^f \\
 \tilde{k}_0 &\approx k_0 \\
 A_{FB}^f &\approx \frac{3}{8} (\epsilon_f + 2 (\mathcal{D}_{\text{eff}} + A_e) A_f)
 \end{aligned}
 \tag{C.17}$$

This study therefore uses the same parameters σ_0^f and k_0 for polarised and unpolarised cases, leading to the unpolarised parametrisation that the fit uses.

$$\frac{d\sigma_{\text{unpol}}^f}{d\cos\theta} = \frac{1}{4} \frac{3}{8} \sigma_0^f \left[(1 + \cos^2\theta) + \frac{8}{3} A_{FB}^f \cos\theta + \frac{k_0}{2} (1 - 3\cos^2\theta) \right]
 \tag{C.18}$$

The forward backward asymmetry

The unpolarised parametrisation contains the forward-backward asymmetry. In its general form

$$A_{FB}^f = \frac{3}{8} \left(\epsilon_f + 2A_f \frac{\mathcal{D}_{\text{eff}} + A_e}{1 + \mathcal{D}_{\text{eff}}A_e} \right)
 \tag{C.19}$$

this parameter describes asymmetry of forward- and backward parts of a single distribution with polarisations \mathcal{D}_{e^\pm} (hence the name).

$$A_{FB}^f (\mathcal{D}_{e^-}, \mathcal{D}_{e^+}) = \frac{\int_0^1 \frac{d\sigma_{\text{pol}}^f}{d\cos\theta} d\cos\theta - \int_{-1}^0 \frac{d\sigma_{\text{pol}}^f}{d\cos\theta} d\cos\theta}{\int_0^1 \frac{d\sigma_{\text{pol}}^f}{d\cos\theta} d\cos\theta + \int_{-1}^0 \frac{d\sigma_{\text{pol}}^f}{d\cos\theta} d\cos\theta}
 \tag{C.20}$$

For an unpolarised scenario with polarisations of exactly zero, this parameter restores the forward-backward asymmetry parameter of the LEP and SLD experiments [2].

$$A_{FB}^f (0, 0) = \frac{3}{8} \epsilon_f + \frac{3}{4} A_e A_f
 \tag{C.21}$$

The ϵ_f parameter is a small correction on the Z-pole and does not explicitly appear in the LEP and SLD formulas of the asymmetry.

C.2. Implementation of the WW chiral cross-section parameters

A technical implementation of the σ_0 and A_{LR} parameters in the fit requires a parametrisation of the changes in these parameters in terms of changes in σ_{LR} and σ_{RL} . A simple common scaling α_0 of both chiral cross-section changes σ_0 without changing A_{LR} . For

independent parameters, an asymmetry deviation ΔA_{LR} also cannot change σ_0 .

$$\begin{aligned}\sigma_0(A_{LR} + \Delta A_{LR}) &= \sigma_0(A_{LR}) \\ A'_{LR}(\Delta A_{LR}) &= A_{LR} + \Delta A_{LR} = \frac{\sigma'_{LR} - \sigma'_{RL}}{\sigma_0}\end{aligned}\tag{C.22}$$

This condition leads to the changed values of chiral cross-sections.

$$\begin{aligned}\sigma'_{LR}(\alpha_0, \Delta A_{LR}) &= \alpha_0 \sigma_{LR} \left(1 + \frac{\sigma_0}{\sigma_{LR}} \Delta A_{LR} \right) \\ \sigma'_{RL}(\alpha_0, \Delta A_{LR}) &= \alpha_0 \sigma_{RL} \left(1 - \frac{\sigma_0}{\sigma_{RL}} \Delta A_{LR} \right)\end{aligned}\tag{C.23}$$

The fits use those two parameters $\alpha_0 = \sigma_0/\sigma_0^{\text{SM}}$ and ΔA_{LR} . While the total cross-section scaling is by default free parameter, the asymmetry is by default fixed and assumed as well known.

C.3. Details on TGC rescanning with WHIZARD

Rescanned TGCs points

The rescanning of the W pair production events uses 18 TGC deviation points, all with the common scale $\delta = 5 \cdot 10^{-4}$ (table C.1).

Example SINDARIN rescan script

The following is an example of a SINDARIN script that WHIZARD uses to rescan one LCIO file that contains $e^-_L e^+_R \rightarrow \mu\nu q\bar{q}$ events from the 250 GeV ILD production.

```
! =====
! This script/template is largely adapted from Mikael's scripts for the ILC-250
! production.
! =====
! ----- Sample production setup -----
sqrt_s = 250 GeV
beams = e1, E1 => circe2 => isr, isr
$circe2_file="/nfs/dust/ilc/user/berggren/whizard_2.8-prod/whizard-2.8.5-plain/energy_spread/250_SetA_eeo24.circe"
! This defines the initial chirality: -,+ -> e-L e+R
beams_pol_density = @(-1.0),@(1.0)
?isr_handler = true
?epa_handler = false
```

Table C.1.: Rescanned TGC points, given in units of $\delta = 5 \cdot 10^{-4}$.

Point	1	2	3	4	5	6	7	8	9	10	11	12	13	14	15	16	17	18
Δg_1^Z	1.0	0.0	0.0	-1.0	0.0	0.0	1.0	0.0	1.0	-1.0	0.0	-1.0	-1.0	0.0	-1.0	1.0	0.0	1.0
$\Delta \kappa_\gamma$	0.0	1.0	0.0	0.0	-1.0	0.0	1.0	1.0	0.0	-1.0	-1.0	0.0	1.0	-1.0	0.0	-1.0	1.0	0.0
$\Delta \lambda_\gamma$	0.0	0.0	1.0	0.0	0.0	-1.0	0.0	1.0	1.0	0.0	-1.0	-1.0	0.0	1.0	1.0	0.0	-1.0	-1.0

Appendix

```
! ILD production script used SM_CKM model
! => Here use SM_ac_CKM, which includes the TGC anomalous couplings
model = SM_ac_CKM

?resonance_history = true
resonance_on_shell_limit = 16
resonance_on_shell_turnoff = 2

! -----
! Aliases
! -----
alias electrons = e1:E1
alias mus = e2:E2
alias taus = e3:E3
alias quark = u:d:s:c:b:U:D:S:C:B
alias up_type_q = u:c:U:C
alias down_type_q = d:s:b:D:S:B
alias lepton = e1:e2:e3:E1:E2:E3
alias not_electron = e2:e3:E2:E3
alias neutrino = n1:n2:n3:N1:N2:N3

! -----
! Cuts
! -----
real default_M_cut = 4 GeV
! (the following is for DBD comparison
! (m_mu was 0 for non-ee processes, hence a 4 GeV cut))
real mumu_M_cut = 0 GeV
alias all_massless_but_electron=quark:not_electron
real default_jet_cut = 10 GeV
real default_E_cut = 10 GeV
real default_Q_cut = 4 GeV
!
alias masslessquark=quark
!
cuts =
let subevt @non_bmrem_electron = [ select if Index > 1 [e1] ]
in
let subevt @non_bmrem_positron = [ select if Index > 1 [E1] ]
in
let subevt @non_bmrem_both = [ select if Index > 2 [e1:E1] ]
in
let subevt @non_isr_photon = [ select if Index > 2 [A] ]
in
all M > mumu_M_cut [e2,E2]
and
all M > default_jet_cut [masslessquark,masslessquark]
and
all E > default_E_cut [@non_isr_photon]
and
all M < - default_Q_cut [incoming e1, [ @non_isr_photon]]
and
all M < - default_Q_cut [incoming E1, [ @non_isr_photon]]
and
all M < - default_Q_cut [incoming e1, e1]
and
all M < - default_Q_cut [incoming E1, E1]
and
all M > default_M_cut [e1,E1]
and
all M < - default_Q_cut [incoming photon , e1:E1 ]
and
all M < - default_Q_cut [incoming photon , all_massless_but_electron ]
and
all M < - default_Q_cut [incoming photon , @non_isr_photon ]

! -----
! Process input
! -----
polarized e1,e2,e3,u,d,c,s,t,n1,n2,n3,E1,E2,E3,U,D,C,S,T,N1,N2,N3,"W+" ,"W-" ,Z,A

! -----
! Parameter input
! -----
! masses not set here are at their PDG values, including e and mu
! All quark masses are zero, or are set to zero here, to
! allow for flavour sums
ms = 0
mc = 0
mb = 0
```

C. Impact of beam polarisation on electroweak fits

```

! No higgs in the general SM samples, to avoid double
! counting with the dedicated higgs samples:
$restrictions = "IH"

! no gluons in Whizard, to avoid double-counting with Pythia-PS :
alphas = 1.e-6

! -----
! Simulation input
! -----
?keep_remnants = true
?keep_beams = true
?hadronization_active = true
!
$extension_stdhep_ev4 = "stdhep"

! OPAL tune:
! (Some linebreaks are inserted for readability, remove them if necessary)
$ps_PYTHIA_PYGIVE = "MSTJ(28)=0;PMAS(25,1)=125.;PMAS(25,2)=0.3605E-02;
#####PMAS(116,1)=0.493677;MSTJ(41)=2;MSTU(22)=2000;
#####PARJ(21)=0.40000;PARJ(41)=0.11000;PARJ(42)=0.52000;
#####PARJ(81)=0.25000;PARJ(82)=1.90000;MSTJ(11)=3;
#####PARJ(54)=-0.03100;PARJ(55)=-0.00200;PARJ(1)=0.08500;
#####PARJ(3)=0.45000;PARJ(4)=0.02500;PARJ(2)=0.31000;
#####PARJ(11)=0.60000;PARJ(12)=0.40000;PARJ(13)=0.72000;
#####PARJ(14)=0.43000;PARJ(15)=0.08000;PARJ(16)=0.08000;
#####PARJ(17)=0.17000;MSTP(125)=2;MSTP(3)=1;MSTP(71)=1"
?ps_fsr_active = true
$shower_method = "PYTHIA6"
?ps_taudec_active = true
! 0=all, 1=e, 2=mu, 3=pi, 4=rho, 5=a_1, ...
ps_tauola_dec_mode1 = 0
ps_tauola_dec_mode2 = 0

! -----
! Beam settings
! -----
?isr_recoil = false
$isr_handler_mode = "recoil"
isr_alpha = 0.0072993
isr_mass = 0.000511
epa_alpha = 0.0072993
epa_mass = 0.000511
epa_q_max = 4.
epa_q_min = 0.1
epa_x_min = 0.00001
?epa_recoil=false
$epa_handler_mode = "recoil"

! (beam-spectrum part)
$circe2_design="ILC"
! NB: this is a bit confusing: It *should* be false, even if beams are
! polarised. It is a place-holder for a future development when polarisation
! is taken into account by GuineaPig
?circe2_polarized = false

beams_pol_fraction = 1.0,1.0

! -----
! Processes
! -----
int nf = 4
int ng = 0

!! # ----- Semi-leptonic
!! # WW : qq l nu
process ww_sl = e1,E1 => (up_type_q,down_type_q,taus,neutrino) + (up_type_q,down_type_q,mus,neutrino) {
    $omega_flags = "-model:constant_width"
    process_num_id = 500082 }

! -----

compile

! ----- Rescanning test -----

?resonance_history = false

! Enable updating of matrix element and weight for event (exactly wanted)

```

Appendix

```
?update_sqme = true
?update_weight = false

! Perform the rescan
rescan "/pnfs/desy.de/ilc/prod/ilc/mc-2020/generated/250-SetA/4f/E250-SetA.P4f_ww_sl.Gwhizard-2_8_5.eL.pR.1500082.o" (ww_sl){
$rescan_input_format = "lcio"
$sample = "cTGC_rescan"
sample_format = weight_stream
?recover_beams = false ! Avoid error from trying to recover the beam
?write_raw = false

! Description of the alternative setups to rescan
! Note that the last two lines in each setup enforce the gauge conditions
alt_setup = {
  g1z = 1.0005
  ka = 1.0
  la = 0.0
  kz = 1.0 - (ka - 1.0) * sw**2/cw**2 + (g1z - 1.0)
  lz = la
},
! ... (many other points)
{
  g1z = 1.0005
  ka = 1.0
  la = -0.0005
  kz = 1.0 - (ka - 1.0) * sw**2/cw**2 + (g1z - 1.0)
  lz = la
}
}
```

C.4. TGC impact on differential distributions

This section presents the checks of how the TGCs change the one-dimensional projections of the differential distribution of semileptonic W pair production (figs. C.1 and C.2). Only the check of the $\cos \theta_{W^-}$ observable of the $e_L^- e_R^+$ initial state appears in the main text (fig. 7.7), since that is the most sensitive shape information (section 7.3.4).

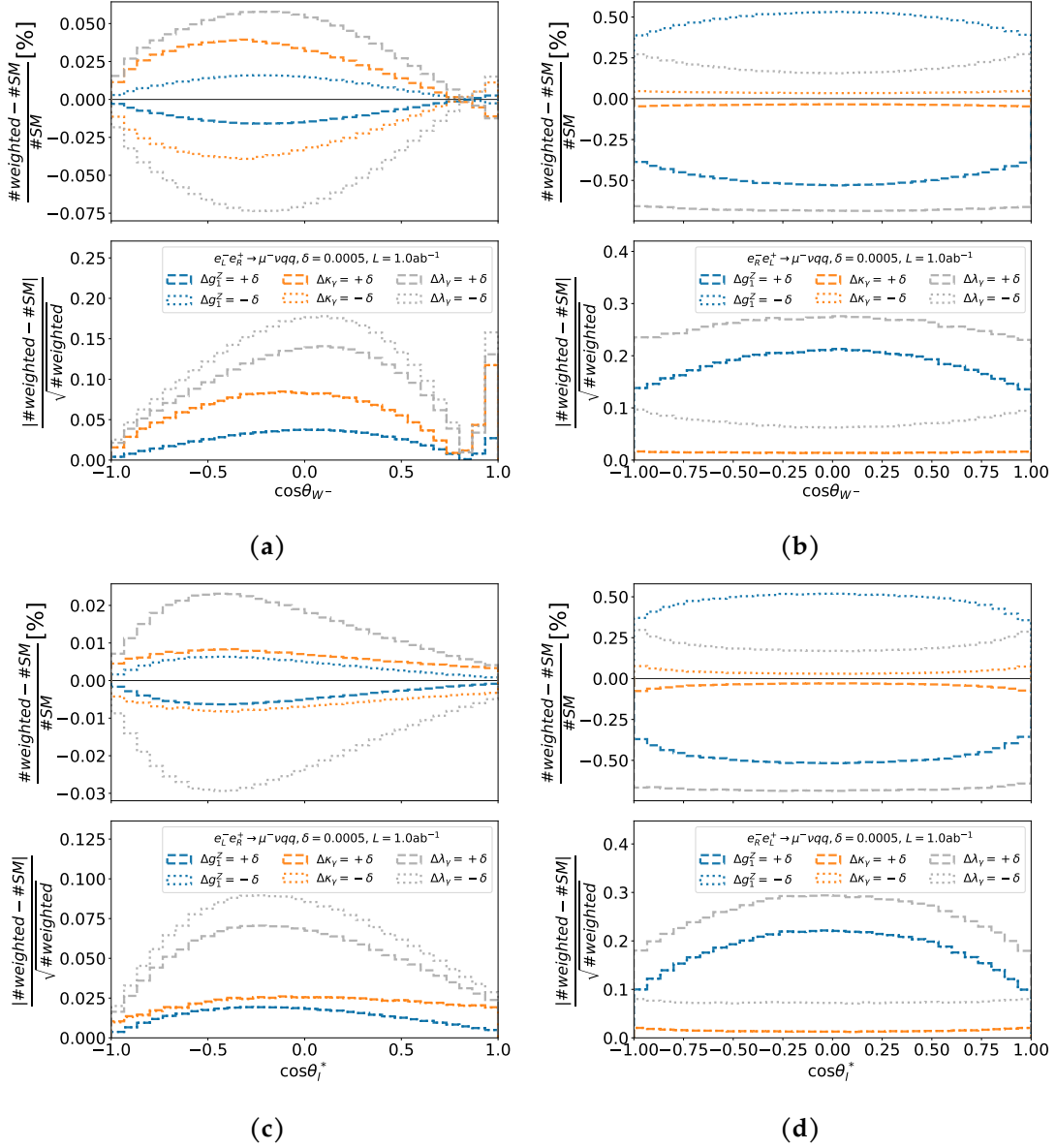


Figure C.1.: $\cos \theta_{W^-}$ (top) and $\cos \theta_l^*$ (bottom) distributions of $\mu^- \nu qq$ final state for $e_L^- e_R^+$ (left) and $e_R^- e_L^+$ (right) initial states. The ones for μ^+ are identical.

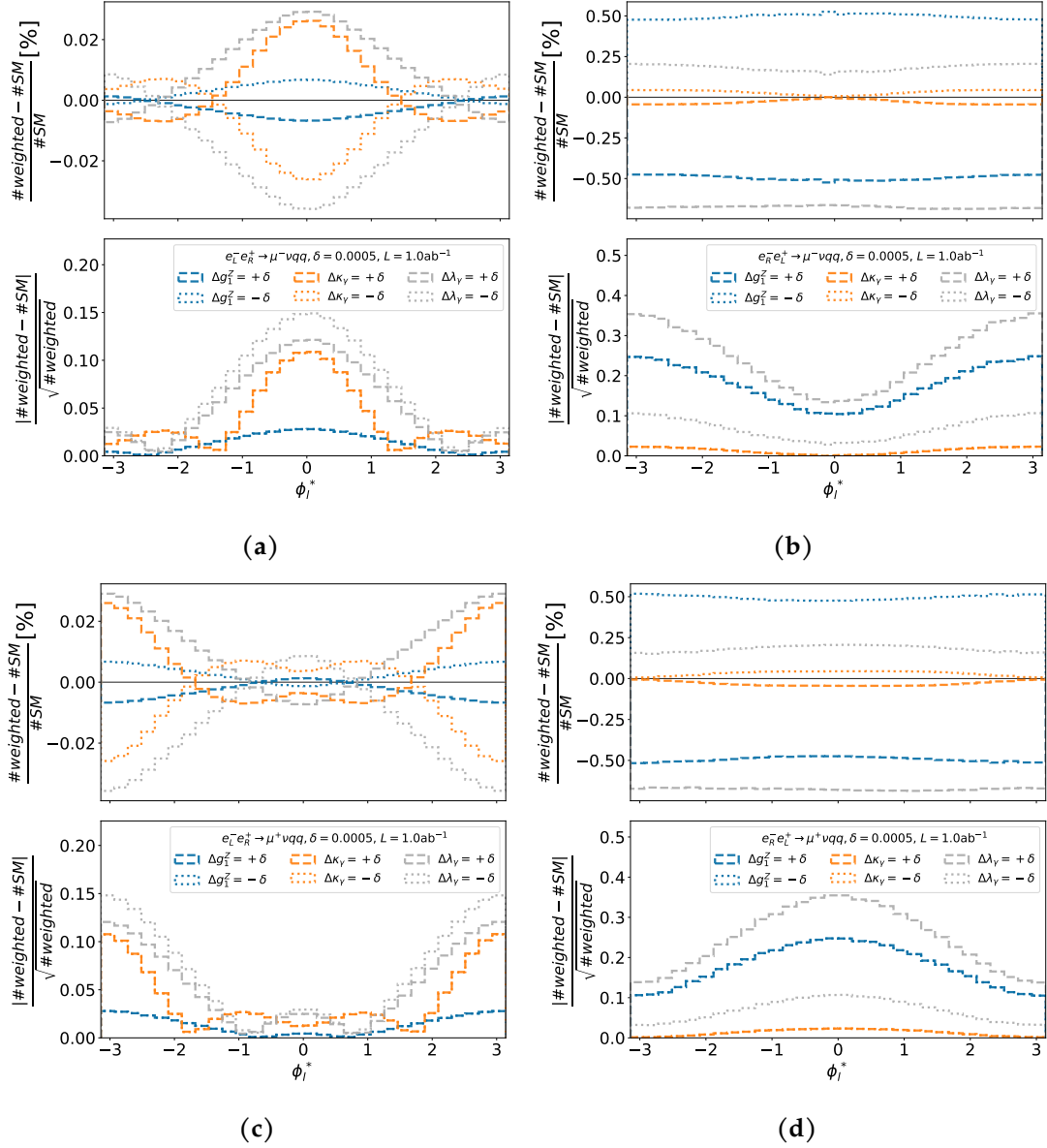


Figure C.2.: ϕ_i^* distributions of $\mu^- \nu q q$ (top) and $\mu^+ \nu q q$ (bottom) final states for $e_L^- e_R^+$ (left) and $e_R^- e_L^+$ (right) initial states.

C.5. Muon acceptance cut impact

This section presents the full set of plots that show the impact of the 7° μ -acceptance cut (see section 7.4.2) on the differential distributions of μ pair production (figs. C.3 and C.4) and semileptonic W pair production (fig. C.5).

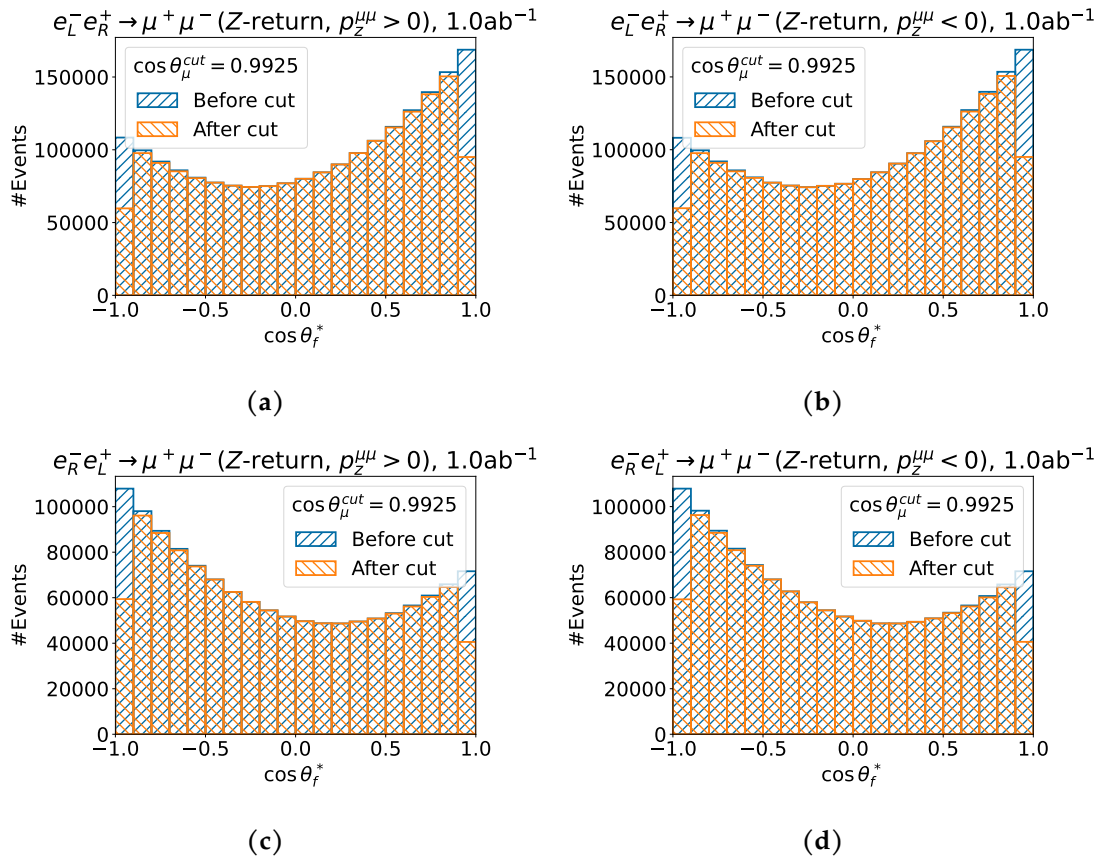


Figure C.3.: Impact of a 7° muon acceptance cut on the return-to-Z event distributions of μ pair production.

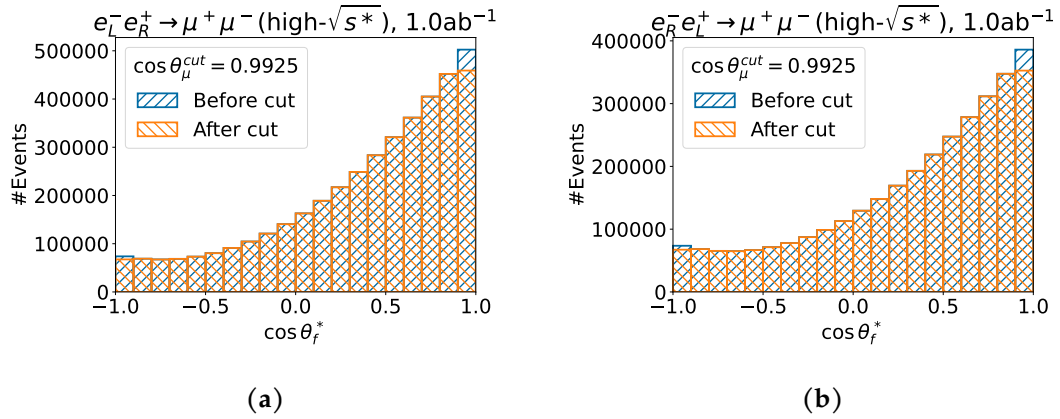


Figure C.4.: Impact of a 7° muon acceptance cut on the high- $\sqrt{s^*}$ event distributions of μ pair production.

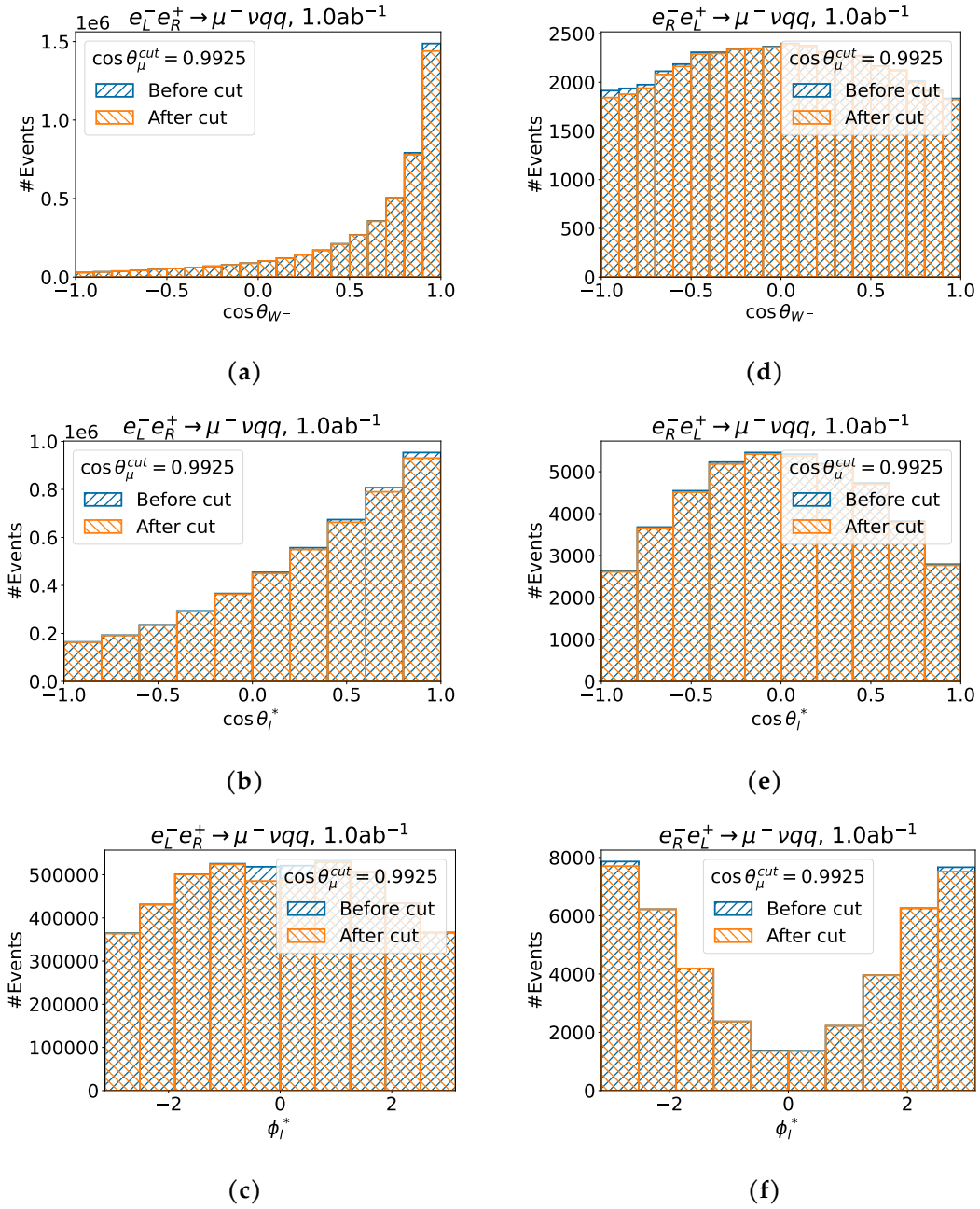


Figure C.5.: Impact of a 7° muon acceptance cut on the $e_L^- e_R^+ \rightarrow \mu^- \nu qq$ (left) and $e_R^- e_L^+ \rightarrow \mu^- \nu qq$ (right) distributions, shown as 1D projections. Distribution for the $\mu^+ \nu qq$ final state look identical except for a shift of π in ϕ_i^* , so that the peak and major cut influence shift to $\pm\pi$.

C.6. Additional muon acceptance validity check plots

This section presents the full sets of validity check plots for the parametrisation of the μ acceptance (see section 7.4.5), for all categories and initial state chiralities of μ pair production (figs. C.6 and C.7) and semileptonic W pair production (fig. C.8). Some validation points fall close to or even in the area of $\chi_{mismodel}^2 > \chi_{shift}^2$ (red area in the plot), in which the parametrisation is not strictly valid. A careful examination of those point shows that the impact of the mismodeling is still negligible compared to the impact on the other initial states or the other processes.

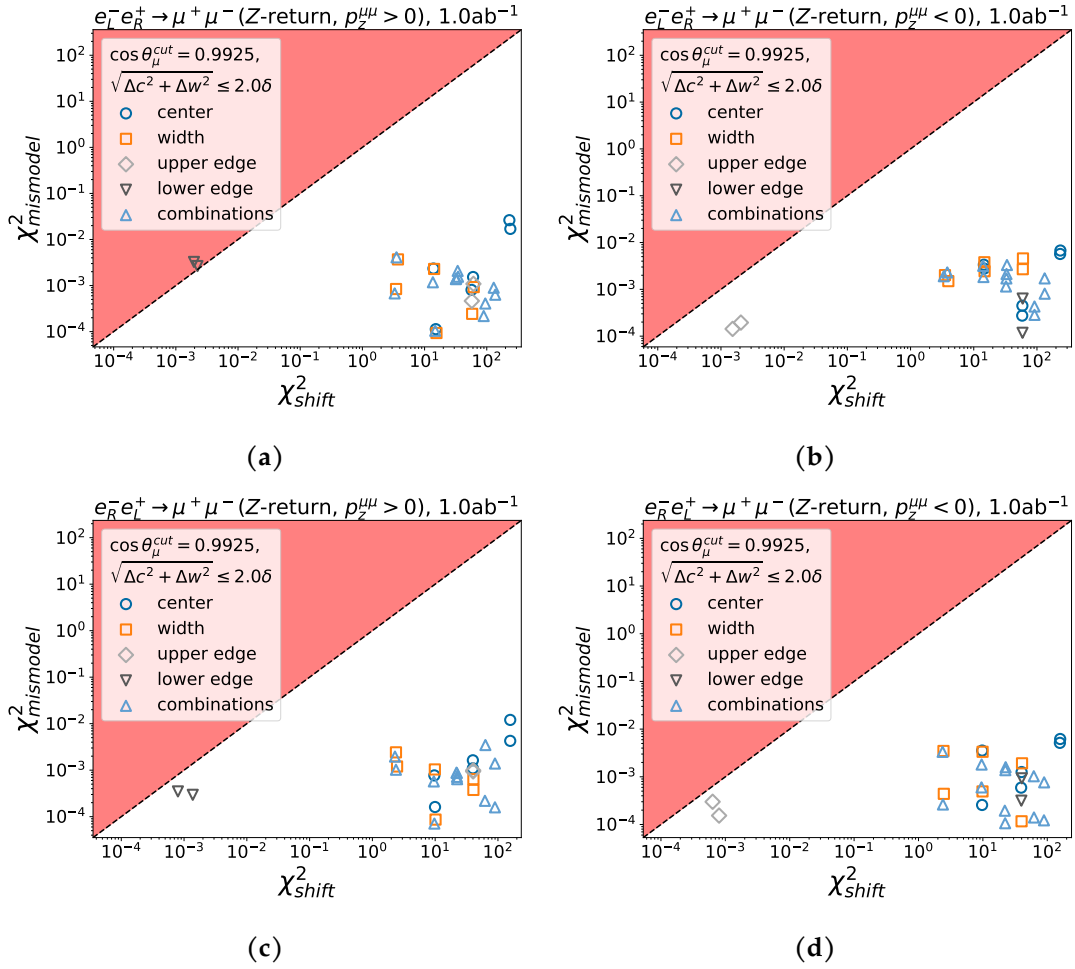


Figure C.6.: Comparison of χ^2 on $e^+e^- \rightarrow \mu^+\mu^-$ ($m_{\mu\mu} \approx m_Z$) shows that polynomial fit-parametrisation of μ acceptance causes negligible mistakes (χ^2_{par}) compared to the impact of parameter-shifts (χ^2_{shift}). (Complementing fig. 7.13 in section 7.4.5.)

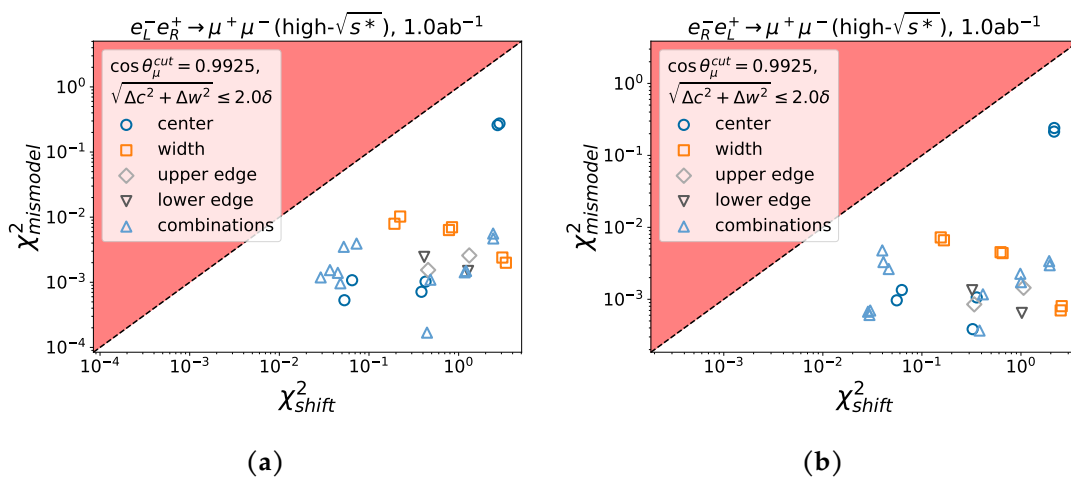


Figure C.7.: Comparison of χ^2 on $e^+e^- \rightarrow \mu^+\mu^-$ ($m_{\mu\mu} \approx 250$ GeV) shows that polynomial fit-parametrisation of μ acceptance causes negligible mistakes (χ_{par}^2) compared to the impact of parameter-shifts (χ_{shift}^2). (Complementing fig. 7.13 in section 7.4.5.)

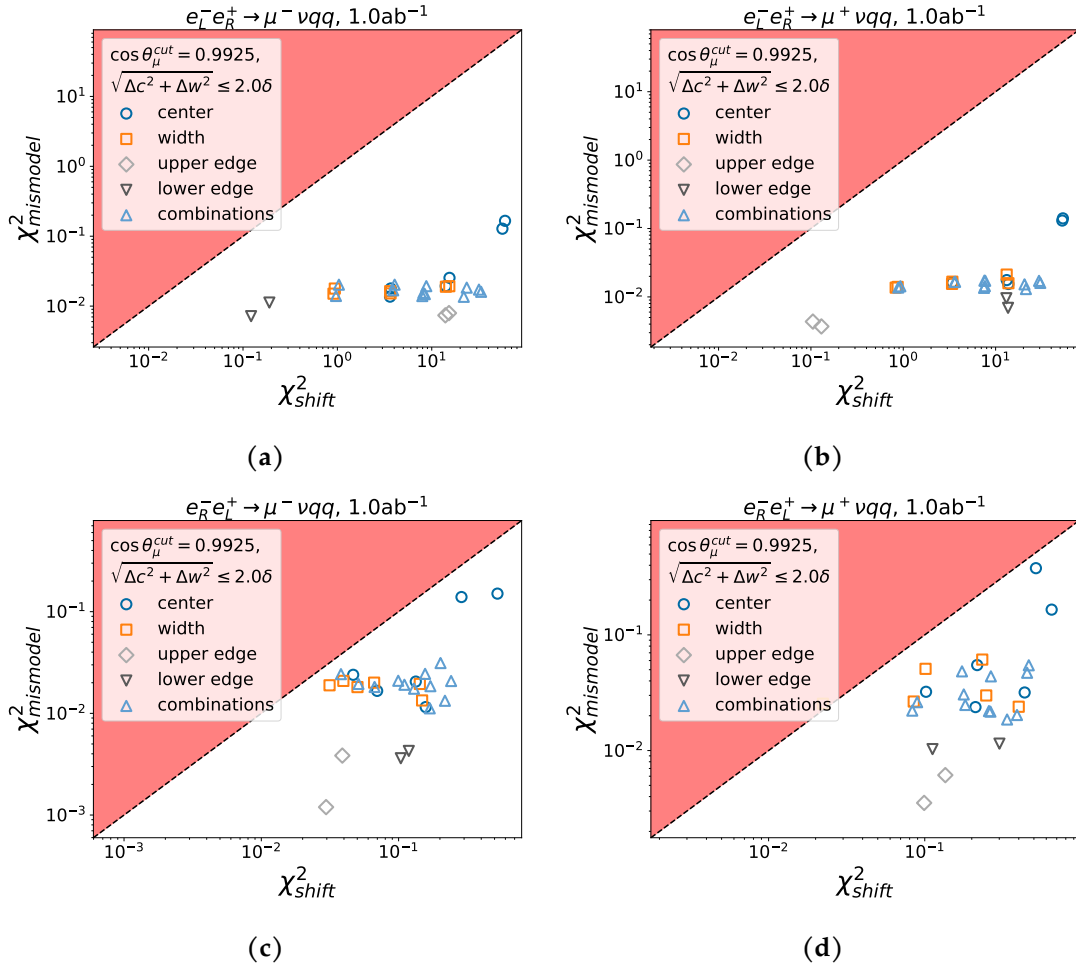


Figure C.8.: Comparison of χ^2 on $e^+e^- \rightarrow \mu\nu qq$ shows that polynomial fit-parametrisation of μ acceptance causes negligible mistakes (χ^2_{par}) compared to the impact of parameter-shifts (χ^2_{shift}). (Complementing fig. 7.13 in section 7.4.5.)

C.7. Fit results in numbers

This section presents the fit results the default fit setups from the electroweak fits (sections 7.6 to 7.8) in numbers. This includes the uncertainties for each polarised scenario for the individual fits:

- μ pair production:
 - With default parameters: table C.2
 - With fixed luminosity: table C.3
 - With fixed polarisation: table C.4
 - With fixed μ acceptance: table C.5
- Semileptonic W pair production:
 - With default parameters: table C.6
 - With fixed luminosity: table C.7
 - With fixed polarisation: table C.8
 - With fixed μ acceptance: table C.9
 - With fixed unpolarised cross-section: table C.10
 - With free left-right asymmetry: table C.11
- Combined:
 - With default parameters: table C.12
 - With fixed luminosity: table C.13
 - With fixed polarisation: table C.14
 - With fixed μ acceptance: table C.15

In addition, the section presents copies of the correlation plots of the fit scenarios with the default parameter sets that include the correlations as numbers (figs. C.9 to C.11).

μ pair production fits

Table C.2.: Absolute uncertainties of fits of the $\mu^+\mu^-$ final state with the default parameter set (table 7.6).

Parameter	True value	Abs. uncertainties [10^{-4}]				
		(80/0, 30/0) 2 ab^{-1}	(80, 30) 2 ab^{-1}	(80, 0) 2 ab^{-1}	(0, 0) 2 ab^{-1}	(0, 0) 10 ab^{-1}
$\sigma_0^f/\sigma_0^{f,SM} _{Z\text{-pole}}$	1	31	31	31	31	30
$A_e _{Z\text{-pole}}$	0.2136	8	8	25	—	—
$A_\mu _{Z\text{-pole}}$	0.2028	9	8	10	—	—
$\epsilon_\mu _{Z\text{-pole}}$	0.0158	14	14	16	—	—
$A_{FB}^\mu _{Z\text{-pole}}$	0.0384	—	—	—	5	2.4
$k_0 _{Z\text{-pole}}$	0.0747	20	20	22	21	9
$\Delta k _{Z\text{-pole}}$	0.0006	21	20	23	—	—
$\sigma_0^f/\sigma_0^{f,SM} _{250\text{GeV}}$	1	31	31	31	31	30
$A_e _{250\text{GeV}}$	0.1125	8	8	26	—	—
$A_\mu _{250\text{GeV}}$	0.0322	6	6	7	—	—
$\epsilon_\mu _{250\text{GeV}}$	1.4260	10	10	11	—	—
$A_{FB}^\mu _{250\text{GeV}}$	0.5375	—	—	—	4	1.8
$k_0 _{250\text{GeV}}$	0.0003	14	13	15	14	6
$\Delta k _{250\text{GeV}}$	0.0003	16	15	18	—	—
$L [\text{ab}^{-1}]$	2 10	60	60	60	60	300
$\mathcal{D}_{e^-}^-$	0.8	18	18	20	—	—
$\mathcal{D}_{e^-}^+$	0.8	17	16	20	—	—
$\mathcal{D}_{e^-}^0$	0.0	21	—	—	25	25
$\mathcal{D}_{e^+}^-$	0.3	7	7	—	—	—
$\mathcal{D}_{e^+}^+$	0.3	7	7	—	—	—
$\mathcal{D}_{e^+}^0$	0.0	15	—	25	25	25
Δc	0.0	0.19	0.18	0.20	0.20	0.09
Δw	0.0	0.4	0.4	0.5	0.5	0.22

Table C.3.: Absolute uncertainties of fits of the $\mu^+\mu^-$ final state with fixed luminosity and otherwise default parameters.

Parameter	True value	Abs. uncertainties [10^{-4}]				
		(80/0, 30/0) 2 ab^{-1}	(80, 30) 2 ab^{-1}	(80, 0) 2 ab^{-1}	(0, 0) 2 ab^{-1}	(0, 0) 10 ab^{-1}
$\sigma_0^f/\sigma_0^{f,SM} _{Z\text{-pole}}$	1	7	7	9	6	2.8
$A_e _{Z\text{-pole}}$	0.2136	8	8	25	—	—
$A_\mu _{Z\text{-pole}}$	0.2028	9	8	10	—	—
$\epsilon_\mu _{Z\text{-pole}}$	0.0158	14	14	16	—	—
$A_{FB}^\mu _{Z\text{-pole}}$	0.0384	—	—	—	5	2.4
$k_0 _{Z\text{-pole}}$	0.0747	20	20	22	21	9
$\Delta k _{Z\text{-pole}}$	0.0006	21	20	23	—	—
$\sigma_0^f/\sigma_0^{f,SM} _{250\text{GeV}}$	1	6	6	6	5	2.4
$A_e _{250\text{GeV}}$	0.1125	8	8	26	—	—
$A_\mu _{250\text{GeV}}$	0.0322	6	6	7	—	—
$\epsilon_\mu _{250\text{GeV}}$	1.4260	10	10	11	—	—
$A_{FB}^\mu _{250\text{GeV}}$	0.5375	—	—	—	4	1.8
$k_0 _{250\text{GeV}}$	0.0003	14	13	15	14	6
$\Delta k _{250\text{GeV}}$	0.0003	16	15	18	—	—
$L [\text{ab}^{-1}]$	2 10	0	0	0	0	0
$\mathcal{D}_{e^-}^-$	0.8	18	18	20	—	—
$\mathcal{D}_{e^-}^+$	0.8	17	16	20	—	—
$\mathcal{D}_{e^-}^0$	0.0	21	—	—	25	25
$\mathcal{D}_{e^+}^-$	0.3	7	7	—	—	—
$\mathcal{D}_{e^+}^+$	0.3	7	7	—	—	—
$\mathcal{D}_{e^+}^0$	0.0	15	—	25	25	25
Δc	0.0	0.19	0.18	0.20	0.20	0.09
Δw	0.0	0.4	0.4	0.5	0.5	0.22

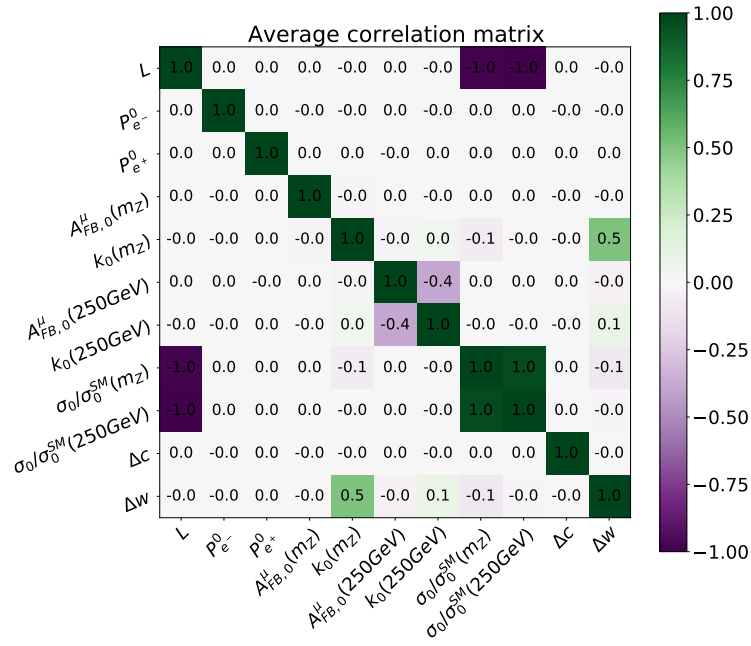
Table C.4.: Absolute uncertainties of fits of the $\mu^+\mu^-$ final state with fixed polarisations and otherwise default parameters.

Parameter	True value	Abs. uncertainties [10^{-4}]				
		(80/0, 30/0) 2 ab^{-1}	(80, 30) 2 ab^{-1}	(80, 0) 2 ab^{-1}	(0, 0) 2 ab^{-1}	(0, 0) 10 ab^{-1}
$\sigma_0^f/\sigma_0^{f,SM} _{Z\text{-pole}}$	1	31	31	31	31	30
$A_e _{Z\text{-pole}}$	0.2136	6	6	7	—	—
$A_\mu _{Z\text{-pole}}$	0.2028	8	8	9	—	—
$\epsilon_\mu _{Z\text{-pole}}$	0.0158	14	13	15	—	—
$A_{FB}^\mu _{Z\text{-pole}}$	0.0384	—	—	—	5	2.4
$k_0 _{Z\text{-pole}}$	0.0747	20	20	22	21	9
$\Delta k _{Z\text{-pole}}$	0.0006	21	20	23	—	—
$\sigma_0^f/\sigma_0^{f,SM} _{250\text{GeV}}$	1	31	30	31	31	30
$A_e _{250\text{GeV}}$	0.1125	6	6	7	—	—
$A_\mu _{250\text{GeV}}$	0.0322	6	6	7	—	—
$\epsilon_\mu _{250\text{GeV}}$	1.4260	10	10	11	—	—
$A_{FB}^\mu _{250\text{GeV}}$	0.5375	—	—	—	4	1.8
$k_0 _{250\text{GeV}}$	0.0003	14	13	15	14	6
$\Delta k _{250\text{GeV}}$	0.0003	16	15	18	—	—
$L [\text{ab}^{-1}]$	2 10	60	60	60	60	300
$\mathcal{P}_{e^-}^-$	0.8	0	0	0	—	—
$\mathcal{P}_{e^-}^+$	0.8	0	0	0	—	—
$\mathcal{P}_{e^-}^0$	0.0	0	—	—	0	0
$\mathcal{P}_{e^+}^-$	0.3	0	0	—	—	—
$\mathcal{P}_{e^+}^+$	0.3	0	0	—	—	—
$\mathcal{P}_{e^+}^0$	0.0	0	—	0	0	0
Δc	0.0	0.19	0.18	0.20	0.20	0.09
Δw	0.0	0.4	0.4	0.5	0.5	0.22

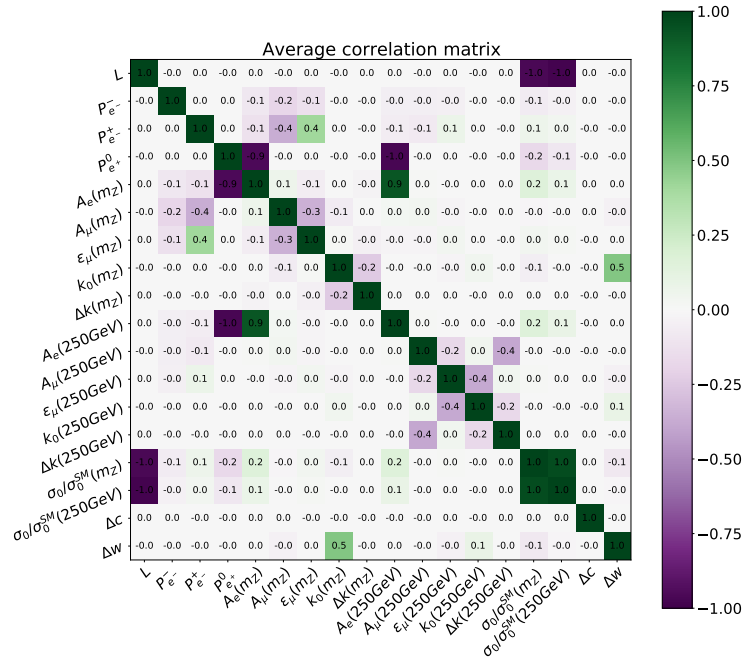
Table C.5.: Absolute uncertainties of fits of the $\mu^+\mu^-$ final state with fixed μ acceptance and otherwise default parameters.

Parameter	True value	Abs. uncertainties [10^{-4}]				
		(80/0, 30/0) 2 ab^{-1}	(80, 30) 2 ab^{-1}	(80, 0) 2 ab^{-1}	(0, 0) 2 ab^{-1}	(0, 0) 10 ab^{-1}
$\sigma_0^f/\sigma_0^{f,SM} _{Z\text{-pole}}$	1	31	31	31	31	30
$A_e _{Z\text{-pole}}$	0.2136	8	8	25	—	—
$A_\mu _{Z\text{-pole}}$	0.2028	9	8	10	—	—
$\epsilon_\mu _{Z\text{-pole}}$	0.0158	14	14	16	—	—
$A_{FB}^\mu _{Z\text{-pole}}$	0.0384	—	—	—	5	2.4
$k_0 _{Z\text{-pole}}$	0.0747	18	17	19	18	8
$\Delta k _{Z\text{-pole}}$	0.0006	21	20	23	—	—
$\sigma_0^f/\sigma_0^{f,SM} _{250\text{GeV}}$	1	31	31	31	31	30
$A_e _{250\text{GeV}}$	0.1125	8	8	26	—	—
$A_\mu _{250\text{GeV}}$	0.0322	6	6	7	—	—
$\epsilon_\mu _{250\text{GeV}}$	1.4260	10	10	11	—	—
$A_{FB}^\mu _{250\text{GeV}}$	0.5375	—	—	—	4	1.8
$k_0 _{250\text{GeV}}$	0.0003	14	13	15	14	6
$\Delta k _{250\text{GeV}}$	0.0003	16	15	18	—	—
$L [\text{ab}^{-1}]$	2 10	60	60	60	60	300
$\mathcal{D}_{e^-}^-$	0.8	18	18	20	—	—
$\mathcal{D}_{e^-}^+$	0.8	17	16	20	—	—
$\mathcal{D}_{e^-}^0$	0.0	21	—	—	25	25
$\mathcal{D}_{e^+}^-$	0.3	7	7	—	—	—
$\mathcal{D}_{e^+}^+$	0.3	7	7	—	—	—
$\mathcal{D}_{e^+}^0$	0.0	15	—	25	25	25
Δc	0.0	0	0	0	0	0
Δw	0.0	0	0	0	0	0

C. Impact of beam polarisation on electroweak fits



(a)



(b)

Figure C.9.: Same as fig. 7.17 (fit to μ pair production), with explicit numbers in each correlation field. (a) (0,0), (b) (80,0), (c) (80,30), and (d) (80/0,30/0).

Semileptonic W pair production fits

Table C.6.: Absolute uncertainties of fits of the $\mu\nu q\bar{q}$ final state with the default parameter set (table 7.6).

Parameter	True value	Abs. uncertainties [10^{-4}]				
		(80/0, 30/0) 2 ab $^{-1}$	(80, 30) 2 ab $^{-1}$	(80, 0) 2 ab $^{-1}$	(0, 0) 2 ab $^{-1}$	(0, 0) 10 ab $^{-1}$
Δg_1^Z	0	9	9	10	13	6
$\Delta\kappa_\gamma$	0	13	12	14	16	8
$\Delta\lambda_\gamma$	0	15	14	16	18	8
$\sigma_0/\sigma_0^{SM}(W^-)$	1	33	33	40	50	50
$\sigma_0/\sigma_0^{SM}(W^+)$	1	33	33	40	50	50
L [ab $^{-1}$]	2 10	60	60	60	60	300
$\mathcal{P}_{e^-}^-$	0.8	19	20	20	—	—
$\mathcal{P}_{e^-}^+$	0.8	5	5	4	—	—
$\mathcal{P}_{e^-}^0$	0.0	15	—	—	25	25
$\mathcal{P}_{e^+}^-$	0.3	6	6	—	—	—
$\mathcal{P}_{e^+}^+$	0.3	7	7	—	—	—
$\mathcal{P}_{e^+}^0$	0.0	13	—	25	25	25
Δc	0.0	0.5	0.5	0.6	0.6	0.25
Δw	0.0	1.0	1.0	1.1	1.1	0.5

Table C.7.: Absolute uncertainties of fits of the $\mu\nu q\bar{q}$ final state with fixed luminosity and otherwise default parameters.

Parameter	True value	Abs. uncertainties [10^{-4}]				
		(80/0, 30/0) 2 ab^{-1}	(80, 30) 2 ab^{-1}	(80, 0) 2 ab^{-1}	(0, 0) 2 ab^{-1}	(0, 0) 10 ab^{-1}
Δg_1^Z	0	9	9	10	13	6
$\Delta \kappa_\gamma$	0	13	12	14	16	8
$\Delta \lambda_\gamma$	0	15	14	16	18	8
$\sigma_0/\sigma_0^{SM}(W^-)$	1	13	14	28	40	35
$\sigma_0/\sigma_0^{SM}(W^+)$	1	13	14	28	40	35
$L [\text{ab}^{-1}]$	2 10	0	0	0	0	0
$\mathcal{P}_{e^-}^-$	0.8	19	20	20	–	–
$\mathcal{P}_{e^-}^+$	0.8	5	5	4	–	–
$\mathcal{P}_{e^-}^0$	0.0	15	–	–	25	25
$\mathcal{P}_{e^+}^-$	0.3	6	6	–	–	–
$\mathcal{P}_{e^+}^+$	0.3	7	7	–	–	–
$\mathcal{P}_{e^+}^0$	0.0	13	–	25	25	25
Δc	0.0	0.5	0.5	0.6	0.6	0.25
Δw	0.0	1.0	1.0	1.1	1.1	0.5

Table C.8.: Absolute uncertainties of fits of the $\mu\nu q\bar{q}$ final state with fixed polarisations and otherwise default parameters.

Parameter	True value	Abs. uncertainties [10^{-4}]				
		(80/0, 30/0) 2 ab ⁻¹	(80, 30) 2 ab ⁻¹	(80, 0) 2 ab ⁻¹	(0, 0) 2 ab ⁻¹	(0, 0) 10 ab ⁻¹
Δg_1^Z	0	9	9	10	13	6
$\Delta\kappa_\gamma$	0	12	12	14	15	7
$\Delta\lambda_\gamma$	0	15	14	16	18	8
$\sigma_0/\sigma_0^{SM}(W^-)$	1	31	31	31	31	30
$\sigma_0/\sigma_0^{SM}(W^+)$	1	31	31	31	31	30
L [ab ⁻¹]	2 10	60	60	60	60	300
$\mathcal{P}_{e^-}^-$	0.8	0	0	0	–	–
$\mathcal{P}_{e^-}^+$	0.8	0	0	0	–	–
$\mathcal{P}_{e^-}^0$	0.0	0	–	–	0	0
$\mathcal{P}_{e^+}^-$	0.3	0	0	–	–	–
$\mathcal{P}_{e^+}^+$	0.3	0	0	–	–	–
$\mathcal{P}_{e^+}^0$	0.0	0	–	0	0	0
Δc	0.0	0.5	0.5	0.6	0.6	0.25
Δw	0.0	1.0	1.0	1.1	1.1	0.5

Table C.9.: Absolute uncertainties of fits of the $\mu\nu q\bar{q}$ final state with fixed μ acceptance and otherwise default parameters.

Parameter	True value	Abs. uncertainties [10^{-4}]				
		(80/0, 30/0) 2 ab^{-1}	(80, 30) 2 ab^{-1}	(80, 0) 2 ab^{-1}	(0, 0) 2 ab^{-1}	(0, 0) 10 ab^{-1}
Δg_1^Z	0	9	9	10	13	6
$\Delta \kappa_\gamma$	0	12	12	14	16	8
$\Delta \lambda_\gamma$	0	15	14	16	18	8
$\sigma_0/\sigma_0^{SM}(W^-)$	1	33	33	40	50	50
$\sigma_0/\sigma_0^{SM}(W^+)$	1	33	33	40	50	50
$L [\text{ab}^{-1}]$	2 10	60	60	60	60	300
$\mathcal{P}_{e^-}^-$	0.8	19	20	20	–	–
$\mathcal{P}_{e^-}^+$	0.8	5	5	4	–	–
$\mathcal{P}_{e^-}^0$	0.0	15	–	–	25	25
$\mathcal{P}_{e^+}^-$	0.3	6	6	–	–	–
$\mathcal{P}_{e^+}^+$	0.3	7	7	–	–	–
$\mathcal{P}_{e^+}^0$	0.0	13	–	25	25	25
Δc	0.0	0	0	0	0	0
Δw	0.0	0	0	0	0	0

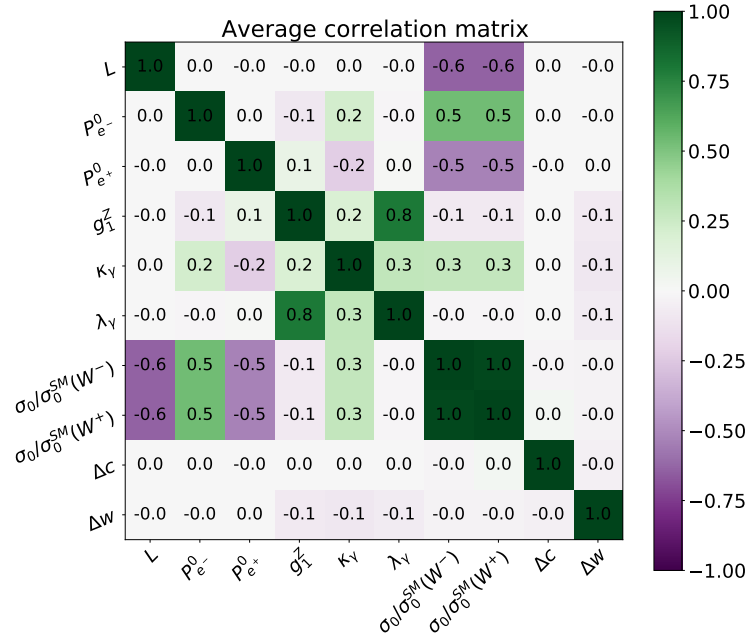
Table C.10.: Absolute uncertainties of fits of the $\mu\nu qq$ final state with fixed total cross sections and otherwise default parameters.

Parameter	True value	Abs. uncertainties [10^{-4}]				
		(80/0,30/0) 2 ab ⁻¹	(80,30) 2 ab ⁻¹	(80,0) 2 ab ⁻¹	(0,0) 2 ab ⁻¹	(0,0) 10 ab ⁻¹
Δg_1^Z	0	9	9	10	13	6
$\Delta\kappa_\gamma$	0	12	12	14	15	7
$\Delta\lambda_\gamma$	0	15	14	16	18	8
$L[\text{ab}^{-1}]$	2 10	23	24	40	50	230
$\mathcal{D}_{e^-}^-$	0.8	18	19	19	–	–
$\mathcal{D}_{e^-}^+$	0.8	4	4	4	–	–
$\mathcal{D}_{e^-}^0$	0.0	15	–	–	21	21
$\mathcal{D}_{e^+}^-$	0.3	6	6	–	–	–
$\mathcal{D}_{e^+}^+$	0.3	7	7	–	–	–
$\mathcal{D}_{e^+}^0$	0.0	13	–	20	21	21
Δc	0.0	0.5	0.5	0.5	0.5	0.24
Δw	0.0	1.0	1.0	1.1	1.1	0.5

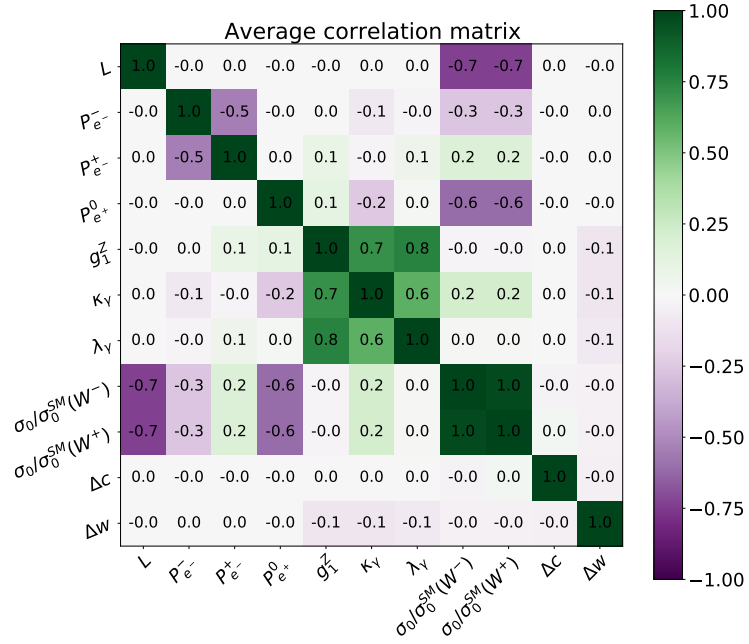
Table C.11.: Absolute uncertainties of fits of the $\mu\nu q\bar{q}$ final state with free left-right asymmetry and otherwise default parameters.

Parameter	True value	Abs. uncertainties [10^{-4}]				
		(80/0, 30/0) 2 ab $^{-1}$	(80, 30) 2 ab $^{-1}$	(80, 0) 2 ab $^{-1}$	(0, 0) 2 ab $^{-1}$	(0, 0) 10 ab $^{-1}$
Δg_1^Z	0	21	20	25	40	18
$\Delta\kappa_\gamma$	0	60	60	70	110	50
$\Delta\lambda_\gamma$	0	15	15	17	19	9
$A_{LR}(W^-)$	0.9816	15	15	18	30	14
$A_{LR}(W^+)$	0.9816	15	15	18	30	14
$\sigma_0/\sigma_0^{SM}(W^-)$	1	33	34	40	50	50
$\sigma_0/\sigma_0^{SM}(W^+)$	1	33	34	40	50	50
L [ab $^{-1}$]	2 10	60	60	60	60	300
$\mathcal{P}_{e^-}^-$	0.8	19	20	20	–	–
$\mathcal{P}_{e^-}^+$	0.8	5	5	4	–	–
$\mathcal{P}_{e^-}^0$	0.0	15	–	–	25	25
$\mathcal{P}_{e^+}^-$	0.3	6	6	–	–	–
$\mathcal{P}_{e^+}^+$	0.3	7	7	–	–	–
$\mathcal{P}_{e^+}^0$	0.0	13	–	25	25	25
Δc	0.0	0.5	0.5	0.6	0.6	0.25
Δw	0.0	1.0	1.0	1.1	1.1	0.5

C. Impact of beam polarisation on electroweak fits

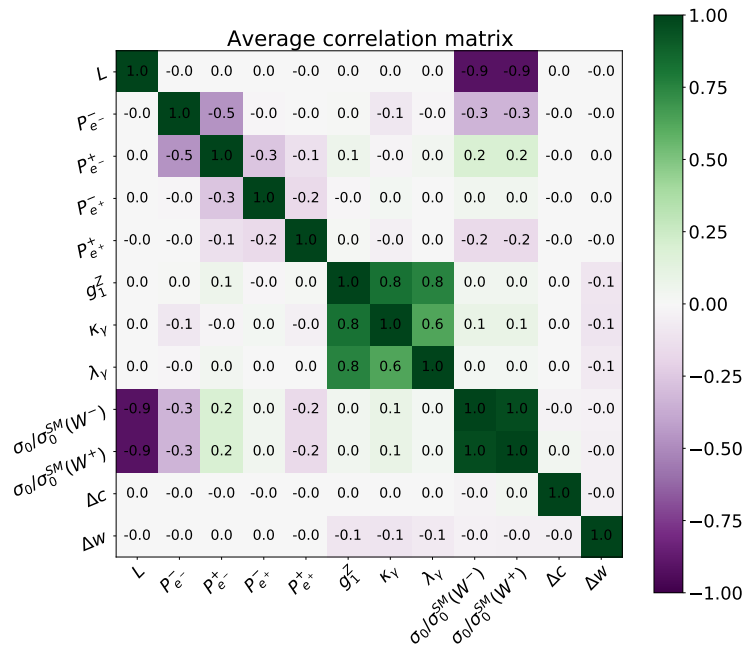


(a)

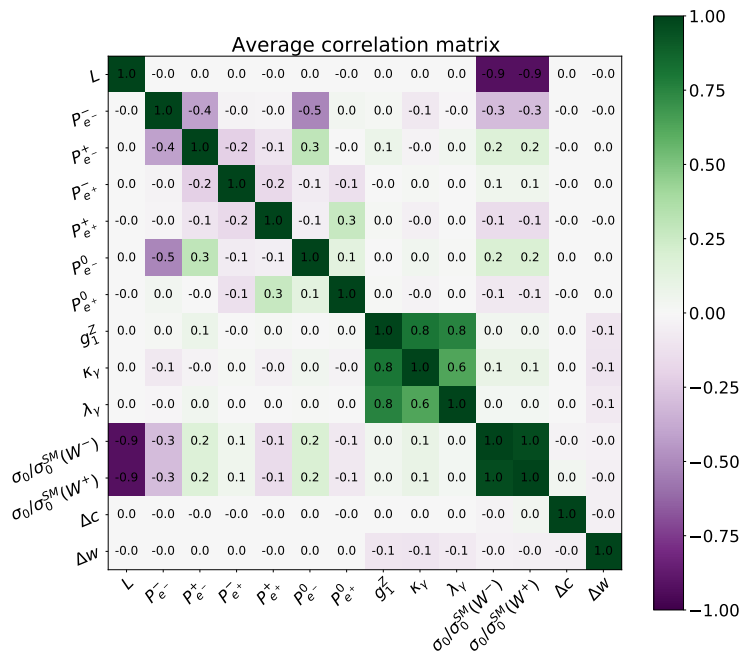


(b)

Figure C.10.: Same as fig. 7.22 (fit to semileptonic W pair production), with explicit numbers in each correlation field. (a) (0,0), (b) (80,0), (c) (80,30), and (d) (80/0,30/0).



(c)



(d)

Figure C.10.: (cont.)

Combined fits

0

Table C.12.: Absolute uncertainties of the combined fits with the default parameter set (table 7.6).

Parameter	True value	Abs. uncertainties [10^{-4}]				
		(80/0, 30/0) 2 ab ⁻¹	(80, 30) 2 ab ⁻¹	(80, 0) 2 ab ⁻¹	(0, 0) 2 ab ⁻¹	(0, 0) 10 ab ⁻¹
$\sigma_0^f/\sigma_0^{f,SM} _{Z\text{-pole}}$	1	31	31	31	31	30
$A_e _{Z\text{-pole}}$	0.2136	8	8	25	—	—
$A_\mu _{Z\text{-pole}}$	0.2028	8	8	9	—	—
$\epsilon_\mu _{Z\text{-pole}}$	0.0158	14	14	15	—	—
$A_{FB}^\mu _{Z\text{-pole}}$	0.0384	—	—	—	5	2.4
$k_0 _{Z\text{-pole}}$	0.0747	20	19	21	21	9
$\Delta k _{Z\text{-pole}}$	0.0006	21	20	23	—	—
$\sigma_0^f/\sigma_0^{f,SM} _{250\text{GeV}}$	1	30	30	31	30	30
$A_e _{250\text{GeV}}$	0.1125	8	7	26	—	—
$A_\mu _{250\text{GeV}}$	0.0322	6	6	7	—	—
$\epsilon_\mu _{250\text{GeV}}$	1.4260	10	10	11	—	—
$A_{FB}^\mu _{250\text{GeV}}$	0.5375	—	—	—	4	1.8
$k_0 _{250\text{GeV}}$	0.0003	14	13	15	14	6
$\Delta k _{250\text{GeV}}$	0.0003	16	15	18	—	—
Δg_1^Z	0	9	9	10	13	6
$\Delta\kappa_\gamma$	0	12	12	14	16	8
$\Delta\lambda_\gamma$	0	15	14	16	18	8
$\sigma_0/\sigma_0^{SM}(W^-)$	1	32	33	40	50	50
$\sigma_0/\sigma_0^{SM}(W^+)$	1	32	33	40	50	50
$L [\text{ab}^{-1}]$	2 10	60	60	60	60	300
$\mathcal{D}_{e^-}^-$	0.8	17	18	20	—	—
$\mathcal{D}_{e^-}^+$	0.8	4	4	4	—	—
$\mathcal{D}_{e^-}^0$	0.0	14	—	—	25	25
$\mathcal{D}_{e^+}^-$	0.3	6	6	—	—	—
$\mathcal{D}_{e^+}^+$	0.3	7	7	—	—	—
$\mathcal{D}_{e^+}^0$	0.0	11	—	25	25	25
Δc	0.0	0.18	0.17	0.19	0.19	0.08
Δw	0.0	0.4	0.4	0.4	0.4	0.20

Table C.13.: Absolute uncertainties of the combined fits with fixed luminosity and otherwise default parameters.

Parameter	True value	Abs. uncertainties [10^{-4}]				
		(80/0, 30/0) 2 ab^{-1}	(80, 30) 2 ab^{-1}	(80, 0) 2 ab^{-1}	(0, 0) 2 ab^{-1}	(0, 0) 10 ab^{-1}
$\sigma_0^f/\sigma_0^{f,SM} _{Z\text{-pole}}$	1	7	7	9	6	2.8
$A_e _{Z\text{-pole}}$	0.2136	8	8	25	—	—
$A_\mu _{Z\text{-pole}}$	0.2028	8	8	9	—	—
$\epsilon_\mu _{Z\text{-pole}}$	0.0158	14	14	15	—	—
$A_{FB}^\mu _{Z\text{-pole}}$	0.0384	—	—	—	5	2.4
$k_0 _{Z\text{-pole}}$	0.0747	20	19	21	21	9
$\Delta k _{Z\text{-pole}}$	0.0006	21	20	23	—	—
$\sigma_0^f/\sigma_0^{f,SM} _{250\text{GeV}}$	1	6	6	6	5	2.4
$A_e _{250\text{GeV}}$	0.1125	8	7	26	—	—
$A_\mu _{250\text{GeV}}$	0.0322	6	6	7	—	—
$\epsilon_\mu _{250\text{GeV}}$	1.4260	10	10	11	—	—
$A_{FB}^\mu _{250\text{GeV}}$	0.5375	—	—	—	4	1.8
$k_0 _{250\text{GeV}}$	0.0003	14	13	15	14	6
$\Delta k _{250\text{GeV}}$	0.0003	16	15	18	—	—
Δg_1^Z	0	9	9	10	13	6
$\Delta\kappa_\gamma$	0	12	12	14	16	8
$\Delta\lambda_\gamma$	0	15	14	16	18	8
$\sigma_0/\sigma_0^{SM}(W^-)$	1	12	13	28	40	35
$\sigma_0/\sigma_0^{SM}(W^+)$	1	12	13	28	40	35
$L [\text{ab}^{-1}]$	2 10	0	0	0	0	0
$\mathcal{D}_{e^-}^-$	0.8	17	18	20	—	—
$\mathcal{D}_{e^-}^+$	0.8	4	4	4	—	—
$\mathcal{D}_{e^-}^0$	0.0	14	—	—	25	25
$\mathcal{D}_{e^+}^-$	0.3	6	6	—	—	—
$\mathcal{D}_{e^+}^+$	0.3	7	7	—	—	—
$\mathcal{D}_{e^+}^0$	0.0	11	—	25	25	25
Δc	0.0	0.18	0.17	0.19	0.19	0.08
Δw	0.0	0.4	0.4	0.4	0.4	0.20

Table C.14.: Absolute uncertainties of the combined fits with fixed polarisations and otherwise default parameters.

Parameter	True value	Abs. uncertainties [10^{-4}]				
		(80/0, 30/0) 2 ab^{-1}	(80, 30) 2 ab^{-1}	(80, 0) 2 ab^{-1}	(0, 0) 2 ab^{-1}	(0, 0) 10 ab^{-1}
$\sigma_0^f/\sigma_0^{f,SM} _{Z\text{-pole}}$	1	30	30	31	31	30
$A_e _{Z\text{-pole}}$	0.2136	6	6	7	—	—
$A_\mu _{Z\text{-pole}}$	0.2028	8	8	9	—	—
$\epsilon_\mu _{Z\text{-pole}}$	0.0158	14	13	15	—	—
$A_{FB}^\mu _{Z\text{-pole}}$	0.0384	—	—	—	5	2.4
$k_0 _{Z\text{-pole}}$	0.0747	20	19	21	21	9
$\Delta k _{Z\text{-pole}}$	0.0006	21	20	23	—	—
$\sigma_0^f/\sigma_0^{f,SM} _{250\text{GeV}}$	1	30	30	30	30	30
$A_e _{250\text{GeV}}$	0.1125	6	6	7	—	—
$A_\mu _{250\text{GeV}}$	0.0322	6	6	7	—	—
$\epsilon_\mu _{250\text{GeV}}$	1.4260	10	10	11	—	—
$A_{FB}^\mu _{250\text{GeV}}$	0.5375	—	—	—	4	1.8
$k_0 _{250\text{GeV}}$	0.0003	14	13	15	14	6
$\Delta k _{250\text{GeV}}$	0.0003	16	15	18	—	—
Δg_1^Z	0	9	9	10	13	6
$\Delta\kappa_\gamma$	0	12	12	13	15	7
$\Delta\lambda_\gamma$	0	15	14	16	18	8
$\sigma_0/\sigma_0^{SM}(W^-)$	1	30	31	31	31	30
$\sigma_0/\sigma_0^{SM}(W^+)$	1	30	31	31	31	30
$L [\text{ab}^{-1}]$	$2 10$	60	60	60	60	300
$\mathcal{D}_{e^-}^-$	0.8	0	0	0	—	—
$\mathcal{D}_{e^-}^+$	0.8	0	0	0	—	—
$\mathcal{D}_{e^-}^0$	0.0	0	—	—	0	0
$\mathcal{D}_{e^+}^-$	0.3	0	0	—	—	—
$\mathcal{D}_{e^+}^+$	0.3	0	0	—	—	—
$\mathcal{D}_{e^+}^0$	0.0	0	—	0	0	0
Δc	0.0	0.18	0.17	0.19	0.19	0.08
Δw	0.0	0.4	0.4	0.4	0.4	0.20

Table C.15.: Absolute uncertainties of the combined fits with fixed μ acceptance and otherwise default parameters.

Parameter	True value	Abs. uncertainties [10^{-4}]				
		(80/0, 30/0) 2 ab^{-1}	(80, 30) 2 ab^{-1}	(80, 0) 2 ab^{-1}	(0, 0) 2 ab^{-1}	(0, 0) 10 ab^{-1}
$\sigma_0^f/\sigma_0^{f,SM} _{Z\text{-pole}}$	1	31	31	31	31	30
$A_e _{Z\text{-pole}}$	0.2136	8	8	25	—	—
$A_\mu _{Z\text{-pole}}$	0.2028	8	8	9	—	—
$\epsilon_\mu _{Z\text{-pole}}$	0.0158	14	14	15	—	—
$A_{FB}^\mu _{Z\text{-pole}}$	0.0384	—	—	—	5	2.4
$k_0 _{Z\text{-pole}}$	0.0747	18	17	19	18	8
$\Delta k _{Z\text{-pole}}$	0.0006	21	20	23	—	—
$\sigma_0^f/\sigma_0^{f,SM} _{250\text{GeV}}$	1	30	30	31	30	30
$A_e _{250\text{GeV}}$	0.1125	8	7	26	—	—
$A_\mu _{250\text{GeV}}$	0.0322	6	6	7	—	—
$\epsilon_\mu _{250\text{GeV}}$	1.4260	10	10	11	—	—
$A_{FB}^\mu _{250\text{GeV}}$	0.5375	—	—	—	4	1.8
$k_0 _{250\text{GeV}}$	0.0003	14	13	15	14	6
$\Delta k _{250\text{GeV}}$	0.0003	16	15	18	—	—
Δg_1^Z	0	9	9	10	13	6
$\Delta\kappa_\gamma$	0	12	12	14	16	8
$\Delta\lambda_\gamma$	0	15	14	16	18	8
$\sigma_0/\sigma_0^{SM}(W^-)$	1	32	33	40	50	50
$\sigma_0/\sigma_0^{SM}(W^+)$	1	32	32	40	50	50
$L [\text{ab}^{-1}]$	2 10	60	60	60	60	300
$\mathcal{D}_{e^-}^-$	0.8	17	18	20	—	—
$\mathcal{D}_{e^-}^+$	0.8	4	4	4	—	—
$\mathcal{D}_{e^-}^0$	0.0	14	—	—	25	25
$\mathcal{D}_{e^+}^-$	0.3	6	6	—	—	—
$\mathcal{D}_{e^+}^+$	0.3	7	7	—	—	—
$\mathcal{D}_{e^+}^0$	0.0	11	—	25	25	25
Δc	0.0	0	0	0	0	0
Δw	0.0	0	0	0	0	0

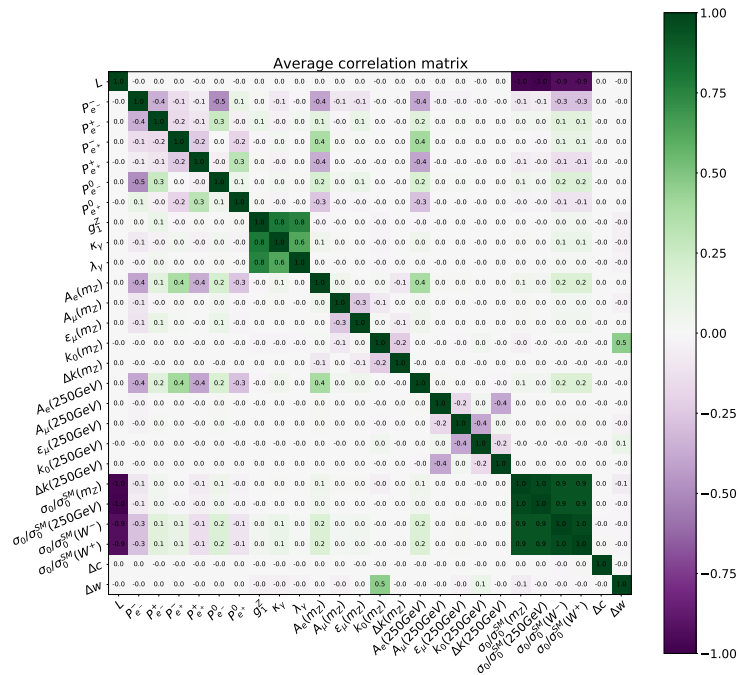
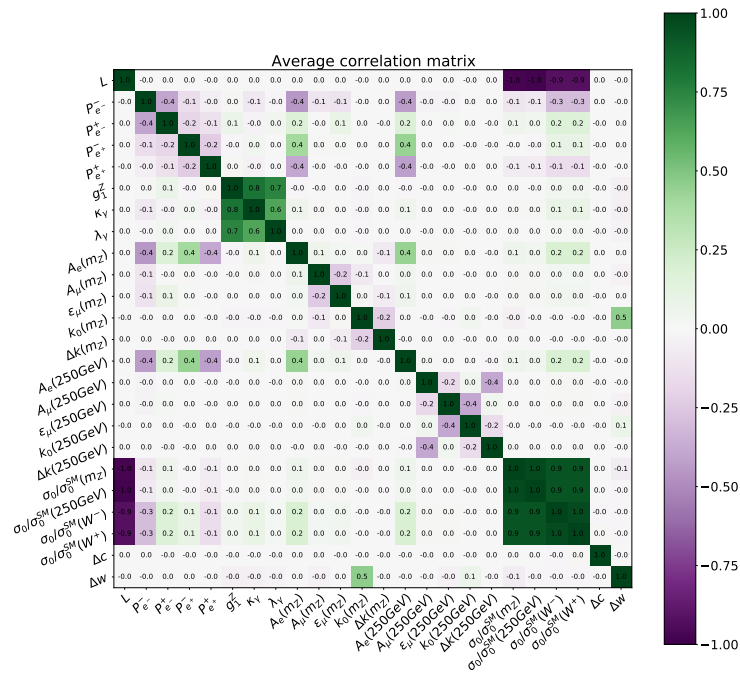


Figure C.11.: (cont.)

C.8. Polarisation measurement with one polarised beam (Details)

The fit on semileptonic W pair production for the scenario with only e^- polarisation observes an \mathcal{D}_{e^-} precision which is a factor 5 worse than the \mathcal{D}_{e^\pm} precision ((80,0) scenario in fig. 7.21c). This begs the question of how the polarisation measurement works in a scenario with only one polarised beam.

Problem definition and notation

In the case of only one polarised beam, the collider measures two datasets (one with positive-sign e^- polarisation and one with negative-sign e^- polarisation). This supplies two event number measurement, one for each dataset. These two event number measurements alone are not sufficient to determine the three involved polarisations (two signed ones for e^- , one unpolarised for e^+).

Fortunately, a measurement of the differential distribution allows a template fit which determines the chiral contributions in each dataset. This leads to $2N_\chi$ measurements, where N_χ is the number of allowed initial states in the considered process. The discussions here will assume $N_\chi = 2$, and that the two allowed initial states are $e_L^- e_R^+$ (shortened “LR” or just “L”) and $e_L^- e_R^+$ (shortened “RL” or just “R”).

Now the measurement consists of four event numbers $\{N_L^+, N_R^+, N_L^-, N_R^-\}$. In reality the measured numbers contain confusion between the LR and the RL initial states, which will typically affect the initial state with lower cross-section more significantly. The calculation here will ignore this correlation to achieve a first estimate of the polarisation uncertainty, and a discussion of the impact of those correlations follows afterwards.

The calculation will further always assume fast helicity reversal, which is necessary for any polarisation measurement from collision data [139]. This means that the two datasets share the same positron polarisation.

The calculation of the uncertainties is rather arduous and lengthy. For this reason, the initial calculation will use a simplified notation, and reintroduce the physical notation afterwards. The simplified notation uses $\{x, y\}$ for the two signed polarisations and z the polarisation for other beam. It combines the chiral cross-sections and the overall normalisation by using the overall normalisation N with a chiral asymmetry A . Like in the W pair production fit, the calculation assumes a free N and a fixed A . Finally, the measurement results are the four event numbers $\{j, k, l, m\}$.

$$\begin{aligned}
 j &= \frac{1}{8}(1-x)(1+z)(1+A)N \\
 k &= \frac{1}{8}(1+x)(1-z)(1-A)N \\
 l &= \frac{1}{8}(1-y)(1+z)(1+A)N \\
 m &= \frac{1}{8}(1+y)(1-z)(1-A)N
 \end{aligned} \tag{C.24}$$

The j and l are the measured LR event numbers, and the k and m are the measured RL event numbers.

Generic calculation for two datasets with a shared polarisation

The problem is now a set of four equations (eq. (C.24)) with four measured values $\{j, k, l, m\}$ and four free parameters $\{x, y, z, N\}$. This problem has a unique solution.

$$x = \frac{j(m-2k) + kl}{kl - jm} \tag{C.25}$$

$$y = \frac{m(j-2l) + kl}{jm - kl} \tag{C.26}$$

$$z = \frac{(1-A)(l-j) + (1+A)(m-k)}{(1-A)(l-j) - (1+A)(m-k)} \tag{C.27}$$

$$N = 2(jm - kl) \frac{(1+A)(k-m) - (1-A)(j-l)}{(1-A^2)(j-l)(k-m)} \tag{C.28}$$

This solution is the starting point for the calculation of the uncertainties on $\{x, y, z\}$. The discussion here will ignore uncertainties on N .

A calculation of the uncertainties on $\{x, y, z\}$ requires a calculation the derivatives with respect to the measured quantities $\{j, k, l, m\}$. For the interpretation of the results it is convenient to express these derivatives again in terms of the physically interesting parameter $\{x, y, z, N, A\}$.

$$\begin{aligned}
 \frac{dx}{dj} &= \frac{-2kl(k-m)}{(jm-kl)^2} = \frac{-4(1+x)(1-y)}{(1+A)N(1+z)(x-y)} \\
 \frac{dx}{dk} &= \frac{2jm(j-l)}{(jm-kl)^2} = \frac{-4(1-x)(1+y)}{(1-A)N(1-z)(x-y)} \\
 \frac{dx}{dl} &= \frac{2jk(k-m)}{(jm-kl)^2} = \frac{4(1-x)(1+x)}{(1+A)N(1+z)(x-y)} \\
 \frac{dx}{dm} &= \frac{-2jk(j-l)}{(jm-kl)^2} = \frac{4(1-x)(1+x)}{(1-A)N(1-z)(x-y)}
 \end{aligned} \tag{C.29}$$

$$\begin{aligned}
 \frac{dy}{dj} &= \frac{-2lm(k-m)}{(jm-kl)^2} = \frac{-4(1+y)(1-y)}{(1+A)N(1+z)(x-y)} \\
 \frac{dy}{dk} &= \frac{2lm(j-l)}{(jm-kl)^2} = \frac{-4(1+y)(1-y)}{(1-A)N(1-z)(x-y)} \\
 \frac{dy}{dl} &= \frac{2jm(k-m)}{(jm-kl)^2} = \frac{4(1-x)(1+y)}{(1+A)N(1+z)(x-y)} \\
 \frac{dy}{dm} &= \frac{-2kl(j-l)}{(jm-kl)^2} = \frac{4(1+x)(1-y)}{(1-A)N(1-z)(x-y)}
 \end{aligned} \tag{C.30}$$

$$\begin{aligned}
 \frac{dz}{dj} &= \frac{-2(1-A)(1+A)(k-m)}{((1+A)(k-m) - (1-A)(j-l))^2} = \frac{-4(1-z)}{(1+A)N(x-y)} \\
 \frac{dz}{dk} &= \frac{2(1-A)(1+A)(j-l)}{((1+A)(k-m) - (1-A)(j-l))^2} = \frac{-4(1+z)}{(1-A)N(x-y)} \\
 \frac{dz}{dl} &= \frac{2(1-A)(1+A)(k-m)}{((1+A)(k-m) - (1-A)(j-l))^2} = \frac{4(1-z)}{(1+A)N(x-y)} \\
 \frac{dz}{dm} &= \frac{-2(1-A)(1+A)(j-l)}{((1+A)(k-m) - (1-A)(j-l))^2} = \frac{4(1+z)}{(1-A)N(x-y)}
 \end{aligned} \tag{C.31}$$

The individual contributions to the Gaussian uncertainty take the usual simple form $(d\alpha/d\beta)^2(\Delta\alpha)^2$, and since the measured values follow a Poisson distribution ($\Delta\alpha = \sqrt{\alpha}$) the contributions each have the form $(d\alpha/d\beta)^2\alpha$.

$$\begin{aligned}
 \left(\frac{dx}{dj}\right)^2 j &= \left(\frac{-4(1+x)(1-y)}{(1+A)N(1+z)(x-y)}\right)^2 \frac{1}{8}(1-x)(1+z)(1+A)N \\
 &= 2\frac{1}{N} \frac{1-x^2}{(x-y)^2} \frac{(1+x)(1-y)^2}{(1+z)(1+A)} \\
 \left(\frac{dx}{dk}\right)^2 k &= \left(\frac{-4(1-x)(1+y)}{(1-A)N(1-z)(x-y)}\right)^2 \frac{1}{8}(1+x)(1-z)(1-A)N \\
 &= 2\frac{1}{N} \frac{1-x^2}{(x-y)^2} \frac{(1-x)(1+y)^2}{(1-z)(1-A)} \\
 \left(\frac{dx}{dl}\right)^2 l &= \left(\frac{4(1-x)(1+x)}{(1+A)N(1+z)(x-y)}\right)^2 \frac{1}{8}(1-y)(1+z)(1+A)N \\
 &= 2\frac{1}{N} \frac{1-x^2}{(x-y)^2} \frac{(1-x)(1+x)(1-y)}{(1+z)(1+A)} \\
 \left(\frac{dx}{dm}\right)^2 m &= \left(\frac{4(1-x)(1+x)}{(1-A)N(1-z)(x-y)}\right)^2 \frac{1}{8}(1+y)(1-z)(1-A)N \\
 &= 2\frac{1}{N} \frac{1-x^2}{(x-y)^2} \frac{(1-x)(1+x)(1+y)}{(1-z)(1-A)}
 \end{aligned} \tag{C.32}$$

$$\begin{aligned}
 \left(\frac{dy}{dj}\right)^2 j &= \left(\frac{-4(1+y)(1-y)}{(1+A)N(1+z)(x-y)}\right)^2 \frac{1}{8}(1-x)(1+z)(1+A)N \\
 &= 2\frac{1}{N} \frac{1-y^2}{(x-y)^2} \frac{(1+y)(1-y)(1-x)}{(1+z)(1+A)} \\
 \left(\frac{dy}{dk}\right)^2 k &= \left(\frac{-4(1+y)(1-y)}{(1-A)N(1-z)(x-y)}\right)^2 \frac{1}{8}(1+x)(1-z)(1-A)N \\
 &= 2\frac{1}{N} \frac{1-y^2}{(x-y)^2} \frac{(1+y)(1-y)(1+x)}{(1-z)(1-A)} \\
 \left(\frac{dy}{dl}\right)^2 l &= \left(\frac{4(1-x)(1+y)}{(1+A)N(1+z)(x-y)}\right)^2 \frac{1}{8}(1-y)(1+z)(1+A)N \\
 &= 2\frac{1}{N} \frac{1-y^2}{(x-y)^2} \frac{(1-x)^2(1+y)}{(1+z)(1+A)} \\
 \left(\frac{dy}{dm}\right)^2 m &= \left(\frac{4(1+x)(1-y)}{(1-A)N(1-z)(x-y)}\right)^2 \frac{1}{8}(1+y)(1-z)(1-A)N \\
 &= 2\frac{1}{N} \frac{1-y^2}{(x-y)^2} \frac{(1+x)^2(1-y)}{(1-z)(1-A)}
 \end{aligned} \tag{C.33}$$

$$\begin{aligned}
 \left(\frac{dz}{dj}\right)^2 j &= \left(\frac{-4(1-z)}{(1+A)N(x-y)}\right)^2 \frac{1}{8}(1-x)(1+z)(1+A)N \\
 &= 2\frac{1}{N} \frac{1-z^2}{(x-y)^2} \frac{(1-z)(1-x)}{1+A} \\
 \left(\frac{dz}{dk}\right)^2 k &= \left(\frac{-4(1+z)}{(1-A)N(x-y)}\right)^2 \frac{1}{8}(1+x)(1-z)(1-A)N \\
 &= 2\frac{1}{N} \frac{1-z^2}{(x-y)^2} \frac{(1+z)(1+x)}{1-A} \\
 \left(\frac{dz}{dl}\right)^2 l &= \left(\frac{4(1-z)}{(1+A)N(x-y)}\right)^2 \frac{1}{8}(1-y)(1+z)(1+A)N \\
 &= 2\frac{1}{N} \frac{1-z^2}{(x-y)^2} \frac{(1-z)(1-y)}{1+A} \\
 \left(\frac{dz}{dm}\right)^2 m &= \left(\frac{4(1+z)}{(1-A)N(x-y)}\right)^2 \frac{1}{8}(1+y)(1-z)(1-A)N \\
 &= 2\frac{1}{N} \frac{1-z^2}{(x-y)^2} \frac{(1+z)(1+y)}{1-A}
 \end{aligned} \tag{C.34}$$

The individual contributions sum up to the squared uncertainty, ignoring any correlations amongst $\{j, k, l, m\}$.

$$\begin{aligned}
 &\left(\frac{dx}{dj}\right)^2 \cdot j + \left(\frac{dx}{dk}\right)^2 \cdot k + \left(\frac{dx}{dl}\right)^2 \cdot l + \left(\frac{dx}{dm}\right)^2 \cdot m \\
 &= 2\frac{1}{N} \frac{1-x^2}{(x-y)^2} \left(\frac{(1+x)(1-y)^2}{(1+z)(1+A)} + \frac{(1-x)(1+y)^2}{(1-z)(1-A)} + \frac{(1-x)(1+x)(1-y)}{(1+z)(1+A)} + \frac{(1-x)(1+x)(1+y)}{(1-z)(1-A)} \right) \\
 &= 2\frac{1}{N} \frac{1-x^2}{(x-y)^2} \left(\frac{(1+x)(1-y)(2-x-y)}{(1+A)(1+z)} + \frac{(1-x)(1+y)(2+x+y)}{(1-A)(1-z)} \right)
 \end{aligned} \tag{C.35}$$

$$\begin{aligned}
 &\left(\frac{dy}{dj}\right)^2 \cdot j + \left(\frac{dy}{dk}\right)^2 \cdot k + \left(\frac{dy}{dl}\right)^2 \cdot l + \left(\frac{dy}{dm}\right)^2 \cdot m \\
 &= 2\frac{1}{N} \frac{1-y^2}{(x-y)^2} \left(\frac{(1+y)(1-y)(1-x)}{(1+z)(1+A)} + \frac{(1+y)(1-y)(1+x)}{(1-z)(1-A)} + \frac{(1-x)^2(1+y)}{(1+z)(1+A)} + \frac{(1+x)^2(1-y)}{(1-z)(1-A)} \right) \\
 &= 2\frac{1}{N} \frac{1-y^2}{(x-y)^2} \left(\frac{(1-x)(1+y)(2-x-y)}{(1+A)(1+z)} + \frac{(1+x)(1-y)(2+x+y)}{(1-A)(1-z)} \right)
 \end{aligned} \tag{C.36}$$

$$\begin{aligned}
& \left(\frac{dz}{dj}\right)^2 \cdot j + \left(\frac{dz}{dk}\right)^2 \cdot k + \left(\frac{dz}{dl}\right)^2 \cdot l + \left(\frac{dz}{dm}\right)^2 \cdot m \\
&= 2 \frac{1}{N} \frac{1-z^2}{(x-y)^2} \left(\frac{(1-z)(1-x)}{1+A} + \frac{(1+z)(1+x)}{1-A} + \frac{(1-z)(1-y)}{1+A} + \frac{(1+z)(1+y)}{1-A} \right) \\
&= 2 \frac{1}{N} \frac{1-z^2}{(x-y)^2} \left(\frac{(1-z)(2-x-y)}{1+A} + \frac{(1+z)(2+x+y)}{1-A} \right)
\end{aligned} \tag{C.37}$$

And finally, the uncertainties emerge from the square-root of the summed contribution.

$$\Delta x = \frac{1}{\sqrt{N}} \sqrt{2} \sqrt{\frac{1-x^2}{(x-y)^2} \sqrt{\frac{(1+x)(1-y)(2-x-y)}{(1+A)(1+z)} + \frac{(1-x)(1+y)(2+x+y)}{(1-A)(1-z)}}} \tag{C.38}$$

$$\Delta y = \frac{1}{\sqrt{N}} \sqrt{2} \sqrt{\frac{1-y^2}{(x-y)^2} \sqrt{\frac{(1-x)(1+y)(2-x-y)}{(1+A)(1+z)} + \frac{(1+x)(1-y)(2+x+y)}{(1-A)(1-z)}}} \tag{C.39}$$

$$\Delta z = \frac{1}{\sqrt{N}} \sqrt{2} \sqrt{\frac{1-z^2}{(x-y)^2} \sqrt{\frac{(1-z)(2-x-y)}{1+A} + \frac{(1+z)(2+x+y)}{1-A}}} \tag{C.40}$$

The uncertainties are symmetric between x and y since the initial problem formulation (eq. (C.24)) is symmetric under them as well.

Reintroducing physical nomenclature

With the more lengthy steps of the calculation out of the way, a more physical nomenclature reintroduces meaning into the equations. The polarisation $\{x, y, z\}$ are identified with the two signed e^- polarisation and the one e^+ polarisation.

$$\begin{aligned}
x &= \mathcal{D}_{e^-}^+ (> 0) \\
y &= \mathcal{D}_{e^-}^- (< 0) \\
z &= \mathcal{D}_{e^+}^0 (= 0)
\end{aligned} \tag{C.41}$$

The normalisation N identifies with the unpolarised total event number and the asymmetry A is the left-right asymmetry (compare eq. (7.13)).

$$\begin{aligned}
N &= N_0 = L\sigma_0 \\
A &= A_{LR}
\end{aligned} \tag{C.42}$$

This gives an exact meaning to the measured event numbers $\{j, k, l, m\}$, since the polarisation signs define the dataset and the asymmetry definition defines the chirality of

each event number.

$$\begin{aligned}
 j &= N_L^+ \\
 k &= N_R^+ \\
 l &= N_L^- \\
 m &= N_R^-
 \end{aligned} \tag{C.43}$$

This physical nomenclature (eqs. (C.41) to (C.43)) yields the physically meaningful versions of problem and solution (eqs. (C.24) and (C.25)).

The measured quantities are the four event numbers.

$$\begin{aligned}
 N_L^+ &= \frac{1}{8} (1 - \mathcal{D}_{e^+}^+) (1 + \mathcal{D}_{e^+}^0) (1 + A_{LR}) N_0 \\
 N_R^+ &= \frac{1}{8} (1 + \mathcal{D}_{e^+}^+) (1 - \mathcal{D}_{e^+}^0) (1 - A_{LR}) N_0 \\
 N_L^- &= \frac{1}{8} (1 - \mathcal{D}_{e^-}^-) (1 + \mathcal{D}_{e^-}^0) (1 + A_{LR}) N_0 \\
 N_R^- &= \frac{1}{8} (1 + \mathcal{D}_{e^-}^-) (1 - \mathcal{D}_{e^-}^0) (1 - A_{LR}) N_0
 \end{aligned} \tag{C.44}$$

The four equations transform into four equations on the polarisations and the unpolarised total event number.

$$\mathcal{D}_{e^+}^+ = \frac{N_L^+ (N_R^- - 2N_R^+) + N_R^+ N_L^-}{N_R^+ N_L^- - N_L^+ N_R^-} \tag{C.45}$$

$$\mathcal{D}_{e^-}^- = \frac{N_R^- (N_L^+ - 2N_L^-) + N_L^- N_R^+}{N_L^+ N_R^- - N_R^- N_L^+} \tag{C.46}$$

$$\mathcal{D}_{e^+}^0 = \frac{(1 - A_{LR}) (N_L^- - N_L^+) + (1 + A_{LR}) (N_R^- - N_R^+)}{(1 - A_{LR}) (N_L^- - N_L^+) - (1 + A_{LR}) (N_R^- - N_R^+)} \tag{C.47}$$

$$N_0 = 2 (N_L^+ N_R^- - N_R^+ N_L^-) \frac{(1 + A_{LR}) (N_R^+ - N_R^-) - (1 - A_{LR}) (N_L^+ - N_L^-)}{(1 - A_{LR}^2) (N_L^+ - N_L^-) (N_R^+ - N_R^-)} \tag{C.48}$$

Simple error propagation yields the uncertainty in the polarisations assuming that

the measured event numbers are uncorrelated.

$$\Delta \mathcal{P}_{e^+} = \frac{1}{\sqrt{N_0}} \sqrt{2} \sqrt{\frac{1 - (\mathcal{P}_{e^+}^-)^2}{(\mathcal{P}_{e^+}^+ - \mathcal{P}_{e^+}^-)^2}} \times \sqrt{\frac{(1 + \mathcal{P}_{e^+}^+) (1 - \mathcal{P}_{e^+}^-) (2 - \mathcal{P}_{e^+}^+ - \mathcal{P}_{e^+}^-)}{(1 + A_{LR}) (1 + \mathcal{P}_{e^+}^0)} + \frac{(1 - \mathcal{P}_{e^+}^+) (1 + \mathcal{P}_{e^+}^-) (2 + \mathcal{P}_{e^+}^+ + \mathcal{P}_{e^+}^-)}{(1 - A_{LR}) (1 - \mathcal{P}_{e^+}^0)}} \quad (\text{C.49})$$

$$\Delta \mathcal{P}_{e^-} = \frac{1}{\sqrt{N_0}} \sqrt{2} \sqrt{\frac{1 - (\mathcal{P}_{e^-}^-)^2}{(\mathcal{P}_{e^-}^+ - \mathcal{P}_{e^-}^-)^2}} \times \sqrt{\frac{(1 - \mathcal{P}_{e^-}^+) (1 + \mathcal{P}_{e^-}^-) (2 - \mathcal{P}_{e^-}^+ - \mathcal{P}_{e^-}^-)}{(1 + A_{LR}) (1 + \mathcal{P}_{e^-}^0)} + \frac{(1 + \mathcal{P}_{e^-}^+) (1 - \mathcal{P}_{e^-}^-) (2 + \mathcal{P}_{e^-}^+ + \mathcal{P}_{e^-}^-)}{(1 - A_{LR}) (1 - \mathcal{P}_{e^-}^0)}} \quad (\text{C.50})$$

$$\Delta \mathcal{P}_{e^+}^0 = \frac{1}{\sqrt{N_0}} \sqrt{2} \sqrt{\frac{1 - (\mathcal{P}_{e^+}^0)^2}{(\mathcal{P}_{e^+}^+ - \mathcal{P}_{e^+}^-)^2}} \sqrt{\frac{(1 - \mathcal{P}_{e^+}^0) (2 - \mathcal{P}_{e^+}^+ - \mathcal{P}_{e^+}^-)}{1 + A_{LR}} + \frac{(1 + \mathcal{P}_{e^+}^0) (2 + \mathcal{P}_{e^+}^+ + \mathcal{P}_{e^+}^-)}{1 - A_{LR}}} \quad (\text{C.51})$$

The uncertainties diverge to infinity if the two electron polarisations are exactly the same (including the sign). This demonstrates that a measurement requires two datasets with different polarisation values, and the more different the smaller the uncertainty. Another notable conclusion is that a polarisation measurement is possible even if $A_{LR} = 0$ as long as the shape measurement can distinguish the initial states.

Uncertainty in scenario with one polarised beam

The scenarios in the fit are a step more specific. They assume that the two beam polarisation settings of the e^- beam are the result of fast helicity reversal, which means that they have approximately the same central value \mathcal{P}_{e^-} . In addition, the polarisation of the positron beam has a central values of zero.

$$\begin{aligned} \mathcal{P}_{e^+}^+ &\approx \mathcal{P}_{e^-} > 0 \\ \mathcal{P}_{e^+}^- &\approx -\mathcal{P}_{e^-} < 0 \\ \mathcal{P}_{e^+}^0 &\approx 0 \end{aligned} \quad (\text{C.52})$$

These assumptions simplify the more general form for the polarisation uncertainties (eq. (C.49)).

$$\begin{aligned}
 \Delta \mathcal{P}_{e^+} &= \frac{1}{\sqrt{N_0}} \sqrt{2} \sqrt{\frac{1 - \mathcal{P}_{e^-}^2}{(2\mathcal{P}_{e^-})^2} \sqrt{2 \frac{(1 + \mathcal{P}_{e^-})(1 + \mathcal{P}_{e^-})}{1 + A_{LR}} + 2 \frac{(1 - \mathcal{P}_{e^-})(1 - \mathcal{P}_{e^-})}{1 - A_{LR}}} \\
 &= \frac{1}{\sqrt{N_0}} \sqrt{\frac{1 - \mathcal{P}_{e^-}^2}{\mathcal{P}_{e^-}^2} \sqrt{\frac{(1 + \mathcal{P}_{e^-})^2}{1 + A_{LR}} + \frac{(1 - \mathcal{P}_{e^-})^2}{1 - A_{LR}}}
 \end{aligned} \tag{C.53}$$

$$\begin{aligned}
 \Delta \mathcal{P}_{e^-} &= \frac{1}{\sqrt{N_0}} \sqrt{2} \sqrt{\frac{1 - \mathcal{P}_{e^-}^2}{(2\mathcal{P}_{e^-})^2} \sqrt{2 \frac{(1 - \mathcal{P}_{e^-})(1 - \mathcal{P}_{e^-})}{1 + A_{LR}} + 2 \frac{(1 + \mathcal{P}_{e^-})(1 + \mathcal{P}_{e^-})}{1 - A_{LR}}} \\
 &= \frac{1}{\sqrt{N_0}} \sqrt{\frac{1 - \mathcal{P}_{e^-}^2}{\mathcal{P}_{e^-}^2} \sqrt{\frac{(1 - \mathcal{P}_{e^-})^2}{1 + A_{LR}} + \frac{(1 + \mathcal{P}_{e^-})^2}{1 - A_{LR}}}
 \end{aligned} \tag{C.54}$$

$$\begin{aligned}
 \Delta \mathcal{P}_{e^+}^0 &= \frac{1}{\sqrt{N_0}} \sqrt{2} \sqrt{\frac{1}{(2\mathcal{P}_{e^-})^2} \sqrt{\frac{2}{1 + A_{LR}} + \frac{2}{1 - A_{LR}}}} \\
 &= \frac{1}{\sqrt{N_0}} \frac{1}{|\mathcal{P}_{e^-}|} \sqrt{\frac{1}{1 + A_{LR}} + \frac{1}{1 - A_{LR}}}
 \end{aligned} \tag{C.55}$$

The formulas for the electron polarisation now give a direct hint for why there can be a stark difference between the uncertainties of the two e^- polarisation: the large $(1 + \mathcal{P}_{e^-})^2$ can get suppressed or enhanced by the asymmetry factor $(1 \pm A_{LR})$. If the asymmetry is large, one of the two e^- polarisations will see a much higher uncertainty than the other, depending on the sign of A_{LR} . Since A_{LR} tends to be positive in the SM, the e^+ polarisation will usually get a lower uncertainty.

Specific case in semileptonic W pair production fit

The specific case of the fit to semileptonic W pair production uses an e^- polarisation of 80% and finds an asymmetry of approximately 0.98 for the process. Entering these two values already demonstrates the difference in the polarisation uncertainties for the two e^- polarisation settings.

$$\begin{aligned}
\Delta \mathcal{D}_{e^-}^+ &= \frac{1}{\sqrt{N_0}} \sqrt{\frac{0.36}{0.64}} \sqrt{\frac{3.24}{1.98} + \frac{0.04}{0.02}} \approx \frac{1}{\sqrt{N_0}} \cdot 0.316 \cdot 1.907 \approx \frac{1}{\sqrt{N_0}} \cdot 0.60 \\
\Delta \mathcal{D}_{e^-}^- &= \frac{1}{\sqrt{N_0}} \sqrt{\frac{0.36}{0.64}} \sqrt{\frac{0.04}{1.98} + \frac{3.24}{0.02}} \approx \frac{1}{\sqrt{N_0}} \cdot 0.316 \cdot 12.729 \approx \frac{1}{\sqrt{N_0}} \cdot 4.02 \\
\Delta \mathcal{D}_{e^+}^0 &= \frac{1}{\sqrt{N_0}} \frac{1}{0.8} \sqrt{\frac{1}{1.98} + \frac{1}{0.02}} \approx \frac{1}{\sqrt{N_0}} \cdot 1.25 \cdot 7.107 \approx \frac{1}{\sqrt{N_0}} \cdot 8.88
\end{aligned} \tag{C.56}$$

The uncertainty on $\mathcal{D}_{e^-}^-$ is around 6.7 times larger than the uncertainty on $\mathcal{D}_{e^-}^+$.

With the values of the luminosity $L = 2 \text{ ab}^{-1}$ and the unpolarised cross-section $\sigma_0 = 18952.6 \text{ fb}$, the calculation makes a specific prediction of the expected polarisation uncertainties.

$$\begin{aligned}
\Delta \mathcal{D}_{e^-}^+ &\approx 9.75 \cdot 10^{-5} \Rightarrow \left| \frac{\Delta \mathcal{D}_{e^-}^+}{\mathcal{D}_{e^-}^+} \right| \approx 1.22 \cdot 10^{-4} \\
\Delta \mathcal{D}_{e^-}^- &\approx 6.53 \cdot 10^{-4} \Rightarrow \left| \frac{\Delta \mathcal{D}_{e^-}^-}{\mathcal{D}_{e^-}^-} \right| \approx 8.16 \cdot 10^{-4} \\
\Delta \mathcal{D}_{e^+}^0 &\approx 1.44 \cdot 10^{-3}
\end{aligned} \tag{C.57}$$

Compared to the fit result of these uncertainties (bars of (80,0) scenario in fig. 7.21c), this prediction is a significant underestimation. In particular, the fit does not show any improvement of the $\mathcal{D}_{e^-}^-$ or $\mathcal{D}_{e^+}^0$ measurement beyond the polarimeter constraints. The discussion below will show that the failure of this estimate comes from the assumption that it is possible to measure each chiral event number in an undisturbed way.

Understanding the uncertainties for highly polarised beam

The reason for why the predicted precisions are much better than the ones in the fit becomes clear when looking at the case of highly polarised beams. In this discussion, this case is roughly fulfilled when the e^- is at or above 90%. The conclusion of the discussion are qualitative, so that a somewhat lower polarisation does not affect the results.

The high level of polarisation affects the ratios of event numbers between the datasets.

$$\begin{aligned}
 \frac{N_L^-}{N_L^+} &= \frac{1 - \mathcal{D}_{e^-}^-}{1 - \mathcal{D}_{e^-}^+} \gtrsim 10 \\
 \frac{N_R^+}{N_R^-} &= \frac{1 + \mathcal{D}_{e^-}^+}{1 + \mathcal{D}_{e^-}^-} \gtrsim 10 \\
 \Rightarrow N_R^+ N_L^- &\gg N_L^+ N_R^-
 \end{aligned} \tag{C.58}$$

This allows an approximation of the formulas for the e^- polarisations (eq. (C.45)) that gives direct insight into what drives the uncertainties.

$$\begin{aligned}
 \mathcal{D}_{e^-}^+ &= \frac{N_L^+ (N_R^- - 2N_R^+) + N_R^+ N_L^-}{N_R^+ N_L^- - N_L^+ N_R^-} = \frac{\frac{N_L^+ N_R^-}{N_R^+ N_L^-} - 2\frac{N_L^+}{N_L^-} + 1}{1 - \frac{N_L^+ N_R^-}{N_R^+ N_L^-}} \\
 &= 1 - 2\frac{N_L^+}{N_L^-} + O\left(\frac{N_L^+ N_R^-}{N_R^+ N_L^-}\right) \\
 \mathcal{D}_{e^-}^- &= \frac{N_R^- (N_L^+ - 2N_L^-) + N_R^+ N_L^-}{N_L^+ N_R^- - N_R^+ N_L^-} = \frac{\frac{N_L^+ N_R^-}{N_R^+ N_L^-} - 2\frac{N_R^-}{N_R^+} + 1}{\frac{N_L^+ N_R^-}{N_R^+ N_L^-} - 1} \\
 &= -\left(1 - 2\frac{N_R^-}{N_R^+}\right) + O\left(\frac{N_L^+ N_R^-}{N_R^+ N_L^-}\right)
 \end{aligned} \tag{C.59}$$

For the positive-sign polarisation $\mathcal{D}_{e^-}^+$, the ratio of left-handed events N_L^+/N_L^- in the two datasets determines the precision. For the negative-sign polarisation $\mathcal{D}_{e^-}^-$, the ratio of right-handed events N_R^-/N_R^+ in the two datasets determines the precision. This result made no assumption about the left-right asymmetry, and only relies on a high degree of polarisation.

A high asymmetry value will cause two things to happen. First, it will lead to a significantly higher number of signal events for one of the initial states (here LR), which then leads to a significantly better precision for one of the e^- polarisations (here $\mathcal{D}_{e^-}^+$). This is already reflected in the previous formulas for the e^- uncertainties (eqs. (C.53) and (C.54)).

The second consequence of a high asymmetry value is that it will be much harder to distinguish the initial state with the lower cross-section from the high-cross-section background. Here, a measurement of the number of LR events is unproblematic due to the high cross-section, which allows a precise $\mathcal{D}_{e^-}^+$ measurement. Meanwhile, a measurement of the RL events suffers a huge background of LR events, which will boost the statistical uncertainty on N_R^+ and N_R^- . The result is that the measurement of $\mathcal{D}_{e^-}^-$ becomes strongly disturbed. This explains why the fit does not see an improvement on the $\mathcal{D}_{e^-}^-$ precision beyond the polarimeter constraint.

Similarly to the e^- polarisation, the formula for the e^+ polarisation (eq. (C.45)) has a structure of ratios that allows an approximation.

$$\mathcal{D}_{e^+}^0 = \frac{(1 - A_{LR})(N_L^- - N_L^+) + (1 + A_{LR})(N_R^- - N_R^+)}{(1 - A_{LR})(N_L^- - N_L^+) - (1 + A_{LR})(N_R^- - N_R^+)} = \frac{1 + \frac{1+A_{LR}}{1-A_{LR}} \frac{N_R^- - N_R^+}{N_L^- - N_L^+}}{1 - \frac{1+A_{LR}}{1-A_{LR}} \frac{N_R^- - N_R^+}{N_L^- - N_L^+}} \quad (\text{C.60})$$

The relevant ratio is $(N_R^- - N_R^+) / (N_L^- - N_L^+)$, and each of the differences in the ratio contains one clearly dominant number (eq. (C.58))

$$\frac{N_R^- - N_R^+}{N_L^- - N_L^+} \approx -\frac{N_R^-}{N_L^+} \quad (\text{C.61})$$

The positron polarisation therefore requires precision on both LR and RL events. In the case of high asymmetry - no matter which sign of the asymmetry - the positron polarisation precision will suffer from the high background on one of the two event numbers.

C.g. Unpolarised polarisation measurement in W pair production

A polarised collider measures the polarisations from the differences between polarised datasets. Unpolarised colliders can not apply this method, as they only have one unpolarised dataset available. The tested unpolarised case in the electroweak fit demonstrates that polarimeter fully determines the polarisation uncertainty (section 7.7.1).

This picture changes when the fit assumes the cross-section of W pair production to be known. In that case, the unpolarised collider shows an improvement of the polarisation precision wrt. the pure polarimeter constraints. The core of this behaviour lies in the measurement of the differential distributions, in the sensitivities of the two allowed initial states to the different parameters, and in the additional constraint from the polarimeters.

To see this, one can start with the assumption that the differential distribution

$$N^{bin} = N_L^{bin} + N_R^{bin} = N_L * f_L^{bin} + N_R * f_R^{bin} \quad (\text{C.62})$$

separates the two contributions sufficiently to essentially treat it as an independent measurement of N_L and N_R ($L/R =$ initial electron chirality). The general formula for $N_{L/R}$ is

$$\begin{aligned} N_L &= L \frac{1 - \mathcal{P}_{e^-}}{2} \frac{1 + \mathcal{P}_{e^+}}{2} \frac{1 + A + \Delta A}{2} (1 + \Delta\alpha) \sigma_0, \\ N_R &= L \frac{1 + \mathcal{P}_{e^-}}{2} \frac{1 - \mathcal{P}_{e^+}}{2} \frac{1 - A - \Delta A}{2} (1 + \Delta\alpha) \sigma_0, \end{aligned} \quad (\text{C.63})$$

where $\delta\alpha = \delta\sigma_0/\sigma_0$ is the deviation of the relative unpolarised cross-section. From this follows the single parameter sensitivity from N_L and N_R on the individual parameters (ignoring any correlation):

$$S_{L/R}^{par} = \frac{1}{\sqrt{N_{L/R}}} \left| \frac{dN_{L/R}}{dpar} \right| \Delta par. \quad (C.64)$$

Equating $S_{L/R}^{par} = 1$ yields the most optimistic achievable precision Δpar from $N_{L/R}$:

$$\begin{aligned} S_L^{\mathcal{D}_{e^+}, \mathcal{D}_{e^-}, \Delta\alpha} &\approx 3.3 \cdot 10^{-4}, & S_L^{\Delta A} &\approx 6.5 \cdot 10^{-4}, \\ S_R^{\mathcal{D}_{e^+}, \mathcal{D}_{e^-}, A} &\approx 3.4 \cdot 10^{-3}, & S_R^{\Delta A} &\approx 6.2 \cdot 10^{-5}. \end{aligned} \quad (C.65)$$

Any free directions in the parameter space, meaning simultaneous changes of parameters that leave N_L and N_R constant, will mean no sensitivity and no constraint from the fit in that direction. The polarisation factors leave one approximately free direction $\mathcal{D}_{e^-} = \mathcal{D}_{e^+}$:

$$(1 \mp \mathcal{D}_{e^-}) (1 \pm \mathcal{D}_{e^+}) = 1 \mp \mathcal{D}_{e^-} \pm \mathcal{D}_{e^+} - \mathcal{D}_{e^-} \mathcal{D}_{e^+}. \quad (C.66)$$

WW data can only constrain this direction if it is sensitive to \mathcal{D}^2 . Remembering that minimal polarisation uncertainties come from polarimeter constraints of $2.5 \cdot 10^{-3}$, the sensitivity to the quadratic polarisation term would need to be in the order of 10^{-6} , far below WW sensitivities. The polarimeters therefore determine precision in otherwise free $\mathcal{D}_{e^-} = \mathcal{D}_{e^+}$ direction.

The constraint in that direction is the best possible precision achievable from WW. Since this is one specific combined direction, the two polarimeters set a combined constraint.

$$\begin{aligned} \chi_{\mathcal{D}\text{-constraint}}^2 &= \left(\frac{\mathcal{D}_{e^-} - 0}{\Delta \mathcal{D}_{e^-}} \right)^2 + \left(\frac{\mathcal{D}_{e^+} - 0}{\Delta \mathcal{D}_{e^+}} \right)^2 \stackrel{\mathcal{D}_{e^-} = \mathcal{D}_{e^+} = \mathcal{D}}{=} \left(\frac{1}{\frac{1}{\Delta \mathcal{D}_{e^-}} + \frac{1}{\Delta \mathcal{D}_{e^+}}} \mathcal{D} \right)^2 \\ &\stackrel{\Delta \mathcal{D}_{e^-} = \Delta \mathcal{D}_{e^+} = \Delta \mathcal{D}}{=} \left(\frac{\mathcal{D}}{\Delta \mathcal{D} / \sqrt{2}} \right)^2 \end{aligned} \quad (C.67)$$

This reflects the behaviour that is visible in the fit with a fixed cross-section and luminosity (fig. 7.21c).

To understand what happens in the case of a free cross-section parameter, one can turn back to individual best sensitivities for 2 ab^{-1} . These show that there is no significant sensitivity to quadratic \mathcal{D} terms in N_L , and almost no sensitivity to \mathcal{D} terms in N_R . Consequently, one can fix the corresponding \mathcal{D} term to zero, simplifying the formulas

Appendix

for N_L and N_R .

$$\begin{aligned} N_L &\approx L \frac{1 - \mathcal{D}_{e^-} + \mathcal{D}_{e^+}}{4} \frac{1 + A + \Delta A}{2} (1 + \Delta\alpha) \sigma_0 \\ N_R &\approx L \frac{1}{4} \frac{1 - A - \Delta A}{2} (1 + \Delta\alpha) \sigma_0 \end{aligned} \quad (\text{C.68})$$

In addition, the unpolarised cross-section sensitivity comes almost exclusively from N_L , and the asymmetry sensitivity almost exclusively from N_R , simplifying again the formulas.

$$\begin{aligned} N_L &\approx L \frac{1 - \mathcal{D}_{e^-} + \mathcal{D}_{e^+}}{4} (1 + \Delta\alpha) \sigma_0 \\ N_R &\approx L \frac{1}{4} \frac{1 - A - \Delta A}{2} \sigma_0 \end{aligned} \quad (\text{C.69})$$

This opens a new (almost) free direction in the 3D parameter plane of the polarisations and unpolarised cross-section

$$\mathcal{D}_{e^-} = \mathcal{D}_{e^+} + \frac{\Delta\alpha}{1 + \Delta\alpha} \approx \mathcal{D}_{e^+} + \Delta\alpha \quad (\text{C.70})$$

leading back to an independence of the two polarisations. When the unpolarised cross-section is a free parameter, the WW process does not yield any additional polarisation constraint in any direction. Only the individual polarimeter precisions determine the polarisation precisions in this case, which reflects the results of the fit. Having the asymmetry as free parameter does not significantly influence polarisation measurement, since it is almost exclusively measured in N_R .

Acknowledgements

I want to express my gratitude for all the people that supported me through these years.

Thank you to Dr. Jenny List for the opportunity of this research project in her group and under her supervision, for our discussions, and your guidance and feedback. I also thank Prof. Dr. Elisabetta Gallo, who took on her role as my second supervisor and also provided me support and guidance.

My gratitude goes to my mentors Dr. Marcel Stanitzki and Dr. Ties Behnke, for their help during my struggles of both technical and professional nature.

I want to thank Dr. Robert Karl, who provided me with his work and experience, and who took time to explain many of the technical and physical details.

Thank you as well to Dr. Daniel Heuchel and Dr. Swathi Sasikumar for proofreading my thesis and for your kind and invaluable feedback.

A general thank-you goes out to the FLC / FTX group, for many fun times on and off campus, inspiring conversations, and for all the ways they helped me through this project. Swathi and Rémi, for all our shenanigans, our lovely and crazy times together, your technical and emotional support, and for your friendships, I cannot thank you enough. Thank you also to all my office mates (Yasser, Rajendra, Olin, ...), for gifting me with a wonderful atmosphere and many enjoyable conversations both around physics and about life in general. Marius, thank you for always providing me - and everyone - with an open ear, and for pushing me to become an active member of society.

Thank you so much to Julien - my flatmate, friend, home office colleague and life coach when necessary - for our countless conversations at all times of the day, for getting me at least mildly interested in football, and for making sure I have at least a minimum of social life even during a pandemic. And thank you to Áron for your friendship and your understanding and support in some of my most troubled times.

My deepest gratitude goes to Buva (and Reiko, obvio). I am infinitely grateful for your support, love and patience. You helped me persist, gave me perspective, and made my days brighter.

Erklärung

Hiermit versichere ich an Eides statt, die vorliegende Dissertationsschrift selbst verfasst und keine anderen als die angegebenen Hilfsmittel und Quellen benutzt zu haben.

Hamburg, den

Unterschrift des Doktoranden